Instituto Alberto Luiz Coimbra de
Pós-Graduação e Pesquisa de Engenharia
COPPE
UFRJ

MOONPOOL DIMENSIONS AND POSITION OPTIMIZATION WITH GENETIC ALGORITHM OF A DRILLSHIP IN RANDOM SEAS

Lucas do Vale Machado

Tese de Doutorado apresentada ao Programa de Pós-graduação em Engenharia Oceânica, COPPE, da Universidade Federal do Rio de Janeiro, como parte dos requisitos necessários à obtenção do título de Doutor em Engenharia Oceânica.

Orientador: Antonio Carlos Fernandes

Rio de Janeiro
Dezembro de 2020

MOONPOOL DIMENSIONS AND POSITION OPTIMIZATION WITH GENETIC ALGORITHM OF A DRILLSHIP IN RANDOM SEAS

Lucas do Vale Machado

TESE SUBMETIDA AO CORPO DOCENTE DO INSTITUTO ALBERTO LUIZ COIMBRA DE PÓS-GRADUAÇÃO E PESQUISA DE ENGENHARIA DA UNIVERSIDADE FEDERAL DO RIO DE JANEIRO COMO PARTE DOS REQUISITOS NECESSÁRIOS PARA A OBTENÇÃO DO GRAU DE DOUTOR EM CIÊNCIAS EM ENGENHARIA OCEÂNICA.

Orientador: Antonio Carlos Fernandes

Aprovada por: Prof. Antonio Carlos Fernandes
Prof. Joel Sena Sales Junior
Prof. Juan Bautista Villa Wanderley
Prof. Marcelo José Colaço
Prof. Guilherme Rosa Franzini

RIO DE JANEIRO, RJ – BRASIL
DEZEMBRO DE 2020

Machado, Lucas do Vale

Moonpool Dimensions and Position Optimization with Genetic Algorithm of a Drillship in Random Seas/Lucas do Vale Machado. – Rio de Janeiro: UFRJ/COPPE, 2020.

XXIX, 151 p.: il.; 29, 7cm.

Orientador: Antonio Carlos Fernandes

Tese (doutorado) – UFRJ/COPPE/Programa de Engenharia Oceânica, 2020.

Referências Bibliográficas: p. 139 – 147.

1. Moonpool. 2. Drillship. 3. Optimization. 4. Genetic Algorithm. 5. Potential Theory. 6. Computational Fluid Dynamics. 7. Random Seas. I. Fernandes, Antonio Carlos. II. Universidade Federal do Rio de Janeiro, COPPE, Programa de Engenharia Oceânica. III. Título.

"Failure is not an option."
Arnold Schwarzenegger

Agradecimentos

This work is a joint effort between Keppel Offshore and Marine and Laboratório de Ondas e Correntes (LOC—COPPE/UFRJ). Due to that, the author would like to express his gratitude to support given by Keppel Offshore and Marine. Mainly to people that made this possible, as Basil, Anis and Aziz, among others.

I would like to offer my special thanks to my supervisor Dr. Antonio Fernandes and also the committee for the critics that improved a lot this work. Dr. Joel Sales, as a friend and member of committee, gave me insightful feedback that improved my thinking and brought my work to a higher level.

I would also like to extend my thanks to the technicians of the laboratory, Luiz and Douglas, and also the department staff for their help in offering me the resources in concluding my studies.

In addition, I wish to thank thank my parents and brothers for their support and encouragement throughout my study. I could not have completed this dissertation without the support of my friends, Daniel, Ricardo, Ana, Emerson, Amini and Peyman. Also to my girlfriend Isabela, who provided stimulating discussions as well as happy distractions to rest my mind outside of my research. Fairly, I would like to thank Mariana for supporting me at the beginning of my doctorate.

Resumo da Tese apresentada à COPPE/UFRJ como parte dos requisitos necessários para a obtenção do grau de Doutor em Ciências (D.Sc.)

OTIMIZAÇÃO DAS DIMENSÕES E POSIÇÃO DO MOONPOOL DE UM NAVIO-SONDA EM MAR ALEATÓRIO UTILIZANDO ALGORITMO GENÉTICO

Lucas do Vale Machado

Dezembro/2020

Orientador: Antonio Carlos Fernandes

Programa: Engenharia Oceânica

Apresenta-se, nesta tese, um método para efetuar a otimização de um perfil de moonpool (dimensões e posicionamento no casco), minimizando movimentos da água no interior do moonpool ou movimentos da embarcação, para um navio-sonda em operação, quando em mar de proa ($\beta = 180.0°$), para uma onda regular ou um mar aleatório.

O estudo é dividido em duas etapas. Na primeira é feito um estudo analítico e numérico do movimento da água no interior do moonpool, com intuito de entender a física do fenômeno e conhecer os parâmetros para realização do objetivo da tese. Na segunda etapa, utiliza-se um algoritmo de otimização, conhecido como *Algoritmo Genético* (AG), para efetuar a otimização do perfil em si.

Na primeira parte, baseando-se em trabalho conhecido na literatura, uma equação para o movimento da água no interior de um *moonpool retangular* é deduzida e dela é possível tirar coeficientes hidrodinâmicos importantes como frequência natural e amortecimento crítico. Atráves de análises numéricas feitas com código comercial em CFD (Computational Fluid Dynamics), algumas observações são feitas sobre a dinâmica desse movimento com relação ao movimento do corpo. Além do mais, é realizado um estudo para implementação de amortecimento viscoso artifical em um código de teoria potencial com uso de uma espécie de *tampa numérica* no moonpool. O objetivo principal da primeira parte é calcular o amortecimento viscoso para implementação na teoria potencial na segunda parte.

Na segunda parte, é mostrada a implementação do Algoritmo Genético (AG) com a utilização de um código desenvolvido para a tese. Resultados mostram a capacidade do algoritmo de encontrar perfis que obedecem os critérios estabelecidos pelo usuário. Outro fator observado é um forte acoplamento entre movimentos de *afundamento* da embarcação com movimentos da água no moonpool. Com isso, é possível otimizar o moonpool para utilização como amortecedor de movimentos da embarcação.

Abstract of Thesis presented to COPPE/UFRJ as a partial fulfillment of the requirements for the degree of Doctor of Science (D.Sc.)

MOONPOOL DIMENSIONS AND POSITION OPTIMIZATION WITH GENETIC ALGORITHM OF A DRILLSHIP IN RANDOM SEAS

Lucas do Vale Machado

December/2020

Advisor: Antonio Carlos Fernandes

Department: Ocean Engineering

In this work, we present a method to optimize the moonpool profile (its dimensions and position in the hull), minimizing water motion inside moonpool or motions of the ship, for a specific drillship hull in operation condition, when in head seas (β = 180.0°), for both a regular wave or a random sea.

The study approach is divided in two main parts. In the first part is presented an analytical and numerical study of the water motion inside moonpool with the aim to understand the physics of the phenomenon and define the parameters for the main goal achievement. In the second part, an optimization algorithm known as *Genetic Algorithm* (GA) is used for the moonpool optimization.

For the first part, based on previous known work in literature, an equation for the water motion inside a *rectangular moonpool* is deduced and from that it is possible to get important hydrodynamic coefficients as natural frequency and critical damping. From commercial CFD (Computational Fluid Dynamics) software analysis, some observation are done about the relative motion between the vessel and the water motion inside moonpool. Furthermore, it is done a study for implementation of an artificial viscous damping in a potential theory code using a *lid technique*. The main goal of the first part is to calculate the viscous damping in order to use in the potential theory at the second part.

The optimization procedures using the in-house software created for this thesis and applies Genetic Algorithm (GA) is the main topic in second part. Results reveal the algorithm ability to find profiles that follows the optimization requirements defined by the user. Another interesting factor observed is the coupling between vessel's *heave* motion and the water motion inside moonpool. Thereby, it is possible to find an optimum profile that acts as a damper of vessel motions.

Contents

List of Figures

List of Tables

List of Symbols

A	Cross-sectional area of the moonpool, p. 8, 9, 59, 61
B	Vessel's breadth moulded - Beam, p. 13, 97
B_{Crit}	Critical damping coefficient, p. 59, 69, 73, 80, 89, 90, 136
B_{eq}	Equivalent linearized damping coefficient, p. 59, 67, 69, 73, 80, 89, 90, 136
B_l	Linear damping coefficient, p. 57–60, 63, 70, 150, 151
B_q	Quadratic damping coefficient, p. 57–60, 63, 70, 150, 151
B_s	Linear damping coefficient for the vessel, p. 60
CS	Surface of control volume, p. 22
CV	Control volume, p. 22
CV	Volume of control volume, p. 22
C^+	Constant, p. 38, 39
D	Depth moulded, p. 13, 97
E_k	Kinetic energy, p. 61
E_p	Potential energy, p. 61
F	Excitation force on ship, p. 18
F_{wh}	Wave force exciting relative motion, p. 57, 60, 151
F_{wz}	Wave force exciting vessel's heave, p. 60
GCI_l^{kl}	Grid convergence index between mesh k and l, p. 55, 74
H	Wave height, p. 23, 82, 101

J_{n0}	Function of moonpool's length and breadth - Sloshing, p. 9, 10
K	Stiffness coefficient, p. 59
K_s	Stiffness coefficient for the vessel, p. 60
K_{xx}	Gy-radius around X axis, p. 13, 97
K_{yy}	Gy-radius around Y axis, p. 13, 97
K_{zz}	Gy-radius around Z axis, p. 13, 97
L'	Distance between wave probes, p. 68, 89, 111
L_{OA}	Vessel's length overall, p. 13, 66, 67, 97
L_{PP}	Vessel's length between perpendiculars, p. 13, 97
M	Mass, p. 61, 63
M_{as}	Added mass for the vessel, p. 60
M_a	Added mass, p. 57–63, 69, 73, 80, 89, 150, 151
M_a	Mach number, p. 28
M_s	Mass of vessel, p. 60
N	Number of cells, p. 53
P	Moonpool's position - Measured from transom, p. 13, 97, 125, 127, 130, 132
P_{jk}	Stress tensor, p. 148–150
RAO_{DoF}	Response Amplitude Operator of DoF motion, p. 18
RAO_{degree}	Response Amplitude Operator of *degree* motion, p. 119
$S_z(\omega_f)$	Response spectrum, p. 119
S_0	Bottom boundary, p. 16, 19
S_B	Body boundary, p. 16, 19
S_F	Free surface boundary, p. 16
S_{Mx}	Source term of momentum in x-component, p. 21

S_{My}	Source term of momentum in y-component, p. 21
S_{Mz}	Source term of momentum in z-component, p. 21
S_M	Moonpool surface boundary, p. 19
S_Ψ	Source term, p. 22
S_Ψ	Source term of Ψ property, p. 22
S_∞	Unbounded surface, p. 16, 19
$S_\zeta(\omega_f)$	Wave spectrum, p. 119
S_m	Source term for mass, p. 21
S_m	Source term of mass, p. 21
T	Period, p. 23, 82, 101
T_d	Damped natural period, p. 62
WP_{Bow}	Wave probe at moonpool closer to bow, p. 68, 70, 89
WP_{Middle}	Wave probe at center of moonpool, p. 68, 89
WP_{Stern}	Wave probe at moonpool closer to stern, p. 68, 89
$X(t)$	Vessel motion, p. 18
$\Delta\zeta_n$	Free surface elevation decrement of *nth* extreme value (Time series), p. 63, 64
Δ_{ship}	Weight displacement of ship, p. 13, 97
Γ	Diffusion coefficient, p. 22
Ω	Volume of control, p. 57, 148, 149
Ψ	Generic tensor, vector or scalar function, p. 22, 27, 148
α	Cutout angle, p. 11, 13, 57, 61, 86, 97, 125, 127, 130, 132
α_q	Volume fraction of q^{th} phase, p. 49
$\bar{\mathbf{v}}$	Steady mean of velocity vector, p. 28
$\bar{p_s}$	Steady mean static pressure, p. 27
β	Wave heading, p. 4, 10, 107, 111, 114, 115

δ	Logarithmic decrement, p. 62, 63, 67
δ_{ij}	Kronecker delta, p. 28
$\frac{D}{Dt}$	Material derivative, p. 148
η	Damping ratio, p. 59, 62, 63, 89
$\vec{\boldsymbol{\nabla}}\phi$	Flow velocity - Gradient of velocity potential, p. 15, 16, 19, 149
$\vec{\boldsymbol{\nabla}}$	Nabla operator, p. 148
κ	Turbulent kinetic energy per unit mass, p. 28, 29
λ	Wavelength, p. 82, 100
λ_n	Wavelength of n^{th} piston mode, p. 9
μ	Dynamic viscosity, p. 21, 26
μ_t	Eddy viscosity, p. 28
∇_{ship}	Volume displacement of ship, p. 13, 97
ν	Kinematic viscosity, p. 28
ν_t	Kinematic eddy viscosity, p. 29, 33
ω_{00}	Natural frequency - Piston mode, p. 9
ω_d	Damped natural frequency, p. 59, 62, 89
ω_f	Angular frequency, p. 119
ω_{n0}	Natural frequency - Sloshing mode (*n-order*), p. 9
ω_n	Natural frequency, p. 8, 9, 59, 62, 63, 69, 73, 80, 89, 90
$\overline{u}$	Steady mean velocity in x-component, p. 27–29, 39
$\overline{v_j}$	Steady mean of velocity vector in j^{th} direction - Index notation, p. 28
$\overline{v}$	Steady mean velocity in y-component, p. 27, 28
$\overline{w}$	Steady mean velocity in z-component, p. 27, 28
ϕ	Velocity potential, p. 15–17, 19, 149, 150

ϕ_{dif}	Diffraction velocity potential, p. 17
ϕ_{inc}	Incicident velocity potential, p. 17
ϕ_{rad}	Radiated velocity potential, p. 17
ρ	Specific density, p. 15, 16, 21, 22, 26, 28, 29, 148–150
ρ_{air}	Specific density of air, p. 149
ρ_w	Specific density of water, p. 9, 57–60, 149–151
τ_{ij}	Reynolds stress tensor, p. 28, 29
τ_w	Wall shear stress, p. 38
θ	Phase in motion, p. 18
θ_0	Function of moonpool's length and breadth - Sloshing, p. 10
$\tilde{\nu}$	Kinematic eddy viscosity parameter, p. 29
Φ_{DoF}	Amplitude of the rotation of DoF, p. 18
ε	Dissipation parameter at damping zone, p. 19, 113, 114
ε_{kl}	Function of the key variable for GCI method, p. 54
φ	Key variable of the simulation, p. 54
φ_{ext}^{kl}	Extrapolated variable of the simulation between mesh k and l, p. 54, 55, 74
φ_k	Key variable of the simulation on the k^{th} grid, p. 54, 55, 74
$\mathbf{B}$	Damping matrix, p. 18
$\mathbf{K}$	Stiffness matrix, p. 18
$\mathbf{M_a}$	Additional mass matrix, p. 18
$\mathbf{M}$	Inertia matrix, p. 18
$\mathbf{X}$	Motion vector of ship, p. 18
$\vec{n}$	Outward-pointing unit normal surface vector, p. 16, 19, 22, 148
$\vec{v}$	Velocity vector, p. 15, 16, 19, 21, 22, 148

$\vec{x}$ Vector position, p. 16

ζ_a Wave amplitude, p. 18

ζ_{fs} Free surface elevation, p. 19

ζ_m Mean of free surface elevation of *nth* extreme value (Time series), p. 63, 64

ζ_n Free surface elevation of *nth* extreme value (Time series), p. 62, 63

a_h Added mass coefficient, p. 9

b Moonpool's breadth, p. 9, 57–61, 149–151

b_b Moonpool's breadth on bottom, p. 13, 97, 125, 127, 130, 132

b_d Moonpool's breadth on deck, p. 13, 97, 125, 127, 130, 132

c Characteristic linear dimension, p. 26

d Draft, p. 8, 9, 13, 57–60, 83, 97, 149–151

$d\Omega$ Surface of control, p. 148, 149

d' Added draft, p. 8

d_{hz} Added mass interaction coefficient between heave and absolute moonpool motion, p. 57, 60, 151

d_{zh} Added mass symmetric interaction coefficient between heave and absolute moonpool motion, p. 60

e_a^{kl} Approximate relative error between mesh k and l, p. 54, 55, 74

e_{ext}^{kl} Extrapolated relative error between mesh k and l, p. 55, 74

e_{hz} Damping interaction coefficient between heave and absolute moonpool motion, p. 57, 60, 151

e_{zh} Damping symmetric interaction coefficient between heave and absolute moonpool motion, p. 60

f_3 Function of moonpool's length and breadth - Piston, p. 9

f_i Body force vector in the *ith* direction, p. 148

g	Gravity acceleration, p. 8, 9, 16, 19, 23, 57–60, 82, 101, 149–151
$h(t)$	Free surface elevation, p. 57, 58, 60, 62, 83, 149–151
h_{coarse}	Representative cell size - Coarse mesh, p. 54
h_{depth}	Water depth, p. 23, 82, 101
h_{fine}	Representative cell size - Fine mesh, p. 54
h_{grid}	Representative cell size, p. 53
h_k	Representative cell size - Mesh k, p. 54
k_{cte}	Von Kármán constant, p. 38
k_{mp}	Parameter k, p. 61
l	Moonpool's length, p. 9, 57–60, 149–151
l_b	Moonpool's length on bottom, p. 13, 61, 97, 125, 127, 130, 132
l_d	Moonpool's length on deck, p. 13, 97
l_m	Mixing length, p. 29
n	Order of resonance, p. 9, 10
n_i	Number of periods, p. 62, 63
n_k	Surface normal vector in the kth direction, p. 148, 149
p	Linear coefficient of PQ analysis, p. 63, 64, 69, 70
$p\,(vecx, t)$	Pressure field, p. 16
p_{atm}	Atmospheric pressure, p. 149, 150
p_g	Apparent order of GCI method, p. 54, 55, 74
p_{lower}	Pressure at lower surface, p. 149, 150
p_s	Static pressure, p. 21, 27, 28
p'_s	Static pressure fluctuation, p. 27
q	Angular coefficient of PQ analysis, p. 63, 64, 69, 70
q_g	Function of apparent order of GCI method, p. 54

r	Breadth-to-length ratio, p. 10
r_{grid}	Grid refinement ratio, p. 54, 73, 87
r_{kl}	Grid refinement ratio between mesh k and l, p. 54, 55, 74
s	Function of ε_{mn} of GCI method, p. 54
t	Time, p. 16, 18, 19, 21, 22, 27, 28, 57, 58, 60–62, 82, 91, 148–151
u	Velocity in x-component, p. 21, 27
u^+	Dimensionless velocity, p. 38
u'	Velocity fluctuation in x-component, p. 27, 28
u_τ	Friction velocity, p. 38
v	Resultant velocity, p. 26
v	Velocity in y-component, p. 21, 27
v'	Velocity fluctuation in y-component, p. 27, 28
v_j	Velocity vector in j^{th} direction - Index notation, p. 30, 82, 100, 148
v'_j	Velocity fluctuation vector in j^{th} direction - Index notation, p. 28
w	Velocity in z-component, p. 21, 27
w'	Velocity fluctuation in z-component, p. 27, 28
x	X component, p. 21, 27, 28
x_{DoF}	Amplitude of DoF motion, p. 18
x_i	Position vector in orthonormal basis - Index notation, p. 28, 30, 148
y	Y component, p. 21, 27–29
y^+	Dimensionless wall distance, p. 38, 39, 76–79
z	Distance in z-axis, p. 16, 149
z	Z component, p. 21, 27, 28

z_h	Heave motion of ship, p. 57, 60, 151
ΔV_i	Volume of the *ith* cell, p. 53
Re	Reynolds Number, p. 26

List of Abbreviations and Acronyms

AIAA	American Institute of Aeronautics and Astronautics, p. 52, 53, 143, 145
AMG	Algebraic Multigrid, p. 48, 84, 85, 101
BL	Baseline, p. 12
BOP	Blowout Preventer, p. 3
BVP	Boundary Value Problem, p. 16, 17
BV	Bureau Veritas, p. 107
CFD	Computational Fluid Dynamics, p. 6–8, 12, 15, 20, 23, 26, 40, 48, 52, 55, 65, 66, 68, 71, 80, 87, 89, 106, 107
CFL	Courant-Friedrichs-Lewy, p. 47
CICSAM	Compressive Interface Capturing Scheme for Arbitrary Meshes, p. 51, 52
CoG	Center of Gravity, p. 13, 97, 103
DES	Detached Eddy Simulation, p. 34, 75
DMGPT	Drillship Mesh Generator for Potential Theory, p. 116
DNS	Direct Numerical Simulation, p. 35
DNV	Det Norske Veritas, p. 57
DP	Dynamic Position, p. 3
DoF	Degree of Freedom, p. 76, 80, 81, 100, 101, 107, 109
DoFs	Degrees of Freedom, p. 8

EA	Evolutionary Algorithm, p. 55
FAS	Full-Approximation Storage, p. 48
FFT	Fast Fourier Transform, p. 90, 93, 95, 105
FSE	Free Surface Elevation, p. 111
FVM	Finite Volume Method, p. 22, 65
GAUFRJ	Genetic Algorithm at UFRJ, p. 116
GA	Genetic Algorithm, p. 5, 12, 13, 15, 55, 135
GCI	Grid Convergence Index, p. 53, 55, 73, 74
HRIC	High Resolution Interface Capturing, p. 51, 52, 85
ITTC	International Towing Tank Conference, p. 53, 145
LCG	Longitudinal center of gravity, p. 13, 97
LES	Large Eddy Simulation, p. 34, 35
LES	Large Eddy Simulations, p. 75
LHS	Left-Hand Side, p. 22, 148
LOC	Laboratório de Ondas e Correntes, p. 137
MARIN	Maritime Research Institute Netherlands, p. 7, 139
MODU	Mobile Offshore Drilling Unit, p. 4
MUSCL	Monotone Upstream-Centered Schemes for Conservation Laws, p. 44
NVD	Normalized Variable Diagram, p. 51
ODECO	Ocean Drilling & Exploration Company, p. 2
OWC	Oscillating Water Column, p. 11
PISO	Pressure Implicit with Splitting of Operators, p. 42, 83
PLIC	Piecewise Linear Interface Calculation, p. 51
QUICK	Quadratic Upstream Interpolation for Convective Kinematics, p. 43–45, 51

RANS	Reynolds-Averaged Navier-Stokes, p. 28, 34, 75
RAO	Response Amplitude Operator, p. 18, 107–111
RE	Richardson Extrapolation, p. 53
RHS	Right Hand Side, p. 16
RHS	Right-Hand Side, p. 22, 28, 149, 150
RMS	Root Mean Square, p. 48, 84, 101
RSM	Reynolds Stress Model, p. 34, 75
SAS	Scale Adaptive Simulation, p. 34
SGS	Sub-Grid-Scale, p. 35
SIMPLEC	Semi-Implicit Method for Pressure Linked Equations - Consistent, p. 42
SIMPLER	Semi-Implicit Method for Pressure Linked Equations Revised, p. 42
SIMPLE	Semi-Implicit Method for Pressure Linked Equations, p. 41
SST	Shear Stress Transport, p. 33, 76
TCG	Transversal center of gravity, p. 13, 97
TVD	Total Variation Diminishing, p. 45
UDF	User-Defined Function, p. 82
VCG	Vertical center of gravity, p. 13, 97
VOF	Volume of Fluid, p. 6, 7, 49, 50, 83, 84, 101
V&V	Verification and Validation, p. 52, 53
WP	Wave Probe, p. 68, 70, 74, 75, 89

Chapter 1

Introduction

This chapter presents a brief historical background and motivation, also the goals of this thesis as well as a general literature review. The geometry of the ship under consideration and a *default moonpool* is shown in Section 1.5. The organization of the thesis is also presented

1.1 Brief History

The first oil well drilled dates back 1859 (previously it was dug) in Pennsylvania (USA). This onshore well is known as Drake's well because it was named after Edwin Laurentine Drake, the first man to successfully drill for oil. In 1987 offshore drilling began at Summerland Oil Field in Santa Barbara County, California (USA), using a pier to support a land rig as it is shown in Figure 1.1.

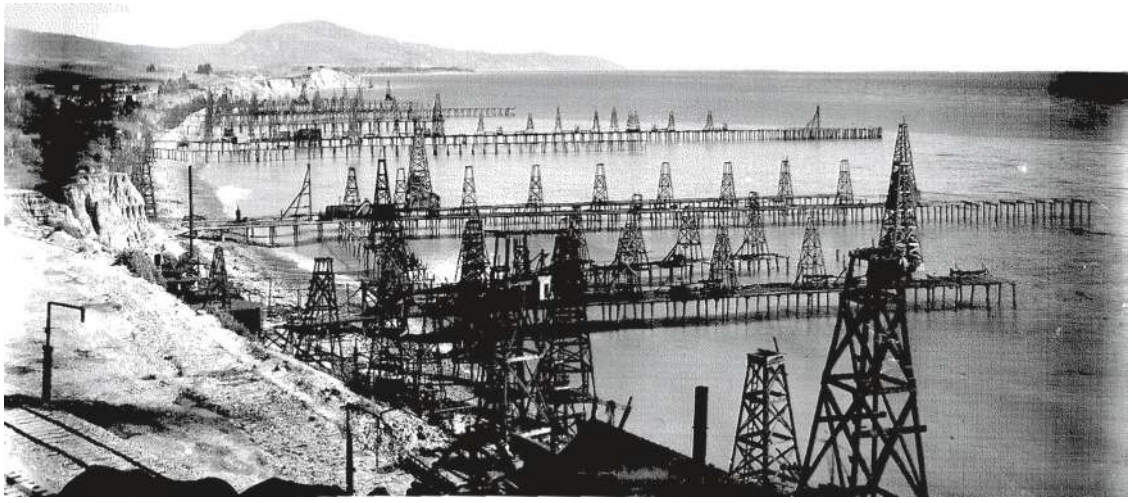

Figure 1.1: Piers and derricks at Summerland, California, 1901. (LEFFLER *et al.* [1])

Only in the early 1930s happened the first "on-water" drilling in the swamps of Louisiana using rectangular shallow-draft barges. Therefore, with the need of

drilling other wells offshore, in 1947, a Tender Assist Drilling (TAD) unit was used in the Gulf of Mexico in only 16 feet of water. Then, in 1949, posting a lattice steel structure above a barge, John T. Hayward designed The Breton Rig 20 (Figure 1.2), a submersible rated for just 20 feet of water. It is considered the first submersible used offshore and it has some stability issues but fortunately did not flip.

Figure 1.2: Breton Rig 20 - Submersible rated for 20-ft water depths. (OFFSHORE MAGAZINE [2])

Few years later, Hayward and Alden J. "Doc" Laborde founded the Ocean Drilling & Exploration Company (ODECO) and they built Mr. Charlie (1954), submersible designed to handle the stability problem. At that time, the population in California coast close to Summerland (Figure 1.1) raised strong objection for building any new permanent offshore platform as long as it was creating a visual pollution and could cause natural disasters. A consortium created by 4 companies, Continental, Union, Shell and Superior Oil and irreverently named the CUSS group, commissioned the Submarex, a drilling ship. They converted a patrol boat by adding a drilling rig (M.V. Submarex), but some engineering problems convinced they to not use for exploratory wells. At least they could learn a lot about stability, mooring, and drilling that the group began design on *CUSS 1*, a purpose-built drilling vessel. This vessel was launched in 1961 and had no self-propulsion, so tugs were needed in order to position it on a site and then moorings would hold it in place. *CUSS 1* performed succesfully in waters up to 350 feet and started a new class of exploratory drilling options, floating platforms called *Drillship*.

This history background is traced in more detail by LEFFLER *et al.* [1].

1.2 Motivation

Drillship is a merchant vessel for use in exploratory offshore drilling. A conventional drillship has a opening in the hull from the deck to baseline in order to give passage to the drill pipe. This opening is called *moonpool* and it has effects on the vessel when it is sailing or when waves are approaching the vessel in the operating mode, at zero speed. Unlike a ship which spends much of its working life moving between ports, a drillship spends much of its working life stationary over a well, maintaining its position. It may utilize their mooring lines and anchors or use their Dynamic Positioning (DP) system (ship's computer-controlled system on board to automatically maintain a vessel's position and heading by using its own propellers and thrusters).

Thus, it is highly important to consider the moonpool effects when the ship is operating, as they may cause increase in the ship's motions or even increase the water motion inside the moonpool. Some specific operations have strict operability criteria and often a drillship is waiting on operational window to perform these operations, such as lowering a BOP (Blowout Preventer) or X-tree (equipment that provides flow control on well) through the splash zone (region of contact of the equipment with free surface). Depending on the moonpool design and the sea state, the operation needs to be delayed as the motions become large and the water flows over the edge of the moonpool, compromising safety for the ship, its crew, its sensitive equipment and also generating high costs, mostly for downtime caused by moonpool inactivity. This problem with water flowing onto deck is known as *Green Water*.

In order to better understand these effects, first of all we need to know how the water motions happens inside the moonpool and what causes that. The water motion happens mainly at natural modes of the moonpool: the *sloshing mode*, back and forth in between the vertical walls and the *piston mode* where the water oscillates vertically, heaving up and down (MOLIN [5]). These motions are shown in Figure 1.3. Regarding to the circumstances that generates the motions, it originates from the match between vertical excitation and the natural frequency of the water column and can be splitted in two components (GAILLARDE and COTTELEER [6]):

- local vertical accelerations at the bottom of the moonpool;
- pressure differences at the bottom of the moonpool.

As *time* is a synonym of *money*, focusing in faster drilling and completion operation, newer generation of offshore rigs, in general, are being designed with dual activity drilling systems. This concept was created by *Transocean Sedco Forex* in the fall of 1995 [23]. Drillships for this purpose have a dual derrick (tall pyramidal

skeleton that supports the weight of the drill string) and each of it has separate draw works, top drives, and pipe-handling facilities. While one system is working the borehole, the other can be raising or lowering a drill pipe in parallel. Hence, a larger moonpool is needed to fit both derrick and consequently increasing the unwanted effects.

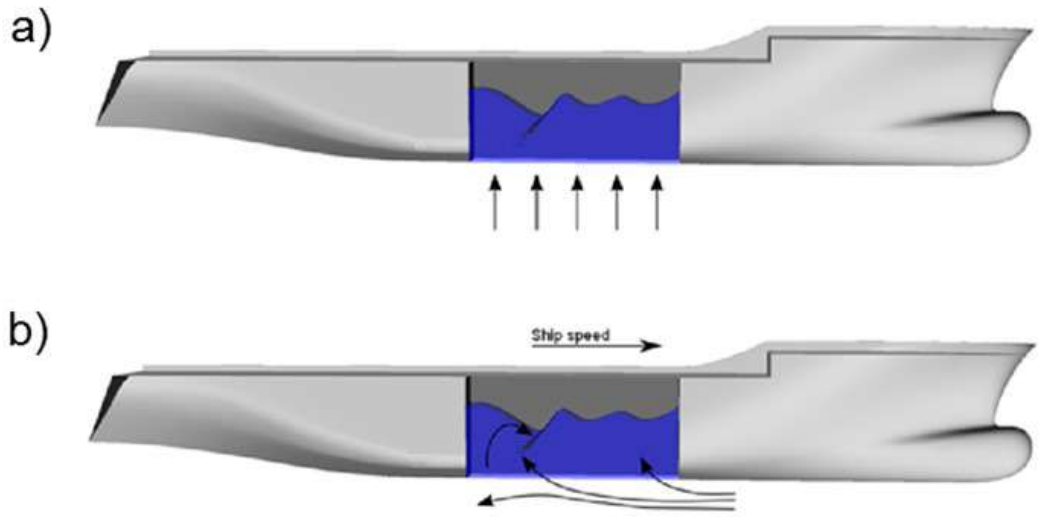

Figure 1.3: Water motion in *a)* piston mode and *b)* sloshing mode. (Adapted from HAMMARGREN and TÖRNBLOM [3])

Since this Mobile Offshore Drilling Unit (MODU) has a huge importance in the offshore exploration, the optimization of the moonpool profile for operating conditions would save a huge quantity of money and time for the companies involved.

1.3 Research Goals and Contributions

The aim of this thesis is to develop a method to optimize the moonpool profile (its dimensions and position in the hull), minimizing water motion inside moonpool or motions of the ship, for a specific drillship hull in operation condition, when in head seas ($\beta = 180.0°$), for both a regular wave or a random sea. Also, due to coupling between water motion inside moonpool and vessel's heave, another important goal is to analyze the contribution that moonpool size and position variation can cause on vessel motion. The moonpool, depending on its characteristics, may be studied as a vessel motion damper.

In order to accomplish these objectives, a study is necessary in order to understand the physics behind phenomenon. So the first part of this thesis concerns the analytic and numerical studies of the water motion inside a rectangular moonpool with cutout angle (trailing wall is angled in relation to ship's baseline). The specific

objectives of this part are:

- Analyze the theory to calculate the resonance period of the water motion inside the moonpool as it can be used as verification of the final results;
- Understand the physical effects of the water motion and the importance of modeling the viscosity;

The second part concerns to propose an optimization software that uses Genetic Algorithm (GA) . The specific objectives of this part are:

- Development of a software to create automatic meshes for potential theory analysis;
- Development of a software to find the optimum moonpool for regular wave or a random sea (Ocean-Wave Spectrum);

The main importance of the first part is to calculate the viscous damping in order to use in the potential theory. This work brings two main originality, that is the deduction of the equation for the rectangle moonpool and the resonance frequency, also the application of an optimization algorithm for the moonpool shape and position on a ship.

1.4 Literature Review

1.4.1 Water Motion

FUKUDA [4] wrote one of the first papers published in the topic took place in the late 1970's. It was an experimental study and until today is very well referenced. FUKUDA [4] built four types of model ships with vertical openings, the experiments were conducted in current at two states, with and without restraint of the ship motion in sway, and the water surface in the opening and the hull movement were measured. He did some variation in the size parameters and analyzed the effect on the moving shapes, as shown in Figure 1.4 it was possible to notice the piston mode (heaving) and sloshing mode (swaying and surging).

AALBERS [24] wrote a well referenced paper and with important result in the mid 1980's. It presents a mathematical model to express the water motion analytically. AALBERS [24] derived a mathematical model and also did experiments for a circular moonpool in waves in order to verify the results from the model. With his model he could show good agreement with the experiments for motion decay for the moonpool water column, forced heave oscillations, test in regular waves with captive vessel and even for free floating ship in waves. The mathematical model can be used

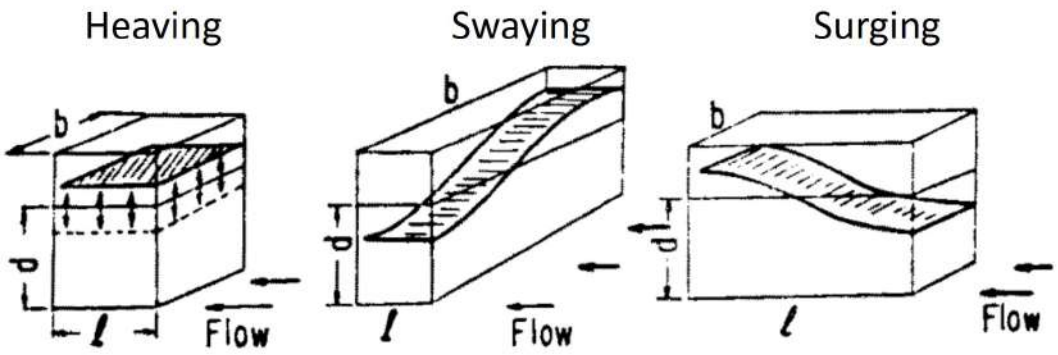

Figure 1.4: Moving shapes of water inside the moonpool. (Adapted from FUKUDA [4])

to predict the motion behavior with some empirical adjustments for the quadratic damping.

MOLIN [5] used linearized potential flow theory to also create a model for a barge of infinite breadth and length with a moonpool inside. Calculations were done for the two-dimensional (2D) and three-dimensional (3D) case. Figure 1.5 shows the water shapes for a rectangular moonpool in piston mode, the first longitudinal sloshing mode and first transverse sloshing mode.

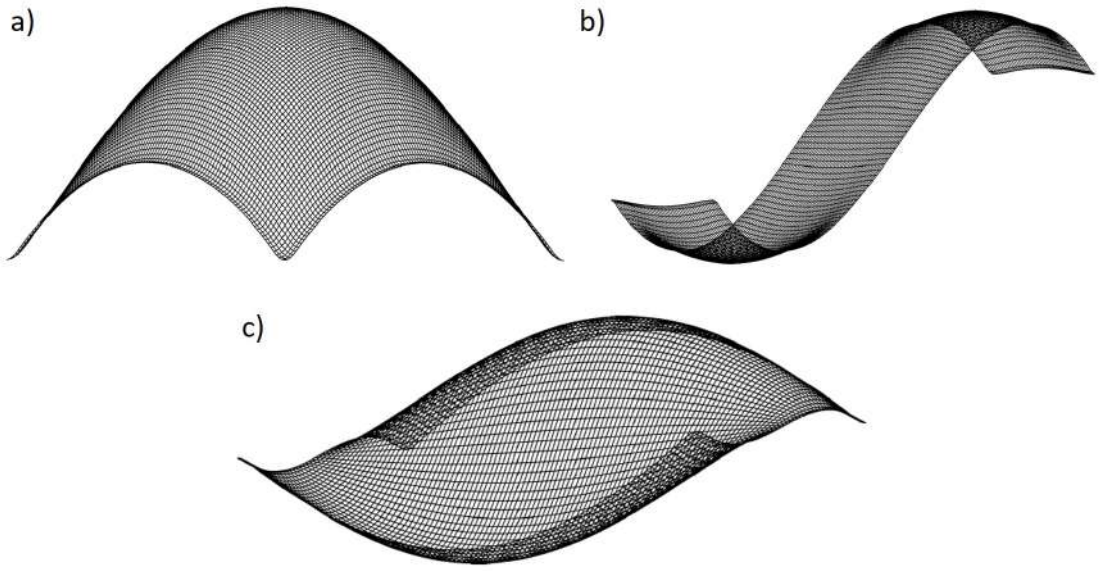

Figure 1.5: Free surface shape in *a)* piston mode for square moonpool, *b)* first longitudinal sloshing mode for a rectangular moonpool (length-to-width ratio of 16) and *c)* first transverse sloshing mode for a rectangular moonpool (length-to-width ratio of 16). (Adapted from MOLIN [5])

Numerical results using Computational Fluid Dynamics (CFD) to solve the flow inside the moonpool were obtained by GAILLARDE and COTTELEER [6] with the software ComFLOW. They used the Volume of Fluid (VOF) algorithm and solved

the incompressible Navier-Stokes equations with a free-surface condition on the free boundary for the approach in calm water, with the vessel sailing at constant speed (Figure 1.6). When this article was written, in 2004, they concluded that some developments should be made to consider CFD simulations a useful design tool for this purpose. These developments for simulation of stationary case in waves were:

- Introduction of the excitation forces into VOF simulations (excitation being calculated, for example, in the frequency domain thanks to existing codes);
- Update of ComFLOW program to take into account moving body and inflow conditions;
- Validation of simulations;
- Comparison with existing techniques and development of a design tool.

This was an effort proposed to be conducted in an upcoming Joint Industry Project initiated by Maritime Research Institute Netherlands (MARIN), one of the leading institutes in the world for hydrodynamic research and maritime technology.

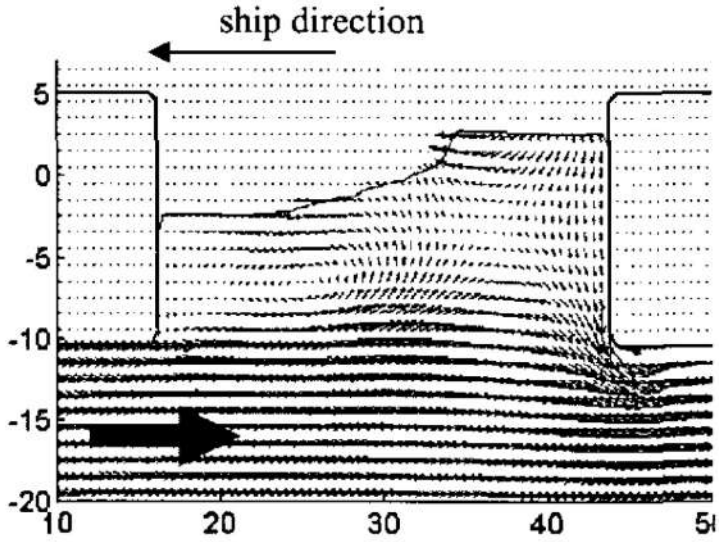

Figure 1.6: CFD simulation of calm water moonpool oscillation. (GAILLARDE and COTTELEER [6])

In 2014, LEE and IM [7] examined the nonlinear fluid characteristics near and inside a moonpool taking into account the viscosity effect by CFD. Numerical calculations were performed in a 2D moonpool with three wave amplitudes of 1/4, 1/8, and 1/12 of the draft, and four wave lengths of 1/3, 1/2, 1, and 2 times the ship's length between perpendiculars. The work showed a piston mode result, in which the free surface remains flat (Figure 1.7), and also that the free surface level increases as the wave length increases.

Some others papers brought CFD and experimental results to show the motion inside moonpool. Normally simulations do not take into consideration the full hull geometry or the vessel is captive in most of the DoFs.

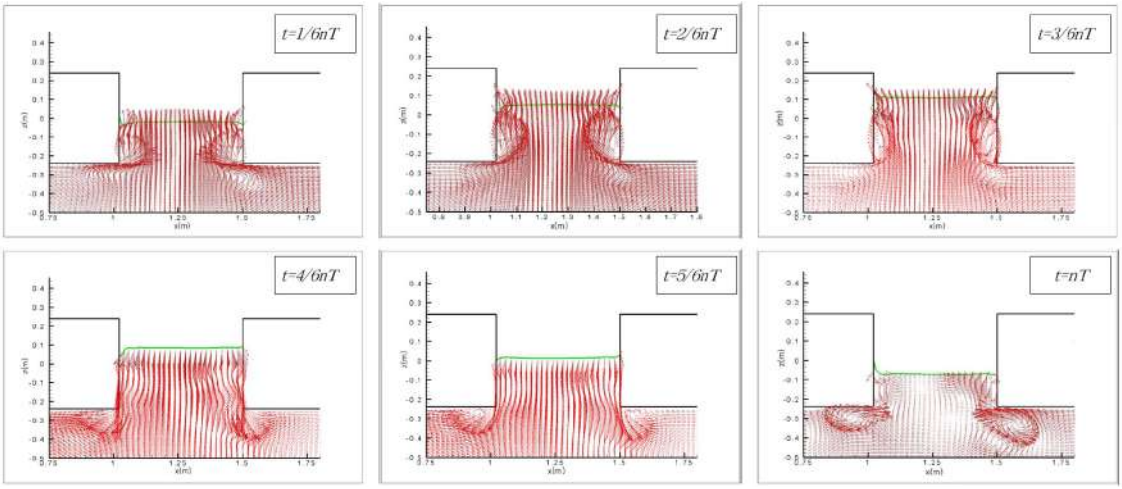

Figure 1.7: Piston mode - Water oscillates up and down while remaining essentially flat (CFD). (LEE and IM [7])

1.4.2 Natural Frequency - Resonance

Resonance frequencies of the piston mode and the sloshing mode due to the effect of a moonpool has been extensively researched in literature. The simplest formula for natural frequency calculation is shown in Equation (1.1) and is formally presented in FALTINSEN [10].

$$\omega_n = \sqrt{\frac{g}{d}}, \tag{1.1}$$

where ω_n is the *Natural Frequency* $[rad/s]$, g is the gravity acceleration $[m/s^2]$ and d is the draft $[m]$.

In 1977, FUKUDA [4] derived resonance frequencies of the piston mode, similar to Equation (1.1) but with an added length, as following:

$$\omega_n = \sqrt{\frac{g}{d + d'}}, \tag{1.2}$$

where d' is usually called *added draft* $[m]$.

Researching squared moonpools, FUKUDA [4] expressed the added draft by the following empirical formula:

$$d' = 0.41\sqrt{A}, \tag{1.3}$$

where A is the cross-sectional area of the moonpool $[m^2]$.

For a rectangular moonpool, this leads to the following equation for the natural

frequency:

$$\omega_n = \sqrt{\frac{g}{d + 0.41\sqrt{bl}}}, \tag{1.4}$$

where b is the moonpool's breadth $[m]$ and l is the moonpool's length $[m]$.

Meanwhile, NEWMAN [25] also presented an expression for the calculation of *n-order* resonance frequency of sloshing mode as shown in Equation (1.5).

$$\omega_n = \sqrt{\frac{n\pi g}{l}}, \tag{1.5}$$

where n is order of resonance.

As aforementioned, AALBERS [24] derived a mathematical model and the resonance frequency of this system is presented in Equation (1.6).

$$\omega_n = \sqrt{\frac{\rho_w g A}{\rho_w A d + a_h}}, \tag{1.6}$$

where ρ_w is the specific density of water $[kg/m^3]$ and a_h added mass coefficient $[kg]$.

Additionally, in 1985, a master thesis concerned with sloshing motion of water in a moonpool was published and MADHANI [26] presented the Equation (1.7) for the natural frequency.

$$\omega_n = \sqrt{\frac{\pi g}{b} \tanh\left(\frac{\pi d}{b}\right)}, \tag{1.7}$$

MOLIN [5] was not just targeting to calculate the free surface, but also the natural frequencies. His work presented separated equations for the piston mode and sloshing mode and also for the 2D and 3D cases. Equation (1.8) is the natural frequency for 3D piston mode and Equation (1.10) is for the 3D sloshing mode.

$$\omega_{00} \simeq \sqrt{\frac{g}{d + b f_3\,(b/l)}}, \tag{1.8}$$

where

$$f_3 = \frac{1}{\pi}\left\{\sinh^{-1}\left(\frac{l}{b}\right) + \frac{l}{b}\sinh^{-1}\left(\frac{b}{l}\right) + \frac{1}{3}\left(\frac{b}{l} + \frac{l^2}{b^2}\right) - \frac{1}{3}\left(1 + \frac{l^2}{b^2}\right)\sqrt{\frac{b^2}{l^2} + 1}\right\}. \tag{1.9}$$

$$\omega_{n0} \simeq \sqrt{g\lambda_n \frac{1 + J_{n0}\tanh\lambda_n d}{J_{n0} + \tanh\lambda_n d}}, \tag{1.10}$$

where λ_n is n^{th} wavelength $[m]$ and

$$J_{n0} = \frac{2}{n\pi^2 r}\left\{\int_0^1 \frac{r^2}{u^2\sqrt{u^2+r^2}}\left[1+(u-1)\cos(n\pi u)-\frac{\sin(n\pi u)}{n\pi}\right]du+\frac{1}{\sin\theta_0}-1\right\}, \tag{1.11}$$

where $r = b/l$ and $\tan\theta_0 = r^{-1}$.

1.4.3 Moonpool Optimization

There is a gap on research concerning of optimization algorithm for that case. PARK *et al.* [8] did a work in which they studied five different moonpool shapes with numerical and experimental analysis. These five different moonpool types varied one from another just by the addition of three damping blocks with different sizes and position (Figure 1.8.a). The criteria to choose was just based on comparison of maximum free surface height in results for sea state of maximum drilling condition and two different wave headings, quartering ($\beta_q = 135.0$) and heading ($\beta_h = 180.0$) sea.

A more recent study was published in 2018 by CHALKIAS and KRIJGER [9], where a generic hull geometry was used and a rectangular moonpool with a cutout step (Figure 1.8.b). Optimization criteria was the operability of the vessel (percentage of time that the vessel can perform a specific operation in a location not limited by environmental conditions). Ten different moonpool variations were investigated with a simple rectangular moonpool and 9 other variations in the cutout step size. They presented results of the operability index for different nautic zones and the choice of the optimum profile depend on that. Another interesting remark of this paper is the investigation of artificial damping to use in potential flow solver by CFD results.

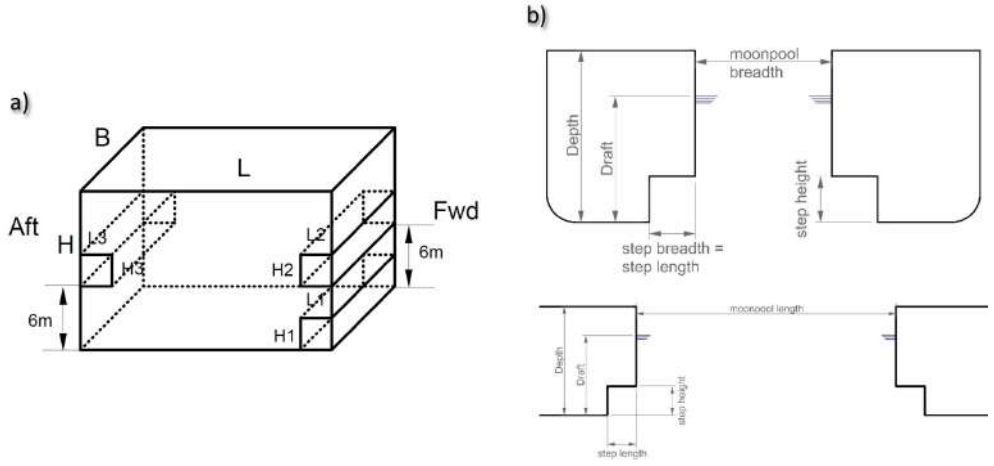

Figure 1.8: *a)* Moonpool with block [8] and *b)* moonpool with a cutout step [9]

HENRIQUES *et al.* [27] presented two algorithm for geometry optimization of a floating oscillating water column (OWC) using *WAMIT*. One of these algorithms used is the Differential Evolution (DE), a population-based metaheuristic method and it is a branch of evolutionary algorithms.

This lack of a research using the concepts of mathematical optimization contributes to the originality and importance of the present thesis.

There is a plenty of other conference papers and journal articles about the moonpool topic, also concerning about damping devices and the water motion effects in moonpool with recess (water above an intermediate work deck and its main purpose is for assembling of drilling equipment and transportation of them to the main moonpool).

1.5 Geometry

1.5.1 Ship

A generic drillship vessel was used in this work and it is called *fKN1*. Its main particulars are presented in Table 1.1. A simple schematic of the hull without moonpool is also shown in Figure 1.9.

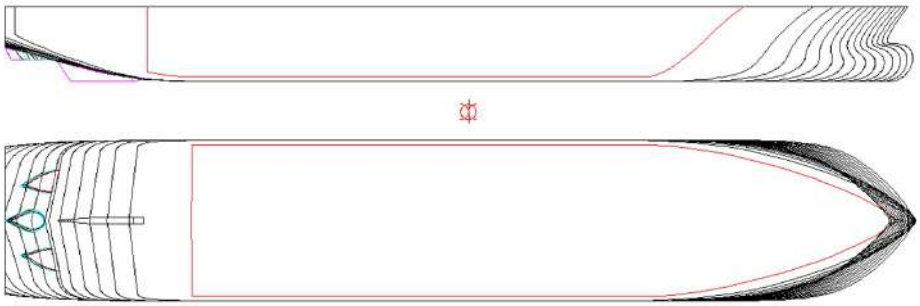

Figure 1.9: Design of *fKN1* Ship

1.5.2 Moonpool

Since the optimization algorithm demands trial of multiple profiles and a comparison among them, one *default moonpool* that fits a dual derrick was chosen. Figure 1.10 shows a schematic view of the *default moonpool* and Figure 1.11 shows the generic vessel (called *fKN2*) with this moonpool configuration. Main particulars of moonpool in *fKN2*, for loading conditions in operating mode, are presented in Table 1.1.

It is possible to check that the moonpool take almost 20% of overall length of the ship. Another important parameter to give attention is the cutout angle (α),

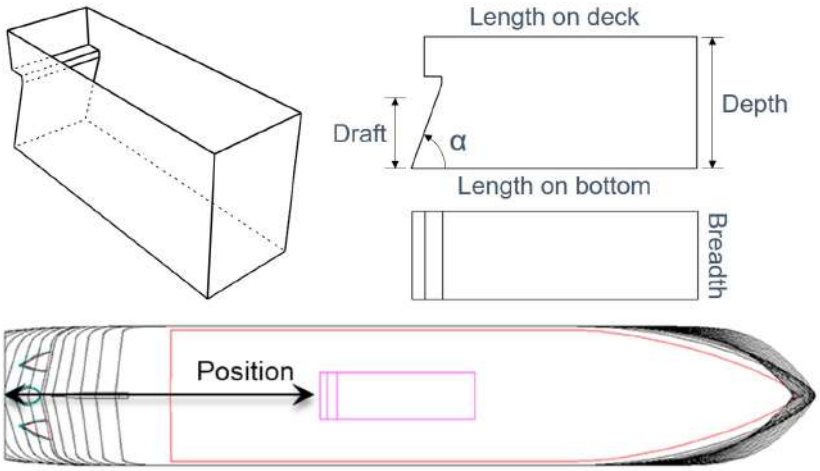

Figure 1.10: Design and position of the *default moonpool*

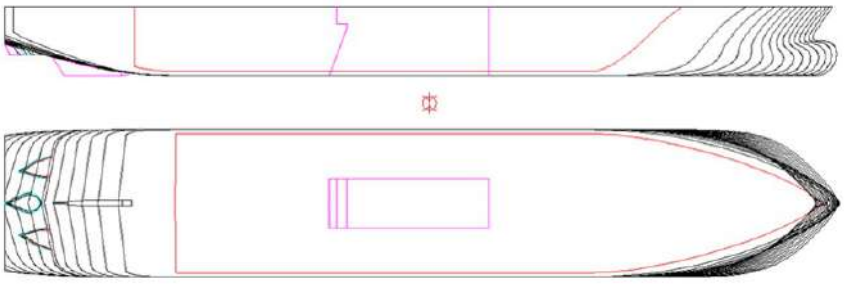

Figure 1.11: Design of *fKN2* Ship (Default Moonpool)

that is the value at which the trailing wall is angled in relation to ship's baseline (BL) as can be seen in Figure 1.10

1.6 Thesis Organization

This thesis is divided into seven chapters. Chapter 1 is an introduction with a history background about drillships and moonpools, the goals of this present work and what has already been studied on the subject. The geometry of the ship and default moonpool that is going to be used as the standard one for comparisons is also presented at this introductory chapter.

Chapter 2 presents the theoretical background of this work. Including potential theory, Computational Fluid Dynamics (CFD) and Genetic Algorithm (GA) .

Chapter 3 shows the analytical results based on theory behind previous works. In this chapter the analytical calculation of damping values based on dimension parameters and decay test of a moonpool is an important step for the optimization as will be seen in following chapters.

Thereafter, in Chapter 4, a numerical analysis using CFD is presented with its

Table 1.1: Main particulars of the generic vessel *fKN1* and vessel *fKN2* (w/ *default moonpool*).

Description	Symbol	Magnitude	Unit
Length Overall	L_{OA}	242.1	m
Length between Perpendiculars	L_{PP}	228.0	m
Breadth Moulded	B	42.0	m
Depth Moulded	D	19.6	m
Design Draft	d	12.0	m
Longitudinal CoG	LCG	116.50	m
Transversal CoG	TCG	-0.01	m
Vertical CoG	VCG	16.77	m
Weight displacement	Δ_{fKN1}	105657	mt
Volume displacement	∇_{fKN1}	103080	m^3
Gy-radius around X axis	K_{xx}	16.15	m
Gy-radius around Y axis	K_{yy}	61.79	m
Gy-radius around Z axis	K_{zz}	61.90	m
Moonpool's length on bottom	l_b	45.5	m
Moonpool's length on deck	l_d	46.2	m
Moonpool's breadth on bottom	b_b	14.0	m
Moonpool's breadth on deck	b_d	14.0	m
Postion (from transom)	P	93.1	m
Cutout angle	α	70.05	$^\circ$
Weight displacement	Δ_{fKN2}	97090	mt
Volume displacement	∇_{fKN2}	94721.4	m^3
Gy-radius around X axis	K_{xx}	16.56	m
Gy-radius around Y axis	K_{yy}	63.92	m
Gy-radius around Z axis	K_{zz}	64.10	m

respective analysis in order to compare and verify the analytical results of previous chapter. Also, the potential theory setup is provided with analysis and comparisons to justify the choices made and with information about a artificial damping that have to be calibrated against measurements.

Chapter 5 is the beginning of second part of this thesis and provides the background for the GA parameters (exposed in Chapter 2) to do analysis in the moonpool optimization problem.

The main findings of this thesis are drawn in Chapter 6 and results for some known spectra are presented too.

Finally, in Chapter 7, the conclusions are outlined and also future works as well as new research topics are presented and discussed.

In addition, all the Bibliography used in this work and an Appendix details the calculation of the equation of motion inside the moonpool given in Chapter 2.

Chapter 2

Theoretical Background

This chapter presents all the theoretical background used through this work. Firstly, Section 2.1 describes the potential theory with information of workaround to numerically add viscous damping inside moonpool. Additionally, some necessary theory of the big branch of Computational Fluid Dynamics (CFD) is presented in Section 2.2. The theory behind the Genetic Algorithm (GA) is discussed in Section 2.3.

2.1 Potential Theory

2.1.1 Hydrodynamic Formulation

There are two main type of surface forces acting on a floating or submerged body, that are the *viscous forces* and the so called *potential forces*. The latter is well established by *Potential Theory* that assumes the fluid as incompressible ($\rho = constant$) and irrotational ($\vec{\nabla} \times \vec{v} = 0$). Thus, a *velocity potential* may be defined as ϕ and it is a solution for *Laplace's Equation* (Equation (2.1)).

$$\nabla^2\phi = \frac{\partial^2\phi}{\partial x^2} + \frac{\partial^2\phi}{\partial y^2} + \frac{\partial^2\phi}{\partial z^2} = 0 \ . \tag{2.1}$$

The fluid velocity at each point of the flow can be written as,

$$\vec{v} = \vec{\nabla}\phi \ , \tag{2.2}$$

The main advantage of potential theory is that the flow calculation is based on solving an equation for a scalar ϕ. Despite all simplification in the flow, they are reasonable for many real applications, such as the case of present work which considers the motion of a ship in waves.

Velocity potential in Equation (2.1) can be calculated and have unique ana-

lytical solution when imposing some boundary conditions, i.e., conditions in the boundary of the fluid region that must be obeyed by the velocity potential ϕ. This is called *Boundary Value Problem* (BVP) and for the specific case of ship motion these boundaries are the hull (S_B), free surface (S_F), bottom (S_0) and also an unbounded far-field connecting free surface and bottom (S_∞ and $S_{-\infty}$). The BVP is shown in Figure 2.1.a). At free surface (S_F) two conditions have to be satisfied, a *kinematic condition*, which establishes that any particle in contact with the free surface remains on it, and a *dynamic condition* that imposes the pressure at surface equals to the ambient pressure. Also there are *impermeability conditions* (fluid velocity normal to the wall is set to the wall velocity in this direction - zero relative velocity at vector area direction) at body moving in the fluid S_B and outer bottom boundary S_0.

The BVP for small wave amplitude (linearized free-surface condition) can be written as follows,

$$\begin{cases} \nabla^2\phi = 0 \quad (in\ fluid\ domain:\ z \leq 0) \\ \dfrac{\partial\phi}{\partial z} + \dfrac{1}{g}\dfrac{\partial^2\phi}{\partial t^2}\ (on\ z = 0) \\ \dfrac{\partial\phi}{\partial n} = \vec{v} \cdot \vec{n}_B\ (on\ S_B) \\ \dfrac{\partial\phi}{\partial z} = 0\ (on\ S_0)\ . \end{cases} \tag{2.3}$$

Kinematic and dynamic conditions are reorganized in the second equation (at $z = 0$) in Equation (2.3) for first-order solution.

Once the velocity is related with the velocity potential by Equation (2.2), knowing ϕ, the pressure field can be calculated using unsteady Bernoulli's equation,

$$p\left(\vec{x}, t\right) = -\rho g z - \rho\frac{\partial\phi}{\partial t} - \frac{1}{2}\rho\left(\vec{\boldsymbol{\nabla}}\phi\right)^2\ . \tag{2.4}$$

So, with solution of BVP it is possible to calculate the hydrodynamic pressure at any point of domain. First term on RHS of Equation (2.4) is the *static pressure* and the second is the *dynamic pressure*. Last term can be neglected for small perturbations.

The potential used to calculate the dynamic pressure can be divided in two parts, and considering a linear superposition these parts can be summed to find the total potential. These two parts are: the *exciting wave potential* and the *radiated potential* as shown in Figure 2.1.b. The exciting wave consist of *incident* and *diffracted* velocity potential. Then, the total velocity potential ϕ is given by,

$$\phi = \phi_{inc} + \phi_{dif} + \phi_{rad} \ , \tag{2.5}$$

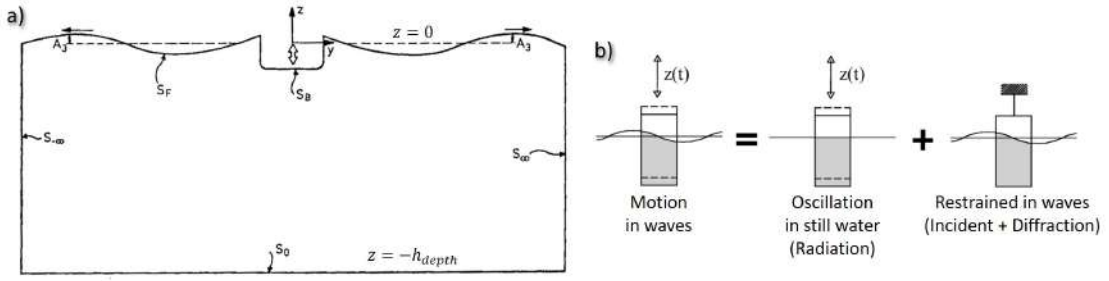

Figure 2.1: *a)* Boundary Value Problem definition (Adapted from FALTINSEN [10]) and *b)* superposition of wave loads (Adapted from JOURNÉE and MASSIE [11]).

Incoming waves, responsible for the two excitation potentials (incident and diffracted), are described by their *amplitude*, *frequency* and *heading*. Wave heading is defined by the angle between the propagation direction and the positive direction of the axis Ox, as shown in Figure 2.2.a. Radiation potential is calculated for each degree of motion, that are *surge*, *sway*, *heave*, *roll*, *pitch* and *yaw*, presented in Figure 2.2.b.

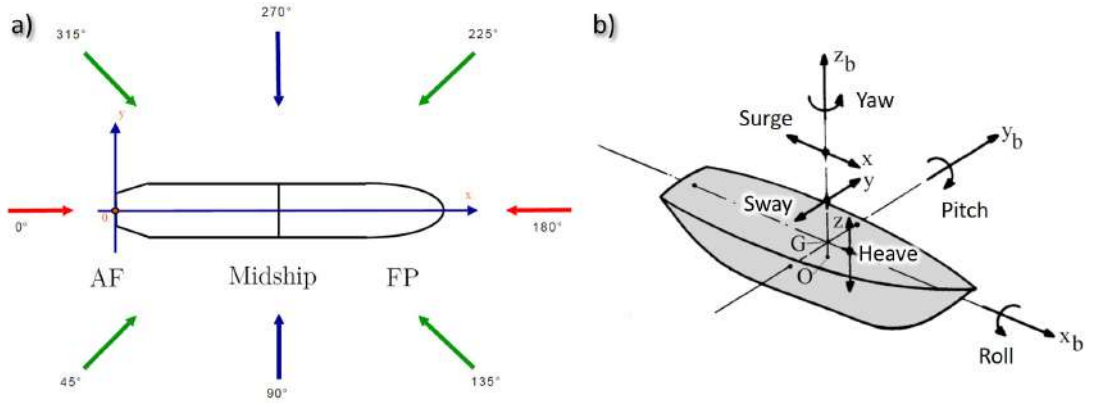

Figure 2.2: *a)* Wave headings (BUREAU VERITAS [12]) and *b)* ship motion with 6 degree of freedom (Adapted from JOURNÉE and MASSIE [11]).

The incident potential is the solution of Equation (2.3) without the body and it is known analytically, while first-order BVP for radiation and diffraction velocity potentials are determined using Green's theorem to derive integral equations on the body boundary. Then, the integral equation may be solved in a discretized body surface, for that, a mesh must be created at body surface, and the elements of this mesh will be called hereafter as *panels*.

There are some specific commercial software for the solution of the 3D diffraction and radiation problem for wave-body interactions with years in the market and very well validated for a large range of cases.

2.1.2 Wave Body Interaction

Knowing velocity potential allows the calculation of pressure field and consequently forces and moments. Using Newton's second law for forces and the analogous for angular momentum and torque it is possible to calculate ship's motions,

$$(\mathbf{M} + \mathbf{M_a})\,\ddot{\mathbf{X}} + \mathbf{B}\dot{\mathbf{X}} + \mathbf{K}\mathbf{X} = F \;, \tag{2.6}$$

where

$\mathbf{M}$ is the inertia matrix of the body $[kg]$;
$\mathbf{M_a}$ is the additional mass matrix coming from radiation solution $[kg]$;
$\mathbf{B}$ is the damping matrix coming from the radiation solution $[Ns/m]$;
$\mathbf{K}$ is the stiffness matrix coming from the hydrostatic properties of the body $[N/m]$;
$\mathbf{X}$ is the displacement vector of ship $[m]$;
F is the excitation force on ship coming from the Froude-Krylov and diffraction solution $[N]$.

It is possible to add some external damping (e.g. viscous damping) and stiffness (e.g. mooring system or liquid in tanks) adding values to the specific matrix.

Response Amplitude Operator - RAO

Considering that the problem is linear, the response for a regular (monochromatic) incident wave is monochromatic, i.e. all the properties varies harmonically in time with the same frequency. Then, velocity potential varies harmonically, as does the pressure field and consequently the forces on the body. The displacement of the body $X\,(t)$ can be written in following way

$$X\,(t) = x\cos(\omega t + \theta) \;, \tag{2.7}$$

where x here is the amplitude of the motion of the ship in a specific degree of motion.

The ratio between the response amplitude x_{DoF} and wave amplitude ζ_a is a transfer function called *Response Amplitude Operator* (RAO), that for all degree of motion can be given by,

$$\begin{aligned} RAO_{surge} &= \frac{x_{surge}}{\zeta_a} \;, \quad RAO_{sway} = \frac{x_{sway}}{\zeta_a} \;, \quad RAO_{heave} = \frac{x_{heave}}{\zeta_a} \;, \\ RAO_{roll} &= \frac{\Phi_{roll}}{k\zeta_a} \;, \quad RAO_{pitch} = \frac{\Phi_{pitch}}{k\zeta_a} \;, \quad RAO_{yaw} = \frac{\Phi_{yaw}}{k\zeta_a} \;. \end{aligned} \tag{2.8}$$

It is important to determine the behavior of a ship when operating at sea. It must be noticed that at this work the transfer functions of the rotations were made *non-dimensional* by dividing the amplitude of the rotations Φ_{DoF} by the amplitude of the wave slope, $k\zeta_a$, instead of wave amplitude, ζ_a.

2.1.3 Free Surface Elevation

In this work, the *free surface elevation* is concerning the *relative free surface elevation*, that is the elevation of the water inside moonpool in relation with a frame of reference attached to the ship. If the objective is to express a relationship with an inertial reference frame (outside the ship), it will be called *absolute free surface elevation*.

It is possible also to calculate the absolute free surface elevation at any point (at $z = 0$) considering the dynamic boundary condition aforementioned,

$$\zeta_{fs} = -\frac{1}{g}\left(\frac{\partial \phi}{\partial t}\right) , \tag{2.9}$$

Due to lack of viscous damping, specially inside moonpool, the free surface elevation may be overpredicted, so an additional damping is necessary for a proper calculation.

2.1.4 Artificial Viscous Damping

Tuning damping coefficient inside moonpool is a difficult task [9]. One way to implement it is to apply a damping region over the whole moonpool for all response modes and then calibrate.

A panel on the free surface, inside moonpool, is added and it is assumed to be free with no external force or moment acting on it, so it will not be used for force calculations but will modify values of diffracted and radiated potential. This panel on the free surface of moonpool will be hereafter called *lid*. It is possible to provide an external damping force on the lid to further increase the damping on the moonpool free surface motion.

Another approach is the modification of the boundary conditions at panels on moonpool wall S_M. For BVP of diffraction and radiation problem may be written with an additional ε parameter,

$$\begin{cases} \dfrac{\partial \phi_7}{\partial n} + \dfrac{\partial \phi_i}{\partial n} = i\varepsilon k \phi_7 \ (on \ S_M) \\ \dfrac{\partial \phi_j}{\partial n} = n_j + i\varepsilon k \phi_j \ (on \ S_M) \ . \end{cases} \tag{2.10}$$

2.2 Computational Fluid Dynamics (CFD)

Computational Fluid Dynamics is a branch in fluid dynamics for analysis of systems involving fluid flow, heat transfer and associated phenomena by means of numerical simulations. This technique is very powerful as it may work with the fluid governing equations in the full form, i.e. including all the characteristics of flows that are encountered in the real world and without neglecting any parameter of the fluid. Differently, for instance, of Euler equations in which the viscosity and thermal conductivity are neglected or the irrotational flow explained above in Section 2.1. These governing equations are briefly described in the Section 2.2.1. Despite it works with full equations, there are some numerical approximations caused by discretization, and in Section 2.2.2 some turbulence models are presented. Then, some information about boundary layer, multiphase theory and the methodology to do a CFD simulation are shown. Last but not least, a discussion on the errors and uncertainties in CFD modeling is made in section Section 2.2.6 with Verification and Validation (V&V).

2.2.1 Governing Equations

In fluid dynamics, there are some conservation laws that describe the motion of it. In the cases studied in this work, the governing equations of the flow are the continuity equation (conservation of mass) and the Navier-Stokes equation (conservation of linear momentum). In general, there are two approaches to deriving these governing equations. One with a fixed point in space and the fluid properties passing through it (Eulerian approach) and other following fluid properties as they travel through the flow (Lagrangian approach). Considering also an imaginary finite closed volume taken within a region of the fluid, let us define it as *control volume* and the closed surface that bounds it as a *control surface*.

Mass Conservation (Continuity Equation)

This conservation law states that the mass of an *isolated system* does not change as the system evolves, so mass can be neither created nor destroyed. Considering a fixed control volume, the net mass flow through boundaries (control surfaces) has to be numerically equal to the time rate of decrease of mass inside the same control volume.

$$\begin{array}{c}\text{Rate of increase of}\\ \text{mass in fluid}\\ \text{element}\end{array} \quad = \quad \begin{array}{c}\text{Net rate of flow of}\\ \text{mass into fluid}\\ \text{element}\end{array}$$

The mathematical equation in the form of partial differential equation is given by

$$\frac{\partial \rho}{\partial t} + \vec{\boldsymbol{\nabla}} \cdot (\rho \vec{v}) = S_m \ , \tag{2.11}$$

where $\vec{v} = (u, v, w)$ is the velocity vector, S_m is the source term of mass $[kg/m^3 s]$ and refers to mass added to the continuous phase from the dispersed second phase (for example, due to vaporization of liquid droplets) or any other kind of mass sources.

Equation derivation is not showed here but it may be easily find in any book of fluid dynamics. The only assumption about the nature of fluid is that it is *continuum*. Therefore, this continuity equation hold in general for three-dimensional, unsteady (time-dependent), viscous, rotational and compressible flow.

Linear Momentum Conservation (Navier-Stokes Equations)

This principle is the Newton's second law applied in a fixed fluid volume of control. It states that the sum of forces acting on the volume control is equal to the time rate of change of momentum.

$$\begin{array}{ccc} \text{Rate of increase of momentum of fluid element} & = & \text{Sum of forces on fluid element} \end{array}$$

Then, considering a *Newtonian* fluid (viscous stresses are proportional to the rates of deformation), we have the following mathematical equation,

$$\begin{aligned} \frac{\partial \rho u}{\partial t} + \vec{\boldsymbol{\nabla}} \cdot (\rho u \vec{v}) &= -\frac{\partial p_s}{\partial x} + \vec{\boldsymbol{\nabla}} \cdot \left(\mu \vec{\boldsymbol{\nabla}} u \right) + S_{Mx} \ , \\ \frac{\partial \rho v}{\partial t} + \vec{\boldsymbol{\nabla}} \cdot (\rho v \vec{v}) &= -\frac{\partial p_s}{\partial y} + \vec{\boldsymbol{\nabla}} \cdot \left(\mu \vec{\boldsymbol{\nabla}} v \right) + S_{My} \ , \\ \frac{\partial \rho w}{\partial t} + \vec{\boldsymbol{\nabla}} \cdot (\rho w \vec{v}) &= -\frac{\partial p_s}{\partial z} + \vec{\boldsymbol{\nabla}} \cdot \left(\mu \vec{\boldsymbol{\nabla}} w \right) + S_{Mz} \ , \end{aligned} \tag{2.12}$$

where p_s is the *static pressure* $[Pa]$, μ is dynamic viscosity $[Pa.s]$ and S_{Mx}, S_{My}, S_{Mz} are the momentum source terms $[kg/m^2 s^2]$.

Again, no other assumption besides that the fluid is *continuum* and that it is a *Newtonian* fluid.

Equations for *conservation of angular momentum* and for *conservation of energy* are not described as they are not part of this work scope, since the first is used for solution of a *polar* fluid [28] (e.g. blood) flow and the second when temperature is being taking into consideration.

Solution of the partial differential equations (Equations (2.11) and (2.12)) in a

computer-based simulation requires *discretization*, that is the process of transferring continuous functions, models, variables, and equations into discrete counterparts. Several methods of discretization are available nowadays, but the most used for fluid simulation is the *Finite Volume Method* (FVM). This method is based in the solution over discrete fixed *control volumes* ensuring the conservation of fluxes through it, so it uses the *conservative form* (divergence form) of governing equations (Equation (2.13)).

Introducing a general variable Ψ, the conservative form of all fluid equations can usefully be written in the following form:

$$\frac{\partial \rho\Psi}{\partial t} + \vec{\boldsymbol{\nabla}} \cdot (\rho\Psi\vec{v}) = \vec{\boldsymbol{\nabla}} \cdot \left(\Gamma\vec{\boldsymbol{\nabla}}\Psi\right) + S_\Psi \ , \tag{2.13}$$

where Γ is the diffusion coefficient and S_Ψ is the source term. This is called *transport equation* of Ψ property [29]. It is important to notice that the second term of LHS is a *convective* term while the first term in the RHS is a *diffusive* term.

Setting Ψ equal to $1, u, v$ or w and selecting appropriate values for diffusion coefficient Γ and source term S_Ψ the transport equation turns into conservative equation of mass (Equation (2.11)) and linear momentum for each direction (Equation (2.12)).

The FVM requires the control volume integration of Equation (2.13). Integrating over a 3D control volume (of volume CV and surface CS) and also in respect to time t, the most general integrated form of the transport equation can be recast as

$$\begin{aligned} \int_{\Delta t} \frac{\partial}{\partial t}\left(\int_{CV} \rho\Psi dV\right) dt + \int_{\Delta t}\int_{CS} \vec{n} \cdot (\rho\Psi\vec{v})\, dA dt = \\ \int_{\Delta t}\int_{CS} \vec{n} \cdot \left(\Gamma\vec{\boldsymbol{\nabla}}\Psi\right) dA dt + \int_{\Delta t}\int_{CV} S_\Psi dA dt \ , \end{aligned} \tag{2.14}$$

Boundary Conditions

Governing equations are a system of partial differential equations that describe the motion of a fluid and following the idea of *well-posed problem* introduced by Jacques Salomon Hadamard [30], this set of equations are solved with the governing equations (Equations (2.11) and (2.12)) and auxiliary (initial and boundary) conditions.

In transient problems the initial values of all the flow variables need to be specified at all solution points in the flow domain.

In the spatial domain also there is a need to specify a condition for each boundary. Every code has it own set of options and particularities but it is possible to list the most common and important ones for this work [14]:

- **Velocity Inlet** - Defines the velocity and scalar properties of the flow at inlet

boundaries;

- **Pressure Outlet** - Defines the static pressure at flow outlets (and also other scalar variables, in case of backflow);
- **Wall** - It bounds fluid regions. In viscous flows, there is the option of *no-slip* condition or to model a *slip wall* by specifying shear (free slip - zero shear);
    - *Stationary* - Fixed wall;
    - *Moving* - Used to specify the translational or rotational velocity of the wall;
- **Symmetry** - Used when the physical geometry of interest, and the expected pattern of the flow solution, have mirror symmetry.

When computing results for a multiphase flow, it is required to specify the phase region in each boundary and all additional parameters for each fluid. Some commercial CFD solvers provides a specific setup for open channel flow. It allows simulation of free surface between the flowing fluid and fluid above it and also regular/irregular waves, for analyzing wave kinematics and wave impact loads on moving bodies [31]. When it is set, some conditions for the primary and secondary phase are defined at the boundaries, for instance, the hydrostatic pressure (setting gravity vector), free surface level and bottom level according to a reference level.

Through *Velocity Inlet* boundary condition, the wave definition must be given. There are multiple possibilities of wave theory to simulate surface gravity waves, mentioning a few of them:

- **Linear Airy** - Simplest and most useful of all wave theories. Assume that wave height is small compared to the wave length or wave depth;
- **Higher Order Stokes** - High steepness finite amplitudes waves operating in intermediate to deep depth range (Nonlinear);
- **Higher Order Cnoidal/Solitary** - Cnoidal displays long flat troughs and narrow crests of real waves in shallow waters while in the limit of infinite wavelength it describes a solitary wave, with a single hump, having no troughs (Nonlinear);
- **Long/Short-crested Wave Spectrums** - Random waves based on a wave energy distribution function (Nonlinear).

Figure 2.3 shows a chart with the validity of each theory, in which H is the wave height $[m]$, g is the gravity $[m/s^2]$, T is period $[s]$ and h_{depth} is the water depth $[m]$. Also, it is possible to observe a physical illustration for the behavior of wave

theories. The spectrum is a summation of different wave frequencies and it physical illustration is a random wave.

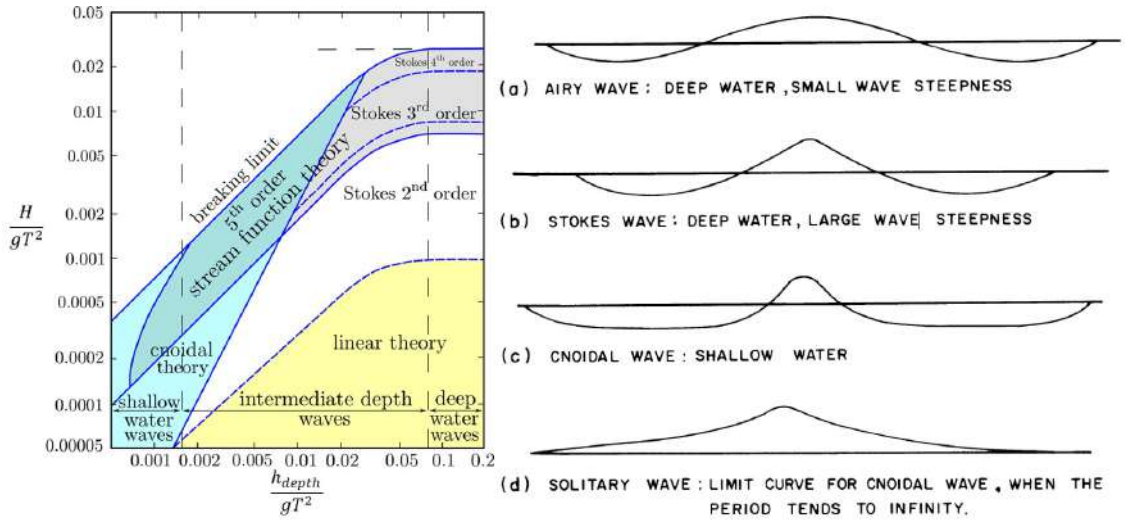

Figure 2.3: Limits of validity and physical illustration of various wave theories (Adapted from MÉHAUTE [13]).

As expected, the most complex and higher the order of a theory, more grid refinement and, therefore, more computational resource it requires for a proper solution of the flow.

There is also a possibility to define a numerical wave beach (Figure 2.4) to suppress numerical reflection near the *Pressure Outlet* boundary for wave dampening by adding a damping sink term in the momentum equation

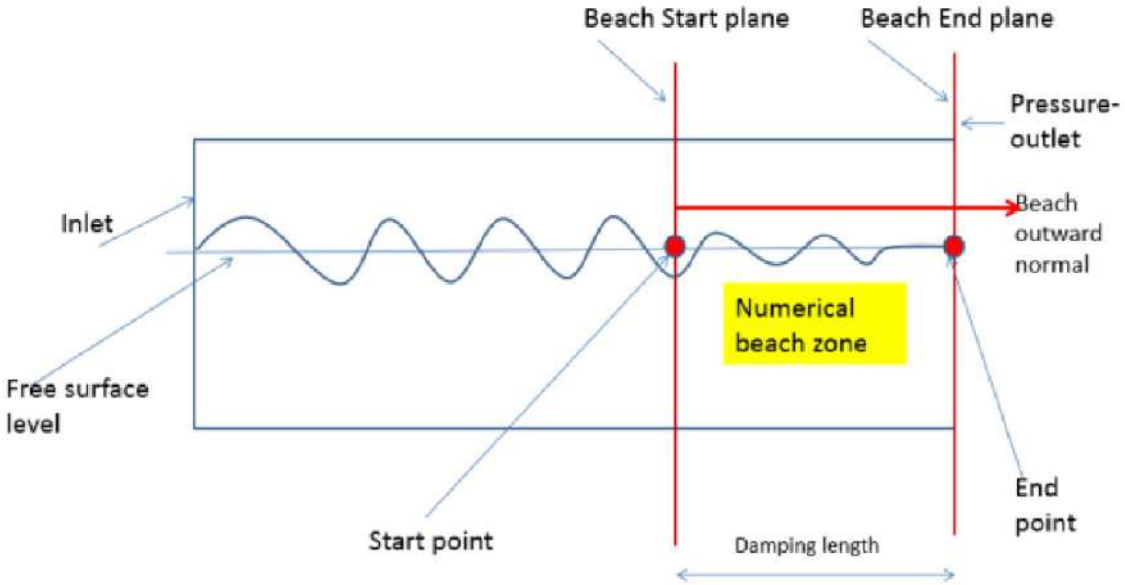

Figure 2.4: Numerical beach sketch (ANSYS, INC. [14]).

At boundaries it is also important to specify the transportation of turbulence quantities. This is shown with more details in Section 2.2.2

2.2.2 Turbulence Modeling

Many, if not most, flows in practical engineering shows an unstable behavior in which the measurement of a physical quantity change continuously with time (Figure 2.5). Turbulent flows are characterized by this random and chaotic variation of flow quantities. Laminar flows, on the other hand, present a smooth behavior with adjacent layer of fluid sliding past each other in an orderly fashion [29] and they are fully described in Section 2.2.1.

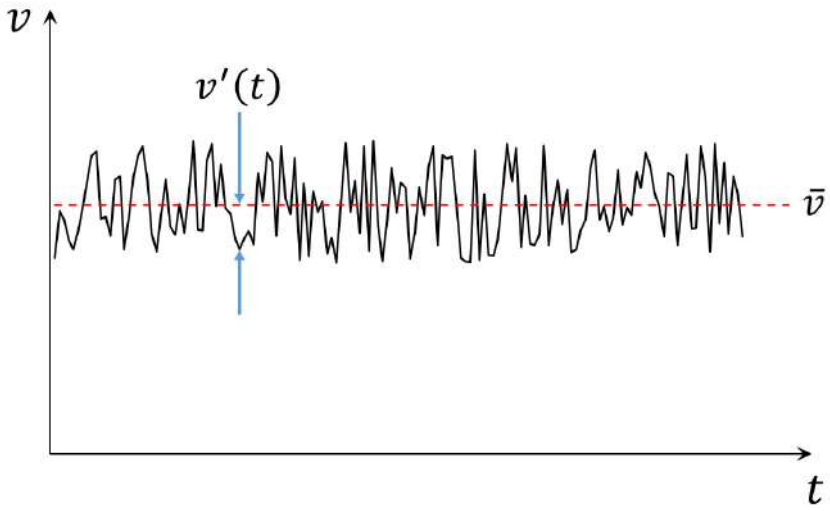

Figure 2.5: Typical measurement in turbulent flow.

REYNOLDS [15] did a famous experiment in a horizontal pipe immersed in a tank filled with water (Figure 2.6). Intake of the pipe is fitted with a trumpet mouthpiece, in order to avoid the formation of vortices along its edges. By varying the velocity of the flow inside the tube and introducing a colored tracer, he was able to provide an image of the velocity field (Figure 2.6). When the flow is laminar the tracer creates a straight line (Figure 2.6.a), increasing speed the regime becomes turbulent and the tracer spread over the pipe (Figure 2.6.b) showing a random and chaotic behavior as aforementioned. Illuminating the flow by a spark, the tracer shows swirls (eddies) formed by elongated filaments that become finer and finer (Figure 2.6.c)), until they mix completely with the surrounding fluid. A property of a turbulent flow is often labeled by *eddy*.

Previously that experiment, STOKES [32] came with the concept of a dimensionless number to predict the fluid flow. Then, REYNOLDS [15] proposed the relation of inertial and viscous forces (Equation (2.15)) and based the experiment aforementioned in variation of it. This dimensionless number was named after *Reynolds* just in 1908, where SOMMERFELD [33] referred to the R number as the *Reynolds number*.

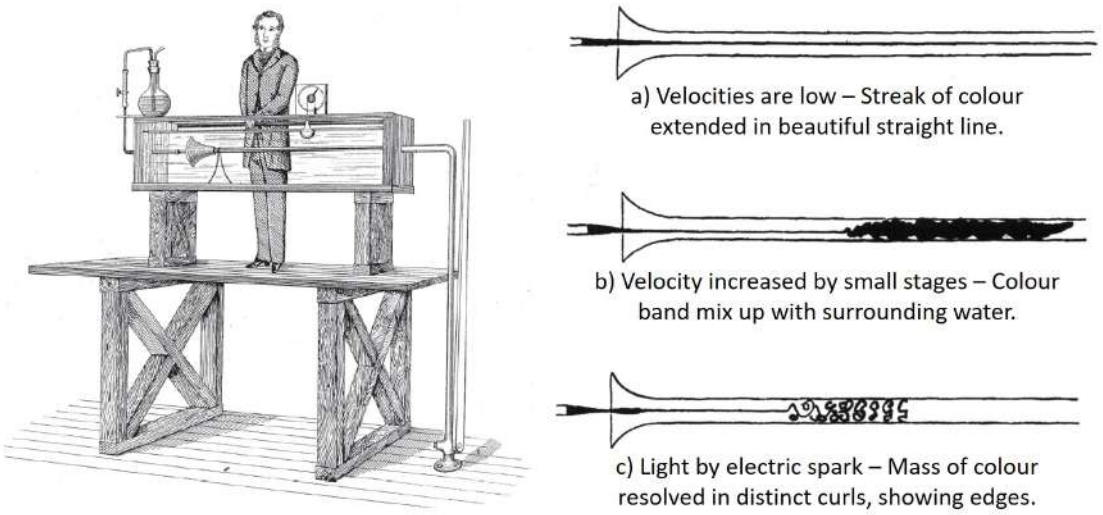

Figure 2.6: Schematic overview of the experimental setup and visualization conducted by Osborne Reynolds (Adapted from REYNOLDS [15]). *a)* Laminar flow, *b)* turbulent flow and *c)* turbulent flow seen in detail.

$$Re = \frac{inertial\ forces}{viscous\ forces} = \frac{\rho v c}{\mu}\ . \tag{2.15}$$

Furthermore, as CFD deals with temporal and spatial discretizations, it is important to have knowledge of turbulence scales. These scales range from above by the dimensions of the flow field and from below by the diffusive action of molecular viscosity. The largest turbulent eddies extract energy from the mean flow by a process called *vortex stretching*. The larger eddies scales are determined by the same order as the velocity and length scale of mean flow. It is considered the *integral turbulence length scale*. The intermediate range of scales is called the *inertial subrange* and the *Taylor microscale* resides in a wavelength range between the large eddies, and the small eddies. Smallest scale present within a flow is called *Kolmogorov microscale* and it is the scale at which energy is dissipated by molecular viscosity. The energy spectrum of turbulence is shown in Figure 2.7 with the logarithm of turbulent kinetic energy by wavenumber ($\log(E(k)) \times \log(k)$). The region of each scale and the direction of *energy cascade*, i.e. the transfer of energy from large scales of motion to the small scales until dissipation by viscosity, is also presented.

It is not possible to solve the instantaneous equations in smallest scales directly for most engineering applications. As the Reynolds numbers (Re) typically presented in real cases have very chaotic turbulent solutions, it is necessary to model the influence of these scales. Most of the time, in engineering applications we are interested in mean or integral quantities, so it is necessary to deduct the governing equations for the mean flow based in classical procedure of REYNOLDS [34] to filter out all, or at least, parts of the turbulent spectrum.

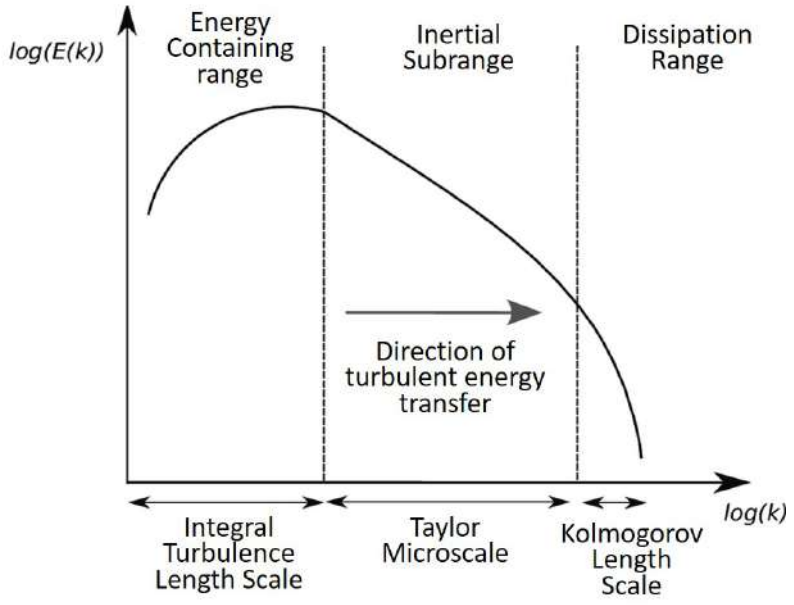

Figure 2.7: Energy spectrum of turbulence (Energy cascade).

Time average of a flow property Ψ is defined as follows:

$$\bar{\Psi} \equiv \frac{1}{\Delta t} \int_{t_0}^{t_0+\Delta t} \Psi dt \ , \tag{2.16}$$

Reynolds decomposition defines a flow property, for instance v, as the sum of a steady mean component $\overline{v}$ and a time varying fluctuating component v' (Figure 2.5). Then, for a 3D variable value, for instance the velocity components (u, v, w) and the static pressure p_s, the momentary value is defined with Reynolds decomposition by:

$$\begin{aligned} u\left(x,y,z,t\right) &= \bar{u}\left(x,y,z\right) + u'\left(x,y,z,t\right) \ , \\ v\left(x,y,z,t\right) &= \bar{v}\left(x,y,z\right) + v'\left(x,y,z,t\right) \ , \\ w\left(x,y,z,t\right) &= \bar{w}\left(x,y,z\right) + w'\left(x,y,z,t\right) \ , \\ p_s\left(x,y,z,t\right) &= \bar{p_s}\left(x,y,z\right) + p_s'\left(x,y,z,t\right) \ , \end{aligned} \tag{2.17}$$

where $\bar{u}, \bar{v}, \bar{w}$ and $\bar{p_s}$ denotes the time-averaged values and u', v', w' an p_s' are deviations from the expectation value (or fluctuations). Analogously the decomposition may be used for other variables like density and temperature.

By definition, time average of a fluctuating quantity is zero. There are some other rules for time averaging that will be not exposed here but may be easily found in a good turbulence book. For a compressible flow, density weighted time averaging (Favre averaging [35]) is convenient, but as BRADSHAW *et al.* [36] stated that small density fluctuations do not appear to affect the flow significantly, specifically

for the Mach number M_a presented in this work, it will not be considered here the compressible equations. Due to that, applying time average in the incompressible Equations (2.11) and (2.12) yields to

$$\vec{\boldsymbol{\nabla}} \cdot \bar{\mathbf{v}} = 0 \,, \tag{2.18}$$

$$\begin{aligned}
\frac{\partial \overline{u}}{\partial t} + \vec{\boldsymbol{\nabla}} \cdot (\overline{u}\bar{\mathbf{v}}) &= -\frac{1}{\rho}\frac{\partial \bar{p}_s}{\partial x} + \nu \vec{\boldsymbol{\nabla}} \cdot \left(\vec{\boldsymbol{\nabla}} \overline{u}\right) \\
&\quad + \frac{1}{\rho}\left[\frac{\partial(-\rho\overline{u'^2})}{\partial x} + \frac{\partial\left(-\rho\overline{u'v'}\right)}{\partial y} + \frac{\partial\left(-\rho\overline{u'w'}\right)}{\partial z}\right] \,, \\
\frac{\partial \overline{v}}{\partial t} + \vec{\boldsymbol{\nabla}} \cdot (\overline{v}\bar{\mathbf{v}}) &= -\frac{1}{\rho}\frac{\partial \bar{p}_s}{\partial y} + \nu \vec{\boldsymbol{\nabla}} \cdot \left(\vec{\boldsymbol{\nabla}} \overline{v}\right) \\
&\quad + \frac{1}{\rho}\left[\frac{\partial\left(-\rho\overline{u'v'}\right)}{\partial x} + \frac{\partial(-\rho\overline{v'^2})}{\partial y} + \frac{\partial\left(-\rho\overline{v'w'}\right)}{\partial z}\right] \,, \\
\frac{\partial \overline{w}}{\partial t} + \vec{\boldsymbol{\nabla}} \cdot (\overline{w}\bar{\mathbf{v}}) &= -\frac{1}{\rho}\frac{\partial \bar{p}_s}{\partial z} + \nu \vec{\boldsymbol{\nabla}} \cdot \left(\vec{\boldsymbol{\nabla}} \overline{w}\right) \\
&\quad + \frac{1}{\rho}\left[\frac{\partial\left(-\rho\overline{u'w'}\right)}{\partial x} + \frac{\partial\left(-\rho\overline{v'w'}\right)}{\partial y} + \frac{\partial(-\rho\overline{w'^2})}{\partial z}\right] \,,
\end{aligned} \tag{2.19}$$

where $\bar{\mathbf{v}}$ is the steady mean velocity vector, given also by Reynolds decomposition.

These are the *Reynolds-Averaged Navier-Stokes* (RANS) equations. Comparing Equations (2.18) and (2.19) to incompressible Equations (2.11) and (2.12), respectively, reveals new terms in the last three terms of the RHS. The *Reynolds stress* tensor are defined as $\tau_{ij} \equiv -\rho\overline{v_i' v_j'}$ and, due to its symmetry, it brings six additional unknown in the time-averaged momentum equation. System cannot be closed as it presents more unknown than equations and this is known as the *closure problem*. For closing the system of equations, an approximation of Reynolds stress tensor (models of the first order) or approximation of unknowns in transport equations for Reynolds stresses (models of the second order) must be modeled. BOUSSINESQ [37] proposed the concept of eddy viscosity relating the turbulence stresses to the mean rates of deformation. The Reynolds stress tensor is given by its constitutive relation:

$$\tau_{ij} \equiv -\rho\overline{v_i' v_j'} = \mu_t \left(\frac{\partial \overline{v_i}}{\partial x_j} + \frac{\partial \overline{v_j}}{\partial x_i}\right) - \frac{2}{3}\rho\kappa\delta_{ij} \,, \tag{2.20}$$

where μ_t is the *turbulent* or *eddy viscosity* $[Pa.s]$, $\kappa = \frac{1}{2}\left(\overline{u'^2} + \overline{v'^2} + \overline{w'^2}\right)$ is the *turbulent kinetic energy per unit mass* $[J/m]$ and δ_{ij} is the *Kronecker delta*. Equation (2.20) is known as *Boussinesq hypothesis*.

The second term on the RHS is to assure that summation of normal stresses ($tr(\tau_{ij})$) gives the correct result, as $-\rho\left(\overline{u'^2} + \overline{v'^2} + \overline{w'^2}\right) = -2\rho\kappa$, and without the term would be zero after applying continuity equation Equation (2.18). In some turbulence models the turbulent kinetic energy is not calculated and the constitutive

relation is presented neglecting this last term. SPALART and ALLMARAS [38] affirmed that this has no major effect in thin shear flows and the addition is an approximation in any case. A specific commercial CFD solver (Fluent) solver manual states that when the turbulent kinetic energy per unit mass is not calculated, the last term in Equation (2.20) is also ignored [31]. Therefore, it does not necessarily require the determination of κ to make use of the eddy viscosity formulation, the main objective is then to determine the eddy viscosity only.

Eddy viscosity is associated with an increase of fluid resistance to deformation, in other words, the turbulence causes an apparent increase on fluid viscosity. Some turbulence models are based on the boussinesq hypothesis in the use of eddy viscosity concept.

Despite Equations (2.18) and (2.19) shown here do not take compressibility into consideration, the following models can consider that with a different constitutive relation between stress and strain rate for a Newtonian fluid [39] with addition of the term $-\frac{2}{3}\mu_t\frac{\partial v_k}{\partial x_k}$ in RHS of Equation (2.20) [39].

Mixing Length Model

It is a zero-equation model, as there is no new *transport equation* needs to be solved in this model. Attempt to describe momentum transfer by the stresses within a Newtonian fluid boundary layer by means of simple algebraic formulae for eddy viscosity as function of position. PRANDTL [40] assumed that the *kinematic eddy viscosity* is given by

$$\nu_t = l_m^2 \left|\frac{\partial \overline{u}}{\partial y}\right| \quad \therefore \quad \tau_{xy} = \tau_{yx} = \rho l_m^2 \left|\frac{\partial \overline{u}}{\partial y}\right| \frac{\partial \overline{u}}{\partial y} \,, \tag{2.21}$$

The mixing length l_m depends on the nature of the flow and, in general, is space dependent. It is a very easy to implement and cheap model, but as Prandtl itself stated: "only a rough approximation"[41]. It is incapable of describing recirculation and separation [29].

Spalart-Allmaras

Spalart–Allmaras model [38] is an one-equation model, differently than previously model, it solves a transport equation for the *kinematic eddy viscosity parameter* $\tilde{\nu}$. The turbulent viscosity is then calculated as

$$\mu_t = \rho\tilde{\nu} f_{\nu 1} \,. \tag{2.22}$$

Transport equation of kinematic eddy viscosity parameter $\tilde{\nu}$ is given by

$$\frac{\partial \rho\tilde{\nu}}{\partial t} + \vec{\boldsymbol{\nabla}} \cdot (\rho\tilde{\nu}\bar{\mathbf{v}}) = \frac{1}{\sigma_\nu}\vec{\boldsymbol{\nabla}} \cdot \left[(\mu + \rho\tilde{\nu})\, \vec{\boldsymbol{\nabla}}\tilde{\nu} + C_{b2}\rho \left(\frac{\partial \tilde{\nu}}{\partial x_i} \right)^2 \right] + G_{\tilde{\nu}} - Y_{\tilde{\nu}} + S_{\tilde{\nu}} \ ,$$

$$G_{\tilde{\nu}} = C_{b1}\rho\tilde{\nu}\tilde{S} \ , \quad Y_{\tilde{\nu}} = C_{w1}\rho \left(\frac{\tilde{\nu}}{\kappa y_{wall}} \right)^2 f_w \ ,$$

$$\tilde{S} \equiv S + \frac{\tilde{\nu}}{\kappa^2 y_{wall}^2} f_{\nu 2} \ , \quad S \equiv \sqrt{2\Omega_{ij}\Omega_{ij}} \ , \quad \Omega_{ij} = \frac{1}{2}\left(\frac{\partial v_i}{\partial x_j} - \frac{\partial v_j}{\partial x_i} \right) \ , \tag{2.23}$$

$$f_{\nu 1} = \frac{\left(\frac{\tilde{\nu}}{\nu}\right)^3}{\left(\frac{\tilde{\nu}}{\nu}\right)^3 + C_{\nu 1}^3} \ , \quad f_{\nu 2} = \left(1 - \frac{\frac{\tilde{\nu}}{\nu}}{1 + \frac{\tilde{\nu}}{\nu} f_{\nu 1}} \right) \ ,$$

$$f_{\nu 3} = g \left[\frac{1 + C_{w3}^6}{g^6 + C_{w3}^6} \right]^{\frac{1}{6}} \ , \quad g = r + C_{w2}\left(r^6 - r \right) \ , \quad r \equiv \frac{\tilde{\nu}}{\tilde{S}\kappa^2 y_{wall}^2}$$

where $G_{\tilde{\nu}}$ is the production of turbulent viscosity, $Y_{\tilde{\nu}}$ is the destruction of turbulent viscosity that occurs in the near-wall region due to wall blocking and viscous damping, and $S_{\tilde{\nu}}$ a source term of the viscosity parameter. Also, there is y_{wall} that is the distance from the wall, S is a scalar measure of the deformation tensor and Ω_{ij} is the mean rate-of-rotation tensor.

Model constants are as follows:

Table 2.1: Values of constants in Spalart-Allmaras model.

$\sigma_\nu = 2/3$	$\kappa = 0.4187$	$C_{b1} = 0.1355$	$C_{b2} = 0.622$	$C_{\nu 1} = 7.1$
$C_{w1} = \frac{C_{b1}}{\kappa^2} + \frac{1 + C_{b2}}{\sigma_\nu}$		$C_{w2} = 0.3$	$C_{w3} = 2.0$	

This model presents a stable behavior with good convergence. It was tuned for external aerodynamic flow giving good performance in boundary layers with adverse pressure gradients, mainly predicting stalled flows. It was not tuned for industrial flows, so it produces relatively larger errors for some free shear flows [31] and lacks sensitivity to transport processes in rapidly changing flows [29].

Standard κ-ϵ Model

Standard κ-ϵ model [42] is considered one of the simplest models and it is very well established in industry. It is a two-equation model, and the eddy viscosity is computed as follows:

$$\mu_t = \rho C_\mu \frac{\kappa^2}{\epsilon} \ , \tag{2.24}$$

where C_μ is a constant, κ is the *turbulent kinetic energy* and ϵ is the *rate of viscous dissipation* of turbulent kinetic energy.

The transport equation of each quantity is given below in Equation (2.25) with

all parameters necessary (considering the assumption of ideal gas).

$$\begin{gathered}
\frac{\partial \rho\kappa}{\partial t} + \vec{\boldsymbol{\nabla}} \cdot (\rho\kappa\bar{\mathbf{v}}) = \vec{\boldsymbol{\nabla}} \cdot \left[\frac{\mu_t}{\sigma_\kappa}\vec{\boldsymbol{\nabla}}\kappa\right] - \rho\epsilon + G_\kappa + G_b - Y_M + S_\kappa \ , \\
\frac{\partial \rho\epsilon}{\partial t} + \vec{\boldsymbol{\nabla}} \cdot (\rho\epsilon\bar{\mathbf{v}}) = \vec{\boldsymbol{\nabla}} \cdot \left[\frac{\mu_t}{\sigma_\epsilon}\vec{\boldsymbol{\nabla}}\epsilon\right] + C_{1\epsilon}\frac{\epsilon}{\kappa}\left(G_\kappa + C_{3\epsilon}G_b\right) - C_{2\epsilon}\rho\frac{\epsilon^2}{\kappa} + S_\epsilon \ , \\
G_\kappa = \mu_t S^2 \ , \quad S \equiv \sqrt{2S_{ij}S_{ij}} \ , \quad S_{ij} = \frac{1}{2}\left(\frac{\partial v_i}{\partial x_j} + \frac{\partial v_j}{\partial x_i}\right) \ , \\
G_b = -g_i\frac{\mu_t}{\rho Pr_t}\frac{\partial \rho}{\partial x_i} \ , \quad C_{3\epsilon} = \tanh\left|\frac{v}{u}\right| \ ,
\end{gathered} \tag{2.25}$$

where G_κ is the generation of turbulence kinetic energy due to the mean velocity gradients, G_b is the generation of turbulence kinetic energy due to buoyancy, Y_M is the contribution of the fluctuating dilatation in compressible turbulence to the overall dissipation rate (not in the scopes of this work) and S_κ, S_ϵ are source terms of kinetic energy and of dissipation rate, respectively. Pr_t is the turbulent *Prandtl* number for energy (default value in the solver of this work $Pr_t = 0.85$ [31]) and g_i is the component of the gravitational vector in the i^{th} direction. The degree to which ϵ is affected by the buoyancy is determined by the constant $C_{3\epsilon}$. In the solver used in this work [31], this constant is calculated according to the relation above (Equation (2.25)) [43], where v is the component of the flow velocity parallel to the gravitational vector and u is the component of the flow velocity perpendicular to the gravitational vector. So it becomes 1 for buoyant shear layers for which the main flow direction is aligned with the direction of gravity. For buoyant shear layers that are perpendicular to the gravitational vector, it will become zero [31].

Model constants of Equation (2.25) are as follows:

Table 2.2: Values of constants in κ-ϵ model.

$\sigma_\kappa = 1.00$	$\sigma_\epsilon = 1.30$	$C_\mu = 0.09$	$C_{1\epsilon} = 1.44$	$C_{2\epsilon} = 1.92$

It is the most widely validated turbulence model [29] and also it has excellent performance for many industrially relevant flows. However, it is known to have poor performance in important cases such as unconfined flows, curved boundary layers, rotating flows and flows in non-circular ducts [29]. In summary, its near-wall performance is unsatisfactory for boundary layers with adverse pressure gradients [14].

Standard κ-ω Model

This an empirical model that also attempts to predict turbulence based on eddy viscosity concept using transport equations for the turbulence kinetic energy (κ)

and, now, the specific dissipation rate (ω) [44], defined as

$$\mu_t = a^* \rho \frac{\kappa}{\omega} \ , \quad \omega \equiv \frac{1}{\beta^*_\infty} \frac{\epsilon}{\kappa} \ , \tag{2.26}$$

where a^* is a coefficient that damps the turbulent viscosity causing a low-Reynolds number correction [31].

The two transport equations, without considering compressibility effects, are described as follows:

$$\begin{gathered}
\frac{\partial \rho\kappa}{\partial t} + \vec{\boldsymbol{\nabla}} \cdot (\rho\kappa\bar{\mathbf{v}}) = \vec{\boldsymbol{\nabla}} \cdot \left[\mu + \frac{\mu_t}{\sigma_\kappa} \vec{\boldsymbol{\nabla}} \kappa \right] + G_\kappa - Y_\kappa + S_\kappa \ , \\
\frac{\partial \rho\omega}{\partial t} + \vec{\boldsymbol{\nabla}} \cdot (\rho\omega\bar{\mathbf{v}}) = \vec{\boldsymbol{\nabla}} \cdot \left[\mu + \frac{\mu_t}{\sigma_\omega} \vec{\boldsymbol{\nabla}} \omega \right] + G_\omega - Y_\omega + S_\omega \ , \\
G_\kappa = \mu_t S^2 \ , \quad G_\omega = \alpha \frac{\omega}{\kappa} G_\kappa \ , \quad S \equiv \sqrt{2 S_{ij} S_{ij}} \ , \quad S_{ij} = \frac{1}{2} \left(\frac{\partial v_i}{\partial x_j} + \frac{\partial v_j}{\partial x_i} \right) \ , \\
\alpha = \frac{\alpha_\infty}{\alpha^*} \left(\frac{\alpha_0 + Re_t/R_\omega}{1 + Re_t/R_\omega} \right) \ , \quad \alpha^* = \alpha^*_\infty \left(\frac{\alpha^*_0 + Re_t/R_\kappa}{1 + Re_t/R_\kappa} \right) \ , \quad Re_t = \frac{\rho\kappa}{\mu\omega} \ , \\
Y_\kappa = \rho \beta^*_i f_{\beta^*} \kappa\omega \ , \quad Y_\omega = \rho \beta_i f_\beta \omega^2 \ , \\
f_{\beta^*} = \begin{cases} 1 & \chi_k \leq 0 \\ \dfrac{1 + 680\chi^2_\kappa}{1 + 400\chi^2_\kappa} & \chi_k > 0 \end{cases} \ , \quad f_\beta = \frac{1 + 70\chi_\omega}{1 + 80\chi_\omega} \ , \\
\chi_\kappa \equiv \frac{1}{\omega^3} \frac{\partial \kappa}{\partial x_j} \frac{\partial \omega}{\partial x_j} \ , \quad \chi_\omega = \left| \frac{\Omega_{ij} \Omega_{jk} S_{ki}}{(\beta^*_\infty \omega)^3} \right| \ , \\
\beta^*_i = \beta^*_\infty \left(\frac{4/15 + (Re_t/R_\beta)^4}{1 + (Re_t/R_\beta)^4} \right) \ ,
\end{gathered} \tag{2.27}$$

where G_κ represents the generation of turbulence kinetic energy due to mean velocity gradients, G_ω represents the generation of specific dissipation rate, Y_κ and Y_ω represent the dissipation of κ and ω due to turbulence, respectively. S_κ and S_ω are source terms of kinetic energy and of specific dissipation rate.

In Table 2.3, the constants of this model are presented.

Table 2.3: Values of constants in κ-ω model.

$\sigma_\kappa = 2.0$	$\sigma_\omega = 2.0$	$\beta_i = 0.072$	$\beta^*_\infty = 0.09$
$\alpha^*_0 = 0.024$	$\alpha^*_\infty = 1.0$	$\alpha_0 = 1/9$	$\alpha_\infty = 0.52$
$R_\kappa = 6$	$R_\omega = 2.95$		$R_\beta = 8$

Comparing with the previous model, the ω-equation offers advantages relative to the ϵ-equation as it is better predicting adverse pressure gradient boundary layer flows and separation. The downside is a relatively strong sensitivity of the solution

depending on the freestream values of and outside the shear layer.

Shear Stress Transport (SST) κ-ω Model

SST is also considered a two equation model that combines the κ-ω turbulence model and κ-ϵ turbulence model such that the κ-ω is used in the inner region of the boundary layer and switches to the κ-ϵ in the outer region at free shear flow [45, 46]. For improved performance in flows with adverse pressure gradients and wake regions, eddy viscosity is obtained by a *limiter* to the formulation

$$\begin{aligned} \mu_t &= \rho\frac{\kappa}{\omega}\frac{1}{max\left[\frac{1}{a^*};\frac{SF_2}{a_1\omega}\right]} , \\ F_2 = \tanh\left(\arg_2^2\right) , \quad \arg_2 &= max\left[2\frac{\sqrt{\kappa}}{0.09\omega y_{dist}};\frac{500\mu}{\rho y_{dist}^2\omega}\right] , \end{aligned} \tag{2.28}$$

where y_{dist} is the distance to the next surface.

The transport equations are slightly different from previous model, with the addition of a cross-diffusion term D_ω in ω-equation. For compressible flows,

$$\begin{aligned} \frac{\partial\rho\omega}{\partial t} + \vec{\boldsymbol{\nabla}}\cdot(\rho\omega\bar{\mathbf{v}}) &= \vec{\boldsymbol{\nabla}}\cdot\left[\mu + \frac{\mu_t}{\sigma_\omega}\vec{\boldsymbol{\nabla}}\omega\right] + G_\omega - Y_\omega + D_\omega + S_\omega , \\ G_\omega = \alpha\frac{\alpha^*}{\nu_t}G_\kappa , \quad Y_\kappa &= \rho\beta_i^*\kappa\omega , \quad Y_\omega = \rho\beta_i\omega^2 , \\ \sigma_\kappa = \frac{1}{F_1/\sigma_{\kappa,1} + (1-F_1)/\sigma_{\kappa,2}} , \quad \sigma_\omega &= \frac{1}{F_1/\sigma_{\omega,1} + (1-F_1)/\sigma_{\omega,2}} , \\ \alpha_\infty = F_1\alpha_{\infty,1} + (1-F_1)\alpha_{\infty,2} , \quad \beta_i &= F_1\beta_{i,1} + (1-F_1)\beta_{i,2} , \\ \alpha_{\infty,1} = \frac{\beta_{i,1}}{\beta_\infty^*} - \frac{\kappa^2}{\sigma_{\omega,1}\sqrt{\beta_\infty^*}} , \quad \alpha_{\infty,2} &= \frac{\beta_{i,2}}{\beta_\infty^*} - \frac{\kappa^2}{\sigma_{\omega,2}\sqrt{\beta_\infty^*}} , \\ D_\omega = 2(1-F_1)\rho\frac{1}{\omega\sigma_{\omega,2}}\frac{\partial\kappa}{\partial x_j}\frac{\partial\omega}{\partial x_j} , \quad F_1 &= \tanh\left(arg_1^4\right) , \\ arg_1 = min\left[max\left(\frac{\sqrt{\kappa}}{0.09\omega y_{dist}};\frac{500\mu}{\rho y_{dist}^2\omega}\right);\frac{4\rho\kappa}{\sigma_{\omega,2}D_\omega^+ y_{dist}^2}\right] , \\ D_\omega^+ = max\left[2\rho\frac{1}{\sigma_{\omega,2}}\frac{1}{\omega}\frac{\partial\kappa}{\partial x_j}\frac{\partial\omega}{\partial x_j};10^{-10}\right] , \end{aligned} \tag{2.29}$$

where is a blending function is the positive portion of the cross-diffusion term (ANSYS, INC. [31] formulas presented here has some terms slightly different of the one presented in MENTER [46] original paper). The blend of the two previous models together (κ-ω and κ-ϵ), the standard κ-ϵ model has been transformed into equations based on κ and ω, which leads to the introduction of a cross-diffusion term D_ω. Terms not shown in Equation (2.29) are identical in Equation (2.27), including the transport of κ.

In Table 2.4, the constants of this model are presented.

Table 2.4: Values of constants in Shear Stress Transport (SST) κ-ω model.

$\sigma_{\kappa,1} = 1.176$	$\sigma_{\omega,1} = 2.0$	$\sigma_{\kappa,2} = 1.0$	$\sigma_{\omega,2} = 1.168$
$a_1 = 0.31$	$\beta_{i,1} = 0.075$	$\beta_{i,2} = 0.0828$	

It has been designed to avoid the freestream sensitivity of the standard κ-ω model, by combining elements of the ω-equation and the ϵ-equation. In addition, the SST model has been calibrated to accurately compute flow separation from smooth surfaces. It is typically somewhat more accurate in predicting the details of the wall boundary layer characteristics than the Spalart-Allmaras model [14].

Reynolds Stress Model (RSM)

It is the most complex classical turbulence model [29]. It is a second-order closure model that abandon the isotropic eddy viscosity hypothesis and closes the RANS equations by solving transport equations for the Reynolds stresses, together with an equation for the dissipation rate. It means that for 2D it requires 5 more equations while for 3D seven additional transport equations are solved. RSM accounts for the effects of streamline curvature, swirl, rotation, and rapid changes in strain rate in a more rigorous manner, so it has greater potential to give accurate predictions for complex flows. The modeling of some terms is particularly challenging, and often considered to be responsible for compromising the accuracy, then might not always yield results that are clearly superior to the simpler models. There are some cases where it is recommended. for instance, cyclone flows, highly swirling flows in combustors, rotating flow passages, and the stress-induced secondary flows in ducts [31].

Hybrid RANS-LES Model

It is a hybrid model as it switches between the RANS models to the LES (commented below). It is related with the turbulence scales mentioned above, when the grid is not fine enough to solve the turbulent length scale (mainly close to solid boundaries) it is assigned the RANS mode of solution and when turbulent length scale exceeds the grid dimension the LES is solved.

Detached Eddy Simulation (DES) model is one of the most popular hybrid RANS-LES models with modification of the Spalart-Allmaras model, and there is also the Scale Adaptive Simulation (SAS), each one with some particularities. Some solvers considers the *DES* acronym for all hybrid RANS-LES models available [14, 31, 47].

Large Eddy Simulation (LES) Model

The Reynolds-Averaged Navier-Stokes equations Equations (2.18) and (2.19) describe all the scales in the flow when averaging the Navier-Stokes equation Equations (2.11) and (2.12). However, smaller eddies are nearly isotropic and have a universal behavior while the larger eddies are more anisotropic and their behavior are more related with the geometry, boundary conditions and body forces. The proposition of *Large Eddies Simulation* is to compute the larger eddies for each problem with a time-dependent simulation and capture the smaller eddies modeling it with a compact model. Instead of averaging, LES works filtering the larger eddies and smaller ones. During this filter procedure, some information related with small eddies are destroyed and gives rise to *Sub-Grid-Scale* (SGS) stresses. Then, the effects of SGS must be modeled. Smagorinsky-Lilly model [48] was used in the first LES simulation [49] and models the eddy viscosity for these smaller eddies. LES falls between DNS and RANS in terms of the fraction of the resolved scales.

Direct Numerical Simulation (DNS)

Direct Numerical Simulation is basically the solution of Navier-Stokes equations completely in space and time. In theory, it means to resolve the whole spectrum of turbulent scales. Nowadays, it is only possible on small computational grids and small time steps when Reynolds numbers are low. No modeling is required in DNS. However, DNS is not feasible for practical engineering problems involving high Reynolds number flows as the cost becomes prohibitive.

In Figure 2.8, a summary of resolutions and modeling of turbulence scales for each turbulence model is presented.

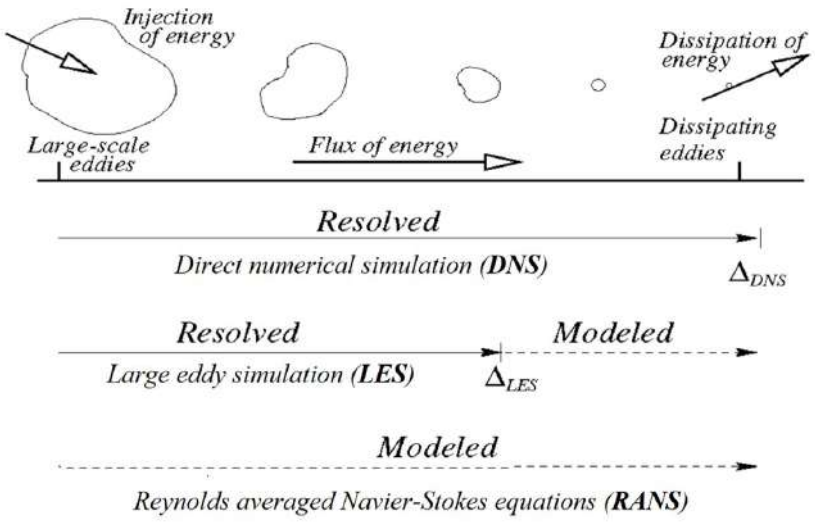

Figure 2.8: Turbulence models with respective resolution and modeling for each scale (Adapted from BAKKER [16]).

This section equations are mainly from Ansys Fluent manual [31].

Q-Criterion

Much was said about *vortices*, including the turbulence definition itself can induce the idea of tangle of vortex filaments, and the word eddies also appeared a lot. However, a real definition of vortex is still lacking. HUNT and MOIN [50] proposed the definition of *Q-Criterion* as

$$\begin{gathered} Q = \frac{1}{2}\left(|\mathbf{\Omega}|^2 - |\mathbf{S}|^2\right) > 0 \ , \\ S_{ij} = \frac{1}{2}\left(\frac{\partial v_i}{\partial x_j} + \frac{\partial v_j}{\partial x_i}\right) \ , \quad \Omega_{ij} = \frac{1}{2}\left(\frac{\partial v_i}{\partial x_j} - \frac{\partial v_j}{\partial x_i}\right) \ , \end{gathered} \tag{2.30}$$

where $\mathbf{S}$ (shear strain rate) and $\mathbf{\Omega}$ (vorticity magnitude) are respectively the symmetric and antisymmetric parts of the velocity gradient tensor $\vec{\boldsymbol{\nabla}}\mathbf{v}$.

Boundary Conditions

The information about how happens the transportation of the turbulence quantities when the flow enters the domain at an inlet, outlet (backflow), or far-field boundary is necessary. Depending on the turbulence model chosen, different parameters need to be set. There are two ways to inform these, one with a profile of each turbulence quantity and other by a uniform specification of it. The first is used to accurately represent a boundary layer or fully-developed turbulent flow known previously by experiment data or analytical solution. The profile can be used to describe:

- **Turbulent Viscosity** - Relation of the turbulence stresses to the mean flow (μ_t);
- **Turbulent Viscosity Ratio** - Relation among viscosities (μ_t/μ);
- **Turbulent Kinetic Energy** - Turbulent Kinetic Energy (κ);
- **Turbulent Dissipation Rate** - Turbulent Dissipation Rate (ϵ);
- **Specific Dissipation Rate** - Specific Dissipation Rate (ω).

In some situations, it is appropriate to specify a uniform value of the turbulence quantity in far-field boundaries, for instance. in terms of more convenient quantities such as:

- **Turbulent Intensity** - Ratio of the root-mean-square of the velocity fluctuations to the mean flow velocity;

- **Turbulent Viscosity Ratio** - Relation among viscosities (μ_t/μ);
- **Turbulence Length Scale** - Physical quantity related to the size of the large eddies;
- **Turbulence Hydraulic Diameter** - For fully-developed internal flows.

Once one of the turbulence model aforementioned (Section 2.2.2) is chosen, all the turbulent quantities related with it need to be specified.

2.2.3 Boundary Layer

Flows near of a wall is significantly affected by the presence of it because of two conditions, impenetrability and no-slip. However, turbulence is also changed by the presence of the wall as very close the viscous damping reduces the tangential velocity fluctuations, while kinematic blocking reduces the normal fluctuations and at the outer part of the near-wall region the turbulence is rapidly increased by the production of turbulence kinetic energy due to the large gradients in mean velocity.

Boundary layer is that layer of fluid in the immediate vicinity of a bounding surface that allows the fluid to transition from the free stream velocity to a velocity of zero at the wall (No-slip condition). It is where the effects of viscosity are significant and the behavior of the flow suffers aforementioned issues. The boundary layer can be laminar or turbulent with a regional transition in between them. In the case of turbulent boundary layer is important to analyze its structure as it is important for the mesh generation.

The structure of the turbulent boundary layer shown in Figure 2.9 is divided in an *inner region* and an *outer region*.

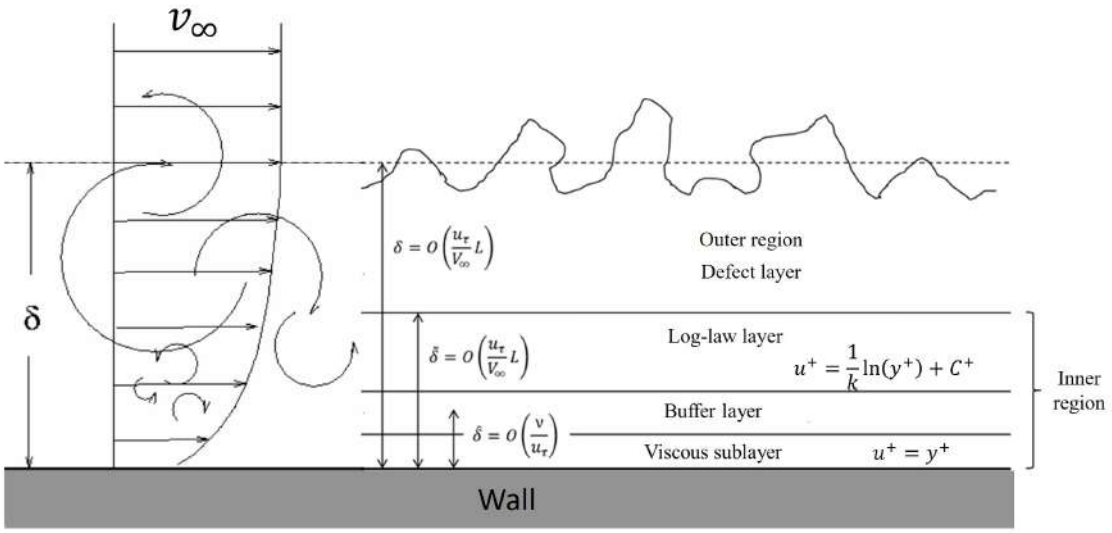

Figure 2.9: Asymptotic structure of turbulent boundary layer.

The inner region is subdivided into three layers. The closest to the wall is where the viscous influence is greater and it is called *viscous sublayer*. Above this region is located the *buffer layer* where the molecular transport is at the same order of magnitude as the turbulent transport. The last region in the inner region is the *log-law layer*, in which the turbulent stress rules the flow completely. It is a very important region. The outer region is where the inertial terms rules the flow.

To distinguish the different regions near the wall the concept of wall y^+ (Dimensionless wall distance) has been formulated and also for velocity calculation at each region, the concept of u^+, that is a dimensionless velocity. They are both given by,

$$y^+ \equiv \frac{\rho u_\tau y}{\mu} \ , \tag{2.31}$$

$$u^+ \equiv \frac{u}{u_\tau} \ , \tag{2.32}$$

where y is the distance from the wall $[m]$, u is the velocity $[m/s]$ parallel to the wall as a function of y and

$$u_\tau = \sqrt{\frac{\tau_w}{\rho}} \ , \tag{2.33}$$

is the friction velocity m/s. τ_w is the wall shear stress $[N/m^2]$.

The *viscous sublayer* exists for $0 < y^+ < 5$ and within that, the non-dimensional velocity profile is linear with the distance and can be described as

$$u^+ = y^+ \ , \tag{2.34}$$

Then, immediately outside the viscous sublayer, is the *buffer layer*, within $5 < y^+ < 30$ and there is no analytical for the velocity profile, but it relies on a curve fitting with the profile of the next layer.

The *log-law layer* ($30 < y^+ < 500$) is where viscous and turbulent effects are both important and the relationship between u^+ and y^+ in the region is logarithmic and given by,

$$u^+ = \frac{1}{k_{cte} d} \ln\left(y^+\right) + C^+ \ , \tag{2.35}$$

where k_{cte} is the Von Kármán constant and C^+ also a constant. It has been determined from many experiments that $k_{cte} = 0.41$ and $C^+ = 5.0$ for *smooth wall* [51].

Outer region, is where the turbulent shear stresses dominate, and the influence from the wall on the velocity is negligible in this region. It cannot be well represented using the wall coordinate.

The experimental velocity profile close to the wall for different Re is shown in Figure 2.10 over a known velocity profile curve (Van Driest profile).

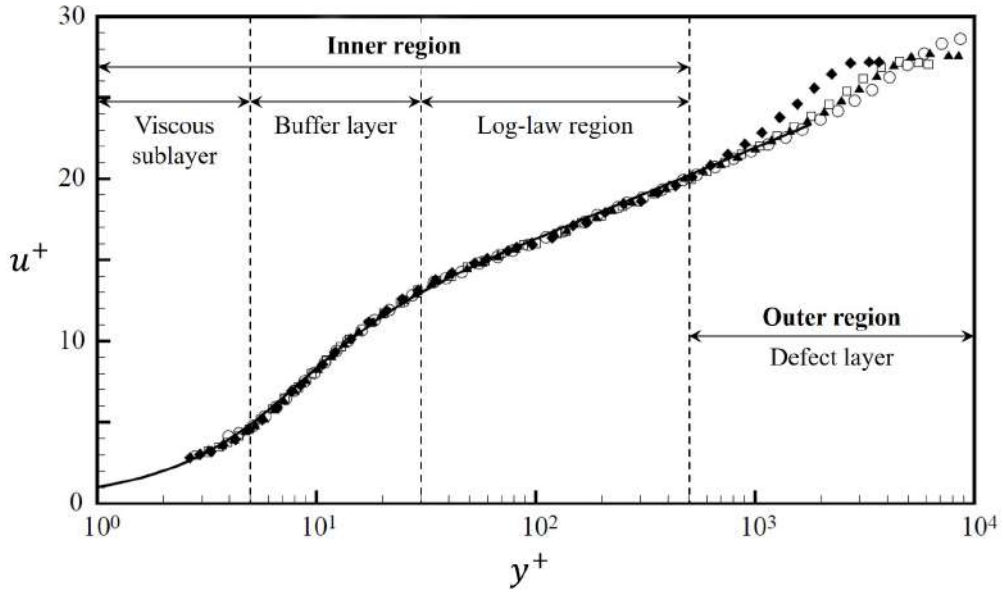

Figure 2.10: Profiles of longitudinal mean velocity $\overline{u}$ obtained with hot-wire anemometry: ♦ - $Re = 8100$; □ - $Re = 11500$; ▲ - $Re = 14800$; ∘ - $Re = 20600$; Over Van Driest profile (Adapted from CARLIER and STANISLAS [17]).

There are two approaches for modeling the near-wall region:

- **Wall function approach** - Viscosity affected region (viscous sublayer and buffer layer) is not calculated and a semi-empirical formula is used to bridge this region to the fully turbulent region;
- **Two layer zonal model approach** - Turbulence models are modified to enable calculation for the viscosity affected region and the mesh must have nodes in the region.

Wall function is robust, economical and reasonably accurate for most flow simulation and the two-layer zonal approach requires finer mesh resolution and so more computational resource. On other hand, in the latter the flow pattern in the boundary layer is calculated explicitly. *Fluent* solver recommends to ensure that around 15 or more nodes cover the boundary layer thickness. The first node closer to the wall boundary is very important for these approaches. Wall function requires first grid point in log-law layer ($30 < y^+ < 500$) and for proper use of two layer zonal, the first grid point must be at $y^+ \approx 1$. The velocity is parallel close to the wall, so another recommendation is that is better to use quad/hex mesh (or prism layer in unstructured mesh) for grid alignment with the flow.

Both approaches produces errors if used outside of their purpose. Due to that, it is important to analyze the y^+ at the no-slip walls when using turbulent models.

If considering wall roughness effects, the value of C^+ changes in Equation (2.35), shifting downward the logarithmic velocity profile (Figure 2.10).

2.2.4 Methodology

When running a CFD simulation, some procedures are followed.

- *Pre-processor*: The geometry and physical bounds of the problem is defined, called *Domain*. Then, the most important part of the simulation, that is the mesh generation in order to discretize the space is done. Physical modeling is defined and also the boundary conditions and initial conditions (for transient problems).
- *Solver*: Simulation starts and all the necessary equations are solved iteratively.
- *Post-processor*: The last step is for analysis and visualization of the resulting solution.

Some important parameters of solver setup are discussed here. Mainly based on the commercial solver *Fluent* of *Ansys Inc.* [14, 31].

Solver Formulation

There are two solver possibilities, the *pressure-based* and *density-based*. Pressure-based solves the governing equations sequentially, i.e. solution variables are solved one after another (momentum equations and the pressure-based continuity equation may be solved coupled). Density-based solves the governing equations of continuity, momentum, energy and species transport simultaneously and then the governing equations for additional scalars (including turbulence models) are solved sequentially. Traditionally, the pressure-based solver has been used for incompressible and mildly compressible flows while the density-based solver was originally designed for a high-speed compressible flow. Nowadays they can be used for a broader range of flows, but they still being recommended according to their historical use as may present more accuracy.

Pressure based solver has two algorithm for the solution of the equation: *segregated algorithm* and *coupled algorithm* (Figure 2.11). Segregated, as the name infers, solves governing equations for the solution variables one after another separately, while coupled algorithm solves a coupled system of equations comprising the momentum equations and the pressure-based continuity equation. Segregated algorithm runs fast and is a good choice for most cases, but the solution convergence is relatively slow and may have problems with supersonic flows. On other hand, coupled algorithm need more computational resource, like memory, as it solves coupled equations for pressure and velocities, but the rate of solution convergence significantly improves.

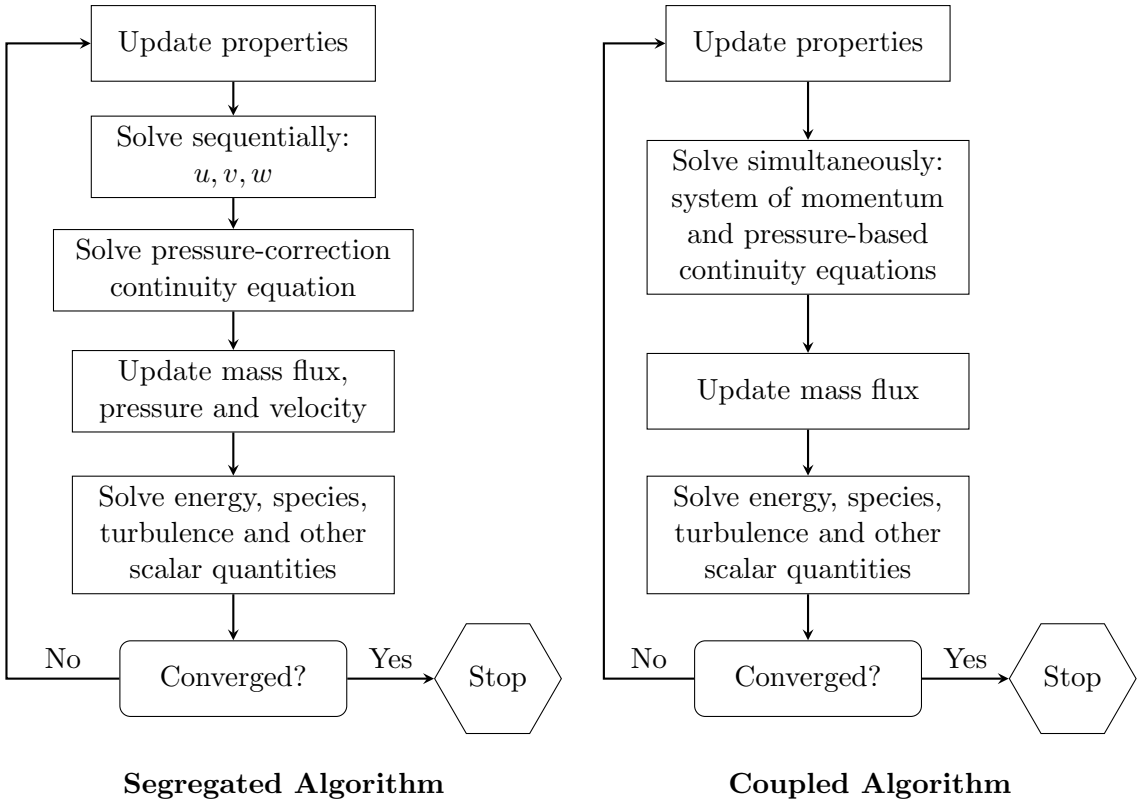

Figure 2.11: Pressure-based solution methods

Coupling Algorithm

Every velocity component appears in each momentum equation (Equation (2.12)) and in continuity equation (Equation (2.11)) while pressure term appears in all momentum equation, but there is no transport equation for pressure (it is calculated from the equation of state in compressible flow). Then, the pressure must be calculated in order to use the pressure gradient for velocity calculation from momentum equations. Coupled algorithm solves the momentum and pressure-based continuity equation together. In segregated algorithm there are some iterative solution strategies to solve this issue, they are known as predictor-corrector approaches:

- **SIMPLE** [52] - Stands for *Semi-Implicit Method for Pressure Linked Equations* and its iterative process starts with a guess of a pressure field, then solving the discretized momentum equation to compute the intermediate velocity field. Afterwards the uncorrected mass fluxes at faces are computed and the pressure correction equation is solved. Correct pressure field is updated (*Under-relaxation factor* may be used to avoid divergence). Boundary pressure corrections are updated also, Correction of face mass fluxes take place and so the corrected velocities are calculated. Finally, the discretization equation for others Ψ's are calculated and the new pressure field is considered as the new

pressure guess for next iteration until convergence. ;

- **SIMPLER** [53] - The SIMPLE Revised is an improvement of SIMPLE that do not use a guessed pressure field but extracts a pressure field from a given velocity field;
- **SIMPLEC** [54] - The SIMPLE-Consistent is similar to SIMPLE procedure with a different expression for the face flux correction;
- **PISO** [55] - Stands for Pressure Implicit with Splitting of Operators and involves one predictor step and two corrector step. It is considered as a SIMPLE extension with a further corrector step to enhance it. Then, it is the same procedure until *Step 3* (Figure 2.12) and after a second pressure correction equation is computed.

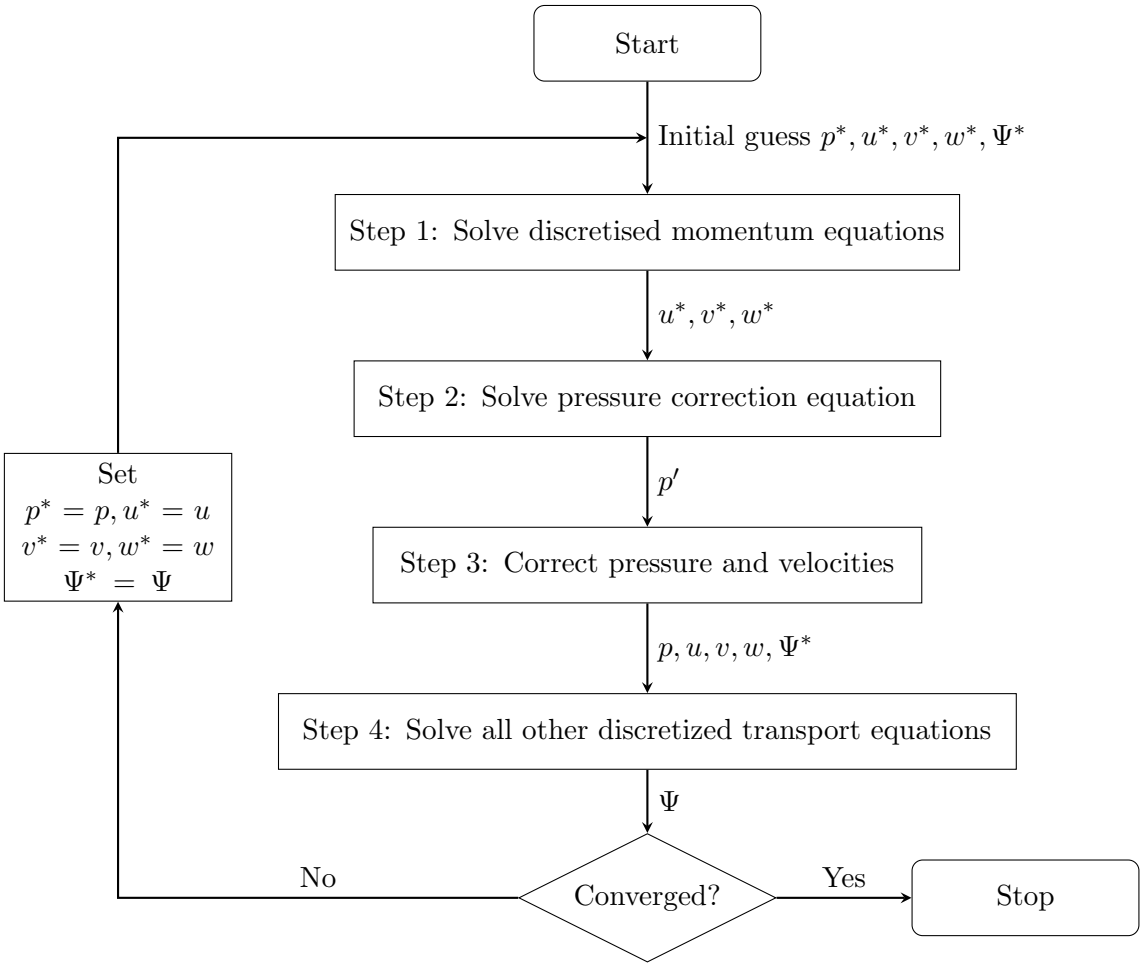

Figure 2.12: SIMPLE algorithm

Relaxation factor is important for cost-effective simulation, in which higher than unity values are considered *over relaxed* and the solution converges faster but it

may lead to oscillatory or even divergent iterative solutions, and a lower value is considered *under relaxed* giving more stability to the solution and will cause an extremely slow convergence.

All of these will eventually converge to the same solution, at least theoretically they must, the differences are in speed and stability. Coupled algorithm usually requires fewer iterations to converge and are usually recommended for steady-state simulations while in transient it has more robustness, especially for large time step sizes. Segregated methods are faster per iteration, but as just mentioned, requires more iterations. *SIMPLEC* is preferred over the *SIMPLE* because of the increased under-relaxation that can be applied [31].

Spatial Discretization

Discrete values nodes of each variable may be placed at the centroid of the control volume (*cell-centered method*) or on the vertices of the grid (*vertex-centered method*), and the sub-volume surrounding the node is the *control volume* for discretization, that was already commented in Section 2.2.1. Nevertheless, the face values of the control volume are required for convection, diffusion and gradient terms calculation and must be interpolated from node values.

There are some schemes for doing that, for convection terms, with different order of accuracy.

- **First-order upwind scheme**[56] - Simplest numerical scheme with first-order accuracy, where te cell faces quantities are identical to the cell node quantities (Figure 2.13.a). Cell face is derived from quantities in the cell node upstream, or "upwind", relative to the direction of the normal velocity;

- **Central differencing scheme** - Second-order scheme that defines the cell face quantity by a linear interpolation between cell centered values (Figure 2.13.b). There is the possibility to change between central differencing and first-order upwind depending on convective and diffusive transport in each cell and this approach is called a *hybrid scheme*;

- **Power-law scheme**[53] - Interpolates the face cell value using the exact solution to a one-dimensional convection-diffusion equation (Figure 2.13.c). It is a first-order accuracy method;

- **Second-order upwind scheme**[57] - In this scheme the cell face is calculated considering two upstream nodes (Figure 2.13.d);

- **QUICK scheme**[58] - Quadratic Upstream Interpolation for Convective Kinematics is a high-order scheme that considers a three-point weighted quadratic

interpolation fitting a curve through two upstream nodes and one downstream node (Figure 2.13.e);

- **MUSCL scheme** [59] - Monotone Upstream-Centered Schemes for Conservation Laws is a third-order convection scheme that blends central differencing scheme (Figure 2.13.b) and second-order upwind scheme (Figure 2.13.d).

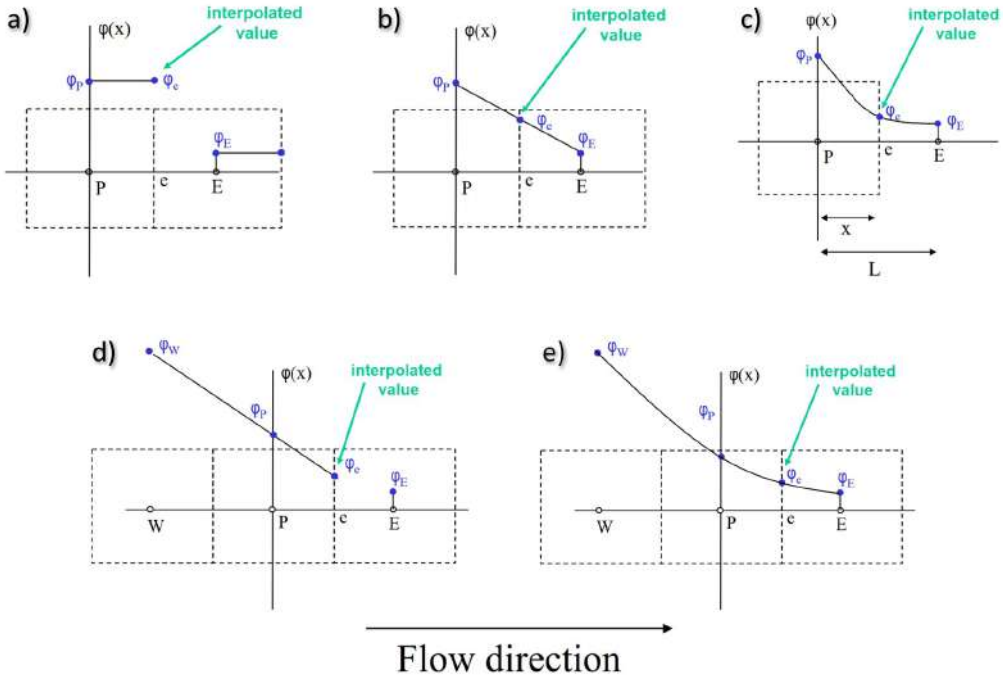

Figure 2.13: Schemes representation for node P and interpolation at face e (Adapted from BAKKER [18]). *a)* First-order upwind scheme, *b)* central differencing scheme, *c)* power-law scheme, *d)* second-order upwind scheme and *e)* QUICK

There is an important number to take in consideration when studying spatial discretization, it is the Peclet number (Pe), given by the ratio between convective and diffusive transport:

$$Pe = \frac{F_c}{D_d} \, , \qquad F_c = \rho v \, , \quad D_d = \frac{\Gamma}{\delta x} \, , \tag{2.36}$$

where F_c represents the convective mass flux per unit area, D_d is the diffusion conductance at cell faces and δx is cell width.

First order upwind is easier to implement and results in very stable calculations, but it also very diffusive, gradients tend to be smeared out. It is considered best scheme to start calculations that are hard to converge. On other hand, central differencing is more accurate than the first order upwind scheme, but it leads to oscillations in the solution or divergence if the local Peclet number is larger than 2. Second-order upwind is more accurate than the first-order upwind scheme, but in

regions with strong gradients it can result in face values that are outside of the range of cell values. It is then necessary to apply limiters to the predicted face values, and this is the more popular numerical schemes because of its combination of accuracy and stability. QUICK is a very accurate scheme, but in regions with strong gradients, overshoots and undershoots can occur. Then, QUICK and also third-order MUSCL discretization schemes may be recommended, for better accuracy, in simulations of rotating or swirling flows.

Low order of accuracy discretization introduces high level of false diffusion and higher order gives spurious oscillations when Pe is high, and when used to solve turbulent quantities, these oscillation may generate unrealistic values. The class of *Total Variation Diminishing* (TVD) [60] schemes has been formulated to address this undesirable behavior of higher-order schemes, adding an artificial diffusion fragment or adding weighting towards upstream contribution [29].

The discretization of diffusion term in Equation (2.14) is central-differenced and so it is always second-order accurate [31].

Pressure Interpolation Schemes

The discretization of the pressure value requires special attention, so calculation of pressures at the faces can be done by one pressure interpolation scheme:

- **Linear** – Computes face pressure as the average of the pressure values in the adjacent cells;
- **Standard** - Interpolates the pressure values at the faces using momentum equation coefficients;
- **PRESTO!** - Stands for PREssure STaggering Option and interpolates using the discrete continuity balance for a "staggered" control volume about the face to compute the face pressure [61];
- **Second Order** – Reconstructs the face pressure using a central differencing scheme;
- **Body Force Weighted** – Assumes that the normal gradient of the difference between pressure and body forces (for example, gravity or surface tension forces) is constant.

Linear must be used only when other options result in convergence difficulties or nonphysical behavior and Standard has reduced accuracy for flows exhibiting large surface-normal pressure gradients near boundaries and should never be used when steep pressure changes are present in the flow, PRESTO! scheme should be used instead. Also for highly swirling flows and strongly curved domains the PRESTO!

is recommended. Second Order is used for compressible flows. When body forces are large body force weighted scheme is the best choice, for instance, high Rayleigh number (Ra) natural convection or highly swirling flows.

Grid Arrangement - Pressure-Velocity Coupling

The pressure gradient term is the main momentum source term in most flows of engineering importance, also the momentum and continuity equation are intricately coupled because of velocity components (as discussed previously in *Coupling Algorithm*). When pressure is known, the momentum equation discretization follows the same calculation procedure of any other transported property of flow, but the pressure variation would be calculated from two alternate grid points and not adjacent ones, what diminish the accuracy of the solution as the pressure value are taken from a coarser mesh. Besides that, other issue is wrong calculation because of this alternate nodes calculation. If we consider for clarification a highly irregular *checkerboard* pressure field, the pressure oscillation may generate close to zero velocities, since the alternate pressure values are everywhere equal, creating a not properly represented velocity field. There are two possible solution for this problem:

- **Staggered grid** for velocity components [62]; or
- **Co-located grid** with Rhie-Chow interpolation [63].

Besides the advantage of no interpolation requirement, staggered grid is very difficult to implement on unstructured meshes.

Temporal Discretization

Transient simulations require temporal discretization also to integrate the terms over each *time step* Δt. Before describe some possibilities for temporal discretization, a nondimensional number important must be defined, that is the Courant number (C), and it relates the length that information travel in the physical space at each time step with the cell length, given mathematically by

$$C = \frac{v\Delta t}{\delta x} \,, \tag{2.37}$$

Now, the most common schemes in the literature for the temporal discretization are:

- **First-order explicit scheme** - Forward Euler method calculates the state of the system at a later time from the state of the system at the current time;
- **First-order implicit scheme** - Contrary to the explicit, backward Euler finds the solution by solving an equation involving the current state of the

system and the later one. It yield an implicit set of algebraic equations that require an iterative solution procedure;

- **Second-order implicit scheme** - Second-order scheme that includes 3 time steps for the calculation and take two steps for calculation. It is also called implicit second order upwind Euler (SOUE);

- **Bounded second-order implicit scheme** - Similar to the SOUE but for stability purpose would always ensure the bounds for variables;

Courant-Friedrichs-Lewy (CFL) condition states that the stability of the temporal discretization is related with a maximum Courant number (C_{max}). Explicit scheme is conditionally stable with $C_{max} = 1$, i.e. if the Courant number in any cell goes higher than unity, it will diverge. In order to use this scheme, if the mesh is to fine in any region with a considerable flow speed, the time step will have a maximum value in order to avoid divergence. Stability do not mean accuracy, then care must be taken when choosing a temporal discretization.

Second order provides more accuracy than first-order but may cause instabilities or even divergence for the solution. Depending on the simulation, sometimes is recommended to start it with a first-order and change it to high order after some time steps. [14] affirms that First Order Implicit formulation is sufficient for most problems. Bounded Second Order Implicit formulation provides the same accuracy as the Second Order Implicit but with more stability.

Gradient Computation

Gradients are needed to be calculated not only for integration of the transport equation given by Equation (2.14) but also for secondary diffusion terms and velocity derivatives. *Fluent* provides three options for that,

- **Green-Gauss Cell-Based**;

- **Green-Gauss Node-Based**;

- **Least Squares Cell-Based**.

Green-Gauss Theorem is used to compute the gradient of a scalar Ψ considering the value of Ψ at the cell face centroid, and it may be computed in a cell-based computation, taking the arithmetic average of the values at the neighboring cell centers (Green-Gauss Cell-Based) or by the arithmetic average of the nodal values on the face, that are constructed from the weighted average of the cell values surrounding the nodes (Green-Gauss Node-Based), providing second-order spatial accuracy. In

general, node-based gradient is more accurate than the cell-based gradient, particularly on irregular unstructured meshes. But as always, it comes with a price to pay in computational cost. Least Squares Cell-Based can be formally calculated in unstructured meshes using a Taylor series expansion of the property being calculated about an specific centroid, neglecting terms proportional to the square of the distance between the node and the face, so it is also a second-order approximation.

The Green-Gauss Node-Based and Least Squares gradient methods accuracy in irregular unstructured meshes are comparable and both are much more superior compared to the Green-Gauss Cell-Based gradient. However, Least Squares gradient is less expensive to compute than the node-based gradient.

Linear System Solution

After all discussion about discretization methods, the application of discretized scalar transport equation in each node will result in a set of algebraic equations with a sparse coefficient matrix. There two possibilities to solve this system, by *direct method* or *iterative method*. The last is much more economical for the purpose of real engineering problems in CFD.

Point-iterative methods are techniques for calculation of the unknowns variable of the system. *Jacobi method* is evaluated only considering the previous iteration values and *Gauss-Seidel* method uses the already calculated of values of the present iteration, but both methods converge significantly slower with increasing mesh sizes. To accelerate solver convergence, it is possible to employ a *Multigrid* method. Multigrid solver uses a sequence of successively coarser grids. Coarse mesh calculations only accelerate convergence and do not change the final answer, so as expected, the final solution is obtained for the original mesh.

In *Algebraic Multigrid* (AMG) method the coarse level equations are generated without the use of any geometry, no coarse meshes have to be constructed or stored, and no fluxes or source terms need to be evaluated. The Full-Approximation Storage (FAS) Multigrid is a geometric technique in which coarse grid cells are created by agglomerating the cells surrounding a node

Convergence Criteria

After any iteration in the calculation of each node value for a specific variable, it is possible to calculate the difference between the result of the equation with this intermediate solution and the exact result with the unknown exact solution. This difference is the *local residual*. Calculating the Root Mean Square (RMS) of all local residual can give an idea if the iterations are converging to or diverging of a "exact" solution.

The convergence criteria may be based on minimum residual (RMS of all residual

or maximum local residual) value for each equation being solved and/or a maximum number of iteration and/or variation of a specific quantity of interest in the solution. Monitoring integrated quantities such as force, drag, or average temperature can give the idea if a simulation already converged once the monitor point values have "flattened out".

2.2.5 Volume of Fluid Method (VOF)

First of all, the concept of phase needs to be discussed. From the thermodynamic point of view, a *phase* refers to solid, liquid or vapor state of matter. However, when we talk about CFD modeling the concept is broader. Phase in CFD is more related to the morphology of the flow than just the state of matter.

There are other interesting and important definitions when analysing different phases in CFD, for instance *mutlicomponent* × *multiphase*, or *disperse* × *continuous* and *eulerian* × *lagrangian* approach and they will be briefly commented for enlightenment purpose of the choices in the work.

When modeling a flow with two phases, the miscibility between them becomes important, so when analyzing substances that mix in a microscopic scale it should be used the *multicomponent* modeling, for instance, water and ethanol simulation. But when modeling two substances that mix in macroscopic scale it should be used the *multiphase* model.

Depending on the morphology of the interface between the phases, they can be considered disperse or continuous. When one phase is uniformly mixed in another continuous phase, as they may appear a quasi-homogeneous mixture or emulsion, this phase is considered dispersed. In other words, a phase is disperse if it occupies disconnected regions of space. The dispersed phase can also be classified in diluted or dense, depending on the concentration of the particles in the continuous phase. However, when phases exists in continuous regions where all elements of each phase is connected it is said that the multiphase flow is continuous.

Eulerian and Lagrangian concept was already defined in Section 2.2.1. It is related with how the parameters are analyzed in the solution. Eulerian the volume is fixed while Lagrangian *tracks* a specific volume.

Simulation of a ship in waves or of water motion inside a moonpool is a simulation of free surface flow with two phases, air and water, and so a multiphase, continuous and eulerian technique must be chosen. A very well known and widely used technique in literature for this purpose is the *Volume of Fluid* (VOF) [64]. It is a surface-tracking model used when the position and shape of the interface is of interest. In this model, just a single set of momentum equations is shared by the fluids and another transport equation must be solved for the phase volume fraction α_q in the

cell, that is defined as the ratio of volume of q^{th} fluid inside the cell by the cell volume (areas in 2D). Each additional phase in the model require a new volume fraction variable and the summation of all volume fractions in a cell has to be equal 1. That statement is logical as long as each cell volume must be full of all the phases of the problem, with no void region, neither it can have more volume of fluid than its own volume. Based on the local value of volume fraction that appropriate properties and variables are assigned to each control volume within the domain.

As aforementioned, a single set of momentum equation is solved throughout the domain, and the resulting velocity field is shared among the phases, respecting dependency on the volume fractions of all phases through the properties ρ and μ. Surface tension and wall adhesion are modeled with an additional source term in momentum equation. For turbulent flows, also only a single set of turbulence transport equations is solved.

Transport equation of the volume fraction is similar to Equation (2.13) without diffusion term and considering a mass transfer between phases. Primary phase do not need a transport equation and it is solved considering the constraint just commented, that the summation of all volume fractions is equal to 1, but for each new phase added a new transport equation must be solved.

Interface Tracking

According to the definition of the volume of fluid variable, if a cell has a volume fraction $\alpha_q = 0$, then the cell is empty of q^{th} fluid and when $\alpha_q = 1$ the cell is full of q^{th} fluid. However, if the values lies within a range $0 < \alpha_q < 1$ the cell contains the interface between the q^{th} fluid and one or more other fluids.

Avoiding smearing of this interface is mandatory for a correct representation, so transport equation must be solved without excessive diffusion. Upwind schemes are unsuitable because of their diffusive nature and central differencing schemes are unbounded and often give unphysical results [31]. Choosing the volume fraction discretization schemes depends on the interface regime that will be modeled, if it is a sharp interface or a dispersed (when the phases are interpenetrating). Considering the sharp interface that is the case of this thesis, the spatial discretization methods for treating VOF can be roughly divided into three categories:

- **Donor-Acceptor** – Identify one cell as donor of an amount of fluid and other as the acceptor of the same amount, preventing diffusion. Amount of fluid that can be convected is limited by the minimum of two values: the filled volume in the donor cell or the free volume in the acceptor cell. Interface orientation is either horizontal or vertical;

- **Higher Order Schemes** - Convective transport equation is discretized with

higher order or blended differencing scheme. Include the Compressive Interface Capturing Scheme for Arbitrary Meshes (CICSAM) and High Resolution Interface Capturing (HRIC);

- **Line Techniques** - It is a geometric reconstruction scheme, representing the interface between fluids using a linear approach. It assumes that the interface between two fluids has a linear slope within each cell, and uses this linear shape for calculation of the advection of fluid.

CICSAM and HRIC are based in the Normalized Variable Diagram (NVD). CICSAM is a blend of two other schemes, one is a variation of QUICK. HRIC presents a nonlinear blend of upwind and downwind differencing. In Fluent solver there is also a *Compressive* scheme with a slope limiter that is used to blend between a first and second order or a second order and compressive scheme.

Fluent also has a *Geo-Reconstruct* scheme in the *Line Technique* category that represents the interface between fluids using Piecewise Linear Interface Calculation (PLIC) approach based in YOUNGS [65] work.

A representation of the interface tracking is shown in Figure 2.14.

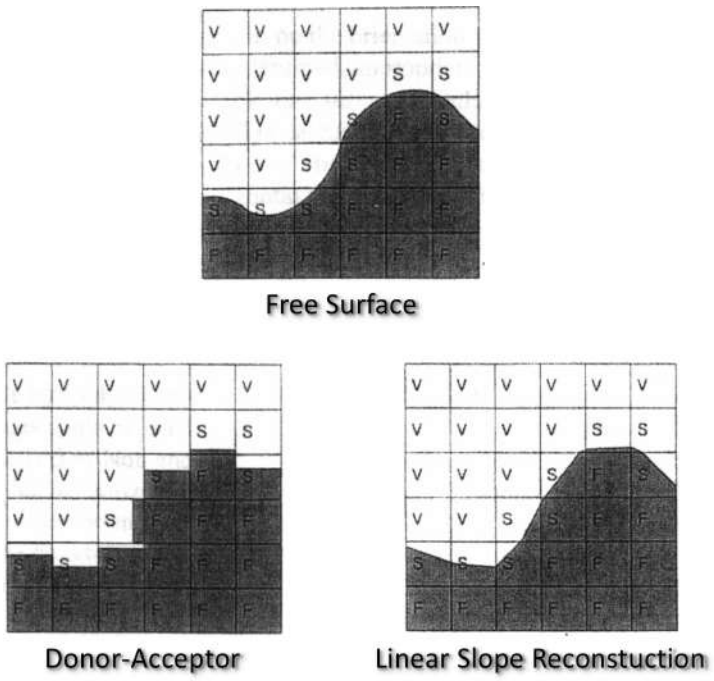

Figure 2.14: Interface tracking schemes (Adapted from BAKKER [19]).

In cases where large velocity differences exist between the phases, the accuracy of the velocities computed near the interface can be adversely affected. The ratio of viscosity between fluid at interface also may lead to convergence difficulties. CICSAM is suitable for flows with high ratios of viscosities, more than 10^3, between the phases.

CICSAM and HRIC are highly dependent on Courant number (Equation (2.37)), becoming incresingly diffusive with higher C. This is explained by the fact that both schemes tends to upwind for high Courant numbers, increasing the total numerical diffusion of interface.

The Compressive scheme provides better accuracy compared with CICSAM and HRIC for most cases and, when used with the second order implicit time scheme, the Compressive scheme produces quite a sharp interface [14].

Geo-Reconstruct is the most accurate scheme in Fluent solver, but is more computationally expensive than the others.

2.2.6 Verification and Validation (V&V)

As CFD became popular and the computers were getting more powerful, with more memory and speed, more companies started to invest and focus the attention on this branch. However, there are some potential consequences of wrong decisions made on the basis of CFD and, besides the time savings and the enhanced understanding of analyzed engineering problem, the CFD application can only be justified on the basis of its accuracy and level of confidence in its results [29].

First of all, it is necessary a definition for *error* and *uncertainty* as long as these are the key terms in the context of trust and confidence in CFD modeling. American Institute of Aeronautics and Astronautics (AIAA) [66] gives the following well accepted definition:

- ***Uncertainty:*** A *potential* deficiency in any phase or activity of the modeling process that is due to the lack of knowledge;
- ***Error:*** A *recognizable* deficiency in any phase or activity of modeling and simulation that is *not* due to lack of knowledge.

There are three recognized sources of *numerical errors*:

  - Roundoff error;
  - Iterative convergence error;
  - Discretization error.

There are yet other causes of error like *coding errors* due to 'bugs' in the software or *user errors* that are simply caused by software misusing. These are not so easy to measure but may be avoided by a qualified user with a well validated code.

Whereas for the *numerical uncertainties* there are two main sources:

  - Input uncertainty;
    - Domain geometry;

    - Boundary conditions;
    - Fluid properties.
  - Physical model uncertainty.
    - Validity of submodels;
    - Simplifying assumptions.

The concern of V&V is to develop rigorous methods to quantify the level of confidence assessing the accuracy of the computational simulation. AIAA [66] also defined these two terms, as follows:

- ***Verification:*** process of determining that a model implementation accurately represents the developer's conceptual description of the model and the solution to the model;
- ***Validation:*** the process of determining the degree to which a model is an accurate representation of the real world from the perspective of the intended uses of the model.

A summary of these definition is wisely given by ROACHE [67], who called the *verification* as 'solving the equations right' while *validation* is 'solving the right equations'. It means that verification quantifies the errors and the validation quantifies the uncertainties.

Verification

Verification assessment for *roundoff error* demands running the simulation in different level of machine accuracy (single precision and double precision) and *iterative convergence error* can be quantified changing the residuals convergence criteria of discretized flow equations.

For discretization errors, that are related with the temporal and spatial derivatives, there are some well-known methods for calculation. One very recommended method for discretization error estimation is the Richardson extrapolation (RE) method and it has large acceptance, being recommended by editorial policy of journal [68] and also it is in the International Towing Tank Conference (ITTC) Recommended Procedures and Guidelines [69]. In this work, the Grid Convergence Index (GCI) method is used, it is based in RE and follows the recommendation mentioned before.

The first step is to define a representative cell size h_{grid}. In a 3D mesh is given by:

$$h_{grid} = \sqrt[3]{\frac{1}{N}\sum_{i=1}^{N}(\Delta V_i)}\,, \tag{2.38}$$

where ΔV_i is the volume of the *ith* cell $[m^3]$, and N is the total number of cells used for the computations.

The discretization error is related with the spatial but also temporal discretization, and so it is related with the size of the temporal mesh. *Temporal mesh* can be seen as 1D mesh, in which, solution time are nodes and time step are the distance between each successive node. A representative cell size in temporal discretization is related with time step average of the transient solution.

Then, the next step is to create a set of at least three grid with successive level of mesh refinement. However, it is desirable that the grid refinement ratio r_{grid} (Equation (2.39)) between two successive meshes is greater than 1.3 [68] (or $\sqrt{2}$ in ITTC Procedures [69])

$$r_{grid} = \frac{h_{coarse}}{h_{fine}} > 1.3 \,, \tag{2.39}$$

where h_{coarse} is one level of a coarser mesh, and h_{fine} is the successive finer one.

Defining the representative cell size of the three meshes as $h_1 < h_2 < h_3$, also respective grid refinement ratio as $r_{21} = h_2/h_1$, $r_{32} = h_3/h_2$ and running simulations in each to determine the values of target quantities (φ), important to the objective of the simulation study. It is possible to calculate the apparent order (p_g) of the method in Equation (2.40)

$$p_g = \frac{1}{\ln(r_{21})} \left| \ln \left| \frac{\varepsilon_{32}}{\varepsilon_{21}} \right| + q_g\left(p_g\right) \right| \,, \tag{2.40}$$

where $\varepsilon_{32} = \varphi_3 - \varphi_2$, $\varepsilon_{21} = \varphi_2 - \varphi_1$, φ_k denoting the solution on the k^{th} grid and

$$q_g\left(p_g\right) = \ln\left(\frac{r_{21}^{p_g} - s}{r_{32}^{p_g} - s} \right) \,, \tag{2.41}$$

$$s = sgn\left(\frac{\varepsilon_{32}}{\varepsilon_{21}} \right) \,, \tag{2.42}$$

in which *sgn* is the signum function, an odd mathematical function that extracts the sign of a real number.

Apparent order p_g is an *iterated function*, i.e. it is a function $p_g \longrightarrow p_g$, and can be solved using fixed-iteration point. Then, the extrapolated value (φ_{ext}^{kl}) can be calculated by:

$$\varphi_{ext}^{21} = \frac{r_{21}^{p_g}\varphi_1 - \varphi_2}{r_{21}^{p_g} - 1} \,. \tag{2.43}$$

Similarly, it is possible to calculate φ_{ext}^{32}.

Relative errors are computed using Equations (2.44) and (2.45).

$$e_a^{21} = \left| \frac{\varphi_1 - \varphi_2}{\varphi_1} \right| \,, \tag{2.44}$$

$$e_{ext}^{21} = \left| \frac{\varphi_{ext}^{21} - \varphi_1}{\varphi_{ext}^{21}} \right| , \tag{2.45}$$

where e_a^{21} is the approximate relative error and e_{ext}^{21} is the extrapolated one.

The GCI now can be defined as:

$$GCI_{fine}^{21} = \frac{1.25 e_a^{21}}{r_{21}^{p_g} - 1} . \tag{2.46}$$

Likewise, the GCI_{medium}^{32} can be calculated using the same apparent order (p_g). This calculated parameter is the respective value error due the discretization error and as explained before does not take into consideration other modeling errors

Validation

Validation assessment, as aforementioned, determines if the computational simulation agrees with physical reality. It requires comparison of CFD results with high-quality experimental results.

2.3 Genetic Algorithm (GA)

Before further discussion on definition and mechanics of genetic algorithm, it is interesting to clarify the goals of *optimization*. Expressing it in a simplified way, it is a process to find the best element following certain criterion in a set of available alternatives. Mathematically consists of maximizing or minimizing a real function by systematically varying the input from a set of allowable values.

Genetic Algorithm are search and optimization algorithms based on the concept of Darwin's theory of evolution. It became popular in the early 1970's through the work of HOLLAND [70]. It is a metaheuristic and naturally inspired algorithm belonging to the class of *Evolutionary Algorithms* (EA).

It combines the idea of survival of fittest with randomized information exchange [71]. The algorithm is presented in a flowchart below (Figure 2.15). A set of *individuals* forms a *population* that is the initial *generation* and according to a *fitness goal* the fittest of these forms a new generation with some random variation (*crossover* and/or *mutation*). Then, the fittest of these are chosen for the process repetition. Each individual are composed of *genes* that describe their behavior and these genes suffer modifications when creating a new creature, a *offspring*. When selecting the fittest creatures, the fittest genes will then be selected.

To create a new set of creatures for a new generation, two approaches may be used, crossover or mutation (Figure 2.16). The former consists of a offspring production by swapping genes from both parents. On other hand, mutation happens when some genes randomly are modified, besides parents genetic code. The crossover

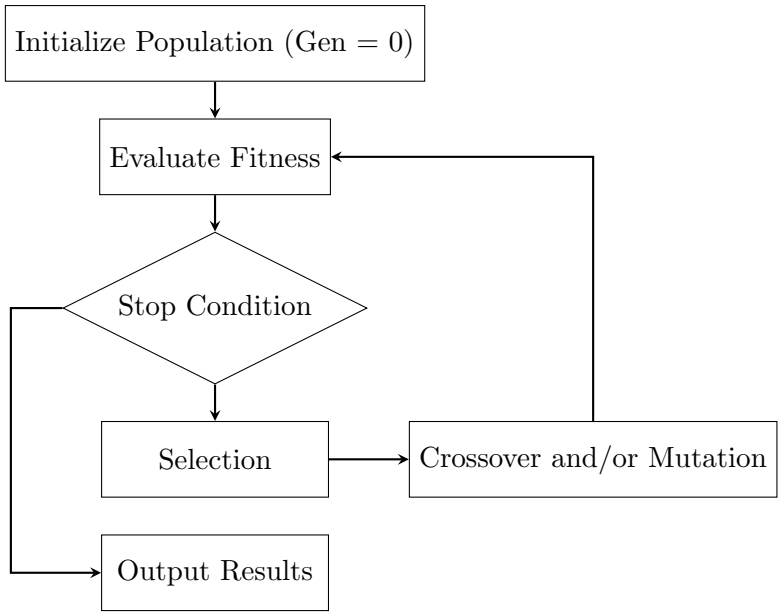

Figure 2.15: Flowchart of Genetic Algorithm

is necessary to keep the genes that are possibly related with the fittest result on the new offspring while mutation is good to introduce variation in the population and by that a new overriding gene value may be found.

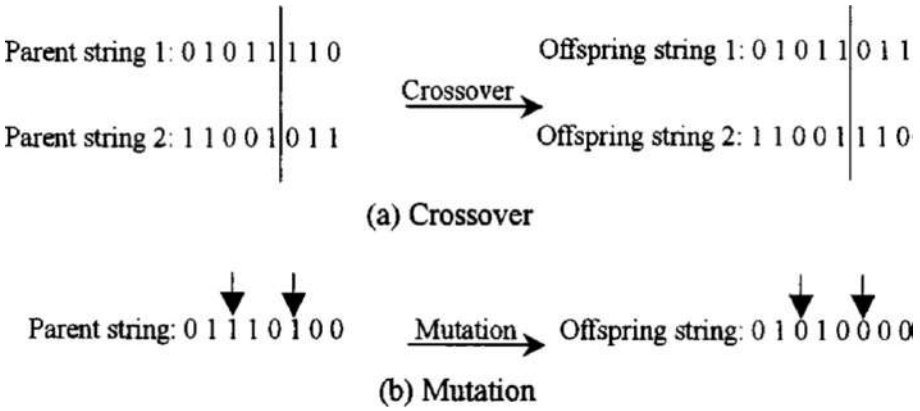

Figure 2.16: Crossover and mutation operations in genetic algorithm [20].

Genetic algorithms are different from other optimization procedures in four ways [71]:

- Use information of objective function, not derivative or auxiliary knowledge;
- They use probabilistic transition rules, not deterministic ones;
- Work with a coding of the parameter set, not the parameter themselves;
- Search from a population of points, not a single point.

At Chapter 5 these definition of individual, population, genes, crossover and mutation will be clarified for the specific purpose of the thesis.

Chapter 3

Analytical Approach

Optimization of design with respect to relative motion is possible but first is necessary to understand more the physics behind the excitation mechanism of the water column in moonpool and also it is important to describe a way to calculate the effective viscous damping, since throughout this work it becomes evident the need to adjust this parameter for further calculations. This chapters brings in Section 3.1 an original analytical description of the water motion inside moonpool for a rectangular moonpool. Also, following a known recommended practice report [72] from a international classification society (DNV), deduce the calculation of resonant period and added mass of the moonpool characteristics used in this work. Then, in Section 3.3 the hydrodynamic coefficients that will be used for the numerical results analysis throughout this thesis.

3.1 Water Motions Inside of Moonpool

Mathematical model for the water oscillation in the rectangle shaped moonpool is derived in this thesis using conservation of momentum in a control volume Ω (Figure 3.1) inside moonpool and deduction is shown in Appendix A. For simplicity, the cutout angle is considered as a right angle ($\alpha = 90°$). More consideration about it are discussed through this work.

Equation of relative motion of water inside moonpool $h(t)$ is given by:

$$\begin{aligned} &\left[\rho_w bl\,(d+h) + M_a\right]\ddot{h} + B_l\dot{h} + B_q\dot{h}|\dot{h}| + \rho_w gblh + \\ &\left[d_{hz} + \rho_w bl\,(d+h) + M_a\right]\ddot{z_h} + \left[e_{hz} + B_l\right]\dot{z_h} + \rho_w gblz_h \\ &= F_{wh}\ , \end{aligned} \tag{3.1}$$

in which:

$h(t)$ is the free surface elevation $[m]$;
z_h is heave motion of ship $[m]$;

b is moonpool's breadth $[m]$;
l is moonpool's length $[m]$;
d is draft $[m]$;
g is gravity acceleration $[m/s^2]$;
ρ_w is specific density of water $[kg/m^3]$;
M_a is added mass $[kg]$;
B_l is linear damping coefficient $[kg/s]$;
B_q is quadratic damping coefficient $[kg/m]$;
d_{hz} is the added mass interaction coefficient between heave and absolute moonpool motion $[kg]$;
e_{hz} is the damping interaction coefficient between heave and absolute moonpool motion $[kg/s]$;
F_{wh} is the wave force exciting relative motion $h(t)$ $[N]$.

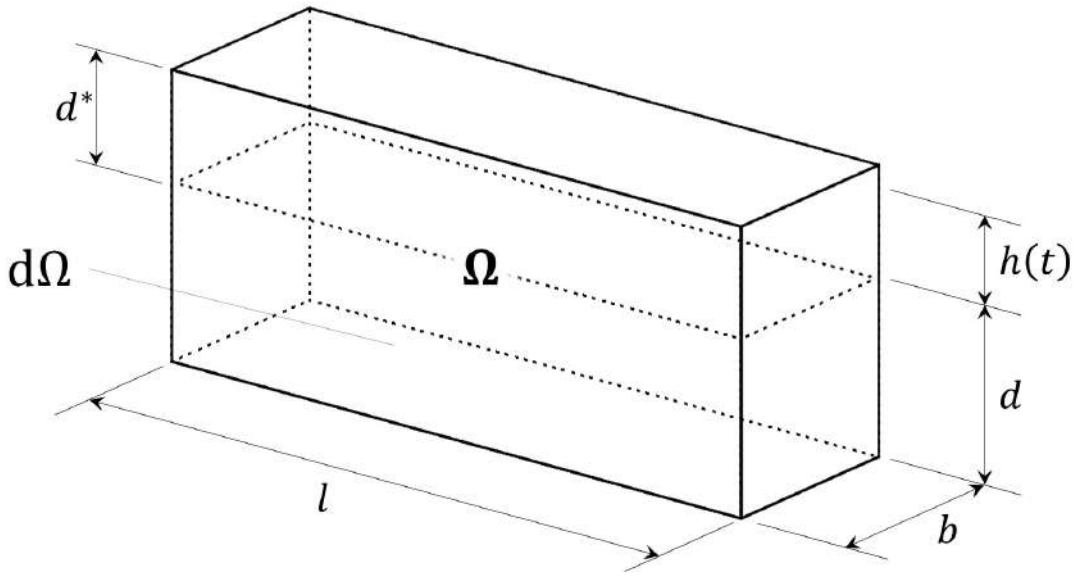

Figure 3.1: The control volume Ω with surface $d\Omega$ of rectangular shaped moonpool.

First line of Equation (3.1) describes the motion of water inside the moonpool while the second line describes the interaction with ship's heave motion. The nonlinear term $B_q\dot{h}|\dot{h}|$ is the damping due to friction and vortex generation and it is researched in more details by KNOTT and FLOWER [73].

Decay

In a decay test, the Equation (3.1) can be written as:

$$\left[\rho_w bl\left(d+h\right)+M_a\right]\ddot{h}+B_l\dot{h}+B_q\dot{h}|\dot{h}|+\rho_w gblh=0\ . \tag{3.2}$$

The *natural frequency* (ω_n) of water oscillation in a rectangle shaped moonpool, assuming that the damping is small, can be calculated as shown in Equation (3.3).

$$\omega_n = \sqrt{\frac{\rho_w g b l}{\rho_w b l d + M_a}} \, . \tag{3.3}$$

In a real decay test of water inside moonpool, a *viscous* damper is added to the model and this outputs a force that is proportional to the velocity of the mass as shown previously in Equation (3.2). This equation is nonlinear and cannot be solved analytically. Higher damping prevents the system from oscillation, and that happens when system has reached the point of *critical damping*. The value of this critical damping is given by:

$$B_{Crit} = 2\sqrt{K\left(\rho_w b l d + M_a\right)} \, , \tag{3.4}$$

where K is the stiffness coefficient and in the piston mode is

$$K = \rho_w g A = \rho_w g b l \, . \tag{3.5}$$

The relation between system damping and the critical damping is defined as *damping ratio* (η):

$$\eta \equiv \frac{system\ damping}{critical\ damping} = \frac{B_{eq}}{B_{Crit}} = \frac{B_l + \frac{8}{3\pi}\omega_n \xi_a B_q}{2\sqrt{K\left(\rho_w b l d + M_a\right)}} \, , \tag{3.6}$$

where B_{eq} is the equivalent linearized damping $[kg/s]$ at a particular amplitude ξ_a $[m]$ of the free surface elevation in the moonpool at which damping decay is calculated.

The frequency at which a system tends to oscillate in this case is called the *damped natural frequency* (ω_d). The damped natural frequency is less than the undamped natural frequency, but for many practical cases the damping ratio (η) is relatively small and hence the difference is negligible ($\eta = 0.1$ - Damped natural frequency is only 1% less than the undamped). Damped natural frequency is given by:

$$\omega_d = \omega_n \sqrt{1 - \eta^2} \, . \tag{3.7}$$

By considering Equation (3.2) it is possible to calculate natural frequency (ω_n), added mass (M_a), linear damping (B_l) and viscous pressure damping (B_q - Quadratic damping) fitting solution with an experimental data. In Section 3.3 it is shown a way to calculate these coefficients with a test result.

Forced Heave Oscillation

Turning now to a forced heave oscillation test, there is the ship motion (z_h) but no wave exciting force ($F_{wh} = 0$) to take into consideration, so the Equation (3.1) can be written as:

$$\begin{aligned}&\left[\rho_w bl\left(d+h\right)+M_a\right]\ddot{h}+B_l\dot{h}+B_q\dot{h}|\dot{h}|+\rho_w gblh\ = \\ &=-\left[d_{hz}+\rho_w bl\left(d+h\right)+M_a\right]\ddot{z_h}-\left[e_{hz}+B_l\right]\dot{z_h}-\rho_w gblz_h\ .\end{aligned} \tag{3.8}$$

Since the hydrodynamic parameters of moonpool are obtained from a decay test using Equation (3.2) and it is assumable that these quantities are constant in the frequency range considered, the forced heave test may be used for the d_{hz} e_{hz} values calculation.

Regular Waves - Captive Vessel

If regular wave with captive vessel ($z_h = 0$) is considered, then the equation of motion is described as:

$$\left[\rho_w bl\left(d+h\right)+M_a\right]\ddot{h}+B_l\dot{h}+B_q\dot{h}|\dot{h}|+\rho_w gblh=F_{wh}\ , \tag{3.9}$$

Freely Floating Vessel

Last but not least, the coupled equation of motion for the freely floating vessel, neglecting the coupling with other motions than heave, is given by:

$$\begin{aligned}&\left[\rho_w bl\left(d+h\right)+M_a\right]\ddot{h}+B_l\dot{h}+B_q\dot{h}|\dot{h}|+\rho_w gblh+\\ &\left[d_{hz}+\rho_w bl\left(d+h\right)+M_a\right]\ddot{z_h}+\left[e_{hz}+B_l\right]\dot{z_h}+\rho_w gblz_h\\ &=F_{wh}\ ,\end{aligned} \tag{3.1 Rev.}$$

$$\begin{aligned}&\left[M_s+M_{as}\right]\ddot{z_h}+B_s\dot{z_h}+K_sz_h+d_{zh}(\ddot{z_h}+\ddot{h})+e_{zh}(\dot{z_h}+\dot{h})+\\ &=F_{wz}\ ,\end{aligned} \tag{3.10}$$

where

M_S is mass of vessel $[kg]$;
M_{as} is added mass for the vessel $[kg]$;
B_s is linear damping coefficient for the vessel $[kg/s]$;
K_s is stiffness coefficient for the vessel $[kg/s^2]$;
d_{zh} is the added mass symmetric interaction coefficient between heave and absolute moonpool motion $[kg]$;
e_{zh} is the damping symmetric interaction coefficient between heave and absolute moonpool motion $[kg/s]$;

F_{wh} is the wave force exciting vessel's heave $[N]$.

3.2 Energy Conservation

Considering the law of energy conservation that gives,

$$\frac{\mathrm{d}\left(E_k + E_p\right)}{\mathrm{d}t} = 0 \,, \tag{3.11}$$

where E_k is the kinetic energy $[J]$ and E_p is the potential energy $[J]$.

Following DNV GL [72] and applying Equation (3.11) to the water motion in a moonpool similar to default moonpool (Figure 1.10) with draft $d = 12.0$ the breadth of moonpool constant, but letting the length on bottom be equal to l_b, the cutout angle equal to α and $A\left(z\right)$ as the cross-sectional are of moonpool at z, that is the vertical distance measurement from the free surface, pointing upward, we can calculate the following relation for resonance period,

$$T_n = \frac{2\pi}{\sqrt{g}}\sqrt{\left(\lambda_{mp} - 12\right)\left(\ln\left(\lambda_{mp}\right) - \ln\left(\lambda_{mp} - 12\right)\right) + \frac{A\left(0\right)}{A\left(-12\right)}k_{mp}\sqrt{A\left(-12\right)}} \,, \tag{3.12}$$

where $\lambda_{mp} = l_b \tan\left(\alpha\right)$, $A\left(0\right) = b\left(l_b - 12/\tan\left(\alpha\right)\right)$, $A\left(-12\right) = bl_b$ and k_{mp} is a parameter within 0.45 and 0.47 for rectangular moonpools with aspect ratios between 0.4 and 1.0 [72].

The mass plus added mass $(M + M_a)$ of the system may also be calculated as,

$$\begin{aligned} M + M_a = \rho A\left(0\right)\Bigg[&\left(\lambda_{mp} - 12\right)\left(\ln\left(\lambda_{mp} - 12\right) - \ln\left(\lambda_{mp} - 24\right)\right) + \\ &\frac{A\left(0\right)}{A\left(-12\right)}k_{mp}\sqrt{A\left(-12\right)}\Bigg] \,. \end{aligned} \tag{3.13}$$

Also, added mass for vertical oscillation can be expressed as,

$$M_a = \rho k_{mp} A\left(-12\right)\sqrt{A\left(-12\right)} \,. \tag{3.14}$$

Equations (3.12) to (3.14) are calculated considering the law of energy conservation (Equation (3.11)), so it neglects any loss due to viscosity effects, but they are important for a calculation of the resonant period and added mass of moonpool just considering the geometry information.

3.3 Hydrodynamic Coefficients - Decay test

Hydrodynamic coefficients, namely *natural frequency*, *added mass* and *damping coefficients*, are important for the analysis of this work. It could be seen in previous *Sections* that these coefficients need to be calculated for the moonpool. A decay test is probably the simplest way to calculate these coefficients.

With results data of decay test is possible to calculate mean peak-to-peak (or mean of the zero up-crossing) damped period T_d and calculate the natural damped frequency:

$$\omega_d = \frac{2\pi}{T_d} \ . \tag{3.15}$$

As previously mentioned, $\omega_n \approx \omega_d$.

Using Equation (3.3), it is possible to calculate the added mass M_a.

Logarithmic Decrement

Then, for the calculation of *damping coefficients*, it is necessary to analyze the time trace of the free surface in the moonpool from the decay tests. Denoting ζ_n as the absolute value of free surface elevation of *nth* extreme value. The Figure 3.2 below shows a typical time trace for a decay test for a weakly damped system with both linear and quadratic damping components.

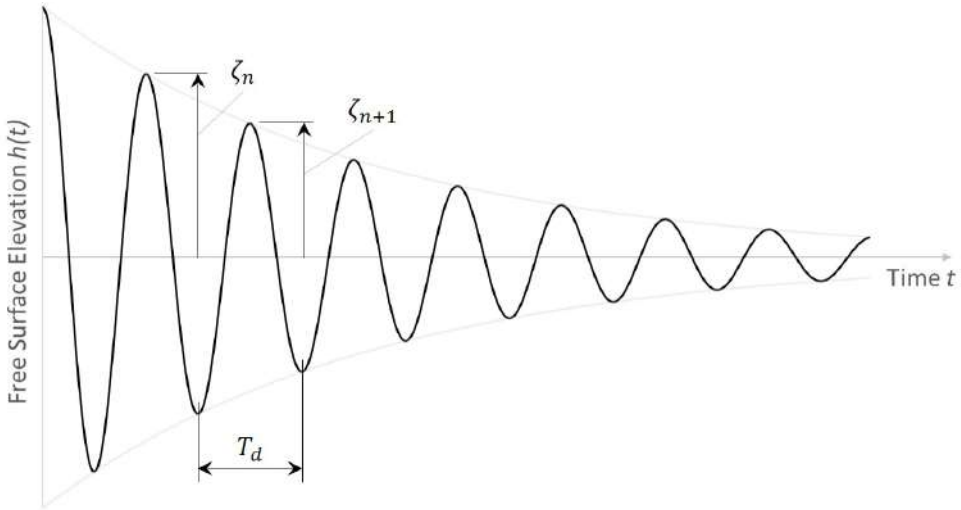

Figure 3.2: Time trace of a decay calculation

In an underdamped system ($\eta < 1$) the logarithmic decrement δ may be used for damping coefficients calculation [74]. It represents the rate at which the amplitude of a free-damped vibration decreases and can be obtained from Equation (3.16).

$$\delta \equiv \frac{1}{n_i} \ln \frac{\zeta_1}{\zeta_n} \quad \therefore \quad \ln \frac{\zeta_1}{\zeta_n} = \delta n_i \ . \tag{3.16}$$

Damping ratio (η), defined in Equation (3.6), can be found by solving:

$$\eta = \frac{\delta}{\sqrt{4\pi^2 + \delta^2}} \, . \tag{3.17}$$

Using Equation (3.17) in Equation (3.6), it is possible to calculate the equivalent linearized damping B_{eq}.

PQ Analysis

Other procedure for damping coefficients, is to compute the dissipated energy during a number of cycles, commonly referred to as the energy method, and as long as it does not require to fit a function, it is generally considered as more reliable and robust. Hereafter this analysis is called *PQ Analysis*. Another advantage of this method, is that it can be used for the calculation of the linear, quadratic and even higher order damping.

The so-called *Extinction Curve* expresses the decrease of ζ_n as a function of mean elevation (ζ_m) [75]. Describing this curve as a two degree polynomial:

$$\Delta\zeta_n = p\zeta_m + q\zeta_m^2 \, , \tag{3.18}$$

where

$$\Delta\zeta_n = \zeta_{n-1} - \zeta_n \, , \tag{3.19}$$

$$\zeta_m = \left[\zeta_{n-1} + \zeta_n\right]/2 \, . \tag{3.20}$$

The coefficients p and q are called extinction coefficients and the relation between these coefficients and damping coefficients can be found integrating the motion inside moonpool (Equation (3.2)), over the time period for a cycle and then equating the energy loss due damping to work done by restoring moment [76]. The result is given by:

$$\Delta\zeta_n = \frac{\pi\zeta_m}{(M + M_a)\omega_n}\left(B_l + \frac{8}{3\pi}\omega_n\zeta_m B_q\right) \, . \tag{3.21}$$

Substitution of Equation (3.21) into Equation (3.18) and after some algebraic manipulations, the linear and quadratic damping are calculated as follows:

$$B_l = \frac{(M + M_a)\,\omega_n}{\pi} p \, , \tag{3.22}$$

$$B_q = \frac{3}{8}\,(M + M_a)\, q \, . \tag{3.23}$$

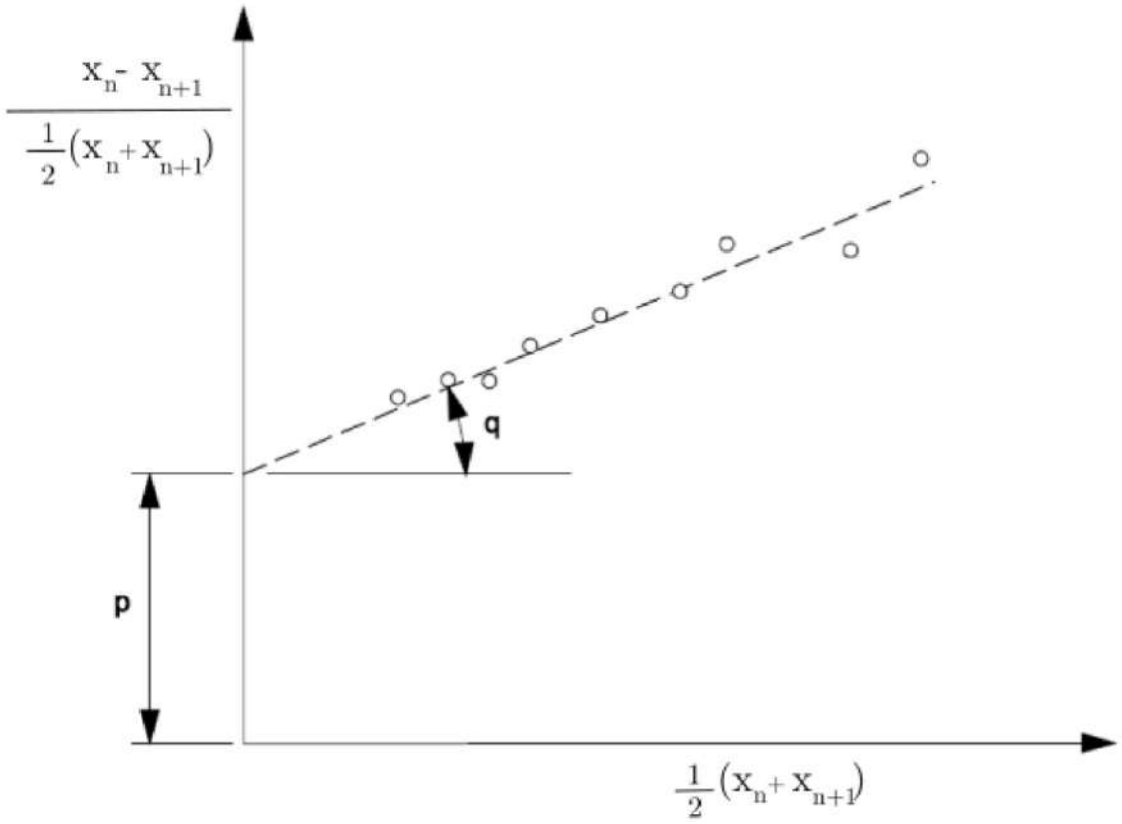

Figure 3.3: PQ Analysis plot (JAOUËN *et al.* [21])

Equation (3.18) may be rewritten in the slope-intercept form of a linear equation,

$$\frac{\Delta\zeta_n}{\zeta_m} = q\zeta_m + p \; . \tag{3.24}$$

At this manner, it is noticeable that if the damping is purely quadratic, i.e. $p = 0$, the data points in the decrement plot all fall on a straight line crossing origin and the slope is a measure of the quadratic damping. Pure linear damping, i.e. $q = 0$, means that the decrement is amplitude-independent and leads to a horizontal line in the decrement plot (Figure 3.3).

Depending on the order of damping desired to calculated, the order of Equation (3.18) can be increased and also a term of the third order is added in the damping force changing Equation (3.21). At this present work we are worried just with linear and quadratic damping, so the two degree polynomial is enough.

Chapter 4

Numerical Approach

In this chapter, Section 4.1 brings CFD analysis with domain and mesh study, also the turbulence modeling in comparison with laminar results and the general setup with boundary and initial conditions (setup and verification stage). The results gathered from simulations can be seen in Section 4.2. Concluding this chapter, some information about the potential theory setup are presented and also the viscosity importance in the calculation of ship motion and also of the free surface elevation inside moonpool (Section 4.3). This last section is crucial for the next chapter objectives, as the optimizer presented is based on potential theory solver.

4.1 CFD Setup

All the simulations in this work was done using a commercial CFD software bundle (*Ansys CFD*), that includes preprocessor (*DesignModeler* and *Meshing* - *Ansys Workbench*), FVM solver (*Fluent*) and postprocessor (*CFD-Post*) software (Section 2.2.4).

Concerning with quality of CFD, some procedures must be done as domain independence study and mesh refinement study. In this work, simulations for decay test and also for some others configurations were executed. Particularly, results of decay test are more important for the damping coefficients calculation, so these studies were conducted specifically for that simulation. The other simulations are just at the end a comparison with analytical as additional resource. Without experiments no validation can be done. However, with a good agreement among CFD results and analytical, we can trust more in the latter to do damping analysis.

4.1.1 Domain

Geometry of a barge with the *default moonpool* is used for decay test and other tests that will be shown in Section 4.2. Its design with main particulars are shown

in Figure 4.1.

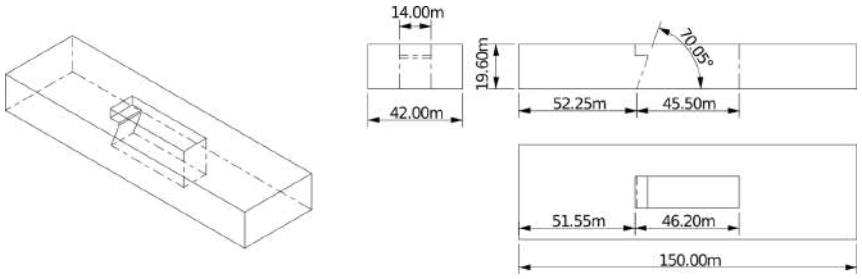

Figure 4.1: Design of the barge for CFD tests with *default moonpool*.

A rectangular shaped domain as presented in Figure 4.2 (half domain) is used for all the following simulations, except for the *Numerical Regular Wave for Freely Floating Vessel Test*, but further details on this are given in Section 4.2.4.

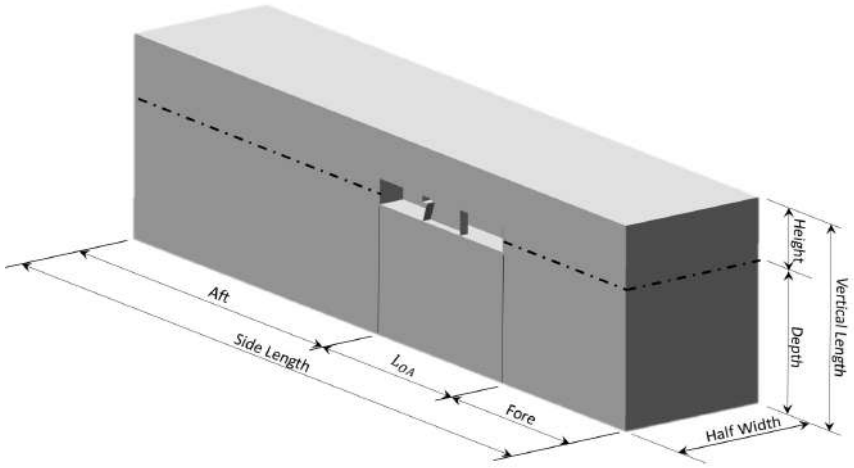

Figure 4.2: Main particulars of domain (Cut in symmetry plane).

Then, three different size of that domain are created for the size dependence analysis and are shown in Figure 4.3. Domain's dimensions, as a function of model's L_{OA} (length overall), with respective number of elements are presented in Table 4.1.

The mesh inside of each domain is created from the previously smaller mesh in a way that almost none variation would occur in the pre-existing mesh and just the domain size is analyzed at that study. Then, it is performed in a region with hexahedra elements by adding more hexahedra following the increase ratio of neighboring cells. It is noticeable that the variation of number of elements between the *Medium* size and the *Small* size is greater than the difference between *Big* size and *Medium*, that is due the fact that as it getting farther of the barge, the mesh tend to increase it element size as long as the gradients are smaller and also it can be used as an artifice to add an artificial dispersion so the flow fits outlet boundary condition

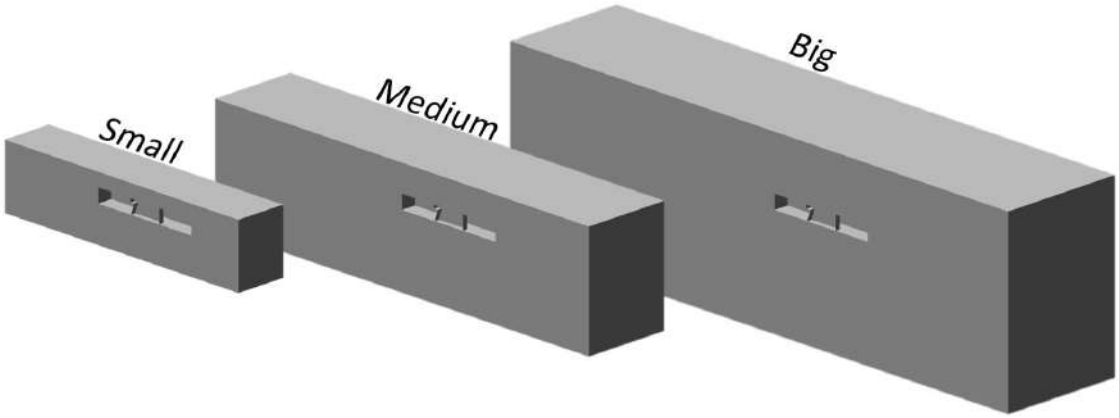

Figure 4.3: Three different domains for the size domain study (Cut in symmetry plane).

Table 4.1: Dimensions of the three domains generated as a function of barge L_{OA}.

	Small	**Medium**	**Big**
Fore	0.5	1.0	1.5
Aft	1.0	2.0	3.0
Half Width	1/3	2/3	1.0
Depth	1/3	2/3	1.0
Height	1/8	1/4	1/2
Number of Elements	**809631**	**971001**	**1041342**

previously. This artifice must be used cautiously because downstream results may change substantially the main result data in the analysis.

Domain Size Study

The result parameters that are of most concern are the hydrodynamic coefficients of *default moonpool*. Three wave probes were located inside moonpool and it location are presented in Figure 4.4. They are distributed horizontally in relation to the length at the top part of moonpool, that is opened to atmosphere.

The free decay time trace of *Wave Probe Bow* is shown in Figure 4.5 and it is used as an example to describe the theory. It is possible to calculate mean peak-to-peak period and with that compute the *damped* natural frequency. Knowing the last and using Equation (3.3), the added mass can be determined.

In order to calculate the equivalent linearized damping B_{eq}, the logarithmic decrement δ is calculated for each domain. According to Equation (3.16), δ can be found considering the angular coefficient of best fitting line (trend line) of peak data in the plot $ln\zeta_1/\zeta_n \times n_i$. The logarithmic decrement plot of the time trace in Figure 4.5 is shown in Figure 4.6.

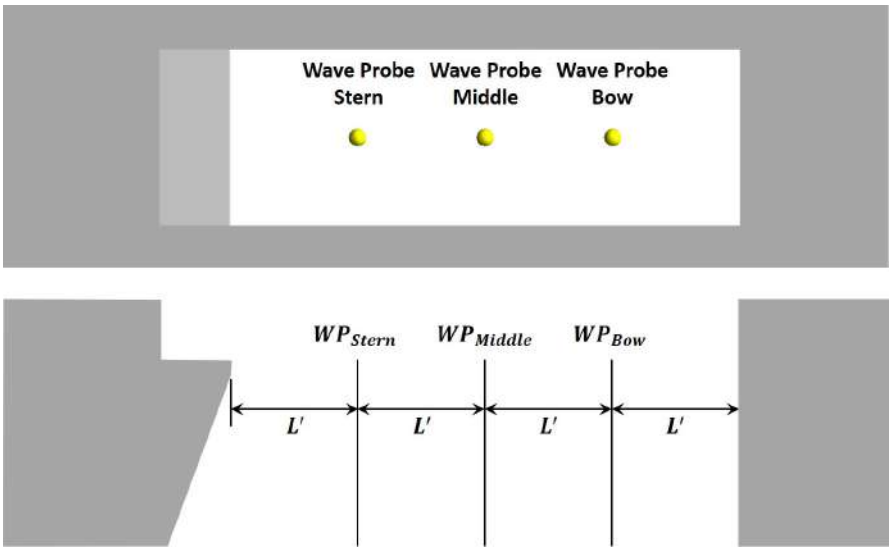

Figure 4.4: Locations of probes in the moonpool (CFD) - $L' = 10.15m$

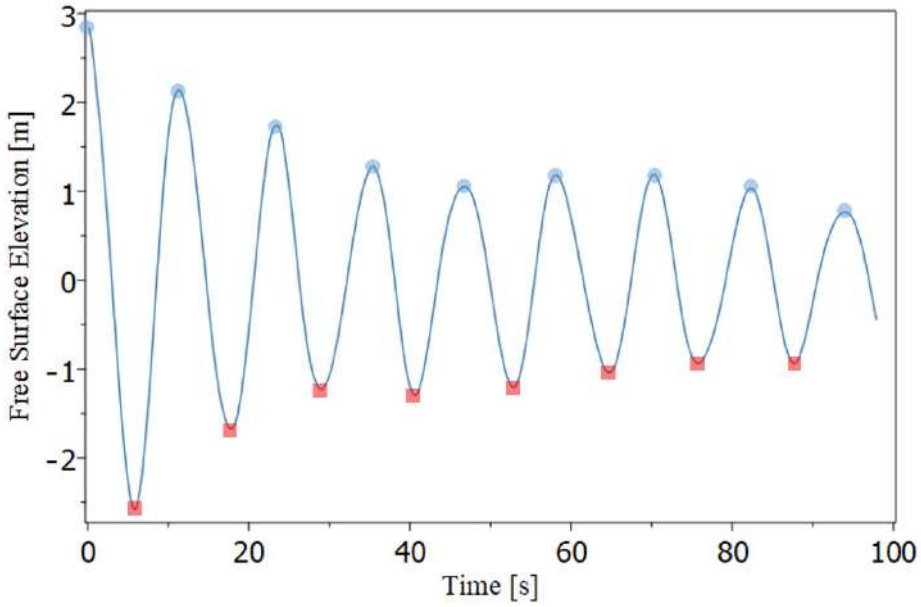

Figure 4.5: Time trace from decay test - *Default moonpool* - WP_{Bow}.

Then, using Equations (3.6), (3.16) and (3.17) and considering average off all three wave probes, the results are computed. The summary of all hydrodynamic coefficients for each domain size and the relative variation of each coefficient in relation to one step smaller domain is presented Table 4.2.

For the quadratic and linear damping coefficients calculation, the results were analyzed using the PQ method, explained above (Section 3.3). Figure 4.7 presents PQ analysis of previous cited time trace (Figure 4.5).

After analyzed all domain size, it is noticeable that the PQ analysis method does *not* capture the physical behavior, as the damping is negative in most of wave probes at different domain size. The average of all three wave probes are used to derive the

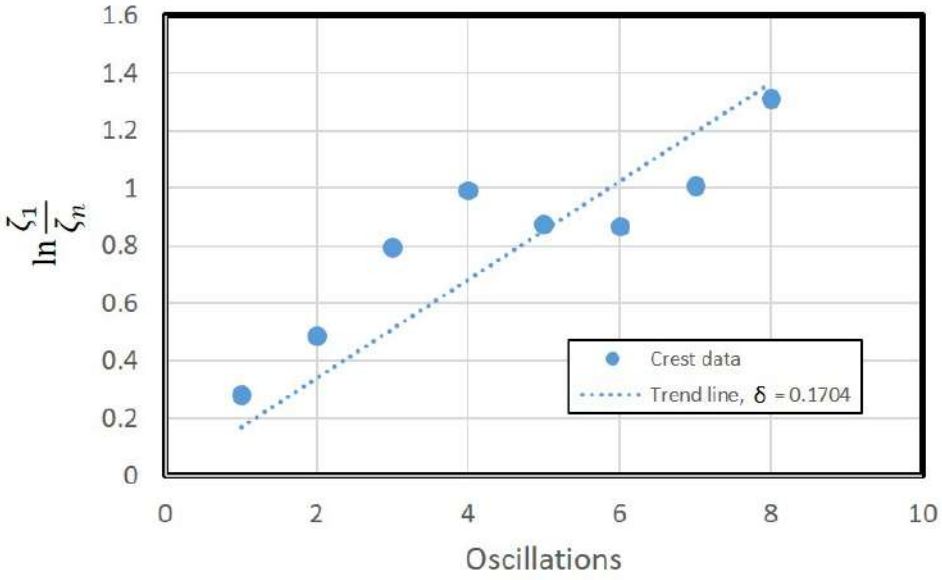

Figure 4.6: Logarithmic decrement plot - *Default moonpool* - WP_{Bow}.

Table 4.2: Hydrodynamic coefficients and relative variations for domain study.

	$\boldsymbol{\omega_n}$ $[rad/s]$	$\boldsymbol{M_a}$ $[kg]$	$\boldsymbol{B_{eq}}$ $[kNs/m]$	$\boldsymbol{B_{Crit}}$ $[kNs/m]$
Small	0.531	1.305×10^7	7.607×10^5	2.180×10^7
Medium	0.536	1.271×10^7	8.833×10^5	2.162×10^7
Big	0.537	1.264×10^7	9.599×10^5	2.158×10^7
Medium - Small	0.83 %	-2.68 %	13.88 %	-0.84 %
Big - Medium	0.18 %	-0.56 %	7.97 %	-0.18 %

final p and q values for each size domain and then the damping. In Table 4.3, the calculated results are presented for all of them.

According to what is shown, it is noticeable that the *Small* domain would already be enough for calculation of natural frequency and the parameter directly related with it, like added mass and critical damping. When considering the results of equivalent damping, there is a variation that may be considerable, so the *Medium* size would be a better choice due that.

The results taken from PQ analysis, linear damping and quadratic damping, did present a non physical behavior with negative damping. Besides the significant variation, it has also shown an oscillatory convergence, as the values slightly increased from the *Small* to *Medium* and then had a significant decrease to the *Big* size. Based on this, the PQ analysis is considerable to *not* bring good results for this decay test. More details are given below in Section 4.2.1.

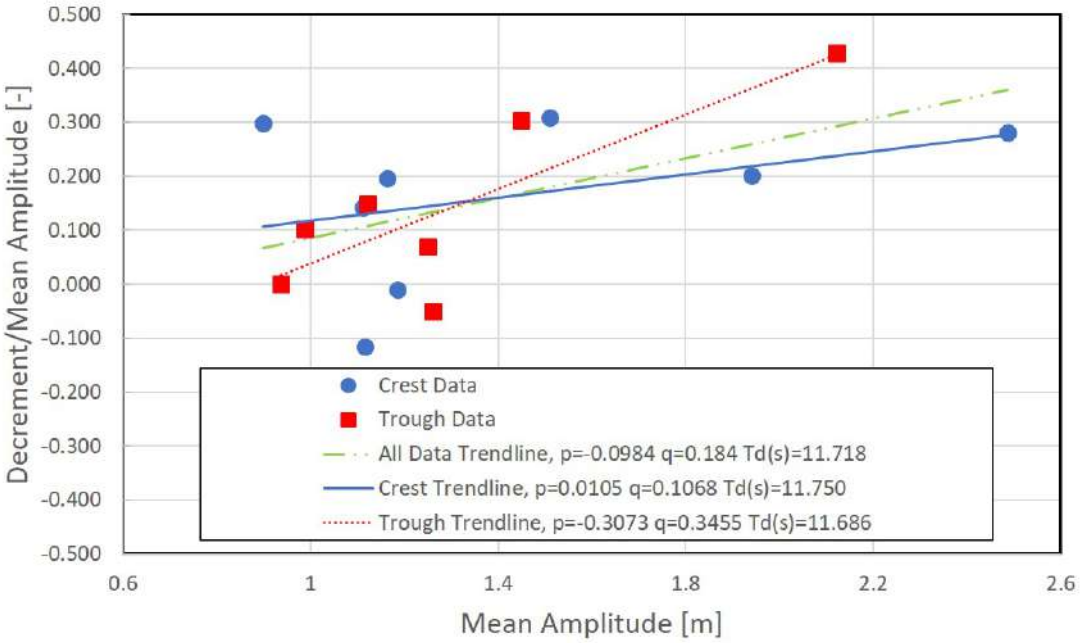

Figure 4.7: PQ analysis - *Default moonpool* - WP_{Bow}.

Table 4.3: PQ Analysis of hydrodynamic coefficients for domain study.

	p	q	B_l $[kNs/m]$	B_q $[kNs^2/m^2]$
Small	-0.127	0.211	-4.363×10^5	1.598×10^6
Medium	-0.141	0.223	-4.851×10^5	1.685×10^6
Big	-0.087	0.184	-3.010×10^5	1.399×10^6

4.1.2 Mesh

Different meshes are used in this work, depending on the simulation. First of all, a structured mesh (regular connectivity for each node - grid points can be mapped into a matrix) was created (Figure 4.8) and some issues took place. For a structured 3D mesh, all the elements are hexahedra and besides the better convergence and higher resolution, there are some drawbacks. In addition to the fact that it is hard and time consuming to generate a mesh like this, some specific quality issues were faced in this work, one is that as long as it is necessary to refine closer to moonpool, the elements far of it presented bad smoothness (rate of change in the magnitude of adjacent element volumes) with less efficient mesh distribution (fine resolution in areas of less importance) and there is a drawback also with aspect ratio (ratio of longest to the shortest side in a cell) far of moonpool, due the need of an anisotropic mesh for discretization of free surface region and moonpool outflow region (Figure 4.8). Dedicating extra time for the mesh generation these issues may be improved, but since *hybrid meshes* are already very well accepted and proven to

bring also good results, they are used at this work.

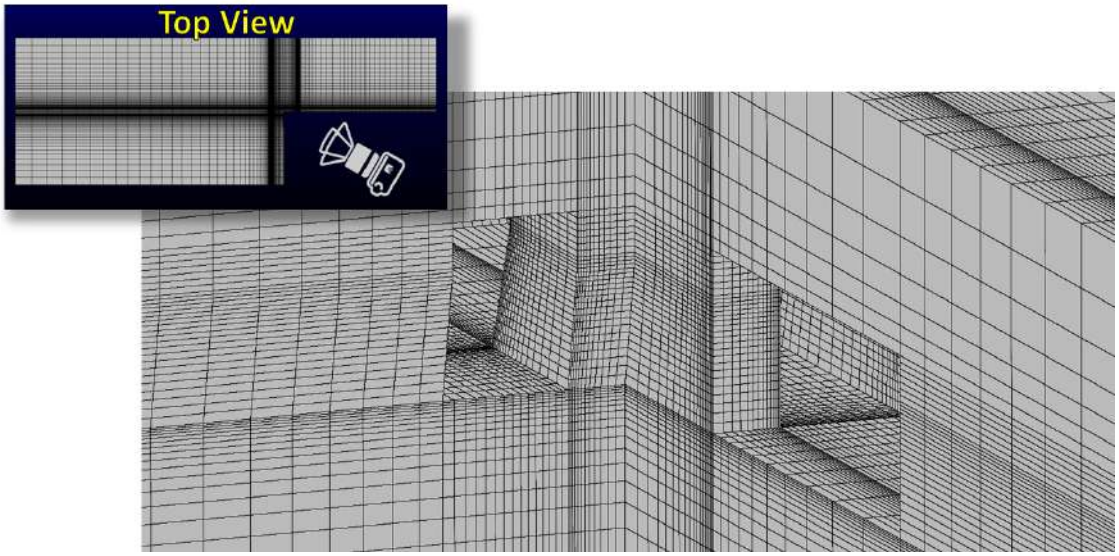

Figure 4.8: Structured Mesh (Hexahedron only - 942120 Elements).

Hybrid meshes are unstructured meshes that contains a structured portion with hexahedra elements and an unstructured portion with any possible element that a solver might be able to use. It is important to know that besides the definition of mesh topology, *Fluent* is an unstructured solver, so it does not map the grid points into a matrix even for structured meshes [14]. It gives more versatility to the code. So, the topology definition in this work is just to inform about the mesh elements.

Another reason for choosing a hybrid unstructured grid is that *Forced Heave Oscillation Test* (Section 4.2.2) has body motion, and in that case tetrahedra elements are much easier to setup and they are also more versatile as they accept higher *time step* (time between each iterative solution).

Mesh for *Numerical Decay Test* is shown in Figure 4.9 and is the same mesh used in *Numerical Regular Wave with Captive Vessel Test* (Section 4.2.3). It has a prismatic layer for boundary layer calculation and it is also used for better resolution of the free surface close to the barge, as this region presents tetrahedra elements. Outside of this closer region of the barge, hexahedra elements are used with a better control of the mesh quality as the element sizes are not directly connected with the element sizes close to moonpool. Inside moonpool it was possible to use hexahedra elements as well.

Mesh of *Numerical Regular Wave for Freely Floating Vessel Test* simulation is shown in Section 4.2.4.

There is a big concern about numerical uncertainty and errors in CFD and some introductory ideas about it are described in Section 2.2.6. Following guidelines about mesh convergence study, three successive level of meshes refinement was set and are shown in Figure 4.10.

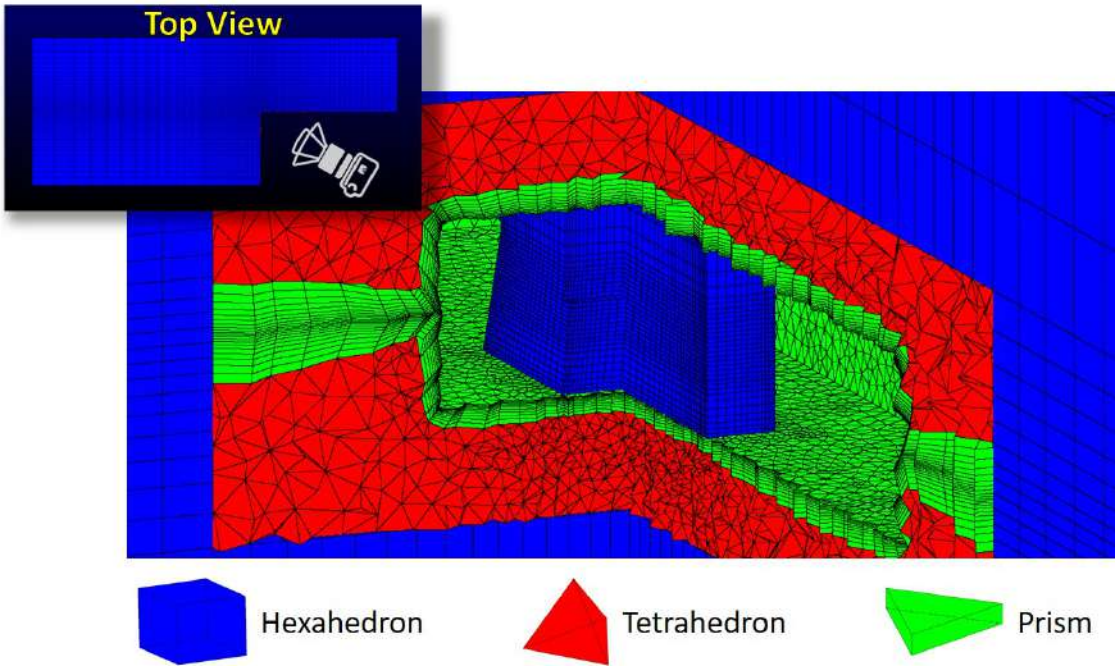

Figure 4.9: Mesh elements (*Medium* mesh).

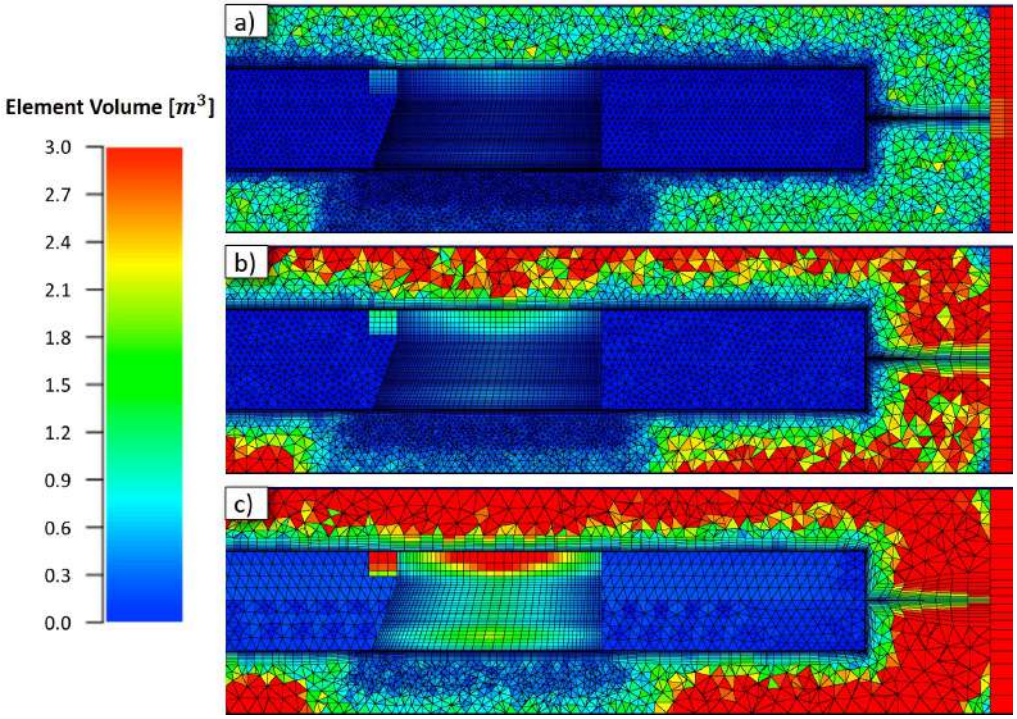

Figure 4.10: Volume size of elements in different mesh refinements close to moonpool. *a)* Fine mesh, *b)* medium mesh and *c)* coarse mesh. (Side view - $Y = 0.0$).

This refinement is done considering a general global refinement by the same factor as long as it is necessary to *not* change the elements distribution. Use of geometrically similar cells are preferable [68], so every region that in Figure 4.9 is kept with the same elements as can be seen in Figure 4.10. In Table 4.4 a summary

of the variation between meshes are shown.

Table 4.4: Properties of decay grid for different refinements ($r_{grid} \approx 1.3$).

	Coarse	**Medium**	**Fine**
Hexahedron	112767	321474	754148
Tetrahedron	170951	373487	913869
Prism	155420	276040	494680
Representative cell size	3.73	2.86	2.19
Number of Elements	439138	971001	2162697

Mesh Convergence Study

Proceeding with same idea of the domain size study (Section 4.1.1), target quantities of interest are the hydrodynamic coefficients and they also are analyzed for the mesh refinement study.

Wave probes are located in same position shown in Figure 4.4 and free decay of each mesh was used to compute natural frequency, added mass and damping coefficients, using also the logarithmic decrement method to calculate equivalent one.

Then, the Table 4.5 is built with all target quantities and relative variation among the successive refinement levels.

Table 4.5: Hydrodynamic coefficients and relative variations for mesh study.

	$\boldsymbol{\omega_n}$ $[rad/s]$	$\boldsymbol{M_a}$ $[kg]$	$\boldsymbol{B_{eq}}$ $[kNs/m]$	$\boldsymbol{B_{Crit}}$ $[kNs/m]$
Coarse	0.535	1.275×10^7	8.529×10^5	2.164×10^7
Medium	0.536	1.271×10^7	8.833×10^5	2.162×10^7
Fine	0.534	1.282×10^7	9.033×10^5	2.168×10^7
Medium - Coarse	0.1 %	-0.31 %	3.44 %	-0.1 %
Fine - Medium	-0.27 %	0.84 %	2.21 %	0.27 %

For more confidence in the results, it is possible to estimate the *discretization error* and the GCI method is chosen. In this work, just spatial discretization error is analyzed, so the simulations were run at the same time step.

The grid refinement ratio r_{grid} is approximately equal to 1.3 [68] (Table 4.4), being a little more conservative then ITTC [69] recommendation of $\sqrt{2}$. Using (Equations (2.38) to (2.46)) for GCI proper calculation, all the respective variables calculated are shown in Table 4.6 below.

Table 4.6: Calculations of discretization error - Grid Convergence Index of each mesh.

	ω_n $[rad/s]$	M_a $[kg]$	B_{eq} $[kNs/m]$	B_{Crit} $[kNs/m]$
r_{21}	1.303			
r_{32}	1.306			
φ_3	0.535	1.275×10^7	8.529×10^5	2.164×10^7
φ_2	0.536	1.271×10^7	8.833×10^5	2.162×10^7
φ_1	0.534	1.282×10^7	9.033×10^5	2.168×10^7
p_g	3.776	3.788	1.613	3.787
φ_{ext}^{32}	0.536	1.269×10^7	9.405×10^5	2.161×10^7
φ_{ext}^{21}	0.534	1.288×10^7	9.405×10^5	2.171×10^7
e_a^{32}	0.096 %	0.305 %	3.565 %	0.096 %
e_a^{21}	0.266 %	0.847 %	2.263 %	0.266 %
e_{ext}^{32}	0.056 %	0.178 %	6.078 %	0.056 %
e_{ext}^{21}	0.153 %	0.478 %	3.952 %	0.152 %
GCI_{medium}^{32}	0.07 %	0.221 %	8.377 %	0.07 %
GCI_{fine}^{21}	0.191 %	0.605 %	5.259 %	0.19 %

According to what is shown in Tables 4.5 and 4.6, it is noticeable that the three simulated cases present close results when considering frequency, added mass and critical damping. Equivalent damping also did not present much variation from mesh to other, but when calculating the GCI, *Medium* mesh has a higher value than *Fine* as expected. An oscillatory convergence may be noted, but due the low variation in the results, this not caused disturbance. The recommendation would be to create a coarser mesh and analyze again the variation.

In analogous way to the experimental uncertainty, it is possible to use error bars to show profiles of variables after GCI calculation. In Figure 4.11 the extrapolated free surface level of decay results for the WP_{Bow} from the three grids is presented with error bars at each time solved. The local order of accuracy p_g calculated from Equation (2.40) ranges from 0.0021 to 30.120, with a global average of 7.496. There were a few of spurious points that were excluded from that extrapolated solution chart.

As more it advances in time, more the error increases, that is probably due to the cumulative error and also may be associated with the neglected contributions due to the high-order terms.

In zoomed region of Figure 4.11 it is possible to observe that the discretization error bar increases closer to zero and that is expected as the absolute value of

error do not decrease to zero, so the relative tends to increase. Another interesting observation is that at peaks and troughs the extrapolated values presents a dispersive behavior and at these *unusual* solutions the error also increases.

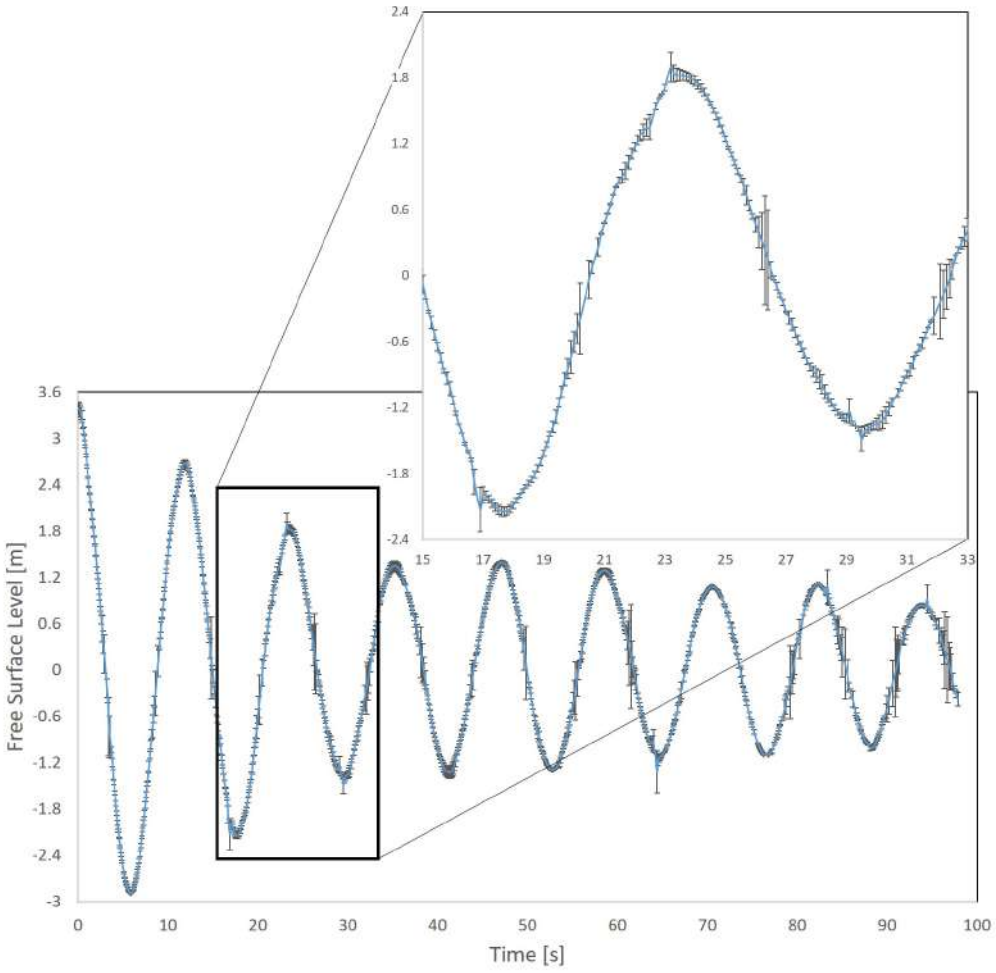

Figure 4.11: Extrapolated solution, with discretization error bars computed - *Default moonpool - WP_{Bow}*.

4.1.3 Turbulence Model

Laminar flows as the previously analyzed, consider the viscosity, but there are some instabilities that may increase into a random and chaotic variation of flow properties. In that case, the flow is *turbulent* and modeling it may improve the result quality, representing better the flow real behavior.

In *Fluent* there are plenty of possibilities of turbulence models. Nowadays, two-equations models are the most used in literature and for commercial purposes, as they can bring very good results with less computational resource than LES, or a hybrid RANS-LES (DES), or even the RSM, that is a RANS seven-equations model. More information about these models are in Section 2.2.2.

WILCOX [39] states that "an ideal model should introduce the minimum amount of complexity while capturing the essence of the relevant physics". It implies that the ideal model depend on how much detail is needed in the simulation. A very important consideration in decay test is the presence of vortices at the in and outflow of water in the borders of moonpool, as these vortices are related with damping and consequently the energy loss of oscillation [73]. The *zero* and *one equation* models described in this work are too simple for the purpose as they lack of effectiveness in separation (mixing length) and in rapidly changing pressure gradients (Spalart-Allmaras). Considering two equations models, κ-ϵ has the drawback of insensitivity to adverse pressure gradients and boundary layer separation, while κ-ω has relatively strong sensitivity of the solution depending on the freestream values of κ and ω outside the shear layer, generally not being recommended for use by the solver manual itself [14]. In this work, the Shear stress transport (SST) κ-ω is the chosen model. It is a two equation model that combines the necessary advantages of κ-ω turbulence model and κ-ϵ turbulence model. The first is important inside the moonpool, where predicting adverse pressure gradient boundary layer flow and separation is necessary and the latter helps convergence in the free shear flow.

Turbulent flows are significantly affected by the presence of walls and near-wall modeling significantly impacts the fidelity of numerical solutions [31]. *Fluent* provides a y^+-insensitive wall treatment, which lets the application of model independent of the near-wall grid resolution as it blends automatically from a viscous sublayer formulation (two layer zonal model approach) to a logarithmic formulation (wall function approach) based on y^+ values. The low-Re is used for $y^+ < 1$ while it reverts to a wall function formulation when $y^+ > 1$. In Section 2.2.3, more is discussed on the topic.

Boundary conditions definitions are the same of the laminar decay and will be presented further, but some turbulent parameters must be set and are shown below in Table 4.7.

Table 4.7: Boundary conditions of turbulence parameters.

	Decay - κ-ω SST
Top	Pressure Outlet
	Intensity and Viscosity Ratio Turbulent Intensity (T_μ) = 5% Viscosity Ratio (μ_t/μ) = 10
Ship and Moonpool	Wall Roughness
	Standard Roughness Height (m) = 0.0 Roughness Constant = 0.5

In *Pressure Outlet* boundary, the backflow was set for definition of turbulent intensity (T_μ) and turbulent viscosity ratio (μ_t/μ) and in *No-Slip Wall* it was set for a *smooth* wall.

More information about other boundary conditions parameters and values are discussed in Table 4.9.

Initial conditions also are the same of laminar decay and the turbulent parameters initialization is done by default, where turbulent parameters are initialized with constant values (domain averaged).

The mesh used for the turbulent simulation is the same used for the laminar results in *Medium* refinement. After finished, the contour of y^+ at no-slip walls of moonpool could be drawn and it is shown in Figure 4.12 considering one full period of oscillation.

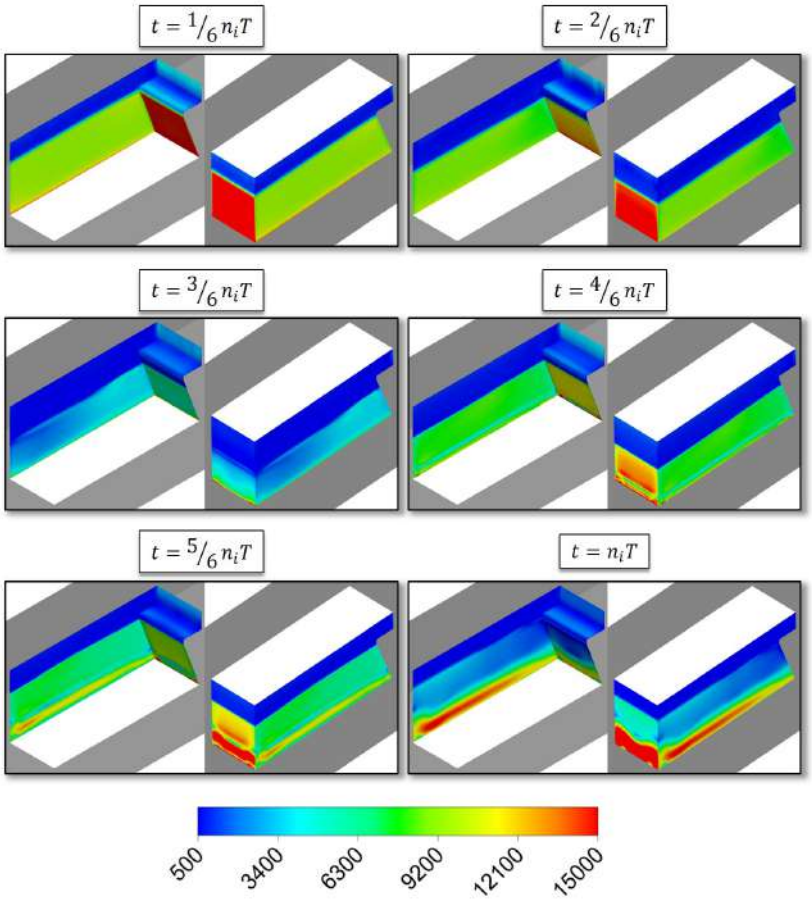

Figure 4.12: One period oscillation for y^+ contour at moonpool walls.

Values of y^+ are very far of the region of a good discretization of it. Some regions have values greater than 15000, at some time steps, what is a clear demonstration that the refinement for the boundary layer calculation is not well done.

In order to solve this issue, the distribution of nodes inside the moonpool was changed without change the quantity of nodes. This redistribution aims to bring

the nodes closer to the wall, improving the quality of calculation on the boundary layer. In other hand, as the number of nodes is not changing, the refinement in the geometrical center of the moonpool becomes coarser. In Figure 4.13 the comparison between the previous mesh and the refined in boundary layer is presented.

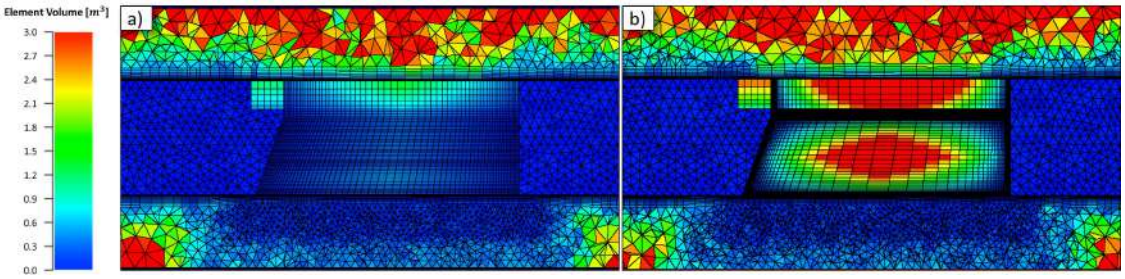

Figure 4.13: Refinement closer to the wall by nodes position redistribution. *a)* Previous mesh and *b)* refined at boundary layer

The y^+ of the simulation using this new mesh and following the same setup aforementioned is shown in Figure 4.14.

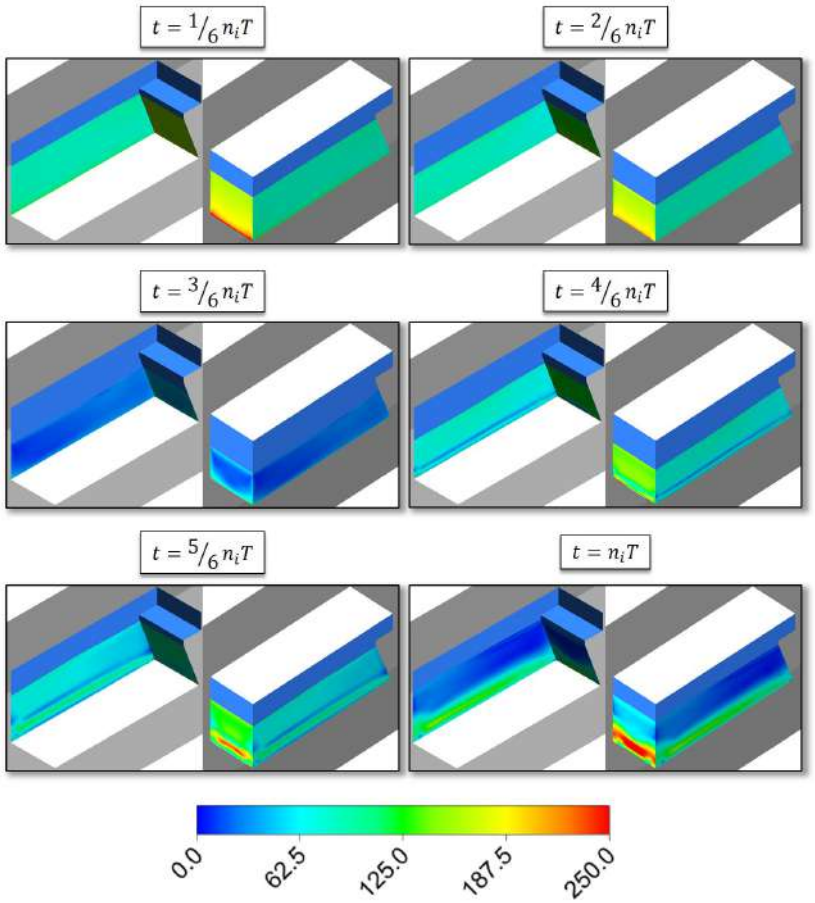

Figure 4.14: One period oscillation for y^+ contour at moonpool walls (New refined mesh at wall).

This mesh is not bringing a perfect y^+ refinement yet but it is a more satisfactory result than the previously one, keeping the mesh size and without losing much quality with high aspect ratio and smoothness (change in neighbor elements size).

Considering this new mesh, another interesting plot for a period oscillation is concerning the vortical structures at moonpool edges. In Section 2.2.2 the q-criterion definition for vortices calculation. So, in Figure 4.15 the q-criterion is drawn for one full period of oscillation.

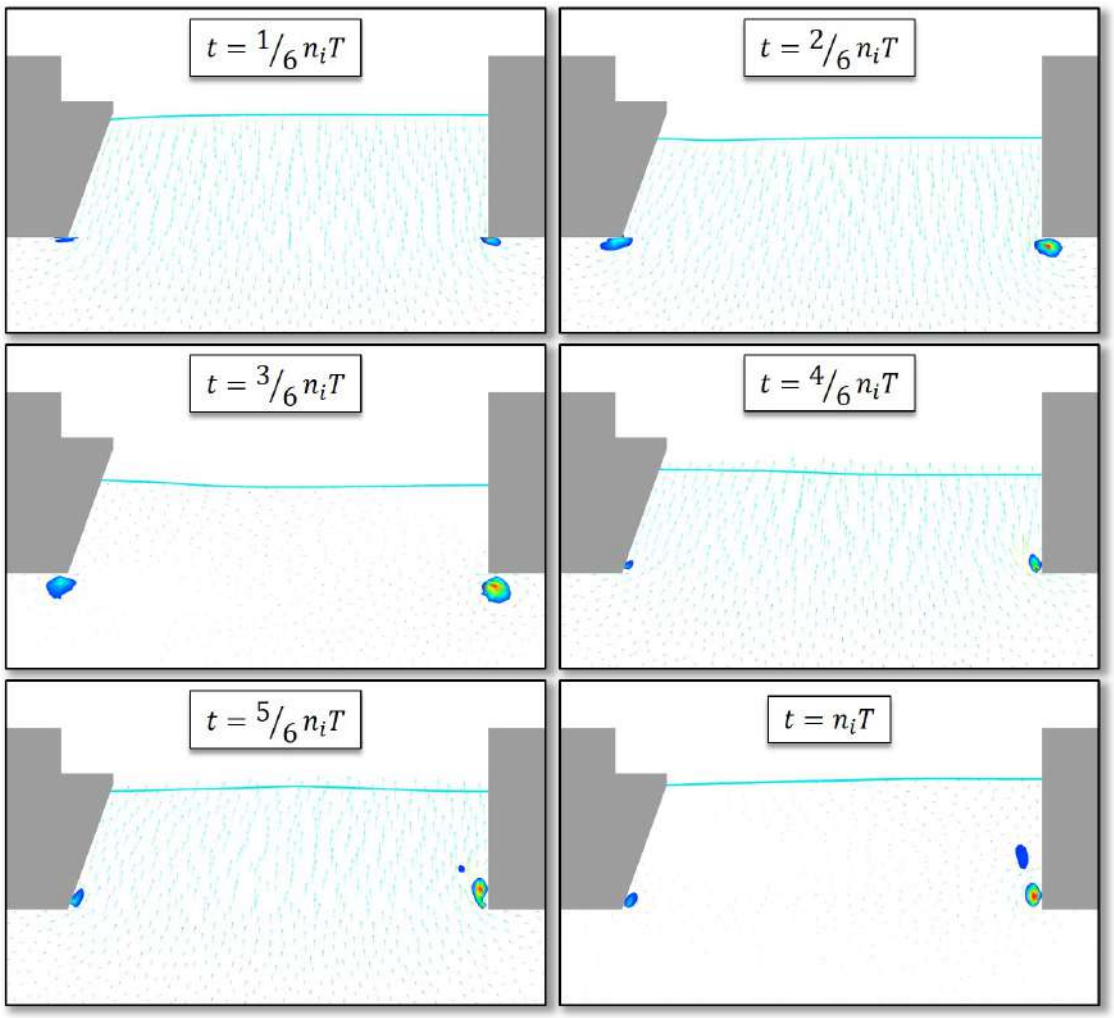

Figure 4.15: One period oscillation with velocity vector and vortical structure (Q-criterion).

Eddy shedding at the boundary is related with the loss of kinetic energy in the moonpool [73]. Observing Figure 4.15 and also following time steps of simulation it could be observed that the leading edge of moonpool (right angle edge) has more significance in this loss as the shedding are more strong and developed at this region.

Results of the target quantities are shown in Table 4.8. *Laminar* results are considering the *Medium* size domain with the *Medium* refinement, same domain

and mesh used for the turbulent simulations.

Table 4.8: Hydrodynamic coefficients and relative variations for turbulence analysis.

	ω_n $[rad/s]$	M_a $[kg]$	B_{eq} $[kNs/m]$	B_{Crit} $[kNs/m]$
Laminar	0.536	1.271×10^7	8.833×10^5	2.162×10^7
κ-ω SST	0.535	1.281×10^7	8.871×10^5	2.167×10^7
κ-ω SST - Laminar	-0.24 %	0.75 %	0.42 %	0.24 %

Less than 1% of variation for all parameters is a very satisfactory CFD comparison. Probably an even better discretization of the boundary layer ($y^+ < 1$) could give more confident when affirming that the turbulence modeling for this simulation is negligible, as long as walls are the main source of vorticity, near wall modeling is very important in turbulence.

4.1.4 Physical Setup

Boundary Conditions

Boundary conditions definition depends on which test is being analyzed. In Figure 4.16, the boundary condition for the decay, forced heave oscillation and regular wave with captive vessel test are presented. More information of each boundary condition can be seen in Section 2.2.1.

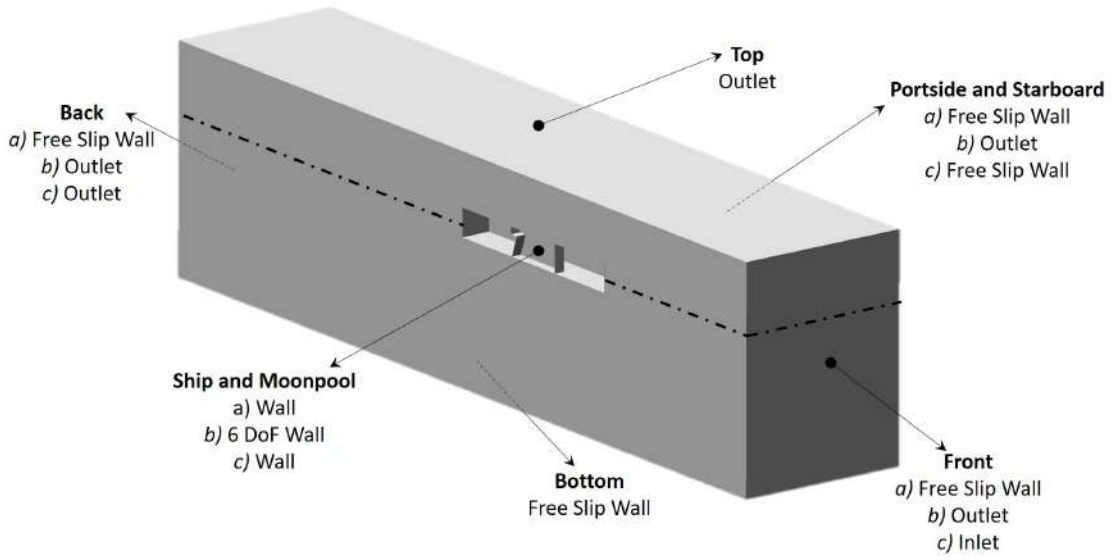

Figure 4.16: Boundary conditions of *a)* decay test, *b)* forced heave oscillation and *c)* regular wave with captive vessel (Cut in symmetry plane).

In *Fluent*, there is a *open channel* condition in which model the effects of a free surface between the flowing fluid and fluid above it, that is the air in this work. It is also possible to configure a *open channel wave boundary* condition for wave definitions. Another important condition that may be applied in the outlet boundary is a *Numerical Wave Beach*, explained with more details in Section 2.2.1. Depending on the turbulence model chosen, there is also a need to set the respective parameters at the boundaries. Summary of all boundary conditions is presented in Table 4.9 below.

Table 4.9: Boundary conditions.

	Decay	**Forced Heave**	**Captive Vessel**
Open Channel	✓	✓	
Open Channel Wave BC			✓
Water Depth	$Depth : 112m$		
Numerical Beach			$Length : 125m$
Front	Wall	Pressure Outlet	Velocity Inlet
	Free Slip	Free Surface Level	First Order Airy Height: $2.5m$ Length: $214.43m$
Back	Wall	Pressure Outlet	Pressure Outlet
	Free Slip	Free Surface Level	Free Surface Level
Top	Pressure Outlet	Pressure Outlet	Pressure Outlet
	Free Surface Level	Free Surface Level	Free Surface Level
Bottom	Wall	Wall	Wall
	Free Slip	Free Slip	Free Slip
Portside and Starboard	Wall	Pressure Outlet	Wall
	Free Slip	Free Surface Level	Free Slip
Ship and Moonpool	Wall	Wall	Wall
	No Slip	No Slip 6 DoF Rigid Body	No Slip

When defining a *Pressure Outlet* condition with *Free Surface Level* method, there is a need to input the *Free Surface Level* and *Bottom Level*, both in meters from the origin. Then, the pressure profile is calculated automatically based on previous definition of fluid phases, its respective density and also the gravity vector.

The motion of the barge in the *Forced Heave* is a sine motion with height of

$2.5m$ and frequency of $0.536rad/s$, as it is the natural frequency computed in the *Numerical Decay* simulation with the *Medium* size and refinement mesh. In *Fluent* is necessary to create a function in C programming language that is called *User-Defined Function* (UDF) for motion setup. The velocity of the barge in the UDF is given by:

$$v_3 = 0.67\cos(0.536t) \ . \tag{4.1}$$

In the *Numerical Regular Wave with Captive Vessel*, the wave is simulated using the *First Order Airy* with wave height $H = 2.5m$ and wave length $\lambda = 214.43m$. The wave height is based on the same magnitude of the motion inside of moonpool in *Numerical Decay* test and also the motion of the barge in the *Force Heave Oscillation* test. Wave length was chosen based on the theory of short gravity waves (wavelength is short relative to the depth of the water $h_{depth} > \lambda/2$) and also for frequency match with other tests.

$$\omega = \sqrt{gk} = \sqrt{g\frac{2\pi}{\lambda}} = \sqrt{9.81\frac{2\pi}{214.43}} \quad \therefore \quad \omega = 0.536rad/s \ . \tag{4.2}$$

Based on Figure 2.3 and calculating chart parameters for that simulation:

$$\frac{H}{gT^2} = \frac{2.5}{9.81 \cdot 11.72^2} = 0.0019 \quad \& \quad \frac{h_{depth}}{gT^2} = \frac{112}{9.81 \cdot 11.72^2} = 0.083 \ . \tag{4.3}$$

It falls in the Stokes 2^{nd} order region. Despite this, the *First Order Airy* was chosen for a preliminary simplified study.

The *Numerical Beach* condition to suppress numerical reflection near the outlet boundary needs the input of a start and end points that are the limits of the damping zone. It is defined as uni-directional beach with end point in the *Back* surface and the distance to the start point is given in Table 4.9 (Length).

Most of the simulations run in this work used *Laminar Viscous Model*, so no specific boundary condition for turbulence models must be set. The case shown in Section 4.1.3 has better description of turbulent boundary conditions configuration for the specific simulation.

Initial Condition

Initial condition for all simulations is simply a flat free surface with both phases (air and water) at rest. The only difference is for *Numerical Decay* test, that the free surface is with a $h(0) = 3m$ (initial height) inside of moonpool.

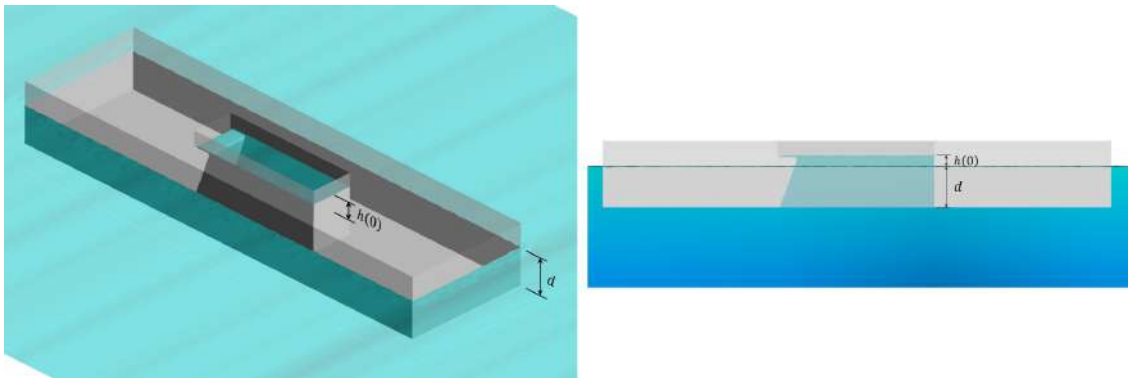

Figure 4.17: Initial condition of *Decay* test.

General Setup

The *solver* needs the input of which equations and how they gonna be solved. These parameters are discussed in more detail in Section 2.2.4. Table 4.10 shows the main parameters set for almost all simulations done in this work. The exception is the *Numerical Regular Wave for Freely Floating Vessel Test*, but more detailed are given in Section 4.2.4.

Fluent solver has both single-precision and double-precision versions and the *double* is chosen seeking for more accuracy in the solution. By default, this solver used in this work stores discrete values of all the scalar at the *cell centers*, including pressure and velocity values, using the same mesh. Then, it uses a *co-located* scheme that require more interpolation but is easier to implement for any unstructured mesh.

All simulation are incompressible, so the *pressure-based solver* is the chosen one for all of them with *segregated algorithm*, as they present low speed and segregated is preferred in this case for a faster overall solution with less computational cost. Coupling algorithm PISO is preferred as it is highly recommended for all transient flow calculations [14].

As discussed in Section 4.1.3, κ-ω *SST* was chosen for a comparison with *Laminar*. All simulations, besides the comparison one, was run using *Laminar* flow setup, as long as it was shown that this provides similar results with less equations to be solved.

Concerning the pressure interpolation scheme, either the PRESTO! or body force weighted schemes should be used and only these schemes are made available in *Fluent* solver when VOF multiphase model is set.

Table 4.10: Physical modeling general setup.

Solver precision		Double precision
Node definition		Cell-centered method
Grid arrangement		Co-located
Solver formulation		Pressure-based - Segregated algorithm
Coupling algorithm		PISO
Turbulence model		Laminar / SST
Pressure interpolation scheme		Body Force Weighted
Discretization scheme	**Momentum**	Second order upwind
	Turbulent Kinetic Energy	Second order upwind
	Specific Dissipation Rate	Second order upwind
Gradient Computation		Least Squares Cell-Based
Multiphase model		Volume of Fluid (VOF)
Interpolation near the interface		Compressive Scheme
Time model		Unsteady
Time step		Fixed - 0.01 s
Simulation time		10000 Time Steps - 100.0 s
Temporal discretization		Second order implicit
Linear system solution		Gauss-Seidel - Algebraic Multigrid (AMG)
Convergence criteria		Maximum iteration per time step - 50 *or* Maximum RMS for all equations - 10^{-3}
Motion		Fixed / Heave oscillation
Reference pressure		1 atm (at free surface level)
Gravity (Z Axis)		$-9.81\ [m/s^2]$

Fluid	**Density** $[kg/m^3]$	**Dynamic viscosity** $[kg/m.s]$
Air	1.18	1.855×10^{-5}
Water	997.28	8.9×10^{-4}

According to ANSYS, VOF cases where body forces dominate and the mesh deviates largely from orthogonality, the *Body Force Weighted* scheme is more robust. Not much information can be found about this scheme in literature.

For spatial discretization schemes, when the flow is not aligned with the mesh, first order convective discretization increases the numerical discretization error (numerical diffusion). In a unstructured mesh with tetrahedral elements the flow is never aligned with the mesh, so generally more accurate results are obtained using the *second order* discretization. QUICK scheme is only used for quadrilateral and hexahedral cells and second-order upwind discretization will be applied to all other cells while MUSCL may be used in all cells, however, in general second-order scheme is sufficient and the higher order scheme will not provide significant improvements in accuracy [14].

Least Squares gradient method has good accuracy in irregular unstructured meshes and is less expensive to compute than the node-based gradient [31].

Multiphase setup, as discussed in Section 2.2.5, for the purpose of simulations in this work the recommended technique is the *Volume of Fluid*. Considering the interpolation near the interface, in Fluent solver, only two options are available for representation of a sharp interface in a implicit formulation, that are the *modified HRIC* and the *Compressive* scheme. The latter, together with the temporal discretization chosen, provides good accuracy with a great sharp interface. It was the one chosen due that.

Time model is *unsteady*, as the evolution in time is important, with a fixed time step of $0.01s$ and enough number of time steps for $100.0s$ of simulation. The temporal discretization is implicit as the fine elements close to moonpool would require a very small time step to use explicit scheme, because of its stability condition of Courant number below 1. The First Order Implicit formulation is sufficient for most problems but for improved accuracy, *Second Order Implicit* is recommended. Bounded Second Order Implicit provides same accuracy, but would provide better stability, anyway, all solutions converged using the unbounded second order scheme.

Linear system is solved using *Gauss-Seidel*, a point implicit linear equation solver in conjunction with an *Algebraic Multigrid (AMG)* method. This multigrid method is particularly attractive for use on unstructured meshes.

Convergence criteria should obey at least one of two requirements, firstly all scaled residuals should decrease lower than 10^{-3} (ANSYS, INC. [14] states that the default convergence criterion is sufficient for most problems), if that does not happen before 50 iterations, then this time step is over due maximum iterations per time step limit. It is also set a *report interval* configuration, that is the number of iterations that will pass before convergence monitors be analyzed, so at least 2 iterations are needed to confirm convergence in each time step. It also reduce communication and

improve parallel performance.

Fixed condition is used for *Numerical Decay* and *Numerical Regular Wave with Captive Vessel* test. In *Forced Heave* there is body motion with heave oscillation of the ship following Equation (4.1).

Reference pressure is defined at free surface level as $1atm$, the gravity is $9.81m/s^2$ and the density and dynamic viscosity of air and water phases are shown also in Table 4.10.

Relaxation factors (Section 2.2.4) used in all simulations are presented in Table 4.11 below.

Table 4.11: Solution controls with relaxation factors.

	Decay	**Forced Heave**	**Captive Vessel**
Pressure	0.3	0.5	0.7
Density	1.0	0.8	1.0
Body Forces	1.0	0.8	1.0
Momentum	0.7	0.3	0.3
Volume Fraction	0.5	0.5	0.5
Turbulent Kinetic Energy	0.8	-	-
Specific Dissipation Rate	0.8	-	-
Turbulent Viscosity	1.0	-	-

In the solver manual, it is stated the for most flows, the default under-relaxation factors do not usually require modification [14], and only if it is observed unstable or divergent behavior that the user need to perform changes. Anyway, to guarantee a faster solution, some values variation could be implemented with a stability analysis.

Data exportation was done every other 10 time steps, i.e. every $0.1s$ simulated a file with transient result was stored.

4.2 Water Motions Inside of Moonpool

4.2.1 Numerical Decay Test

Two geometries are used for the decay analysis. Both are different moonpool profiles in the same barge dimensions. One is the *cutout geometry* (Figure 4.1), and the domain analyzed at this section is the *Medium* one created for the *default moonpool* presented in Section 4.1.1. Another geometry is a barge that presents a cutout angle as a right angle ($\alpha = 90°$). It is called hereafter as *no cutout* geometry and it is shown in Figure 4.18. The length of the moonpool in this latter geometry is based on the length of *default moonpool* in the free surface level. The motivation to

simulate this other design is to analyze the difference of the decay behavior due the presence of the cutout angle. It is presumed that the cutout angle would produce more horizontal motions and the decay test will present characteristics of *piston mode* and *sloshing mode* simultaneously.

Domain used for *no cutout* has same dimensions of *Medium* domain (Table 4.1) and mesh is based on the specifications used for the *Medium* mesh. Table 4.12 shows the quantity of each element in mesh.

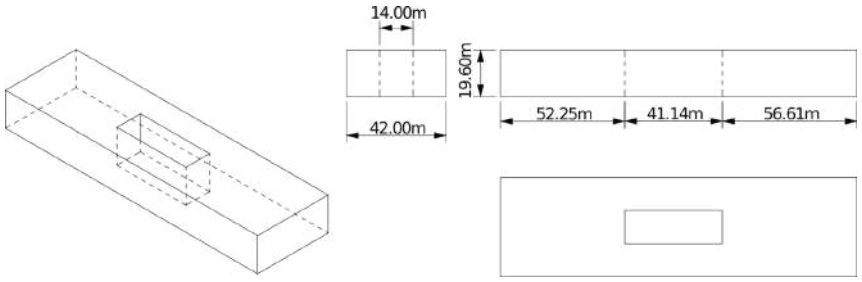

Figure 4.18: Design of the barge for CFD tests with *no cutout moonpool*.

Table 4.12: Properties of grid for *no cutout* moonpool.

	No Cutout
Hexahedron	333376
Tetrahedron	368316
Prism	271800
Representative cell size	2.86
Number of Elements	973492

Mesh is shown in Figure 4.19 and is pretty similar to the Figure 4.9 used for the default moonpool.

For means of comparison also, the Figure 4.20 shows elements volume in the half-domain plane, as it is shown for the default moonpool in Figure 4.10.

Wave probes are displayed with same distribution in the no cutout geometry considering the constant length of the moonpool itself, as it is shown in Figure 4.21.

As done in other previous analysis (Sections 4.1.1 to 4.1.3), the logarithmic decrement method was used to calculate the linearized damping inside no cutout moonpool, based on the result of the wave probes in decay test, and the results in comparison with the default moonpool is shown in Table 4.13.

According to CFD results shown in Table 4.13, the no cutout geometry has more damping, probably due the increase in vortex shedding at the other right angle edge at trailing edge.

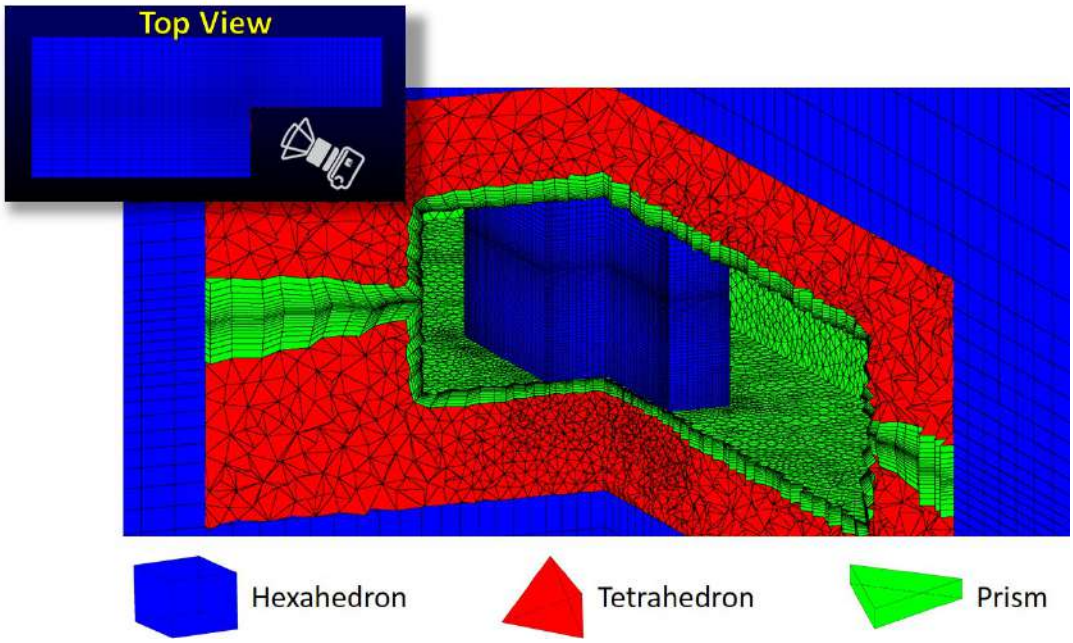

Figure 4.19: Mesh elements for no cutout moonpool.

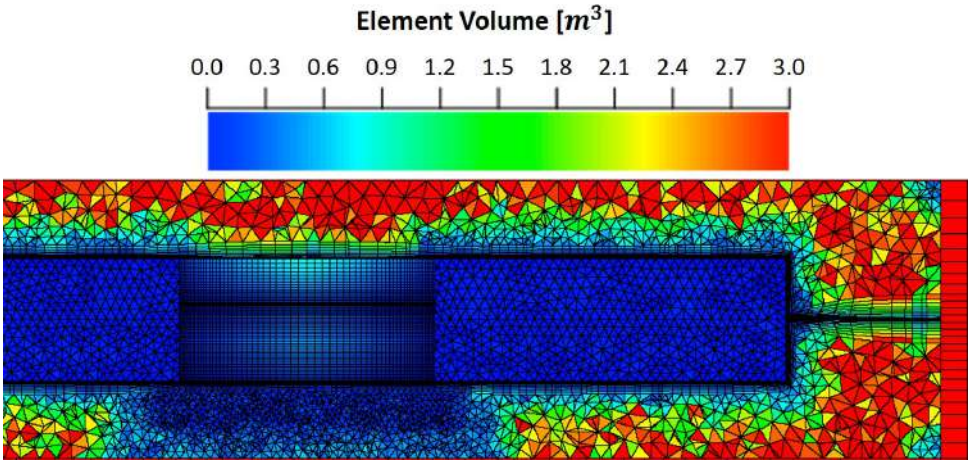

Figure 4.20: Volume size of elements close to moonpool for no cutout moonpool (Side view - $Y = 0.0$).

A new attempt of using the PQ analysis to calculate the linear and quadratic damping specific for the no cutout geometry was done and once again some negative damping values appeared. Then, just the logarithmic decrement procedure is implemented.

Another approach that is interesting now, is to use the analytical Equations (3.12) to (3.14) from energy conservation, for the calculation of the frequency and added mass based on each moonpool geometry. Then, for the cutout geometry,

$$\begin{aligned} \omega_n &= 0.666 rad/s\,,\ B_{Crit} = 1.79 \times 10^7 kNs/m\,, \\ M + M_a &= 1.38 \times 10^7 kg\,,\ M_a = 7.75 \times 10^6 kg\,. \end{aligned} \tag{4.4}$$

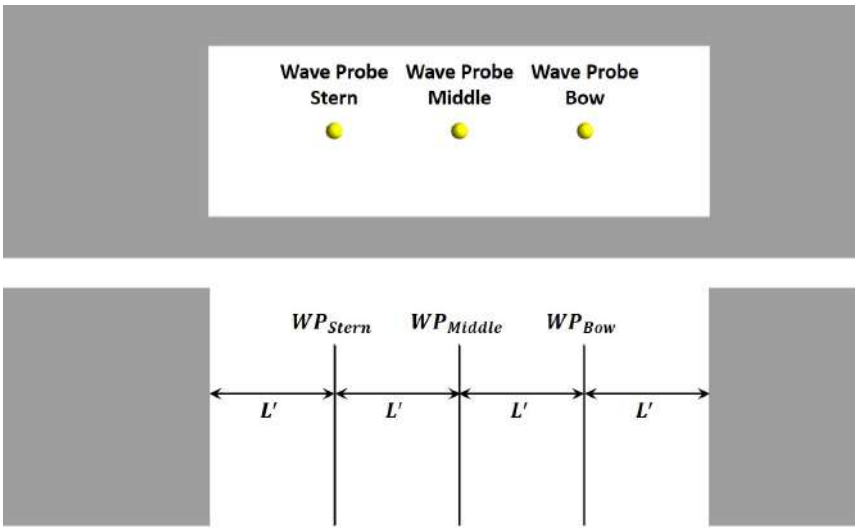

Figure 4.21: Locations of probes in the *no cutout* moonpool (CFD) - $L' = 10.286m$

Table 4.13: Hydrodynamic coefficients for cutout analysis.

	ω_n $[rad/s]$	M_a $[kg]$	B_{eq} $[kNs/m]$	B_{Crit} $[kNs/m]$
Cutout	0.536	1.271×10^7	8.833×10^5	2.162×10^7
No cutout	0.526	1.388×10^7	1.017×10^6	2.204×10^7

And for the no cutout,

$$\begin{aligned} &\omega_n = 0.649 rad/s\,,\ B_{Crit} = 1.78 \times 10^7 kNs/m\,, \\ &M + M_a = 1.37 \times 10^7 kg\,,\ M_a = 6.66 \times 10^6 kg\,. \end{aligned} \tag{4.5}$$

There is a big difference between the frequency calculated in CFD and by energy conservation. Despite the conservation formula do not take viscous damping into consideration and in numerical result the damped frequency ω_d is calculated, the difference imposes a damping ratio $\eta \approx 0.6$ (Equation (3.7)), that is very high for a naked moonpool.

Considering also previous works formulas for calculation of the resonant frequency of the water motion in moonpool, presented in Section 1.4.2, and the formula purposed for the rectangular moonpool (Equation (3.3)), we can perceive that it is hard to calculate it analytically. These analytical frequency results are shown in Table 4.14 below.

The previous works formulas do not take in consideration the cutout angle, so they give the same natural frequency for both geometries used at this work, as the length at free surface level is also the same for both. The formula purposed at this work, presented in Equation (3.3), depends on the added mass of the system, then it is possible to calculate the cutout and the results in Equations (4.4) and (4.5),

Table 4.14: Analytical calculation of natural frequencies according to previous works (Section 1.4.2).

	ω_0 Piston Mode $[rad/s]$		ω_1 First Sloshing Mode $[rad/s]$
Faltinsen (Eq.1.1)	0.904		-
Fukuda (Eq.1.2)	0.670		-
Newman (Eq.1.5)	0.865		1.224
Madhani (Eq.1.7)	-		1.477
Molin (Eq.1.8 and Eq.1.10)	0.793		0.803
Machado (Eq.3.3)	Cutout	No cutout	-
	0.625	0.649	

from energy conservation law, was used.

Then, for that purpose of natural frequency calculation, besides counting the peaks's time distance, the experimental data in *time domain* may be displayed in *frequency domain*, sometimes called the *frequency spectrum*, and it allows the visualization a waveform according to its frequency content. Using *Fast Fourier Transform* (FFT), Figure 4.22 is plotted for the cutout and no cutout geometry.

It is possible to observe that for the cutout moonpool there are 3 peaks regions with $\omega_0 \approx 0.5 rad/s$, $\omega_1 \approx 0.61 rad/s$ and $\omega_2 \approx 0.83 rad/s$ while for the no cutout it presents a small range of frequency with high magnitude and peak at $\omega_0 \approx 0.553 rad/s$. It is also noticeable a slightly higher difference among wave probes results in the moonpool with cutout angle due to its asymmetry.

Also, we may notice from Table 4.13 that the $B_{eq} \approx 5\%\ B_{Crit}$ and that B_{Crit} may be calculated using Equations (3.4) and (3.14) depending only of the moonpool profile particulars. That result will be used forward when analyzing the artificial damping for the potential theory calculations.

4.2.2 Numerical Forced Heave Oscillation Test

This simulation require motion of the vessel in the mesh and that may be performed better with a different mesh than the one shown for the decay test (Figure 4.9), and it is presented in Figure 4.23. The ship is considered a rigid body together with the prismatic layer, so they move in conjunction and only tetrahedra elements deforms. Just the forces in the ship wall are considered for the calculation of ship's motion. Due to this configuration that the prismatic layer around the vessel and the hexahedra elements inside the moonpool could not be used for better resolution. Quantity of each different element are presented in Table 4.15.

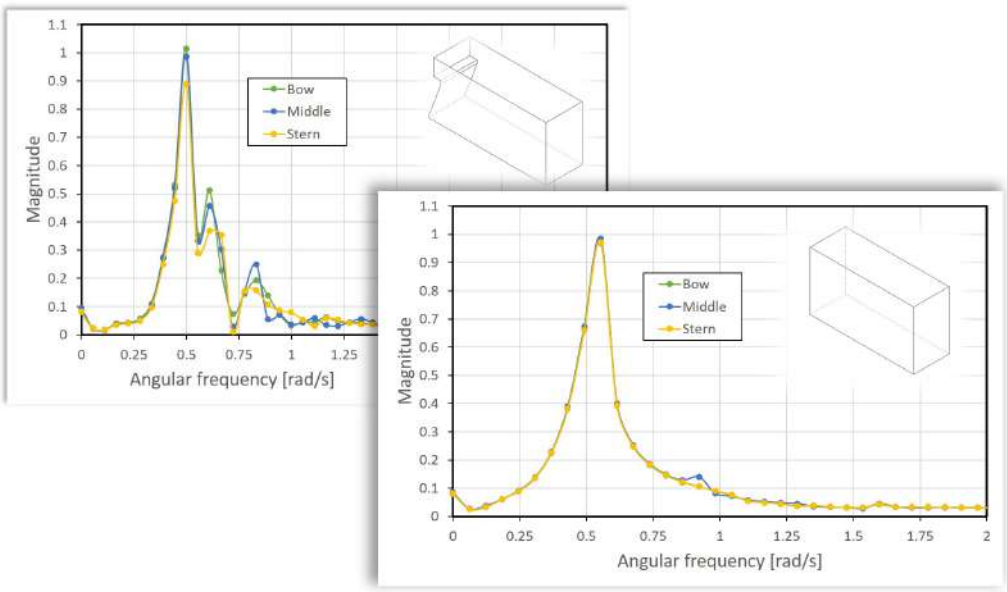

Figure 4.22: Decay data in frequency domain.

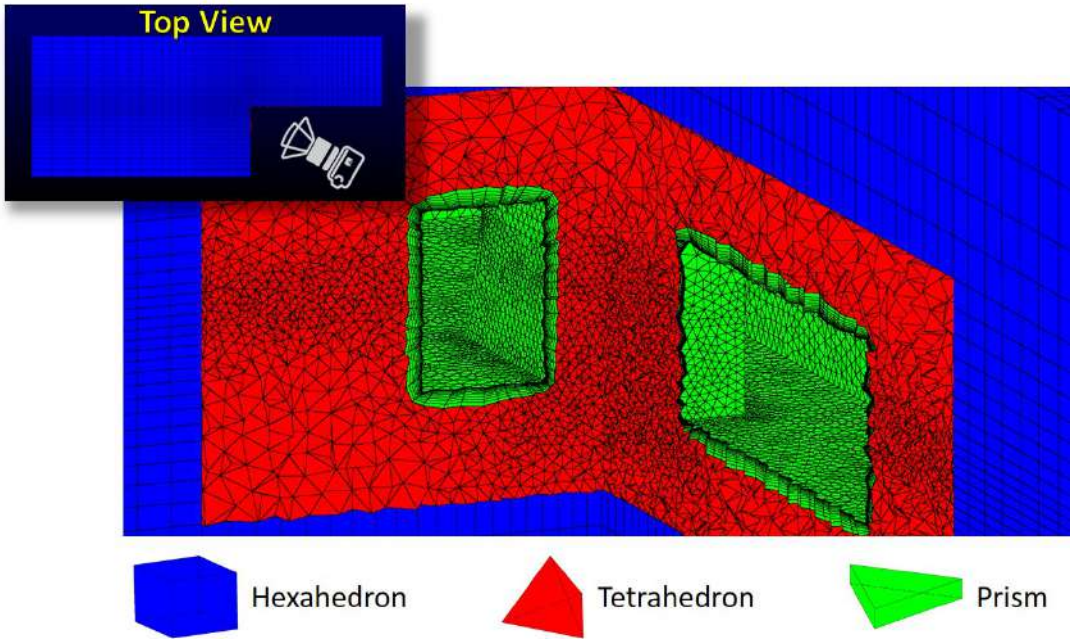

Figure 4.23: Mesh elements for forced heave oscillation test.

The elements size inside the mesh was created obeying the same proportion of the *Medium* mesh used in decay as they already passed through the whole verification process. For a comparison it is shown in Figure 4.24 the element volume close to the moonpool.

The oscillation of the ship was already explained in Section 4.1.4 and given by Equation (4.1).

Three wave probes were added inside moonpool (Figure 4.4) to measure absolute water motion inside moonpool. Starting at rest at time $t = 0$ it is possible to see

Table 4.15: Properties of grid for forced heave oscillation test.

	Forced
Hexahedron	200024
Tetrahedron	1270975
Prism	262000
Representative cell size	2.36
Number of Elements	1732999

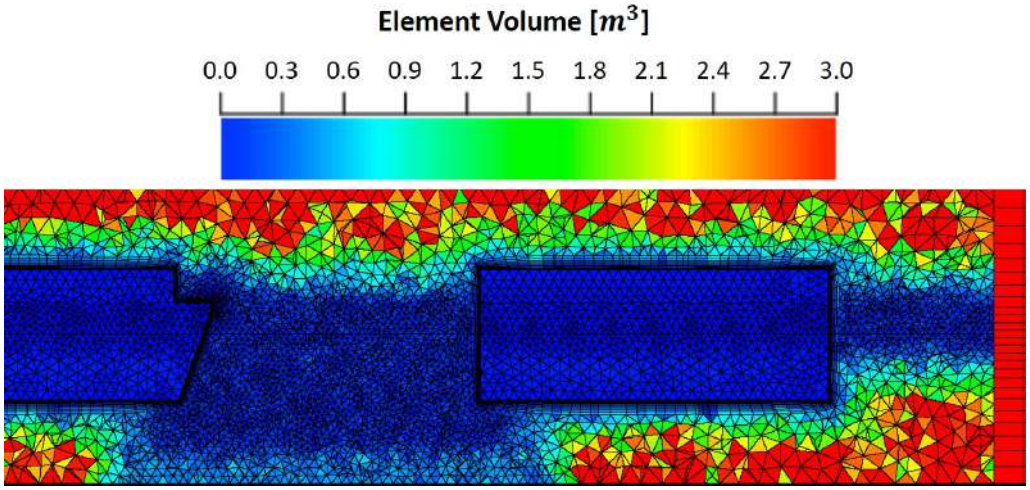

Figure 4.24: Volume size of elements close to moonpool for forced heave oscillation test (Side view - $Y = 0.0$).

in Figure 4.25 that as the ship moves the water motion starts to be excited in a counter phase behavior but then it shifts to an almost in phase configuration.

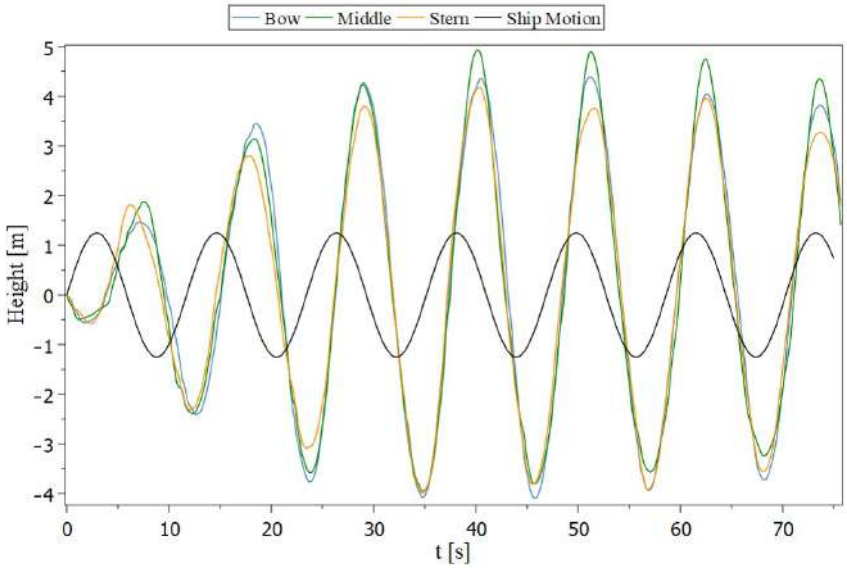

Figure 4.25: Time trace of each wave probe and ship motion in the forced test.

The relative motion of the water inside moonpool may be easily calculated by the

difference and it is shown in Figure 4.26. We can see that the relative amplitude of motion reduces as the absolute water motion and the ship decrease the phase value in between. The cutout wall may be seen as wedge wave-maker inducing sloshing motion as the vessel heaves up and down. Probably with more simulation time would be possible to analyze properly this behavior.

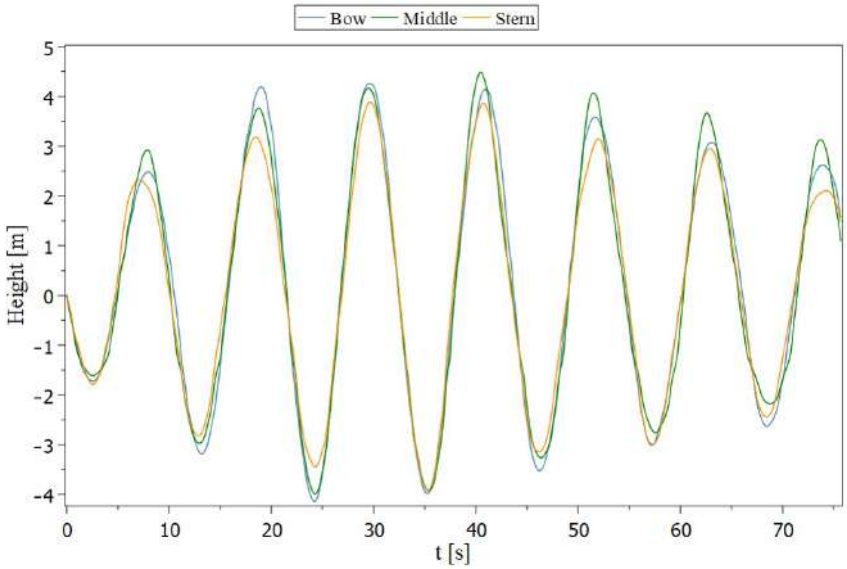

Figure 4.26: Time trace of relative water motion inside moonpool in forced test.

Then it is possible to calculate the period of the water motion inside moonpool by the peak difference and then the angular frequencies are $\omega_{bow} = 0.570 rad/s$, $\omega_{middle} = 0.573 rad/s$ and $\omega_{stern} = 0.561 rad/s$, remembering that ships motion frequency is $\omega_{ship} = 0.536 rad/s$.

Also, a FFT is computed for this relative motion signal and is plotted in Figure 4.27 below,

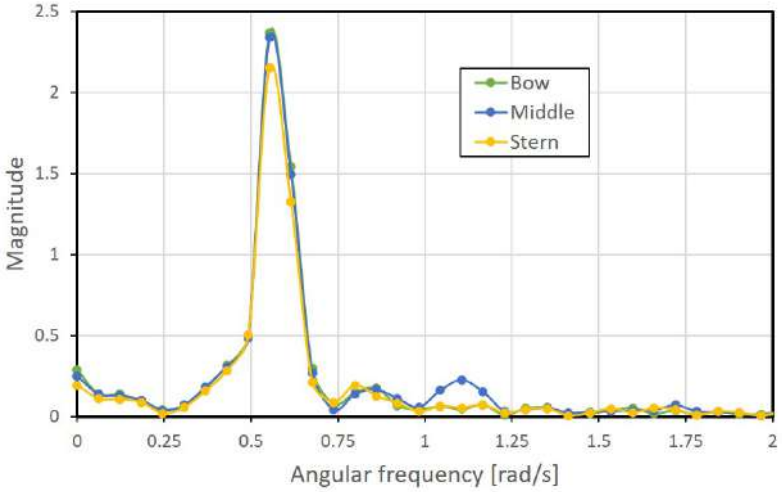

Figure 4.27: Forced data in frequency domain.

The frequency with higher magnitude is $\omega_0 \approx 0.553 rad/s$ and different from the moonpool decay, no other frequency has reasonable magnitude.

4.2.3 Numerical Regular Wave with Captive Vessel Test

This simulation use the exactly same *Medium* domain (Figure 4.3) and the *Medium* mesh (Figure 4.10) refinement used in the decay test. As it started in a flat free surface level, took a longer time for the wave encounter the vessel. A wave with angular frequency $\omega = 0.536 rad/s$ based in the natural frequency calculated in Section 4.2.1 and wave height $H = 2.5m$ was set. Using a wave probe at inlet is possible to compare the numerical wave with the analytical in Figure 4.28.

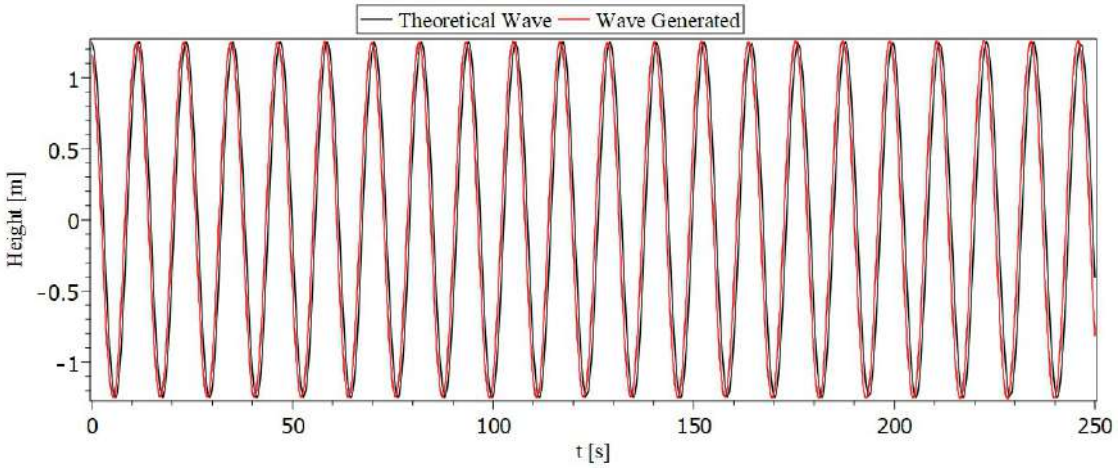

Figure 4.28: Numerical and theoretical wave at domain's inlet.

Proofing that the configuration was set properly for the right analytical wave generation. However, as long as the initial condition is a flat free surface level, a 90° phase should have been added at inlet to start the generation from the same condition. Probably it would give more stability to the solution at the beginning converging faster the first time steps.

Considering also the same position of the three wave probes and same nomenclature use for them (Figure 4.4), the data gathered from each is presented in Figure 4.29.

There is a transient region, but after $200s$ the wave amplitude inside moonpool tends to get an average value of $3.457m$ with slight variation in the subsequently periods. Then, inside moonpool there is an increase of 2.766 (= 3.457/1.25) of inlet wave amplitude. Angular frequency analyzing peaks is $\omega \approx 0.54 rad/s$ for all probes.

Using wave probes outside the vessel as shown in Figure 4.30, we can notice that the wave is disturbed by the body and do not have constant amplitude anymore (blockage effects may also be the reason, but domain size variation would be required for more proper analysis of the real variation concerning this issue).

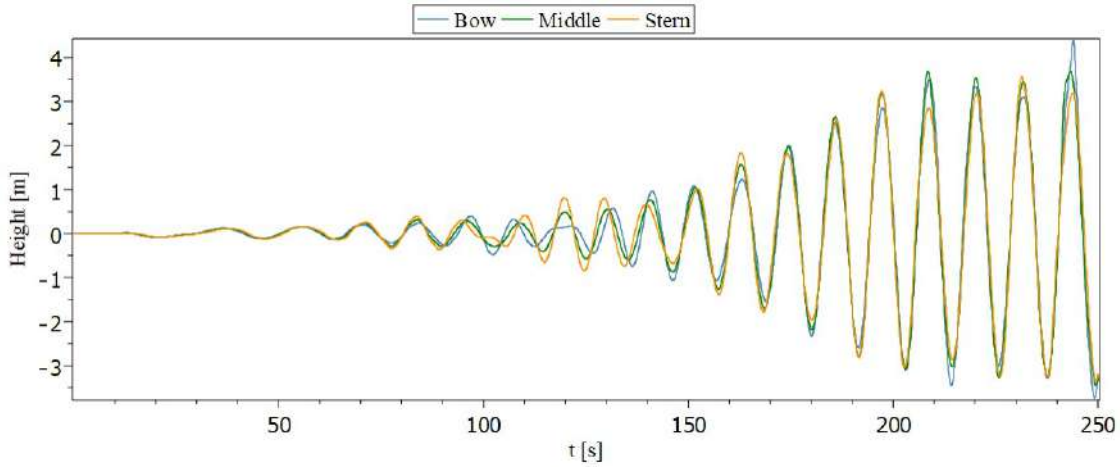

Figure 4.29: Time trace of each wave probe in the regular wave test.

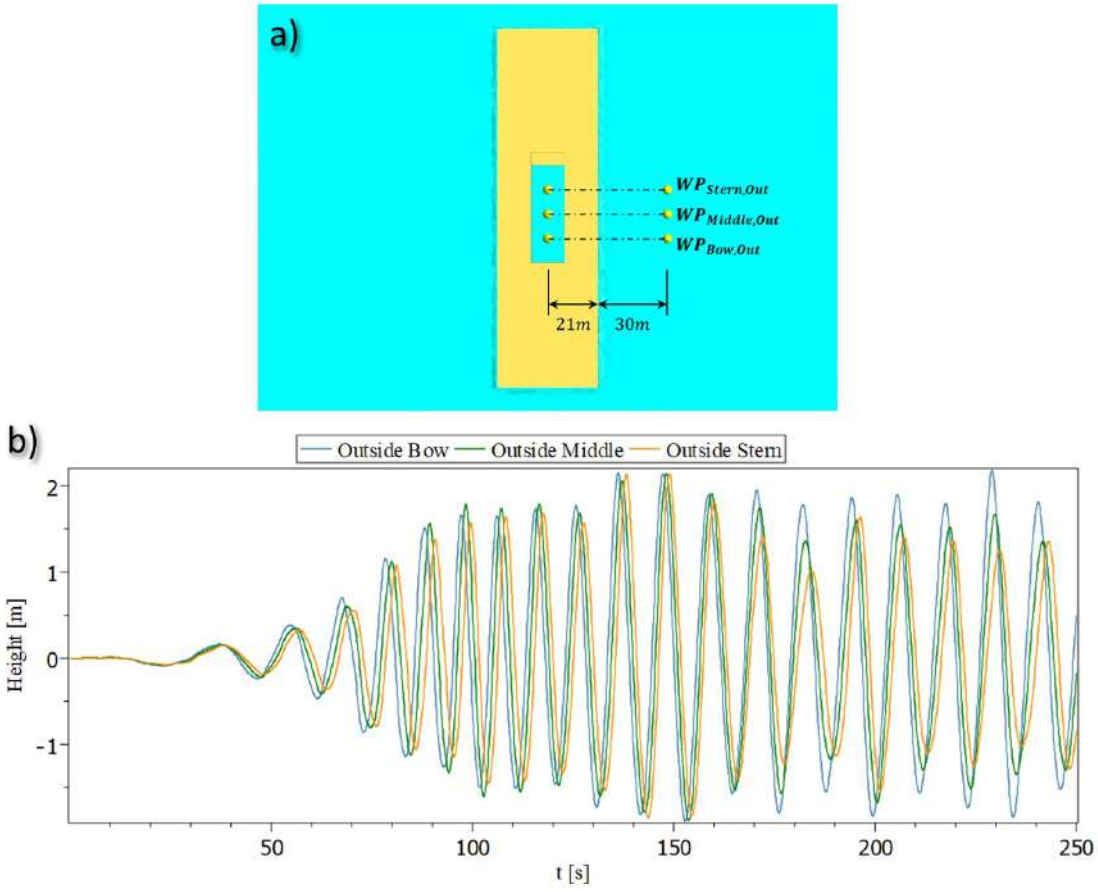

Figure 4.30: *a)* Position of wave probes outside barge and *b)* Time trace of outside wave in the regular wave test.

Considering also the wave data after $t = 200s$, the average amplitude of the wave around the barge is $1.6m$ and angular frequencies are $\omega_{bow} = 0.539rad/s$, $\omega_{middle} = 0.532rad/s$ and $\omega_{stern} = 0.527rad/s$

To proceed with a FFT in the wave inside moonpool (Figure 4.29) and outside (Figure 4.30), the number of data points operated on must be a number that is a

power of two, so as the time step is $0.1s$ and the more important range of data are the last time steps, it was excluded all data before $t = 147.6s\,(= 250.0 - 2^{10} \cdot 0.1)$. Results are shown in Figure 4.31 and it is observable that the most prominent angular frequency inside and outside moonpool is $\omega = 0.552rad/s$ for all three probes.

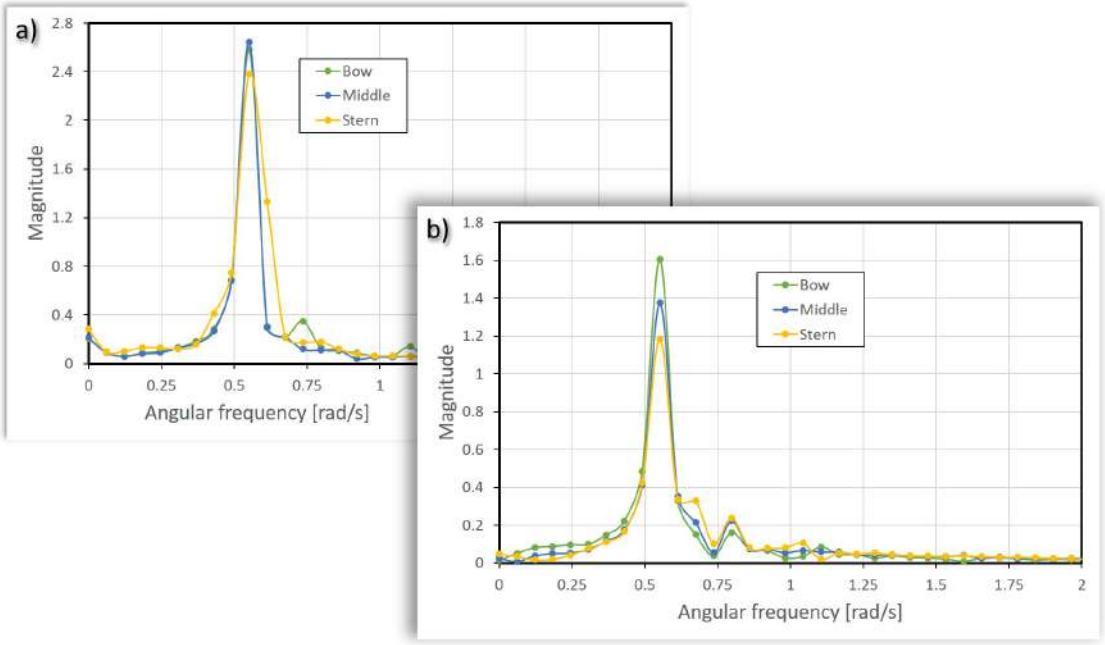

Figure 4.31: Captive vessel data in frequency domain. *a)* Wave signal inside moonpool and *b)* outside barge

4.2.4 Numerical Regular Wave for Freely Floating Vessel Test

Different from previous simulations, this simulations considers the model scale of *fKN1* (Figure 1.9) and *fKN2* (Figure 1.11). The possibility of a experimental result for validation led the work to this analysis. Due to that difference of geometry and scale, other domain, mesh and setup are discussed here also before the results.

Domain

Only one domain size was created and used for both ship geometries. The domain is shown in Figure 4.32 and in this case the symmetry condition was used, so the domain is exactly what is presented.

In Table 4.16 the main particulars of domains and ships in model scale are presented.

Table 4.16: Main particulars of models *fKN1* and *fKN2* and dimensions of domains generated as function of ship $L_{OA,model}$.

Description	Symbol	Magnitude	Unit
Length Overall	$L_{OA,model}$	1.476	m
Length between Perpendiculars	$L_{PP,model}$	1.391	m
Breadth Moulded	B_{model}	0.256	m
Depth Moulded	D_{model}	0.120	m
Design Draft	d_{model}	0.061	m
Longitudinal CoG	LCG_{model}	0.7031	m
Transversal CoG	TCG_{model}	0.0	m
Vertical CoG	VCG_{model}	0.0664	m
Weight displacement	$\Delta_{fKN1,model}$	17.820	kg
Volume displacement	$\nabla_{fKN1,model}$	0.018	m^3
Gy-radius around X axis	$K_{xx,model}$	0.104	m
Gy-radius around Y axis	$K_{yy,model}$	0.327	m
Gy-radius around Z axis	$K_{zz,model}$	0.329	m
Moonpool's length on bottom	$l_{b,model}$	0.278	m
Moonpool's length on deck	$l_{d,model}$	0.282	m
Moonpool's breadth on bottom	$b_{b,model}$	0.085	m
Moonpool's breadth on deck	$b_{d,model}$	0.085	m
Postion (from transom)	P_{model}	0.568	m
Cutout angle	α_{model}	70.05	$^\circ$
Weight displacement	$\Delta_{fKN2,model}$	17.613	kg
Volume displacement	$\nabla_{fKN2,model}$	0.018	m^3
Gy-radius around X axis	$K_{xx,model}$	0.104	m
Gy-radius around Y axis	$K_{yy,model}$	0.327	m
Gy-radius around Z axis	$K_{zz,model}$	0.329	m

	fKN1	***fKN2***
Fore	2	
Aft	3	
Half Width	1.5	
Depth	2	
Height	2.5	
Number of Elements	1839857	1218032

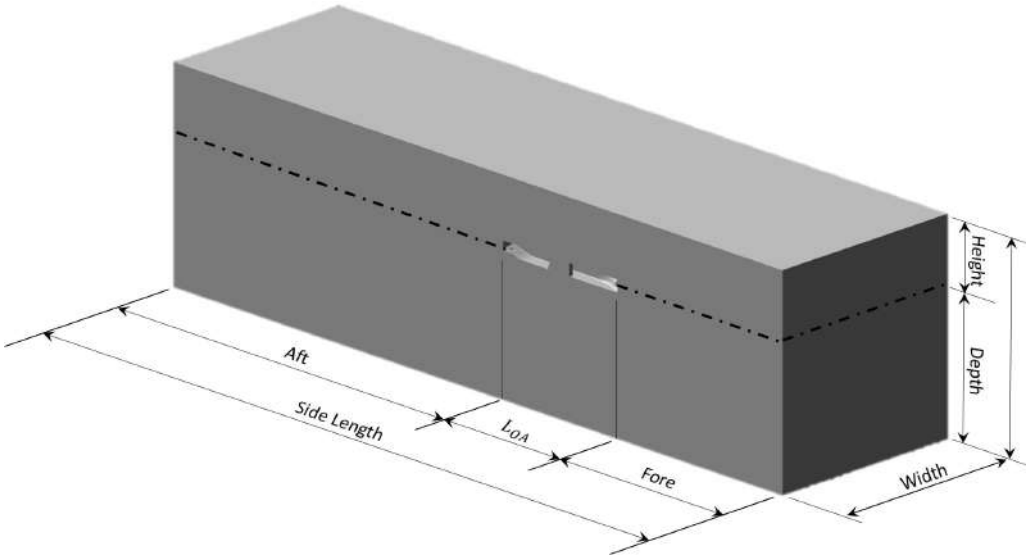

Figure 4.32: Main particulars of domain for freely floating vessel test with model ships.

Reader must be aware that the ship is in an ultra reduced scale (1 : 163.9) and all the measurements done at this Section 4.2.4 is not directly related with the full scale ship (prototype scale) and some extrapolation calculation would be required.

Mesh

Following the same requirements for mesh creation as expressed in Section 4.2.2, as long as there is body motion of the ship, it was created with a prismatic layer for boundary layer calculation and this layer is considered in the motion as a rigid body together with ship, besides forces calculation for the motion are just calculated at ship's wall. Around the ship, there is a box with tetrahedra elements that can be deformed and out of the edges of this box, hexahedra elements are used for discretization of the remainder domain. Then, for clarification purpose, Figure 4.33 shows the mesh elements of *fKN2* ship and Table 4.17 presents the property of each grid created. When comparing the representative cell size with previous simulations, take into consideration the scale difference.

Table 4.17: Properties of grid for freely floating vessel test.

	fKN1	**fKN2**
Hexahedron	774368	205200
Tetrahedron	755419	723082
Prism	310070	289750
Representative cell size	2.676×10^{-2}	3.071×10^{-2}
Number of Elements	1839857	1218032

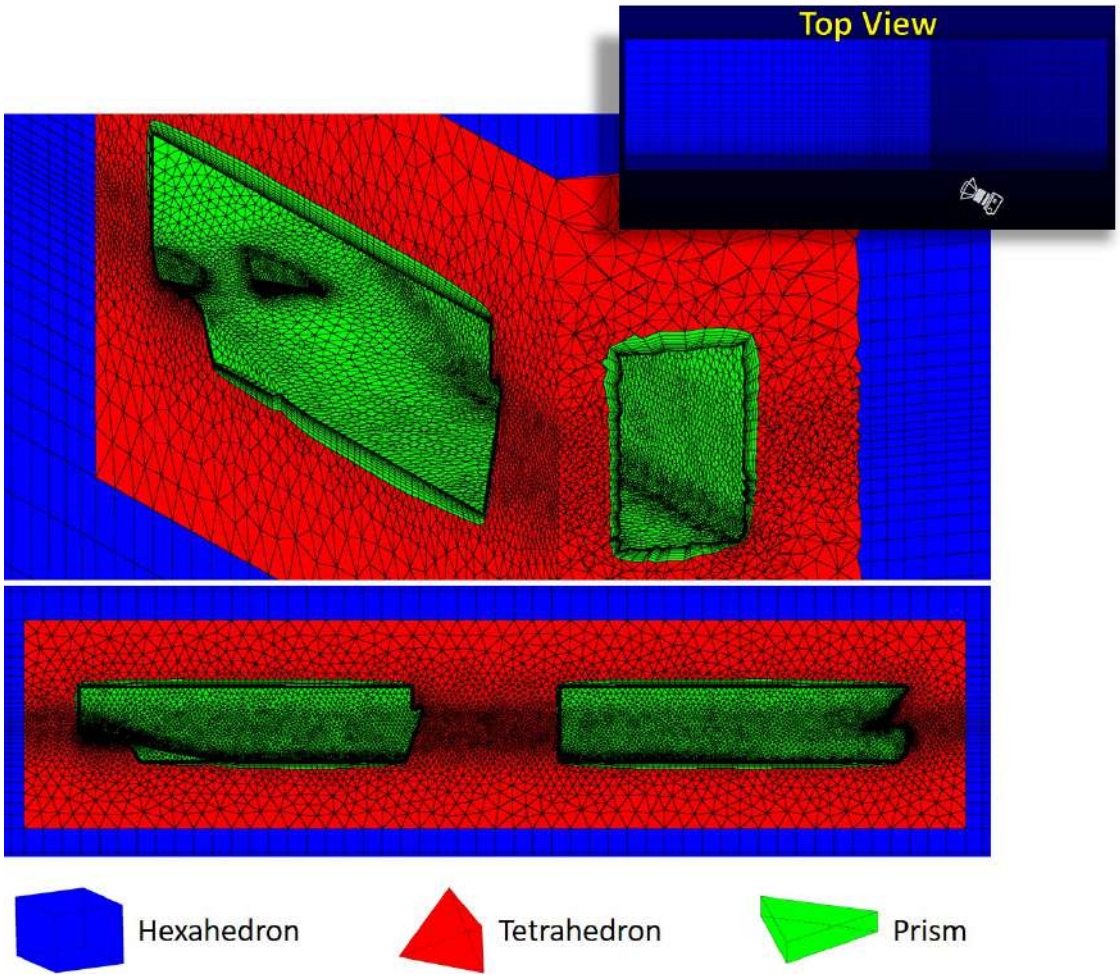

Figure 4.33: Mesh elements for freely floating vessel test.

Due the difference in geometry, some areas had different refinement than the previous simulations, for instance bulbous bow and appendages for retractable thrusters at stern region, and then volume refinement was also done differently. Figure 4.34 give us an idea of mesh distribution and refinement regions.

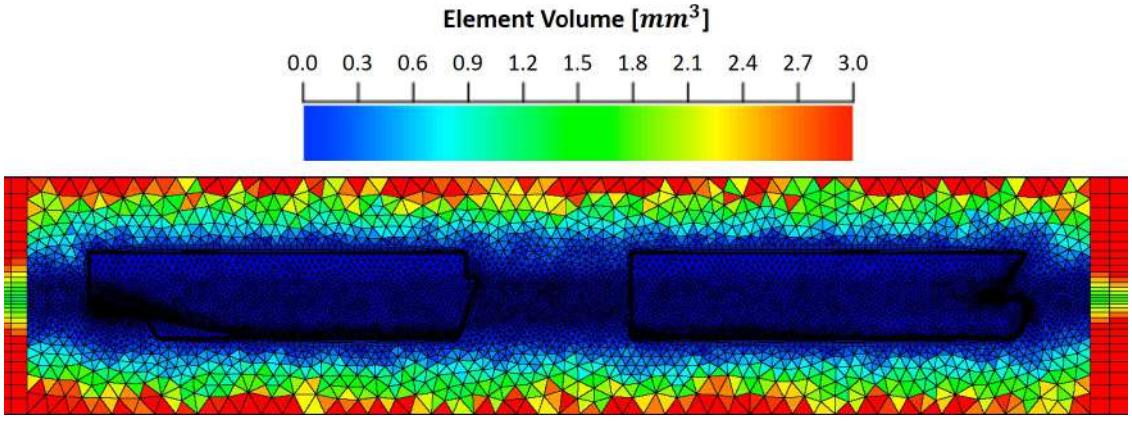

Figure 4.34: Volume size of elements close to moonpool for freely floating vessel test (Symmetry plane view).

Boundary Condition

Boundary conditions are also different as now just half domain is simulated. The only main difference from previously discussed is the symmetry boundary, it has the practical benefit of reducing the size of the computational domain and also to improve the mesh refinement with less elements. This condition assume that the gradients perpendicular to the plane are equal to zero, then, the requirement of symmetry is not related only with geometry but also with the dynamical behavior of flow around the body. That is very reasonable to assume for this simulation that the flow is symmetrical also. The wake pattern produced across the water surface is known as *Kelvin wake* and it was first explained by Lord Kelvin [77] (William Thomson), within the context of linear potential flow theory. There also countless works on this topic in literature showing this symmetry of the wake experimentally [78] and numerically [79].

All defined boundary conditions for this simulation are shown in Figure 4.35 and Table 4.18 presents the setup of each one.

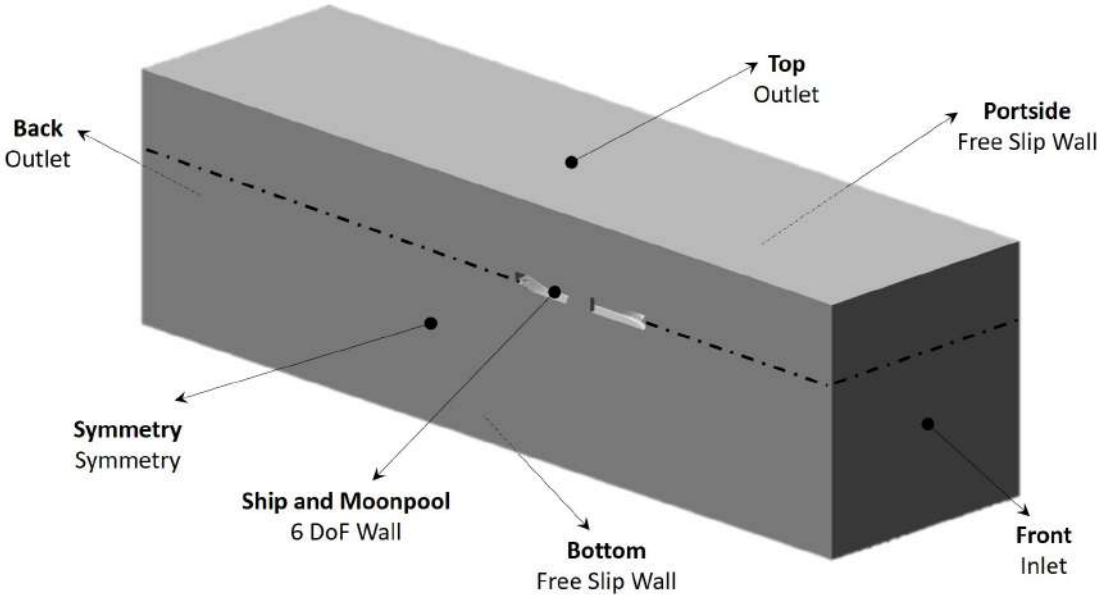

Figure 4.35: Boundary conditions of freely floating vessel simulation.

As done in *Numerical Regular Wave with Captive Vessel* test (Section 4.2.3), the wave was simulated using the *First Order Airy*. At this model scale, wave height is $H_{model} = 4.0cm$ and wave length $\lambda_{model} = 2.00m$. Wave length follows the requirement to use theory of short gravity waves ($h_{depth,model} > \lambda_{model}/2$).

$$\omega = \sqrt{gk} = \sqrt{g\frac{2\pi}{\lambda}} = \sqrt{9.81\frac{2\pi}{2}} \quad \therefore \quad \omega_{model} = 5.55rad/s \; . \tag{4.6}$$

Table 4.18: Boundary conditions for freely floating vessel test.

	fKN1	fKN2
Open Channel Wave BC	✓	
Water Depth	$Depth : 1.461m$	
Numerical Beach	$Length : 2.2m$	
Front	Velocity Inlet	
	First Order Airy Height: $4.0cm$ Length: $2.00m$	
Back and Top	Pressure Outlet	
	Free Surface Level	
Bottom and Portside	Wall	
	Free Slip	
Ship and Moonpool	Wall	
	No Slip 6 DoF Rigid Body	

Based on Figure 2.3 and calculating chart parameters for that simulation:

$$\frac{H}{gT^2} = \frac{0.04}{9.81 \cdot 1.13^2} = 0.0032 \quad \& \quad \frac{h_{depth}}{gT^2} = \frac{1.461}{9.81 \cdot 1.13^2} = 0.117 \, . \tag{4.7}$$

It is also in the Stokes 2^{nd} order region, but once again the *First Order Airy* was chosen for a simplified study.

Initial condition for both ship is the same, flat free surface level at rest with the ship without *trim* (difference between the forward and aft drafts [80]) and without *sinkage* (steady state lowering of a ship's position of flotation in the water [80]).

Setup

General setup is similar to previous discussed for others simulations and is presented in Table 4.10. There are few differences that are shown in Table 4.19 below,

Table 4.19: Physical modeling general setup for freely floating vessel test.

Turbulence model	Laminar
Time model	Unsteady
Time step	Fixed - 0.001 s
Simulation time	20000 Time Steps - 20.0 s
Motion	Two degree of freedom (Pitch and Heave)
Release Time	100 Time Steps - 0.1 s

Ship motion could not be started from the beginning due some numerical instabilities that may cause it to diverge or weird spikes in the motion would appear also by shock effect. It is possible to configure a *release time*, that is the time before calculation of body motion begins, to allow some time for the fluid flow to initialize. In unsteady model, recommendation is to at least wait for more than 10 time steps [47]. It was chosen 100 time steps for both simulation. *Ramp time* is recommended for a more robust solution by reducing oscillation and it is related with the application of forces and moments proportionally during the set interval. It was not used and solution did not diverge neither presented shock effect.

Relaxation factors for both ships are identical to used in *Forced Heave* (Table 4.11) simulation.

For transient results the data was exported every other 100 time steps, what gives $0.1s$ of resolution. Ship's motion resolution is different and is stored every other time step, i.e. at each $0.001s$.

Results

Following same procedure of Section 4.2.3, a wave probe is added at inlet for analysis of undisturbed wave generated into the domain. It is shown in Figure 4.36.

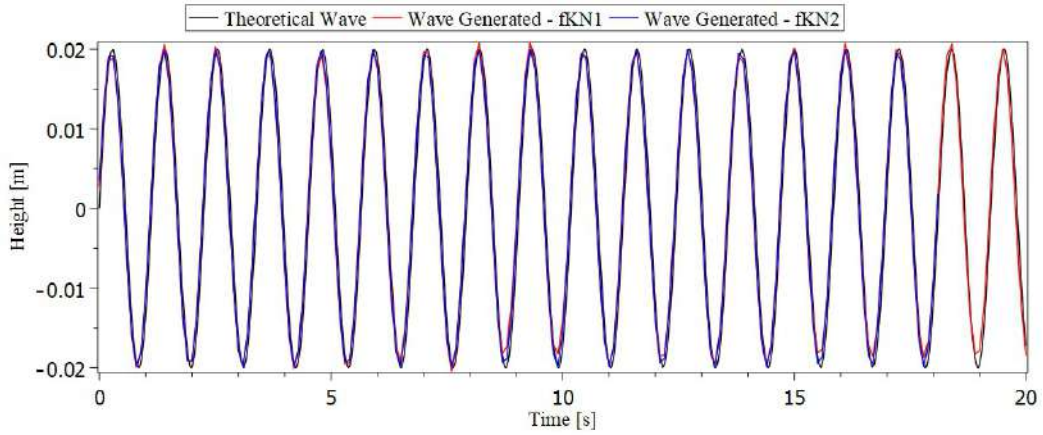

Figure 4.36: Numerical and theoretical wave at domain's inlet for freely floating vessel.

Now the wave phase is adjusted for starting in free surface level at initial condition.

Then, it is possible to also visualize the absolute motion inside the moonpool. Besides it was simulated in model scale, the wave probes are distributed following the same arrangement as all simulations before (Figure 4.4) with $L' = 6.385cm$. Time trace of wave probes are presented below together with *fKN2* motion in heave,

In Figure 4.37 we can observe that after a transient variation from the initial condition, ship and wave heaving inside moonpool are in phase. Then, the relative

motion of water inside moonpool may be calculated and it is shown in Figure 4.38. After $6s$ relative water motion inside moonpool start to oscillate with an almost constant amplitude ($H_{Bow}/2 \approx 0.94cm$, $H_{Middle}/2 \approx 0.88cm$ and $H_{Stern}/2 \approx 0.81cm$) and we can calculate the relation between amplitude inside moonpool and inlet wave amplitude, that is equal to $0.437\,(= 0.875/2.0)$. For the *Numerical Regular Wave for Freely Floating Vessel Test* the same was calculated and we could notice that for the specific frequency it was simulated, and considered captive vessel, the amplitude increased inside moonpool and in this present case, amplitude decreased compared to the wave exciting the motion.

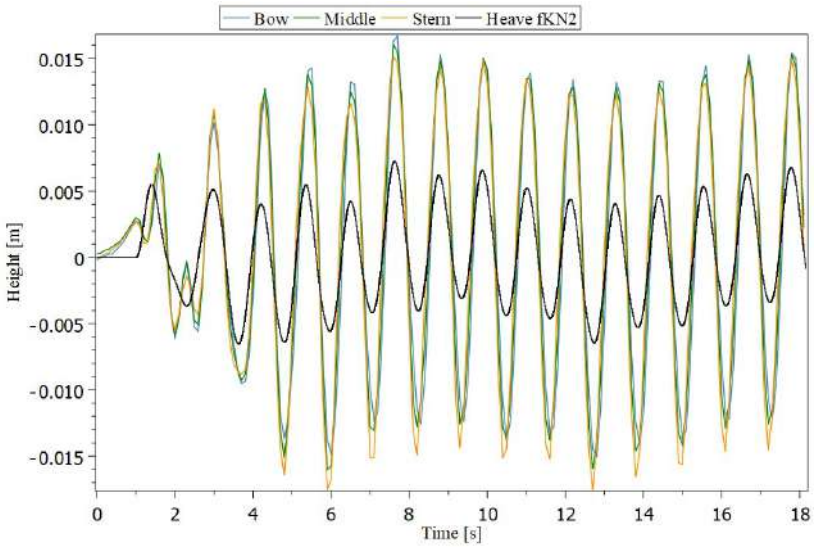

Figure 4.37: Time trace of each wave probe and *fKN2* ship motion in heave.

Calculating angular frequency of ship motion and of water motion oscillation inside moonpool, ate each wave probe, the results are pretty similar and equal to $\omega = 5.59rad/s$.

Concerning the motion of ship, the CoG heave translation motion was tracked and also the rotation in pitch of ship as rigid body. In Figure 4.39 the time trace are shown for the *fKN1* and *fKN2*. It is interesting to notice that the heave motion amplitude as well the pitch rotation are higher in *fKN1*.

Figure 4.40 show the pressure field on the wetted surface of each ship. Besides *fKN2* presents higher pressure gradient, the pressure integration over the area (force) is has greater variation in a period, and that explain the smaller range of motion for *fKN2*. The moonpool, at least for the wave frequency and amplitude set in this simulation, damps the heave and pitch of *fKN1*.

Average trim position of *fKN1* is $\approx 0.55^{\circ}$ and sinkage average is $\approx 4.5mm$, while for *fKN2* these values are $\approx 0.48^{\circ}$ and $\approx 0.4mm$.

Also adding three wave probes outside the ship and at same distance from inlet as the wave probes inside the moonpool, we can conclude at this case that the

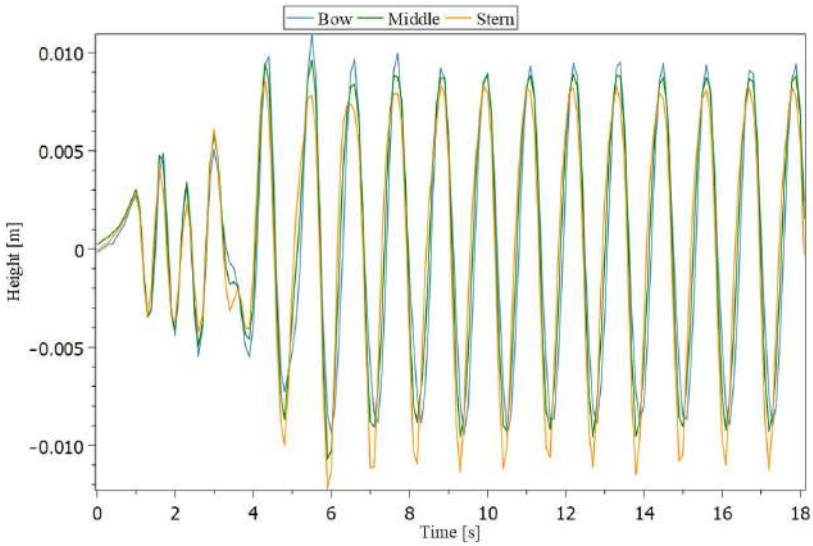

Figure 4.38: Time trace of relative water motion inside *fKN2* moonpool in free floating test.

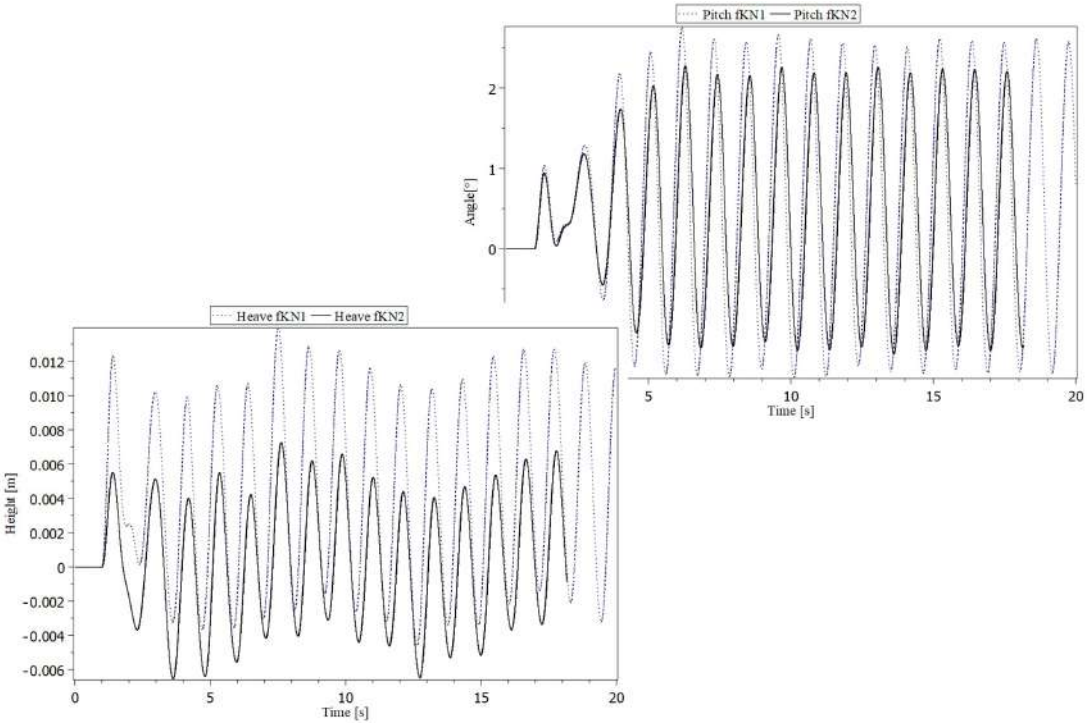

Figure 4.39: Time trace of relative water motion inside *fKN2* moonpool in free floating test.

wave amplitude decrease ($H_{wave,fKN1}/2 \approx 1.8cm$, $H_{wave,fKN2}/2 \approx 1.61cm$), but the phases are kept the same and few disturbances are presented. It is shown in Figure 4.41 the position of wave probes and time traces for each probe and wave generated for *fKN1* and *fKN2*.

Different from the result presented in Figure 4.30 in Section 4.2.3, the lower disturbance of wave around the body, even considering motion of it and consequently

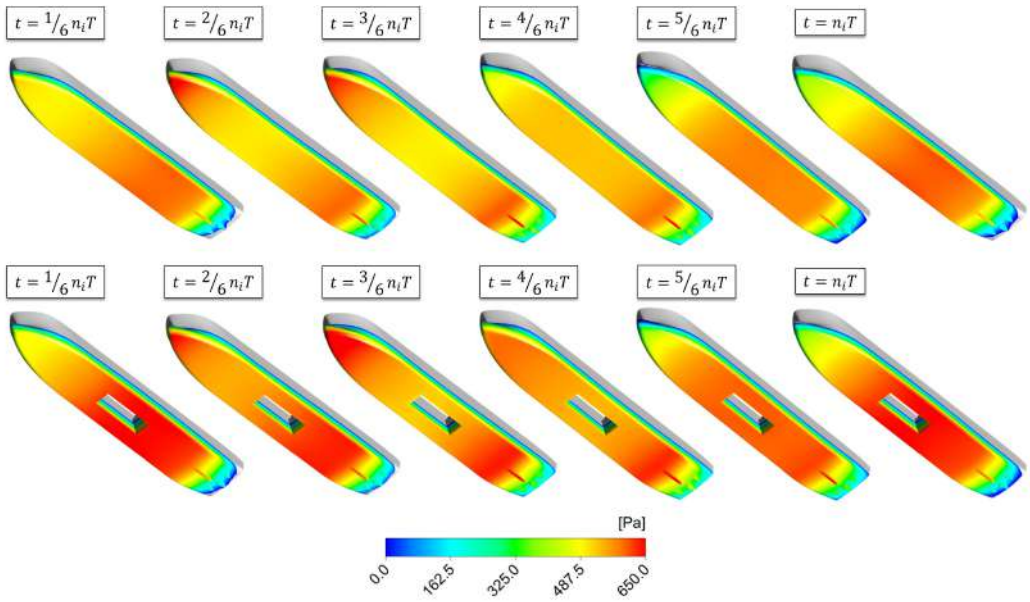

Figure 4.40: One period oscillation variation of pressure field in wetted surface for *fKN1* and *fKN2* in free floating test.

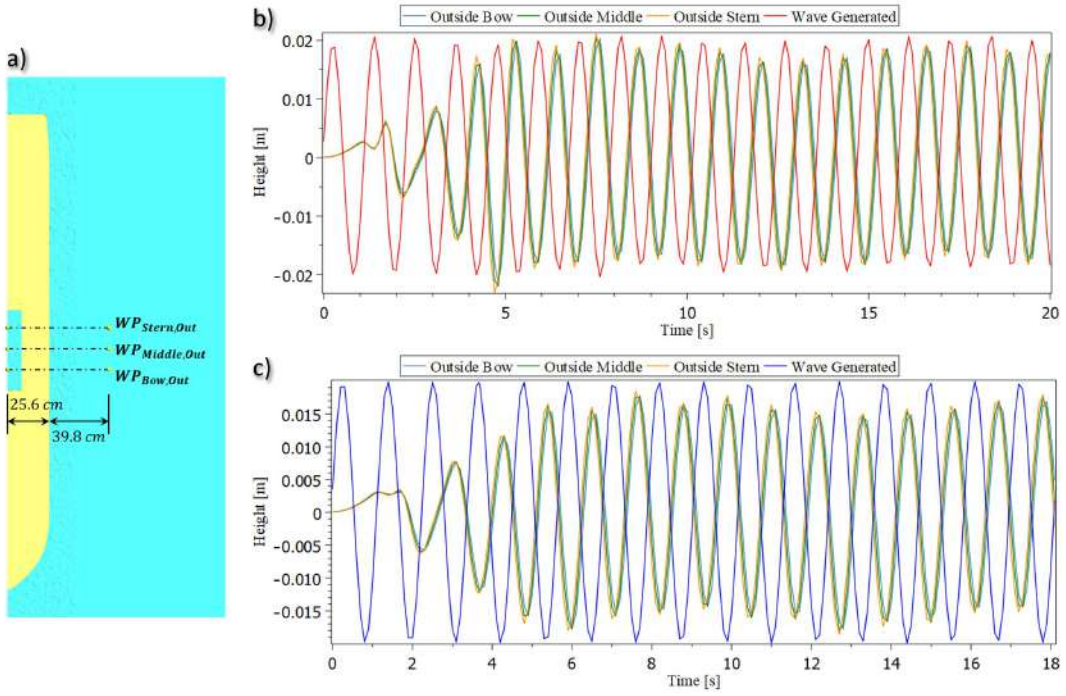

Figure 4.41: *a)* Position of wave probes outside *fKN2* and time trace of outside wave and numerical generated wave at inlet for *b) fKN1* and *c) fKN2*.

the radiation wave generated from it, may be related with the frequency of generated wave and simulation of other frequencies would give more information about its relation.

Finally, for a frequency analysis, the FFT can be calculated for ship motions and water motion inside moonpool. They are all plotted in Figure 4.42

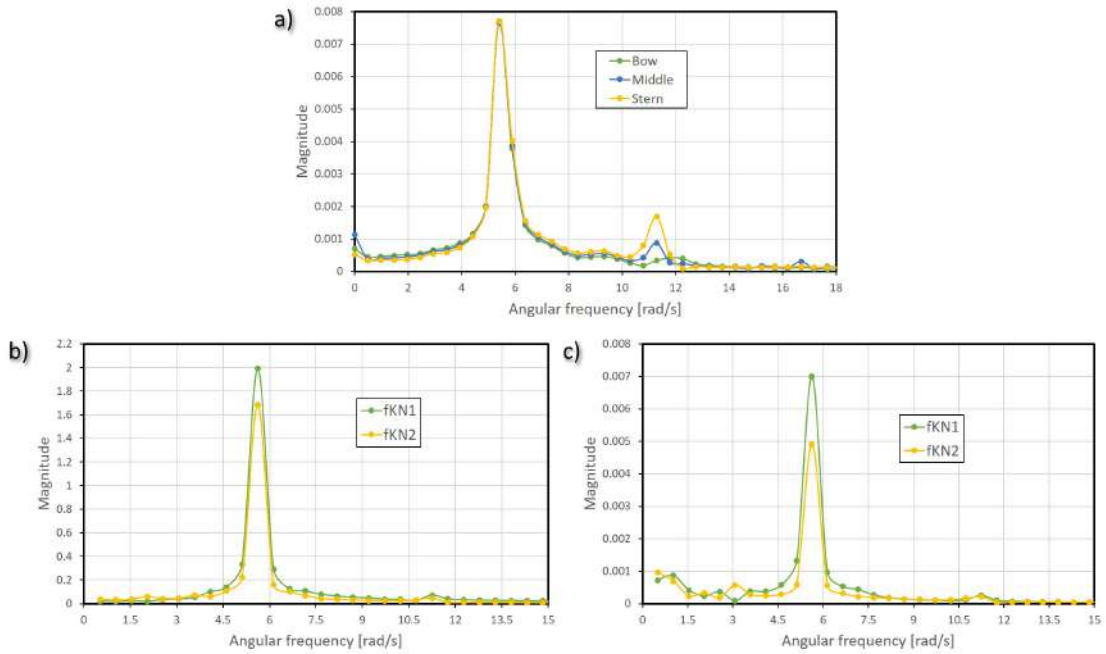

Figure 4.42: Free floating test data in frequency domain. *a)* Water motion inside moonpool, *b)* heave and *c)* pitch

As expected and seen from previous simulation, the prominent frequency inside moonpool is directly related with the exciting frequency. The second small peak is the double value of the wave frequency and also there is smaller peak that is 3 times the same frequency.

On the other hand, have and pitch motion of both ships present the same frequency behavior and the moonpool just changed the amplitude of each motion.

It took approximately 18 days to run each free floating ship simulation in a computer with *Windows 10 Professional* (64 bits), processor Intel®Core™ i7-4790 CPU @ 3.60 GHz, 32 Gb RAM. Depending on simulation, more than 1Tb of hard disk was required to keep storage of all transient results.

These analysis proof us that the CFD is a great tool for studying the water motion inside moonpool and the influence of that in the vessel motion. More complex analysis using this tool would require computational effort beyond available and then the idea to use an also powerful tool came up, that is the potential theory and it will be discussed in next section.

4.3 Potential Theory Setup

Were shown in Sections 4.1 and 4.2 some simulations done using CFD. As aforementioned, although it is a very powerful tool if well used, it require a lot of computational resources, also a lot of cautious, sometimes rerun simulations fixing some

issues, to finally have more confidence in results as commented in Section 2.2.6. When talking about optimization, as the main goal of this work, plentiful quantity of geometries have to be inspected in order to find the best one for the purpose that is being studied. Also, in the specific case of this work, analysis of moonpool in ocean requires calculation of a broad range of wave frequencies, that is not so easy to set, due mesh requirements, neither fast to run simulation in CFD. Anyway, it is useful to comprehend the behavior of water motion inside moonpool and how would work the mechanisms to damp it.

However, others tools are available with some simplification, for different purposes, but that can be adjusted and used for this work objective. *Potential Theory* explained in Section 2.1 do not calculate the flow behavior inside moonpool as CFD but some important parameter as harmonic free surface elevation inside moonpool and motion behavior of the ship may be gathered from it. It do not take viscosity effects into consideration in its formulation, but some artificial viscous damping may be calibrated for proper analysis of a drillship motion. That is the main reason of the CFD study done in Section 4.2, to quantify this viscous damping.

Two commercial software for the solution of the potential theory for the wave diffraction and radiation problem are used in this work. One is *WAMIT*, developed by researchers at Massachusetts Institute of Technology, hence the acronym *WaveAnalysisMIT*, in 1987. Other is *Hydrostar*, developed in Bureau Veritas (BV) since 1991. This simultaneous application provides an indirect way of validation and also makes the genetic algorithm solver created on this thesis more versatile for the end-user.

At this section, potential results for *fKN1* and *fKN2*, both at prototype scale, are presented and also how to add and calibrate the viscous damping inside moonpool for using it in next part of the thesis, the optimization.

4.3.1 Ships Motions

First of all, two meshes was created for the *fKN1* and *fKN2* with different refinements and then RAO for both ships and meshes were calculated, for all 6 DoF, in order to analyze a mesh dependency at the results. Two different heading for each DoF is plotted, $\beta_1 = 90.0$ and $\beta_2 = 180.0$, excpet for *Yaw*, that $\beta_2 = 120.0$ since this heading causes greater disturbances at this DoF. These results are shown in Figure 4.43 for *fKN1* and Figure 4.44 for *fKN2*, using both commercial software available. Depth is set mathematically as infinity in all simulations.

There are almost no difference between meshes refinement results, being just noticeable in some resonant peaks. Unlike CFD, the potential theory solver runs very fast, as it calculates only one scalar in a domain from a surface mesh, and it

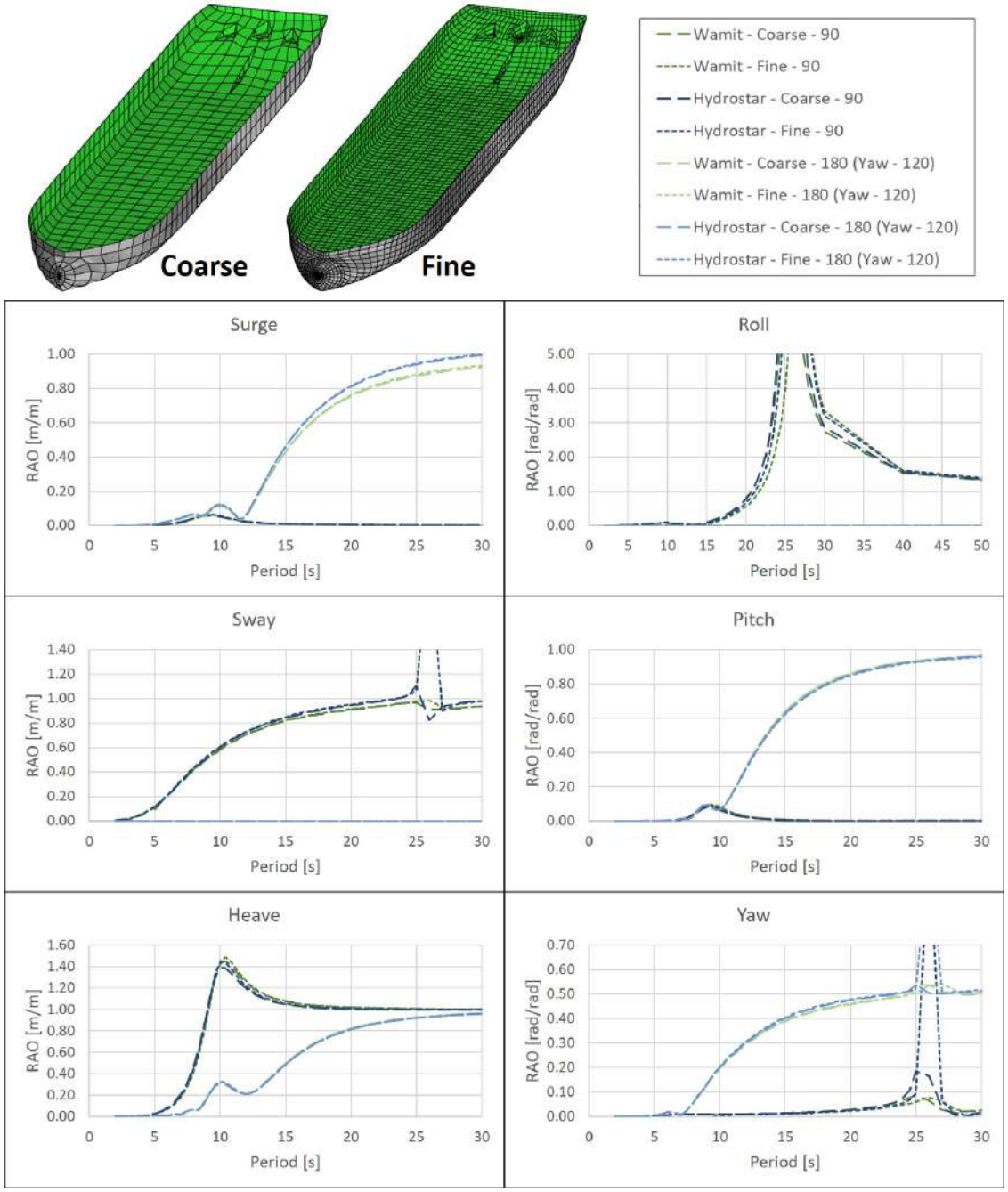

Figure 4.43: RAOs of all degree of motions at different mesh refinement for *fKN1*.

gives result for a broad range of frequencies and headings in minutes (sometimes few seconds). Despite this, from one mesh to another there were some minutes of difference to run the solver, it took almost 1 minute for *fKN1 Coarse* mesh while for *Fine* mesh it took 16 minutes, so it may seem sometimes preferable to use the *Fine* mesh to get a ship data as it provides better resolution at resonant peaks, but when considering the idea of using this solution in a optimization process, that may run thousands of different profiles, these minutes difference may turn into exhaustive hours more without necessity. Considering that, the next analyzes will be done with

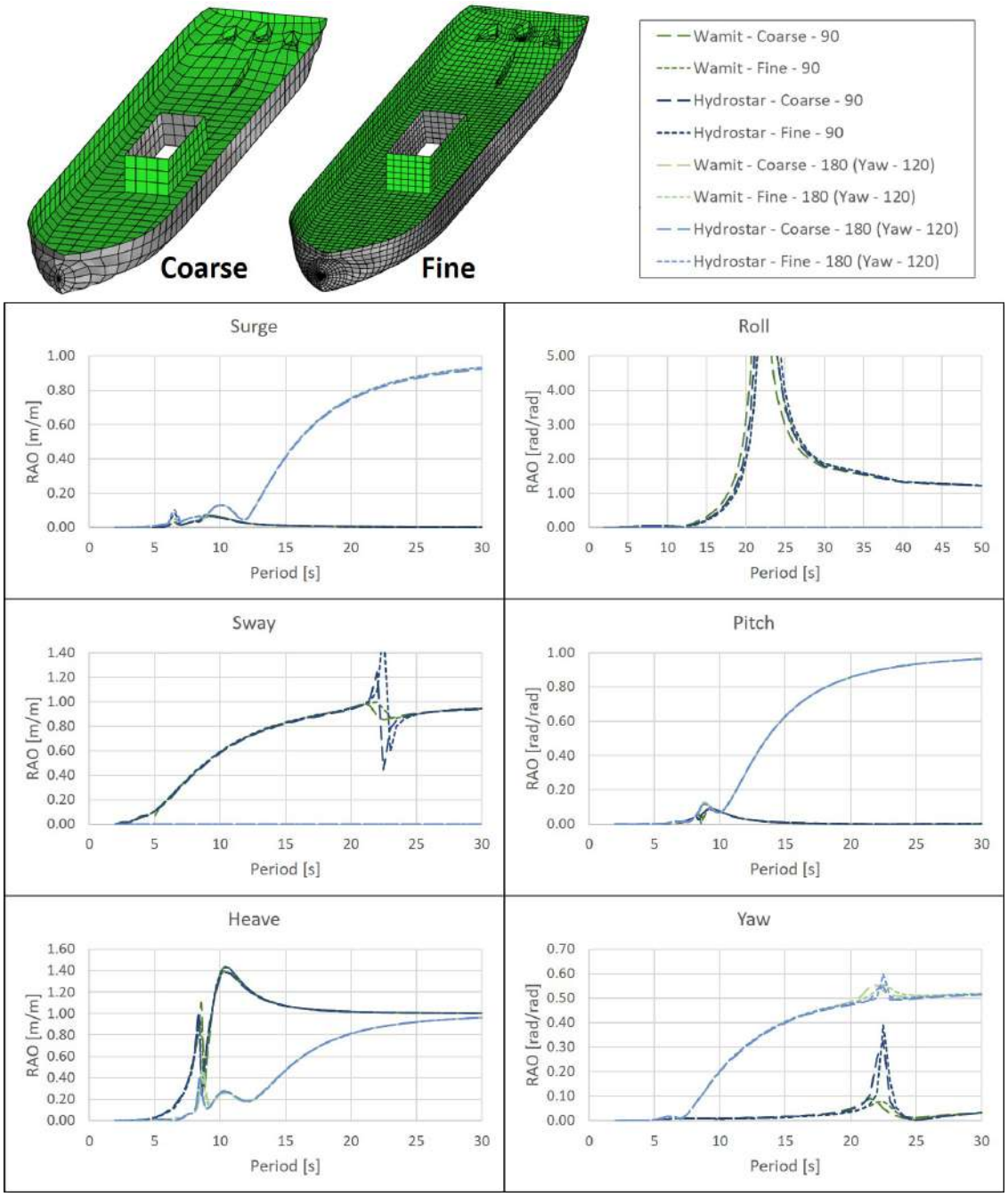

Figure 4.44: RAOs of all degree of motions at different mesh refinement for *fKN2*.

Coarse mesh.

Comparing also results from different solvers, fortunately they do not show considerable dissimilarity, that was expected if both setup was set properly, as long as both solvers are based in the same theory and they have a very similar calculation procedure.

Now, we must consider that there are three DoF that has restoring forces, *Heave*, *Roll* and *Pitch*. Each of these has an associated natural frequency, and they are dependent of mass and restoring coefficients. Undamped natural periods are calculated

using the following relation,

$$T_{ii} = 2\pi\sqrt{\frac{M_{ii} + M_{a,ii}}{C_{ii}}} \, . \tag{4.8}$$

Added mass are calculated at the potential theory solution and restoring coefficients are given by,

$$C_{33} = \rho_w g A_{wp} \, , \quad C_{44} = \rho_w g V \overline{GM_T} \, , \quad C_{55} = \rho_w g V \overline{GM_L} \, , \tag{4.9}$$

where $\overline{GM_T}$ is the transverse metacentric height and $\overline{GM_L}$ is the longitudinal metacentric height.

Then, it is possible to calculate the natural period for fKN1 and fKN2. The Table 4.20 shows the computed results,

Table 4.20: Undamped natural periods of *fKN1* and *fKN2*.

	Heave	**Roll**	**Pitch**
fKN1	10.43	26.36	10.65
fKN2	10.77	22.72	10.63

Another important detail to take into consideration is that a ship has vertical-longitudinal plane of symmetry, so its motions can be divided into symmetric (surge, heave and pitch) and anti-symmetric (sway, roll and yaw) components [11]. These components do not have effect at each other, if ship is not anchored, so two sets of three coupled equations of motion can be distinguished for ships. For instance, a vertical perturbation can cause surge, heave and pitch motions, but will not result in sway, roll or yaw motions. The similar behavior happens with horizontal motion for the anti-symmetric components.

After analyzed mesh independence and choosing the coarser one, the difference between RAO of *fKN1* and *fKN2* may show us the consequences of the moonpool presence in the general behavior of the ship in operation. Analyzing again Figures 4.43 and 4.44 for this difference assessment, we can see that in lateral motions (*sway*, *roll* and *yaw*) the resonant peak changed from $26s$ (*fKN1*) to $22.5s$ (*fKN2*). That are the calculated resonant periods for *roll* motion in each ship (Table 4.20) and it happens at the exactly same value for others anti-symmetric components only, not generating any kind of motion in the symmetric components.

Vertical plane motions (*surge*, *heave* and *pitch*) also have a slight peak for period around $10s$, that is the calculated resonant period of *heave* and *pitch*. As expected, the peak appears in *surge* as it is one of the symmetric components. Another difference in vertical motions is a high amplitude resonant period in *heave* motion at $8.4s$ and another, with smaller amplitude, in surge motion at $6.5s$.

4.3.2 Moonpool - Free Surface Elevation (FSE)

The consequence that concerns the industry is not related only with ship motions but also with the relative free surface elevation inside moonpool. With respect to operability, these motions may delay the drilling procedure and bring risks also, whatsoever it means high costs. Due that, it is important to analyze the relative free surface elevation inside moonpool. Two points were chosen for that calculation and they are approximately positioned drilling risers locus. Figure 4.45 shows the position of these wave probes.

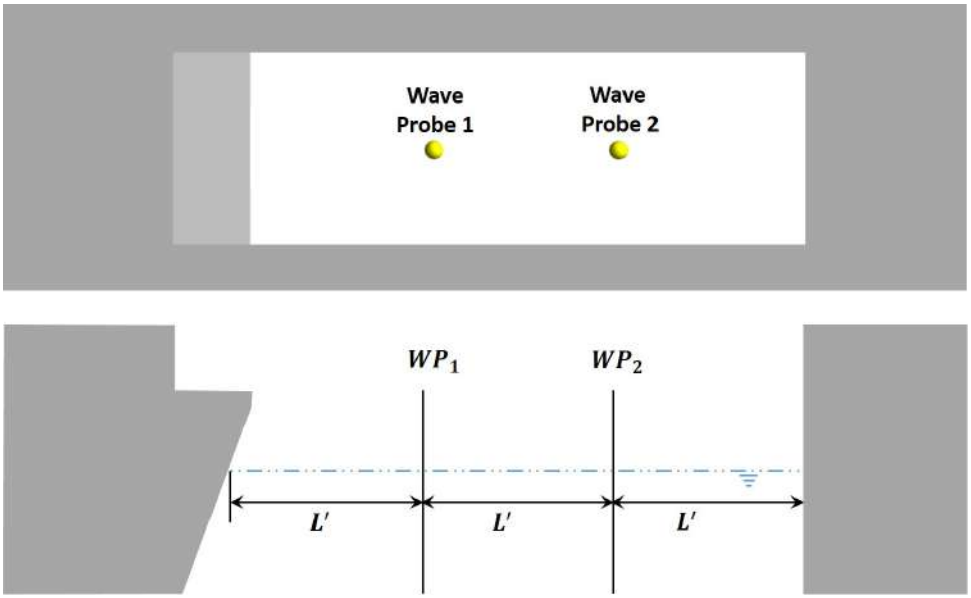

Figure 4.45: Locations of probes in the moonpool (Potential Theory). - $L' = 13.72m$

Wamit outputs the water motion in relation to the global reference frame while the Hydrostar already outputs the relative water motion. Then, in Figure 4.46 the RAO of calculated relative free surface elevation, considering phase difference, at each wave probe is presented for $\beta_1 = 90.0$ and $\beta_2 = 180.0$.

Once again were considered different mesh refinements to see if it would generate different results for the FSE. Finer mesh shows again better resolution at resonant peaks but both grids shows the same behavior. Now, we can notice a difference between Hydrostar and Wamit solvers, the former has three peaks frequency ($0.748rad/s$, $0.966rad/s$ and $1.256rad/s$) while the latter has only on big peak at $0.731rad/s$. A smaller peak appears at $0.966rad/s$ and $1.571rad/s$. These resonant peaks are related with the *piston* and *sloshing mode* of the default moonpool. Then, according to *undamped* potential theory, the piston mode is $\approx 0.71rad/s$ and first and second sloshing modes are $\approx 0.966rad/s$ and $\approx 1.256rad/s$. Converting these frequencies to period, we have piston at $8.85s$, first sloshing at $6.5s$ and second at $5.00s$. Comparing once again the difference of ship motion in Figures 4.43 and 4.44,

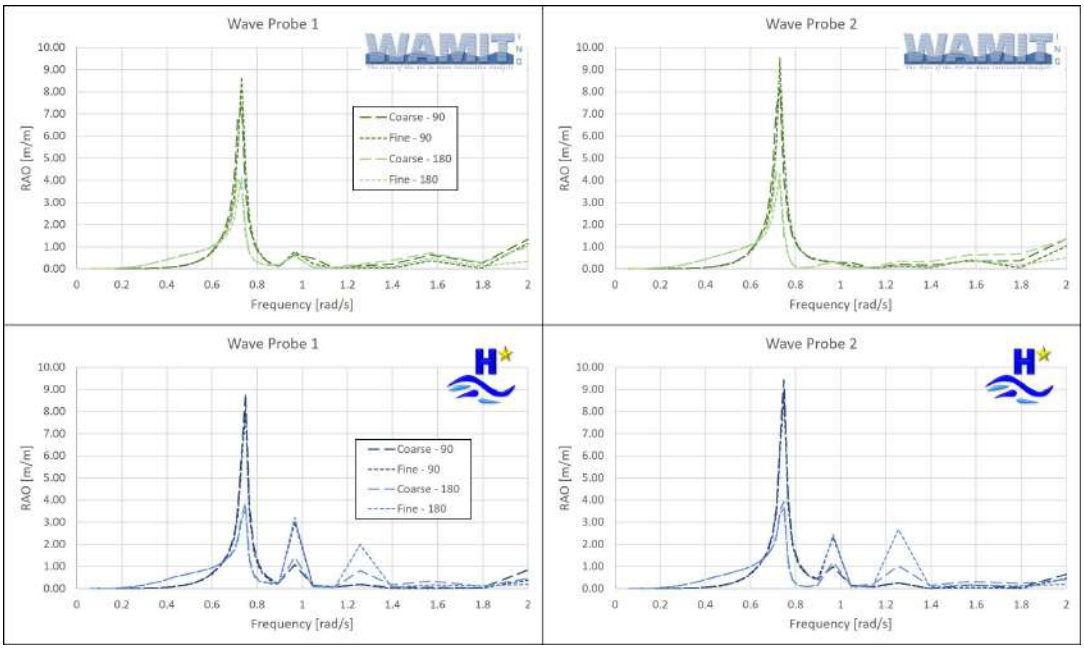

Figure 4.46: Free surface elevation inside *default* moonpool for *Wave Probe 1* and *Wave Probe 2* at different mesh refinement and headings. Wamit results (above) and Hydrostar results (below).

it is possible to see that the resonant periods inside moonpool generates variation in vertical motions only, as the piston mode period generate a high amplitude in *heave* and the first sloshing a slight peak in *surge* motion. The heave motion is highly coupled with the moonpool piston mode.

Although the resonant period of lateral motions changed, the variation caused by moonpool in vertical motions are more important, mainly heave, as new peaks appears and these are directly related with the resonant frequencies of the water motion inside moonpool. The heading that produces more vertical motions is $\beta = 180.0°$ and the lateral motions are prominent just for headings different than that. So, for optimization it is necessary to be more aware of vertical motions and at $\beta = 180.0°$.

4.3.3 Artificial Viscous Damping

As commented in Section 2.1.3, the proper calculation of the motion inside moonpool requires an additional artificial viscous damping. Beside the different nomenclature used between solvers, this damping is added with the same procedure. A *panel* over the opening, at free surface level is added, Wamit call this as *lid* and Hydrostar reference it as *zone damping*. In Wamit, another two uncoupled degree of motion are included in the solution for the heave (piston - $j = 7$) and pitch (sloshing - $j = 8$) motion of water inside moonpool and it is possible to add damping coefficients to this lid. In Hydrostar, the zone damping (herafter called *lid* also) requires

a *dissipation parameter* ε that is given in Equation (2.10).

Lid Position

According both manuals [12, 81], the *lid* must be added at free surface level. It was done and a simulation with no additional damping was run to check the lid influence at the results. Wamit lid position was adjusted using a in-house *python script* to find its best position, as the panel at free surface outputted a warning message: *Physical panel in free surface for body=1*, and the result without damping was different than the result without lid. After this lid position correction, the result plotted in Figure 4.47 could be calculated.

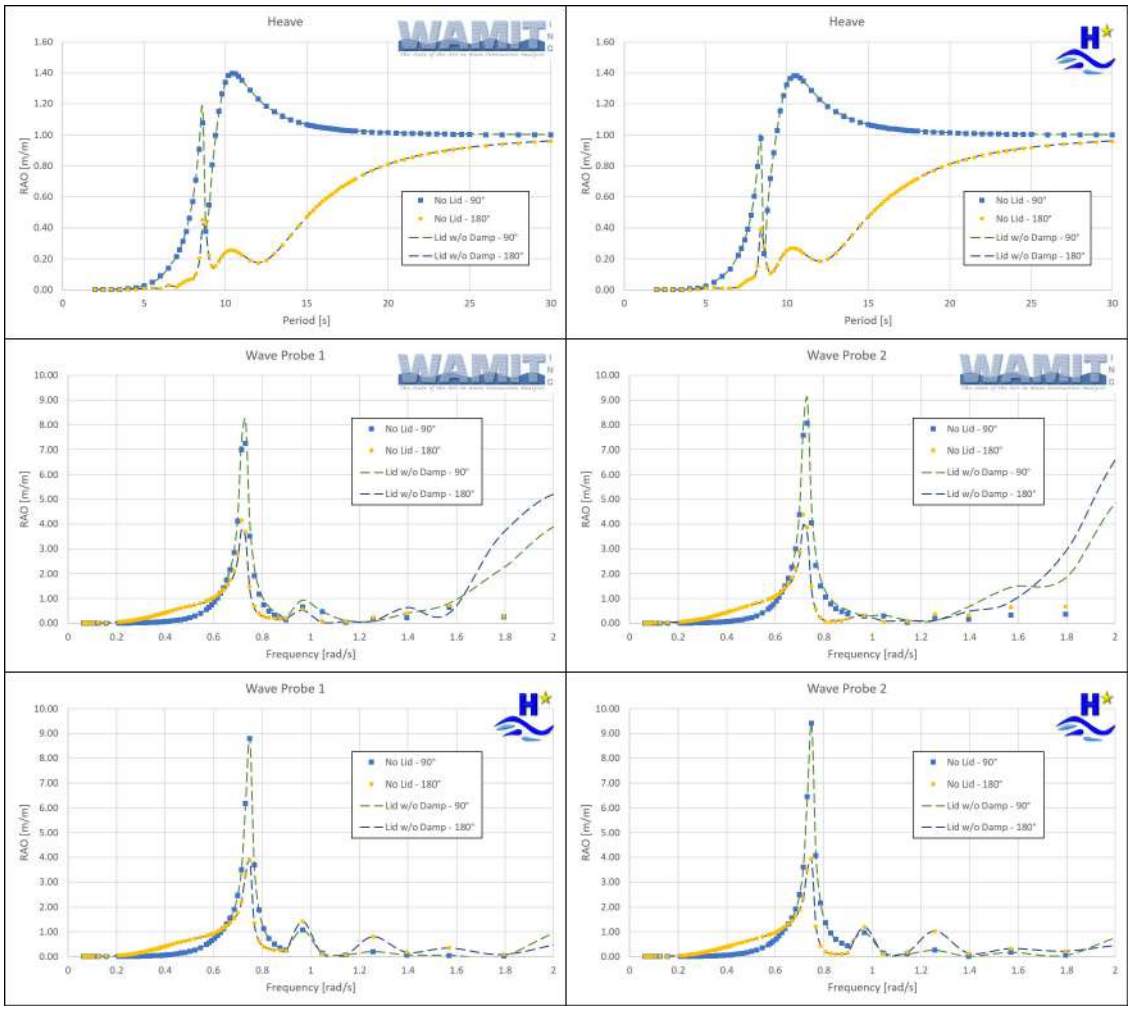

Figure 4.47: Heave and free surface elevation RAO comparison with lid, without damping, for heading $\beta = 90.0$ and $\beta = 180.0$ in both solvers.

This procedure is just to show that the lid is just a mathematical tool to include the viscous damping and the panel for doing that should not alter the final result. There were some variation between the result without lid and with lid without damping for high frequency values in Wamit solver.

Damping Magnitude

To see the variation in damping magnitude, some values were chosen for each solver. In Wamit a relation with the analytical critical damping (Equation (4.4)) was used, and these values are $b_{77} = 0.01B_{Crit}$, $b_{77} = 0.05B_{Crit}$, $b_{77} = 0.1B_{Crit}$ and $b_{77} = 0.5B_{Crit}$, while for Hydrostar they were $\varepsilon = 0.01$, $\varepsilon = 0.05$, $\varepsilon = 0.1$ and $\varepsilon = 0.5$. This damping variation in RAOs may be seen in Figure 4.48 for Wamit results and in Figure 4.49 for Hydrostar solver

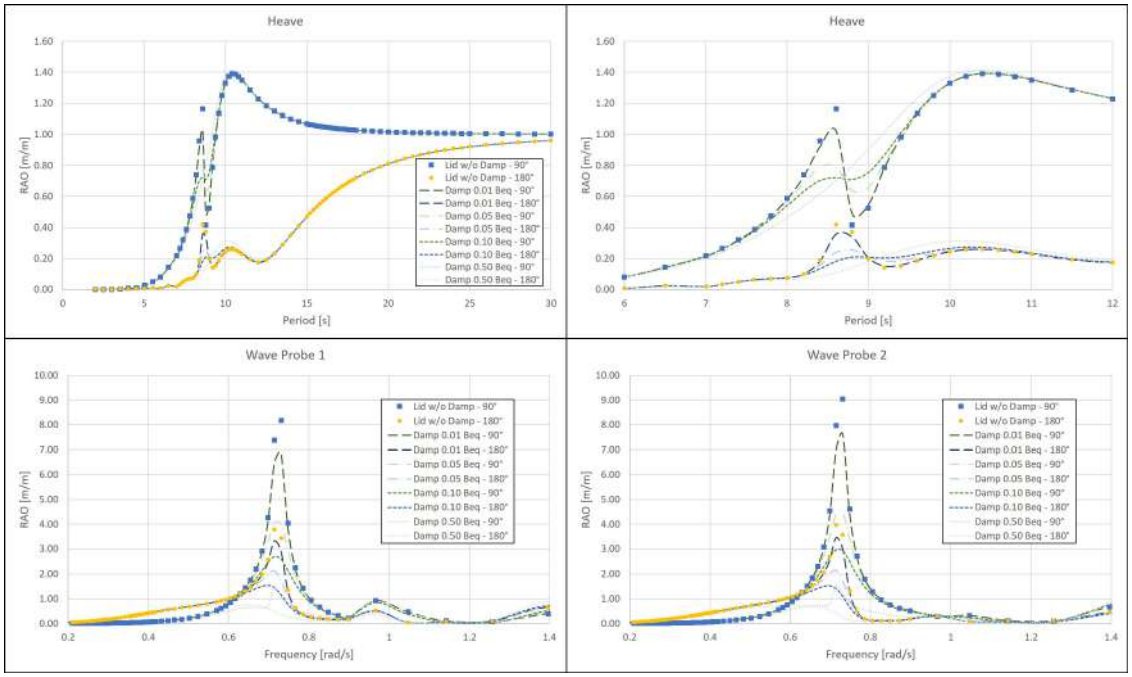

Figure 4.48: Free surface elevation and heave RAO with damping variation in lid for heading $\beta = 90.0$ and $\beta = 180.0$ in Wamit.

As expected by the conclusion previously done, that the water motions inside moonpool are uncoupled of the anti-symmetric components, the lateral motions did not change substantially with damping magnitude variation. Also is possible to see that the dissipation parameter ε is comparable to the percentage of critical damping calculated previously.

Following the calculated values of damping from CFD approach, we may see that is approximately 5% of the critical damping (Section 4.2.1). For these values, we may notice a decrease in amplitude values on resonant peaks but there is almost no variation of its position neither in the results on other frequencies besides resonant ones.

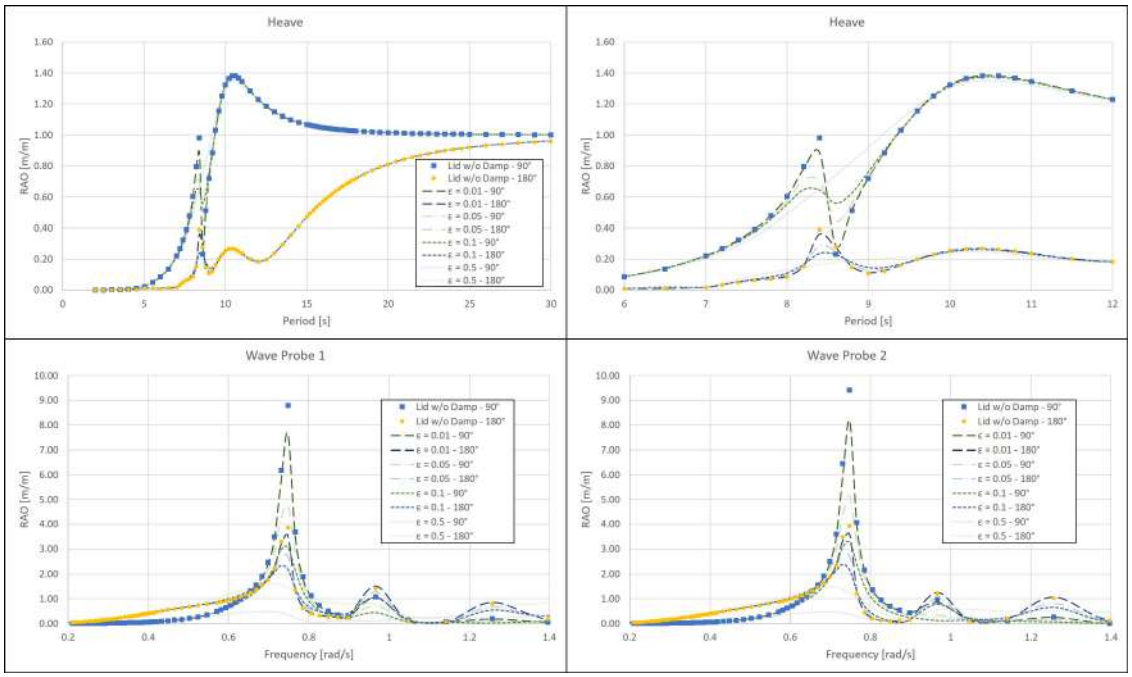

Figure 4.49: Free surface elevation and heave RAO with damping variation in lid for heading $\beta = 90.0$ and $\beta = 180.0$ in Hydrostar.

Chapter 5

Moonpool Optimization

This chapter is dedicated to the Genetic Algorithm application in the thesis problem, according to what is explained in Section 2.3. Also briefly show how it is implemented with creation of two software, one for automation of the mesh generation (Drillship Mesh Generator for Potential Theory - DMGPT) and another for setup and calculations of genetic algorithm (Genetic Algorithm at UFRJ - GAUFRJ). In order to clarify the importance of each software and how they are arrange in the whole picture of optimization process, a diagram is presented in Figure 5.1.

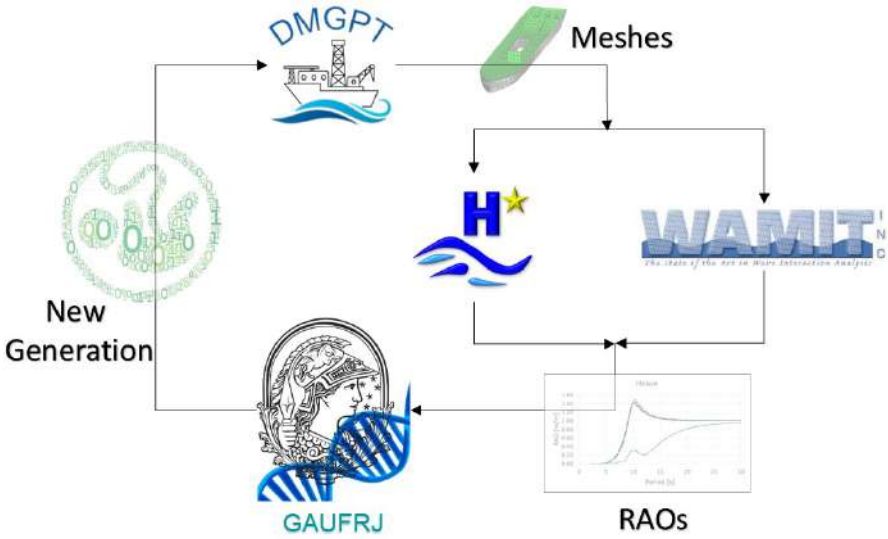

Figure 5.1: Diagram of software integration.

5.1 Genetic Algorithm Parameters

Following the explanation in Section 2.3, an *individual* is a single ship with a specific moonpool and the *genes* of each ship are the particulars that will suffer variation as we try to optimize. For this work, four moonpool parameters were

chosen for this variation, so the genes are:

- **Length**;
- **Width**;
- **Position**;
- **Trailing Edge Angle**.

A certain quantity of ships are created and they form a *population*. All these ships are analyzed for a fitness criterion (Section 5.2) and the fittest ones are selected. From these fittest, new offspring is generated by crossover and mutation of the aforementioned genes and these are considered the new *generation* of ships. These definitions are presented in Figure 5.2.

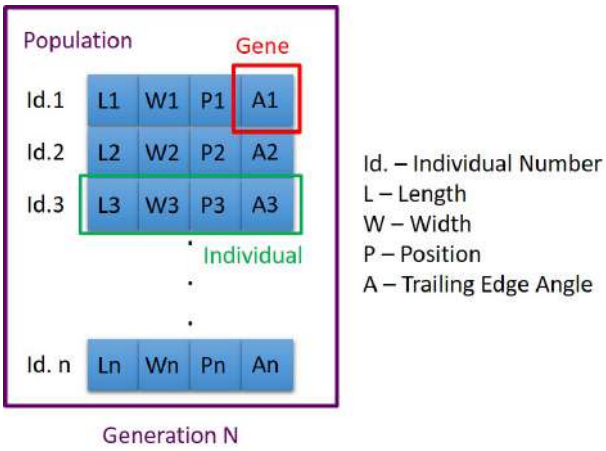

Figure 5.2: Genetic algorithm definitions on thesis problem.

5.2 Fitness Criteria

The main goal of optimization for this problem is related with the water motion inside moonpool and from previous result we know that this is hardly dependent of the frequency of exciting wave. Also, from potential theory results (Section 4.3) we can conclude that moonpool cause variation in ship vertical motion, mainly heave. Due the strong coupling between heave and pitch, we must worry with this also. So, for this work we decided to minimize either:

- **Ship's heave** or;
- **Ship's pitch** or;
- **Relative free surface elevation inside moonpool**.

Any of these may be chosen by the user and the fitness criteria value calculated will depend on that.

The *free surface elevation* is calculated always in two points equally spaced from moonpool wall and from each other at free surface level, like shown in Figure 4.45. *Wave Probe 1* is always the closer to the stern.

The optimization may be run for a regular wave or for a sea spectrum and that is an user input. If the the former is chosen, the user may choose also the frequency of this wave and *fitness criteria* will be given by RAO value for that specific frequency. The latter requires another input from user, the *ocean-wave spectrum*, and from that is possible to calculate a response of the minimization parameter defined previously. In following section it is described a better explanation on how it is done.

5.2.1 Ocean-Wave Spectrum

When a ship is operating in ocean it is not subjected to just one frequency. Sea is a train of waves, mainly generated by the interaction between wind and the water surface, and it is very irregular, as high waves are followed unpredictably by low waves and vice versa. There is a called *superposition principle* that states that the irregular sea can be analyzed as a superposition of many simple regular harmonic wave components, each with its own amplitude, length, period and direction of propagation. It may be explained graphically in Figure 5.3.

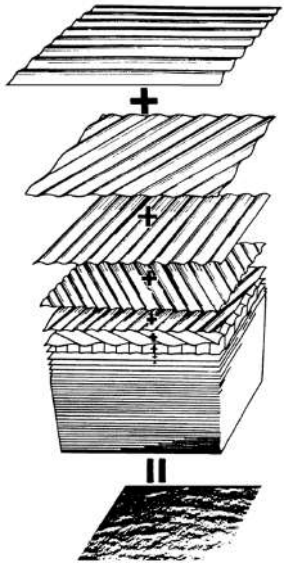

Figure 5.3: A sum of many simple sine waves make a sea. (PIERSON *et al.* [22])

As a sea can be study as a superposition of regular sinusoidal waves, it can be done using Fourier series analysis. With that, is possible to describe the irregular wave using a *Energy Density Spectrum* from a measured wave record, as seen in Figure 5.4.

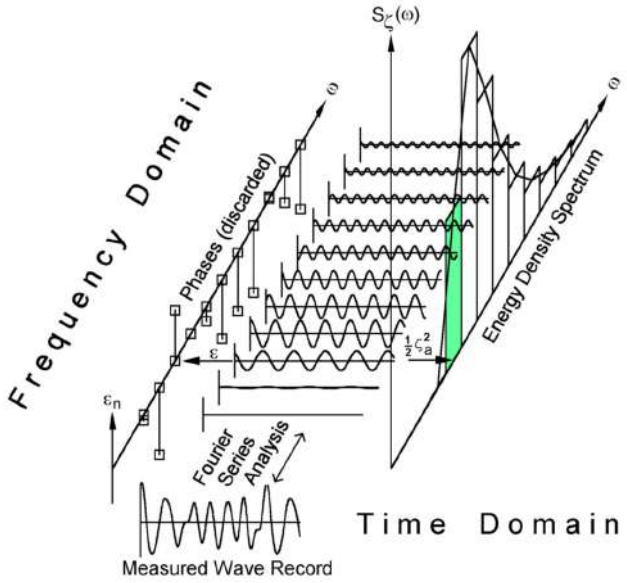

Figure 5.4: Wave record analysis (JOURNÉE and MASSIE [11])

There are four main spectrum density known to describe irregular sea:

- **Neumann**;
- **Pierson-Moskowitz**;
- **Jonswap**;
- **Bretschneider**.

When choosing a ocean-wave spectrum, RAO is not the best choice of optimization, so we can calculate a *response spectrum*. It is given by,

$$S_z(\omega_f) = |RAO_{degree}|^2 \cdot S_\zeta(\omega_f) \ , \tag{5.1}$$

where $S_z(\omega_f)$ is the response spectrum and $S_\zeta(\omega_f)$ is the wave spectrum. Then, the fitness criteria in this case is considered the area of this response spectrum and so the lower area values are considered the fittest. In the software this value is shown normalized with the value calculated for the *default* moonpool, i.e., the *fKN2*. It means that a value greater than unity is computed for a moonpool profile that has worse behavior for the specific minimization parameter in the specific ocean spectrum.

5.3 Solution Algorithm

Then, we decided to create a software to solve the Genetic Algorithm (Genetic Algorithm at UFRJ - GAUFRJ) specifically for the *fKN1* hull with addition of a moonpool. Software interface and more details are shown in Section 5.5.

This software can run any of the potential theory solver previously shown in order to calculate the fitness goals aforementioned. It also do all calculation needed for the whole algorithm implementation as shown in Figure 2.15.

There is a specific library in *Python*, called by the acronym *DEAP*, that has some defined functions already for calling a genetic algorithm procedure. This library presents customizable framework, where is possible to create a code for setting the initialization, fitness evaluation and also how both the mutation and crossover of new generation formation happens.

The software has a Graphical User Interface (GUI) that is shown in Figure 5.6. According to information of the number of individuals, the initial generation (Generation 0) is randomly created, so for each individual four genes are set following some size limitation rules. In order to run these created ships in the potential theory solver, a mesh needs to be created, then the software calls another in-house code (programmed specifically by this thesis) created for the specific purpose of mesh creation for using in any of the solvers. This software is called *Drillship Mesh Generator for Potential Theory* (DMGPT) and more details when running it standalone are given in Section 5.4.

After the mesh generation, it can be used by potential theory solver and then the fittest are chosen. The code was created for heading $\beta = 180°$. The *fitness criteria* is also an input by the user, according to what is described in Section 5.2.

Following user input for probability of crossover and mutation, and depending on the algorithm chosen also, the routines for newer offspring is called. *Crossover* routine chooses two individuals from the number of fittest individuals (μ) selected from previous generation, called *parents*, and choose each of offspring four genes from the parents by equal chances (50% of chance to get from *parent 1* or *parent 2*). *Mutation* routine chooses one individual only of the fittest selected and then for each gene it may randomly change its value, also following a 50% of probability to change any gene. It may happen to create an offspring with four new random created genes (totally different of parents) and it also may create an offspring that is a *clone*, i.e., it is exactly the same genetic code of parent. The odds for the clone generation is just 6.25% ($= 50\% \times 50\% \times 50\% \times 50\%$).

Every generation has new offspring based on the fittest from previous generation. The idea behind this is that after some generations the optimum moonpool profile characteristics will appear more often and any mutation may help the solver to discover if there is any other possible modification that can generate an improvement in the result. Anyway, information of each individual is kept for comparisons, so not necessarily the optimum moonpool will be at the last generation.

Both software created were generated planning to solve the case using either Wamit or Hydrostar. As previously shown, both solvers are powerful for that pur-

pose and they bring similar results, so the idea was to create a more generic and accessible Genetic Algorithm software.

5.4 Drillship Mesh Generator for Potential Theory - DMGPT

This software was created for this thesis in *Visual Basic* code an it may be used with a GUI or by *Command Line Interface* (CLI), as presented in Figure 5.5. The former is better for a creation of a simple mesh and the latter is better for automation process. The user may choose all four genes values, the addition of damping (a window popup asking the damping magnitude in the GUI), mesh refinement and also if wants discretization of free surface (required for second order calculations). *Default* button modifies the input values for matching the *fKN2* ship. Hitting *Generate* button it automatically generates two meshes, one for Wamit and other for Hydrostar, following all the requirements of each solver.

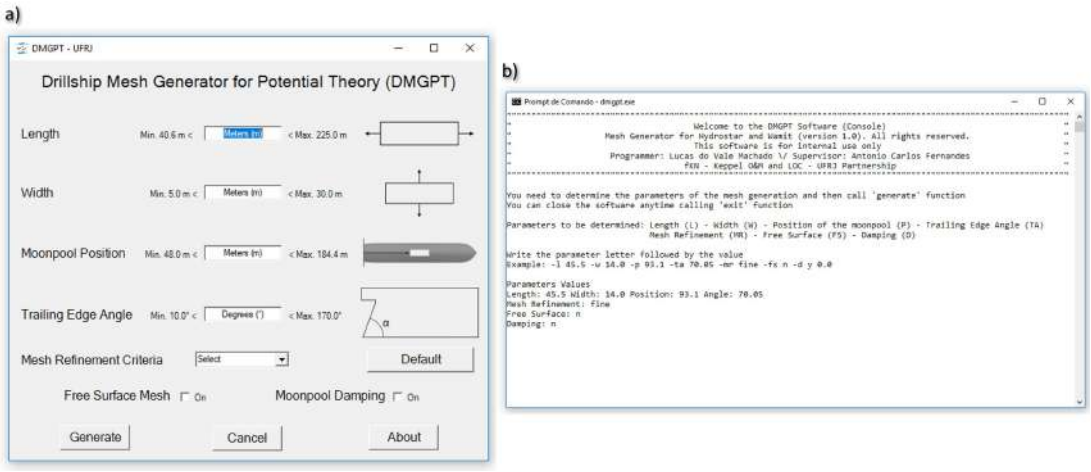

Figure 5.5: *a)* Graphical User Interface and *b)* Command Line Interface of DMGPT software

5.5 Genetic Algorithm at UFRJ - GAUFRJ

The GUI of the GAUFRJ software is shown in Figure 5.6.a. The user must input the configuration of the genetic algorithm, as *number of generations*, *number of individuals selected* at each generation (it is also the number of initial individuals - Generation 0), *number of children* (quantity of new offspring at each generation) and optional *hall of fame*, that is the number of fittest profiles that will be presented in the output file. Besides that, the percentage of *crossover* and *mutation* must be set as the specific algorithm that will be used, the solver and the wave for fitness

criteria calculation, if it is a regular wave with specified frequency or a ocean-wave spectrum. Hitting *Breed* button, the software asks a name for the project and the fitness goal Figure 5.6.b. When a case is running, below the window appears a blank area with log information of the process and also a progress bar.

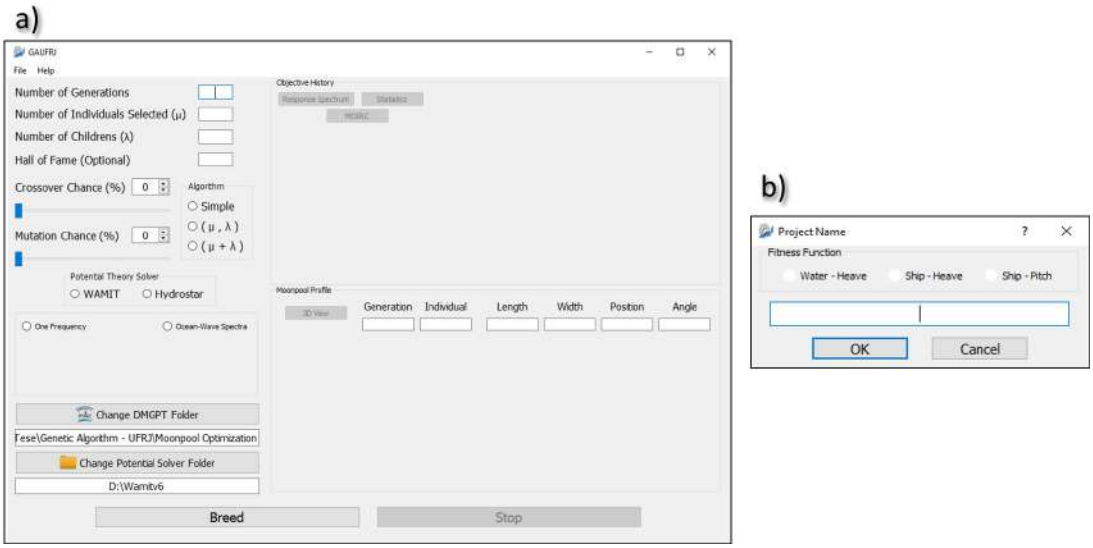

Figure 5.6: *a)* Graphical User Interface of GAUFRJ software and *b)* setup of the fitness criterion and the project name

There is a section *Objective History* that shows the calculated values for each ship and present it in a graphic and another section called *Moonpool Profile* with design of the moonpool and particulars that is running, and also information of generation, individual and wave probes position.

In *File*, there is a option *Change Limits* (Figure 5.7.a). This open a window (Figure 5.7.b) where the user can select the limits of each gene and also may lock one or more particular in order to find optimum moonpool with controlled dimensions.

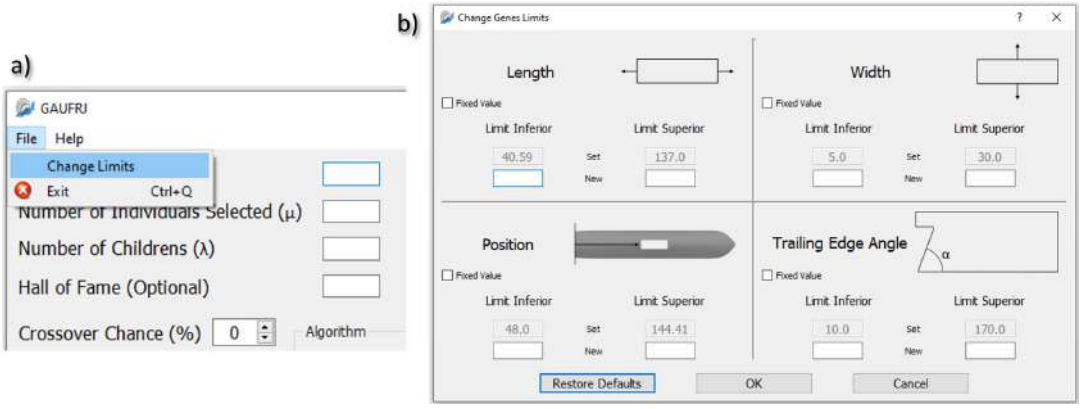

Figure 5.7: Option for changing limits of moonpool dimensions or to modify the number of optimization parameters (genes). *a)* How to access and *b)* the setup window.

Chapter 6

Results and Discussions

The result of some case run with the GAUFRJ are shown in this chapter. Firstly, in Section 6.1, it will be presented the optimization for a regular wave only, considering the fitness criteria of minimization of the water free surface elevation inside moonpool and then the minimization of vessel heave motion. In Section 6.2, the optimization for a spectrum of a random sea represented by JONSWAP is shown. It will also follow the approach of a first case minimizing the free surface elevation and then the vessel heave motion. In these analysis, all four parameters (*genes*) included in the code will be used and the limitation of these sizes are just based on the extent of ship, but as explained in Section 5.5, user limitations to moonpool size may be applied. The idea is to deal with the most possible variety of moonpool design in order to show the behavior of the optimizer finding the best solution.

6.1 Regular Wave

6.1.1 Optimization of Free Surface Elevation

For this case, it was chosen the piston mode natural frequency computed previously for the *fKN2* ship, that is $0.731 rad/s$. The idea is to find the profile that would give the minimum water motion inside the moonpool for the specific frequency that causes the higher response in *default* moonpool. The calculation was setup for 10 generations with the 20 fittest individuals selected at each to *breed* the 50 new offspring of ships. The percentage chosen for crossover is 70% and for mutation 30%. These values was a initial guess and they provided good results in the optimization. It used Wamit as solver and it took 3 hours and 40 minutes to run this solution with 520 ($= 20\ (initialization) + 10 \times 50$) possible different profiles.

The GAUFRJ generates various outputs. The most important one brings the information of each individual created with its moonpool characteristics (genes) and the calculated fitness criteria value. Figure 6.1 shows the variation of fitness criteria

for each individual.

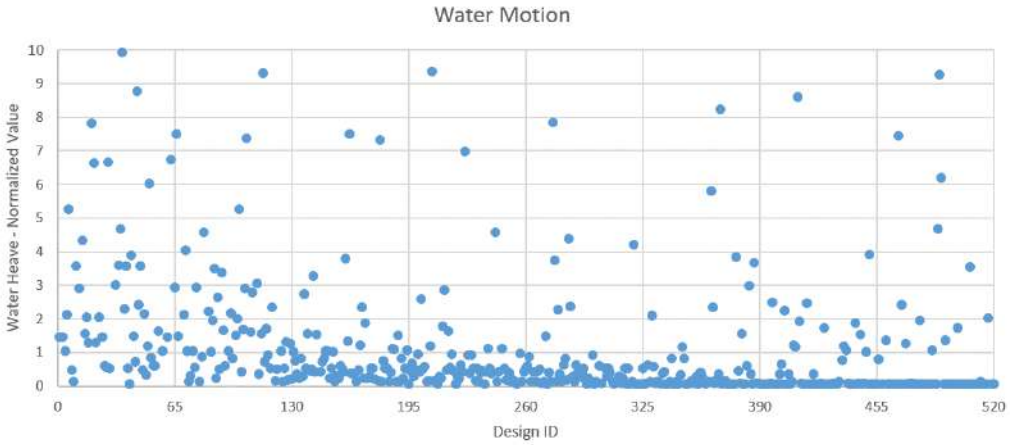

Figure 6.1: Objective History - Regular wave of $0.731 rad/s$ - Fitness criteria: Free Surface Elevation.

Software also calculates the mean and the standard deviation of the fitness criteria normalized value at each generation. This result is shown in Figure 6.2. We can observe that the fitness criteria mean tends to values lower than one, that implies in an average result better than *default* moonpool (as the criteria is already normalized with that case) for that generation individuals.

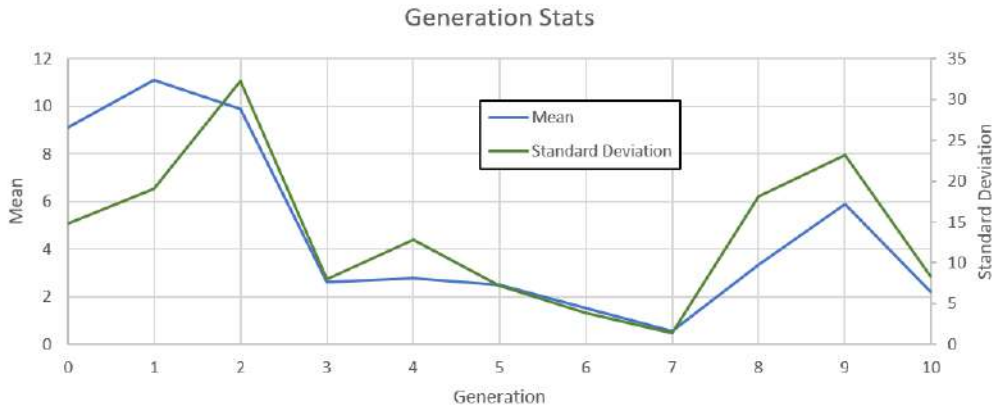

Figure 6.2: Generation Statistics - Regular wave of $0.731 rad/s$ - Fitness criteria: Free Surface Elevation.

As generation evolves, each population tends to be with more individuals with lower water motion, but it also mean that new offspring generated by mutation may cause more discrepancies in the results. This is a possible explanation of why the standard deviation in the 8^{th} generation increases and also the fitness criteria mean increases together.

From the final results we can get the optimum moonpool and its particulars are given in Table 6.1. This optimum profile appeared for the first time in simulation

at the 7^{th} generation and it kept showing up until the 10^{th} generation.

Table 6.1: Optimum moonpool particulars - Regular wave of $0.731 rad/s$ - Fitness criteria: Free Surface Elevation.

Description	Symbol	Magnitude	Unit
Moonpool's length on bottom	l_b	43.5	m
Moonpool's breadth on bottom	b_b	27.9	m
Moonpool's breadth on deck	b_d	27.9	m
Postion (from transom)	P	105.02	m
Cutout angle	α	92.62	°

Using Wamit is now possible to calculate the water motion inside moonpool and also heave motion for comparison with the *default* moonpool and the comparison is shown in Figure 6.3.

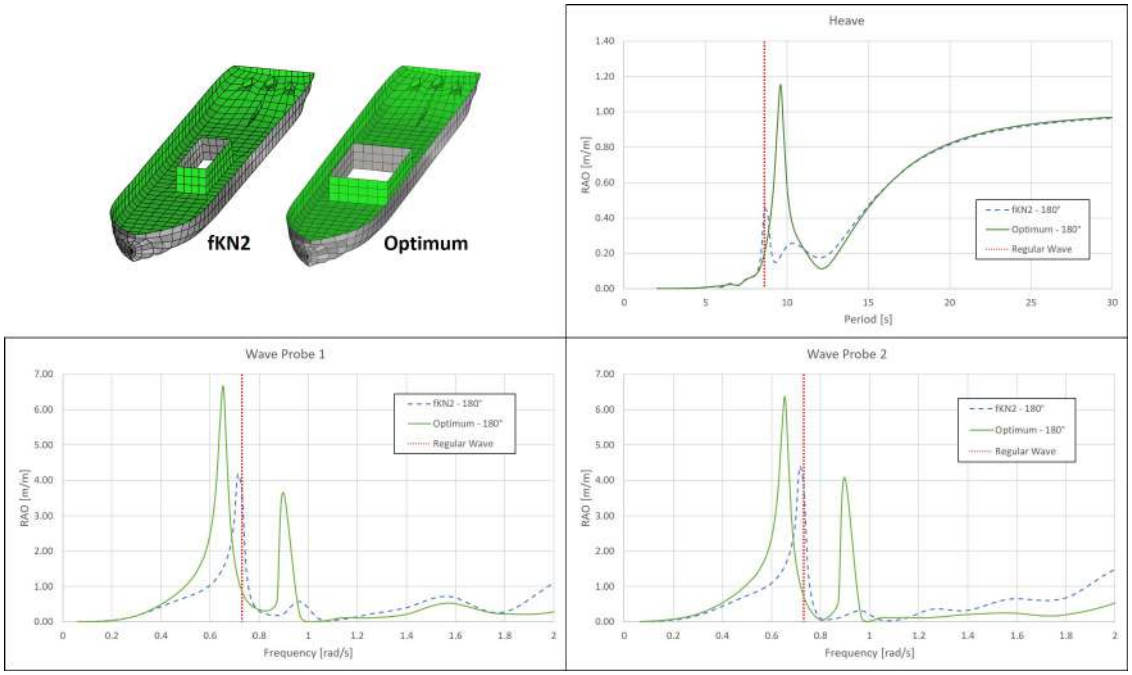

Figure 6.3: Comparison of RAOs between optimum and *default* moonpool - Regular wave of $0.731 rad/s$ - Fitness criteria: Free Surface Elevation.

The setup at this section was done for calculation of the water lower relative amplitude motion inside moonpool for a regular wave with frequency $0.731 rad/s$. At this frequency, the RAO calculated in the wave probes are given in Table 6.2 and we may notice that the motion is just approximately 21% of the *default*.

From Figure 6.3 is noticeable that ship heave motions and also motion inside moonpool in general increases for other frequencies, but the optimization for the specific purpose of a regular wave with known frequency and just considering the water motion inside moonpool was properly achieved.

Table 6.2: Comparison of wave probe RAO values between optimum and *default* moonpool - Regular wave of $0.731 rad/s$ - Fitness criteria: Free Surface Elevation.

	Wave Probe 1	**Wave Probe 2**
fKN2	3.69	3.85
Optimum	0.87	0.72

6.1.2 Optimization of Vessel Heave Motion

Considering now the same previous setup for a regular wave with frequency $0.731 rad/s$, just changing the fitness criteria for ship heave motion. This case took 3 hours and 54 minutes and objective history of all simulation run is given in Figure 6.4. Also, generation statistics are given in Figure 6.5.

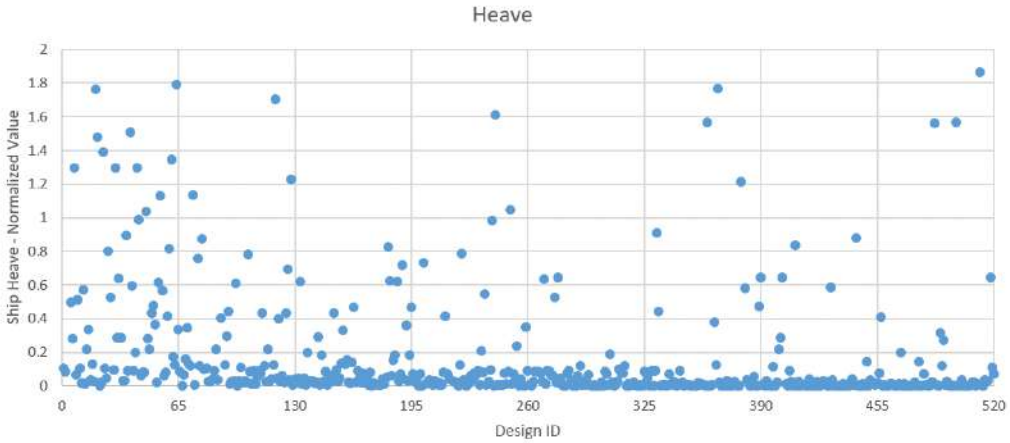

Figure 6.4: Objective History - Regular wave of $0.731 rad/s$ - Fitness criteria: Vessel Heave Motion.

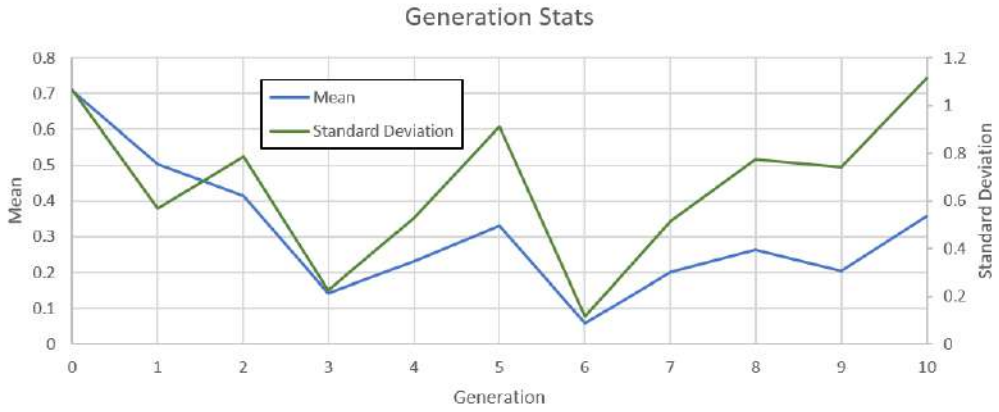

Figure 6.5: Generation Statistics - Regular wave of $0.731 rad/s$ - Fitness criteria: Vessel Heave Motion.

Once again we may observe that newer generations tends to have more profiles with lower values of the fitness criteria and the mutation creates a diversity that may lead to a new minimum.

The optimum moonpool appeared the first time in 7^{th} generation and also kept showing up in others generations. Particulars of it are given in Table 6.3.

Table 6.3: Optimum moonpool particulars - Regular wave of $0.731 rad/s$ - Fitness criteria: Vessel Heave Motion.

Description	Symbol	Magnitude	Unit
Moonpool's length on bottom	l_b	46.94	m
Moonpool's breadth on bottom	b_b	17.24	m
Moonpool's breadth on deck	b_d	17.24	m
Postion (from transom)	P	106.90	m
Cutout angle	α	137.55	°

Both heave of the vessel and the water motion inside moonpool are shown in Figure 6.6. At this case, the algorithm minimization focus is in the heave ship motion. At the specified frequency the RAO is shown in Table 6.4 and it is observable that the heave is lower and is just approximately 1% of the *default* moonpool RAO value. There is a deterioration of other frequencies RAO, but the setup goal for a regular wave was reached. At Section 6.2, the random sea shows the optimizer behavior when considering a range of frequencies.

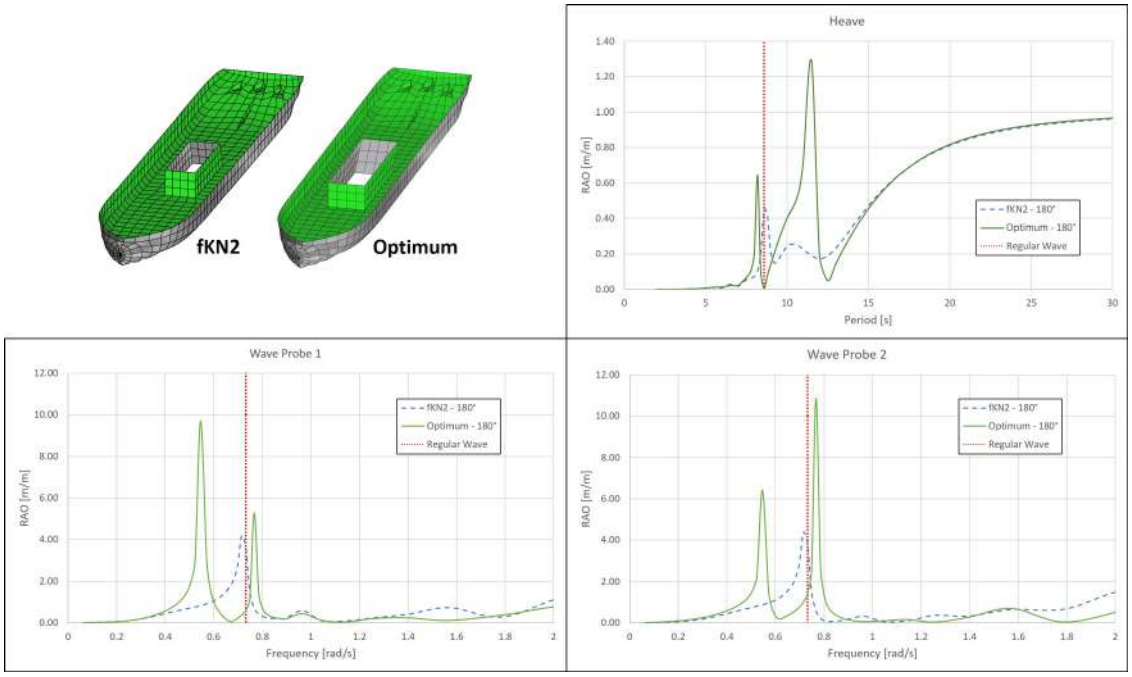

Figure 6.6: Comparison of RAOs between optimum and *default* moonpool - Regular wave of $0.731 rad/s$ - Fitness criteria: Vessel Heave Motion.

Table 6.4: Comparison of heave RAO values between optimum and *default* moonpool - Regular wave of $0.731 rad/s$ - Fitness criteria: Vessel Heave Motion.

	Heave
fKN2	0.45
Optimum	4.59×10^{-3}

Relative motion measured at wave probes in optimum moonpool is lower than *default* for that regular wave frequency, but is higher than the previous optimum profile shown in Table 6.1, as expected. It means that the optimization of heave motion not necessarily means lower relative motion inside moonpool and vice versa.

6.2 Random Sea - Case Study

Although the regular wave optimization is good for enlightenment, in real cases the ship operates at sea in irregular waves. According explained in Section 5.2.1, that can be described by a spectrum and it is possible to calculate a response spectrum of ship and water motion using Equation (5.1). For this section, it was chosen the JONSWAP spectrum due to its importance as it is may be used for parametrisation of known sea as North Sea or Santos Basin. The parameters for the spectrum definition were calibrated in order to have more wave energy at resonant frequency of *default* moonpool. So the spectrum with significant height $H_S = 2.0m$ and peak wave period $T_P = 8.6s$ ($0.731 rad/s$) is graphically shown in Figure 6.7.

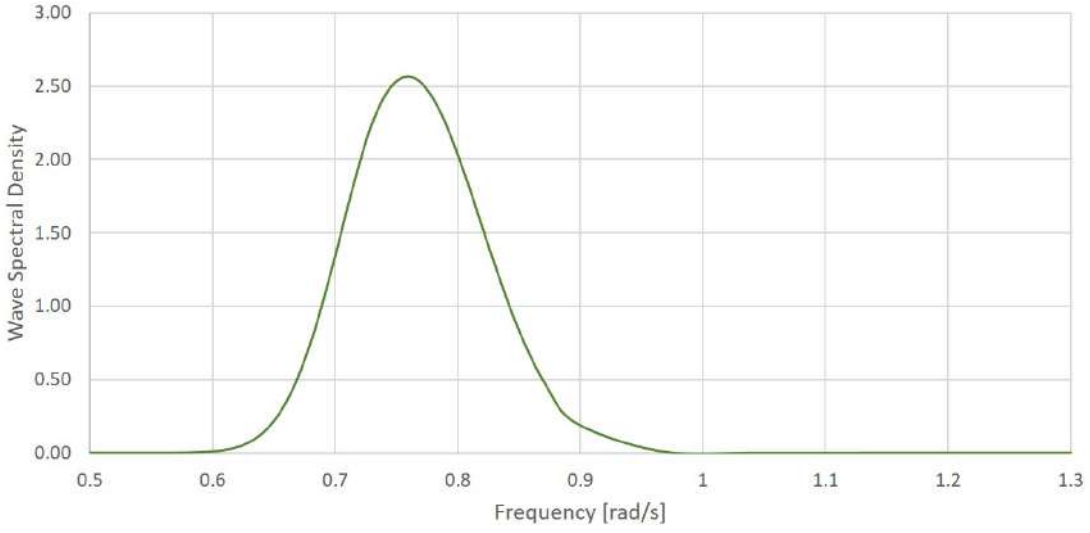

Figure 6.7: JONSWAP spectrum representing ocean for case study - $H_S = 2.0m$ and $T_P = 8.6s$.

6.2.1 Optimization of Free Surface Elevation

Following same setup of regular wave, just changing exciting wave for the spectrum presented in Figure 6.7, the software took only 3 hours and 11 minutes to run all the possible opportunity for all individuals. Objective history is then shown in Figure 6.8.

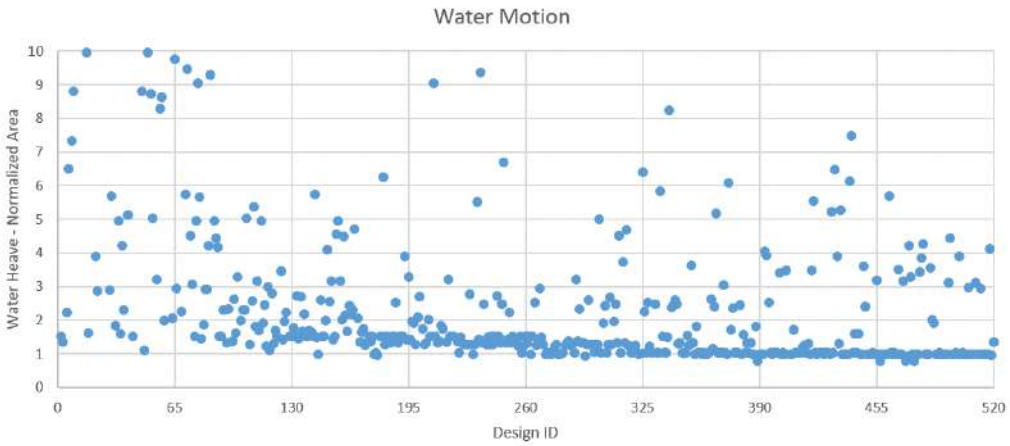

Figure 6.8: Objective History - JONSWAP spectrum ($H_S = 2.0m$ and $T_P = 8.6s$) - Fitness criteria: Free Surface Elevation.

Here we can see the same behavior as more advances the generations, more individual fitting the criteria appears and mutation still generating random individuals. It is hard to go below unity in this case, as we are considering a frequency range for analysis now. The generation statistics is also presented in Figure 6.9.

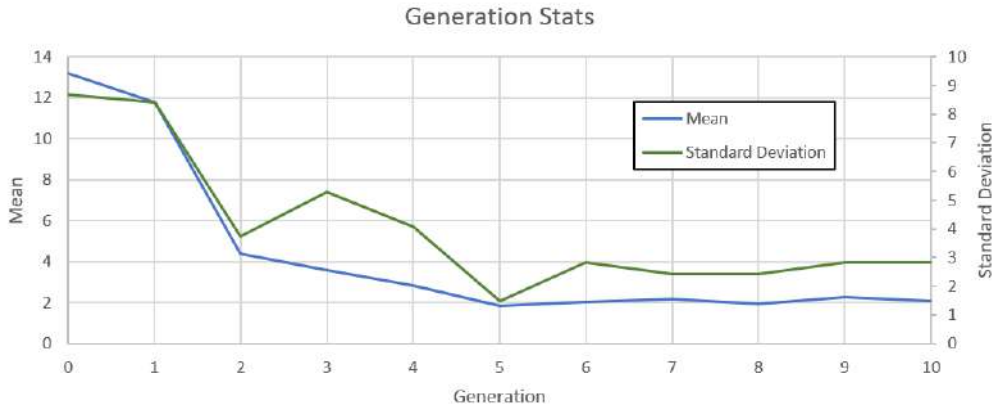

Figure 6.9: Generation Statistics - JONSWAP spectrum ($H_S = 2.0m$ and $T_P = 8.6s$) - Fitness criteria: Free Surface Elevation.

The fitness criteria mean of each generation decreases and after 6^{th} generation does not change substantially, besides the fact that we can see that mutation still happening. That is a good demonstration that in general, most of the individu-

als in newer generation are providing better good minimization of the free surface elevation.

Optimum moonpool for this case is given in Table 6.5. It appeared just after the 8^{th} generation.

Table 6.5: Optimum moonpool particulars - JONSWAP spectrum ($H_S = 2.0m$ and $T_P = 8.6s$) - Fitness criteria: Free Surface Elevation.

Description	Symbol	Magnitude	Unit
Moonpool's length on bottom	l_b	48.30	m
Moonpool's breadth on bottom	b_b	7.27	m
Moonpool's breadth on deck	b_d	7.27	m
Postion (from transom)	P	66.58	m
Cutout angle	α	126.53	$^\circ$

As it was done for previous cases, the heave RAO comparison is presented in Figure 6.10 and also the water motion RAO in Figure 6.11.

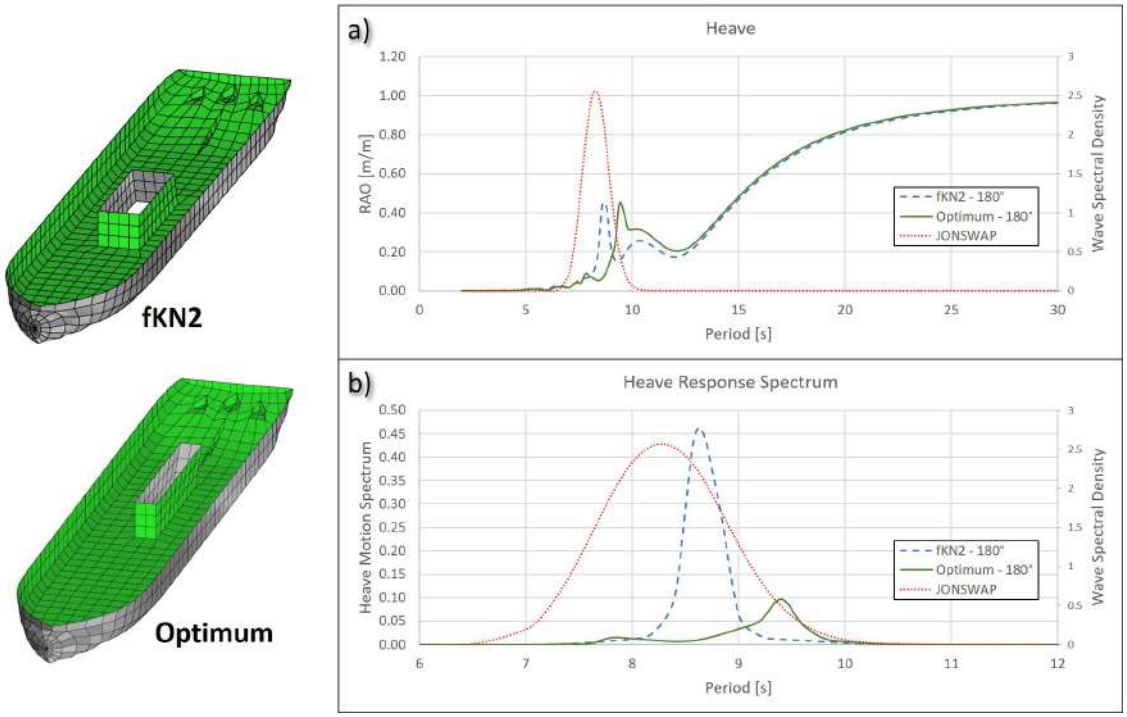

Figure 6.10: Comparison of heave *a)* RAO and *b)* response spectrum between optimum and *default* moonpool - JONSWAP spectrum ($H_S = 2.0m$ and $T_P = 8.6s$) - Fitness criteria: Free Surface Elevation.

Now the response spectrum is also calculated using Equation (5.1) and it also presented for both RAO. Visually we can distinguish the area os each response spectrum and conclude that the motions are lower in general for the optimum moonpool. We can deduce that the optimum moonpool, even having two resonant peak with

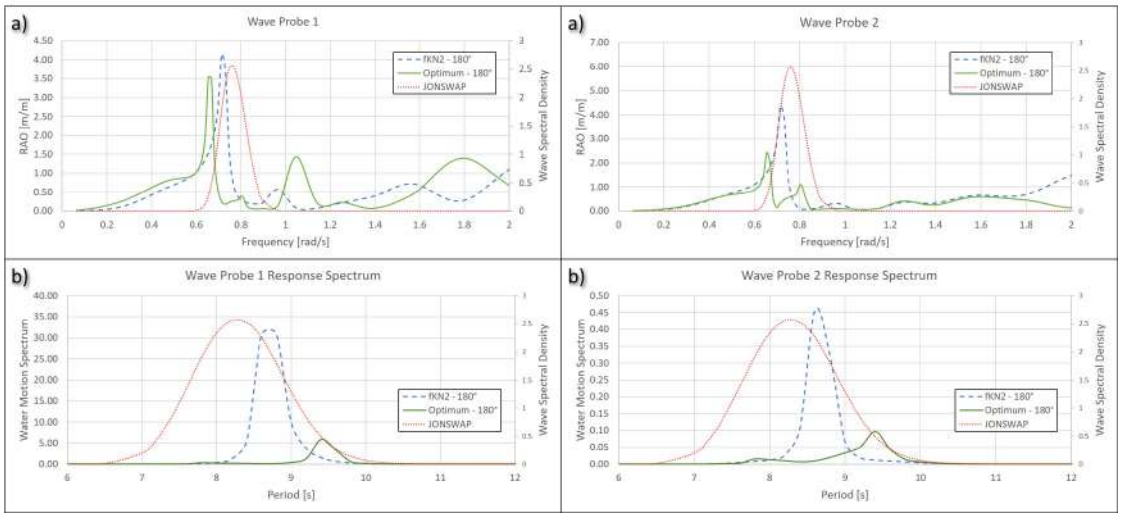

Figure 6.11: Comparison of free surface elevation *a)* RAOs and *b)* response spectra between optimum and *default* moonpool - JONSWAP spectrum ($H_S = 2.0m$ and $T_P = 8.6s$) - Fitness criteria: Free Surface Elevation.

considerable magnitude, but with different frequencies than the *default* moonpool peak, it may reduce the downtime of this drillship when operating in a sea with the spectrum given. In this case the spectrum was chosen purposefully to have more energy at the resonant frequency of the *default* moonpool in *fKN2*, but even without previous knowledge of a comparison moonpool and using a specific operation sea it will provide satisfactory profile.

6.2.2 Optimization of Vessel Heave Motion

Same procedure was done for ship heave motion optimization considering the spectrum. This case took 3 hours and 35 minutes. The objective history is shown in Figure 6.12 and it follows exactly the same behavior from previous optimization cases, with newer generation having more individual presenting lower value of the fitness criteria and some random individuals expected because of mutation.

Generation statistics (Figure 6.13) in this case shows a continuous decrease of the fitness criteria mean value.

Optimum moonpool appeared only at the last generation. Its particulars are shown in Table 6.6 and we may notice that has some similarities to the optimum moonpool of the optimization in the same spectrum with the fitness criteria decreasing water motion inside moonpool (Table 6.5). These motions are strongly coupled so some similarities are interesting to happen. The prominent difference is the width of moonpool.

Heave RAO and response spectrum of that case is shown in Figure 6.14 and the response is clearly lower than the *default* one. Analyzing the heave RAO separately,

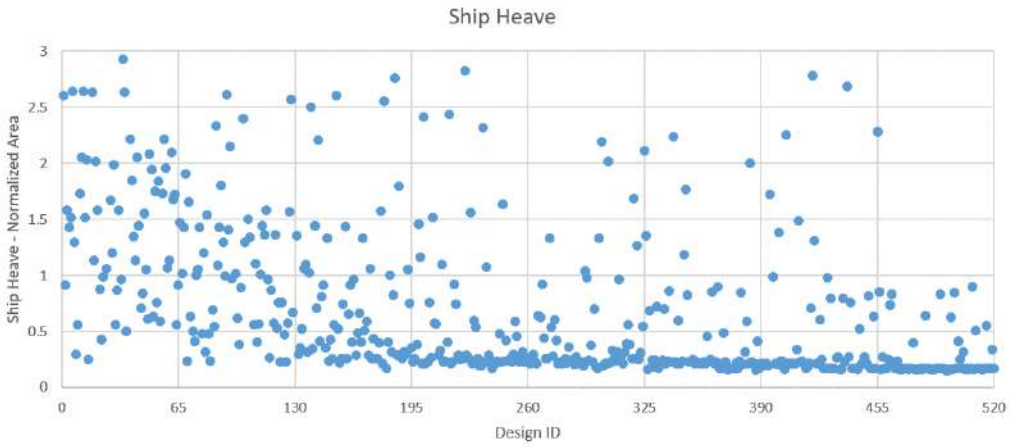

Figure 6.12: Objective History - JONSWAP spectrum ($H_S = 2.0m$ and $T_P = 8.6s$) - Fitness criteria: Vessel Heave Motion.

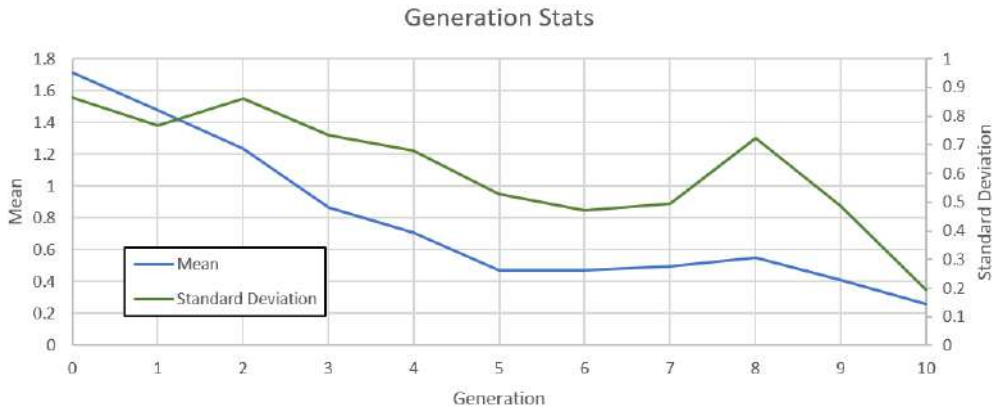

Figure 6.13: Generation Statistics - JONSWAP spectrum ($H_S = 2.0m$ and $T_P = 8.6s$) - Fitness criteria: Vessel Heave Motion.

Table 6.6: Optimum moonpool particulars - JONSWAP spectrum ($H_S = 2.0m$ and $T_P = 8.6s$) - Fitness criteria: Vessel Heave Motion.

Description	Symbol	Magnitude	Unit
Moonpool's length on bottom	l_b	41.09	m
Moonpool's breadth on bottom	b_b	29.48	m
Moonpool's breadth on deck	b_d	29.48	m
Postion (from transom)	P	56.56	m
Cutout angle	α	121.52	$^\circ$

frequency $0.59rad/s$ ($10.6s$) is a high amplitude resonant peak, but as long as the sea do not have considerable wave energy density at this value, it does not have weight in the optimization process.

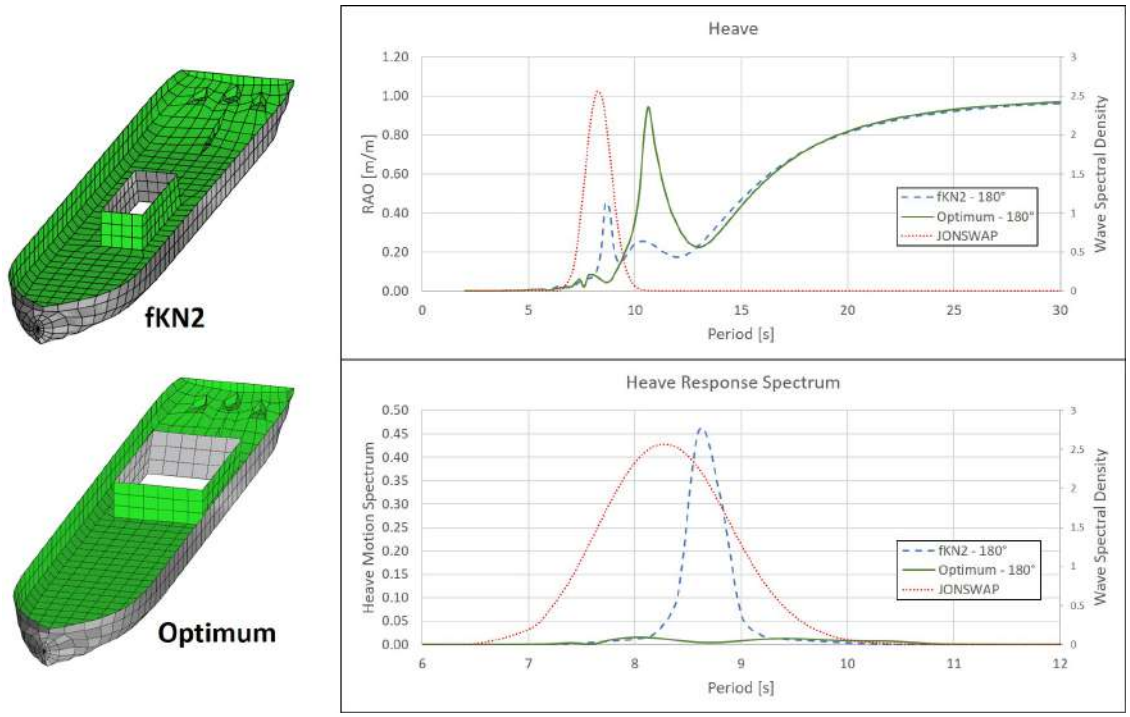

Figure 6.14: Comparison of heave RAO and response spectrum between optimum and *default* moonpool - JONSWAP spectrum ($H_S = 2.0m$ and $T_P = 8.6s$) - Fitness criteria: Vessel Heave Motion.

The RAO of water motion inside moonpool and response spectrum is presented in Figure 6.15. It is interesting here to notice that this ship provides slightly lower water motion inside moonpool than the considered optimum moonpool on previous analysis. This shows that variation in percentage of mutation or increase in the number of individuals or generations would provide more reliable results.

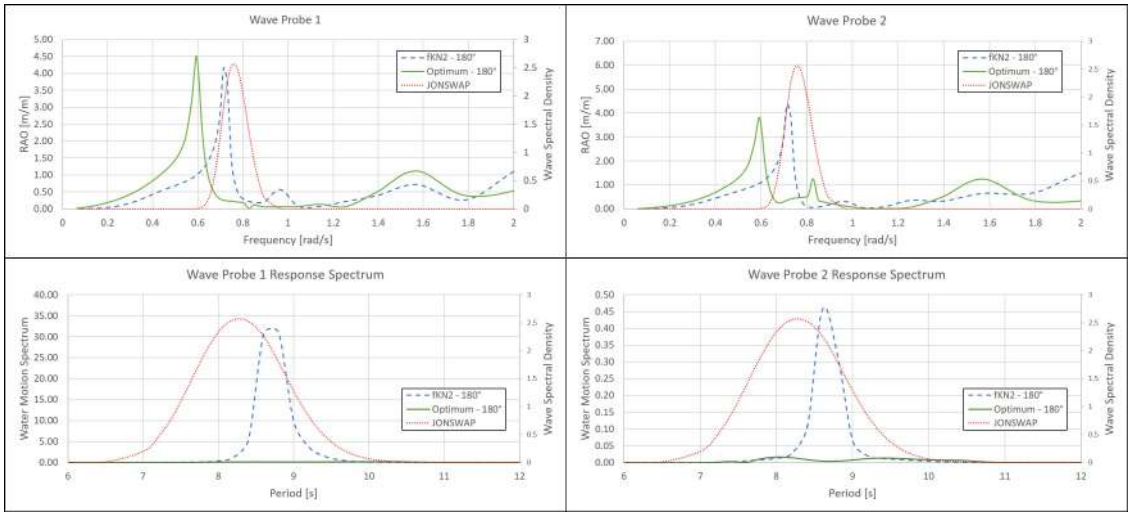

Figure 6.15: Comparison of free surface elevation RAOs and response spectra between optimum and *default* moonpool - JONSWAP spectrum ($H_S = 2.0m$ and $T_P = 8.6s$) - Fitness criteria: Vessel Heave Motion.

Observing Figures 6.10, 6.11, 6.14 and 6.15 we may notice an interesting characteristic confirming the purpose of the optimizer, that is the fact of the *default* moonpool higher peak inside the spectrum range of frequencies disappears in the *optimum* profile but it may appear a new peak (maybe even higher) on another frequency that is not related with the sea being analyzed. It reinforces the idea that there is no optimum moonpool for general uses but an optimum for a specific purpose.

Chapter 7

Conclusions and Future Work

7.1 Conclusions

This is a relatively recent topic and the quantity of papers published shows this is a state-of-art problem. This brings a motivation of using an optimization algorithm in order to discover a moonpool design that has better performance in a specific random sea. Thus, it is possible to design a drillship that may reduce downtime in critical operations. This bring technological contribution to the offshore area, as for the first time, this thesis applies the GA methodology for a drillship. The moonpool size influences the drillship behavior, which influences the internal motion on the moopool. It may be easily used in the preliminary design process.

Analytical Approach

Mathematical model derived for a squared moonpool using conservation of momentum in a control volume was first deduced in this thesis based on AALBERS [24] work, where the cylinder moonpool is analyzed.

Numerical Approach

Turbulence analysis provided us the information that the turbulence modeling in this case may be negligible and we also could notice that the edge angle plays important role on the eddy shedding, and thus the edges angle are related with the damping of water motion inside moonpool.

We may notice that is hard to predict analytically frequency and consequently other variables of motion, so numerical and experimental are hardly necessary for this kind of study.

Moonpool presence varies the ship motion and it may be seen as damper of that. There are other works in literature studying it for this purpose.

Regarding the *lid technique* is a good mathematical workaround to consider viscous effects inside moonpool. In this work we calculate numerically the equivalent linearized damping coefficient B_{eq} relative to the critical damping coefficient B_{Crit} that may be calculated for a specific squared moonpool design by Equation (3.4). Then, it is possible to see the variation in the RAO values calculated in potential theory when considering the viscous damping. The variation is mainly in the resonant peaks amplitude.

Genetic Algorithm

Heave and water motion inside moonpool are strongly coupled but the optimization of one does not necessarily means the optimization of the other motion as noticed in the results, so the engineer must be aware of the necessary purpose for better optimization. That also brings discussion on one of the main goals of this thesis as long as with the genetic algorithm solver we may find an optimum moonpool that would change the overall ship motions.

An apparently obvious conclusion that is reinforced by the results is that moonpool optimization depends on where it will exactly operate, so it is important to previously study the sea where it will be acting most part of the time in preliminary design.

7.2 Future Works

This thesis was divided in two parts and there are possibilities of future works in both ways.

Analytical Approach

A possible addition in future works would be the consideration of the cutout angle and that would clarify the importance of the angle in natural frequency and also in the damping calculation.

Numerical Approach

In the V&V process, other verification steps like *roundoff error* (changing machine accuracy), *iterative convergence error* (change residuals), *temporal discretization error* (using different time steps in the temporal mesh) would give more confidence in the numerical results, making the result more robust. Besides it is not used directly in the optimization, it enriches the work and also bring more understanding in the physics of phenomenon.

The turbulence analysis would be improved in future works, considering better refinement increasing the number of nodes inside moonpool and enhancing the discretization on boundary layer.

In parallel to this work, the author already started a study based on KNOTT and FLOWER [73] work simulating outflow in a cylinder moonpool (Figure 7.1). It is an important analysis to show the consequence of vortice shredding and maybe it would bring knowledge of other possible variation in moonpool profile for damping increasing. It contribution in the motion may be seen in the non-linear term of the Equation (3.1).

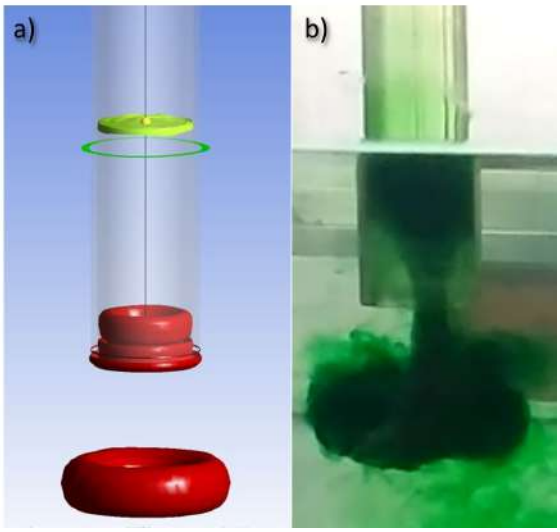

Figure 7.1: *a)* Numerical analysis and *b)* experimental test of outflow vortices in decay test inside a cylinder done in LOC facilities.

It would be adequate in *Numerical Forced Heave Oscillation* simulation to run more time steps in order to see the phase behavior and also how the relative motion decreases. In *Numerical Regular Wave with Captive vessel*, shifting the phase of inlet wave (Figure 4.28) to fit with initial condition will help convergence and probably will make the simulation to run faster. Another issue in this simulation and in *Freely Floating Vessel Test* is about use the right wave theory for the values of depth and wave amplitude. The first order Airy was used instead of Second Order Stokes that is the proper one for better representation.

Validation of numerical results with experimental analysis would enlighten all the physics simulated and give the final confidence necessary in the results. The results in model scale of freely floating tests were done purposefully as the Laboratory of Waves and Currents (Laboratório de Ondas e Correntes - LOC) already has available the two models, with the same particulars presented in Table 4.16, as they were used in previous researches. Also, in LOC facilities we have the necessary tools and wave basin for proper analysis.

In potential theory solvers, is possible to analyze each wave component separately, i.e., incident, diffraction and radiation. This may show us more information about the physic behavior with modification of some moonpool parameters and may bring new conclusions.

For artificial damping generic proper calculation, using lid technique, more studies for validation and application of correct values in other moonpool profiles is necessary.

Genetic Algorithm

The code can be modified to include other position and size parameters, for instance it is possible to include a cutout step like the one in CHALKIAS and KRIJGER [9] work (Figure 1.8.b) increasing the possibilities of design.

It is already in code a routine for other headings instead of just using $\beta = 180°$. This option is not available for the user to choose yet, but is easy to implement as it is already in algorithm. Another improvement in the code is the addition of finite depth water calculation with depth setting being an option for the user.

This work did not consider the addition of fitting inside moonpool for damping increase, as cofferdam, guidance structures and others damping devices in general. It may be think as opportunity for future works with genetic algorithm, considering a moonpool profile and varying damping devices position and size.

Experimental analysis with optimum moonpool in model scale would validated the GAUFRJ software giving the final confidence in the results making it ready for final users.

Bibliography

[1] LEFFLER, W. L., PATTAROZZI, R., STERLING, G. *Deepwater Petroleum Exploration & Production: A Nontechnical Guide*. 2nd ed. Tulsa, Oklahoma, USA, PennWell Corporation, 2011. ISBN: 1593702531.

[2] OFFSHORE MAGAZINE. "Modern offshore fleet comprised of same rig types as in the 1950s". Available: `https://www.offshore-mag.com/drilling-completion/article/16760817/modern-offshore-fleet-comprised-of-same-rig-types-as-in-the-1950s`, 2007. Accessed: 2020-06-23.

[3] HAMMARGREN, E., TÖRNBLOM, J. *Effect of the Moonpool on the Total Resistance of a Drillship*. M.sc. thesis, Chalmers University of Technology, Gothenburg, Sweeden, 2012.

[4] FUKUDA, K. "Behavior of Water in Vertical Well with Bottom Opening of Ship, and its Effects on Ship-Motion", *Journal of the Society of Naval Architects of Japan*, v. 141, pp. 107–122, May 1977. doi: 10.2534/jjasnaoe1968.1977.107.

[5] MOLIN, B. "On the piston and sloshing modes in moonpools", *Journal of Fluid Mechanics*, v. 430, pp. 27–50, 2001. doi: 10.1017/S0022112000002871.

[6] GAILLARDE, G., COTTELEER, A. *Water Motion in Moonpools, Empirical and Theoretical Approach*. Nr. 2435, Maritime Research Institute Netherlands (MARIN) and HMC Heerema, Netherlands, June 2004.

[7] LEE, S.-M., IM, N.-K. "The Numerical Study on the Flow Characteristics in Two-Dimensional Moonpool in Waves", *Journal of Navigation and Port Research*, v. 141, n. 5, pp. 443–450, October 2014. doi: 10.5394/KINPR.2014.38.5.443.

[8] PARK, J. J., KIM, M. S., LEE, H. S., et al. "Development of Design Technologies for Optimum Moonpool Shapes of Drill Ship". In: *Proceedings of the 26th International Conference on Offshore Mechanics and Arctic Engineering*,

OMAE2007-29182, pp. 421–426, San Diego, California, USA, June 2007. doi: 10.1115/OMAE2007-29182.

[9] CHALKIAS, D., KRIJGER, J. W. "Effect of Moonpool Shape and Dimensions on Drillship Operability". In: *Proceedings of the ASME 2018 37th International Conference on Ocean, Offshore and Arctic Engineering*, OMAE2018-77499, Madrid, Spain, June 2018. doi: 10.1115/OMAE2018-77499.

[10] FALTINSEN, O. M. *Sea Loads on Ships and Offshore Structures*. 1st ed. Cambridge, UK, Cambridge University Press, 1990. ISBN: 0521458706.

[11] JOURNÉE, J., MASSIE, W. *OFFSHORE HYDROMECHANICS*. 1st ed. Delft, Netherlands, Delft University of Technology, January 2001.

[12] BUREAU VERITAS. *Hydrostar for Experts User Manual*. Bureau Veritas, Neuilly-sur-Seine, France, May 2018. Version V7.3.

[13] MÉHAUTE, B. L. *An Introduction to Hydrodynamics and Water Waves*. 1st ed. Pasadena, California, USA, Springer Science+Business Media, LLC, 1976. ISBN: 3642855695.

[14] ANSYS, INC. *ANSYS Fluent User's Guide*. ANSYS, Inc., Canonsburg, PA, USA, August 2019. Release 2019 R3.

[15] REYNOLDS, O. "An experimental investigation of the circumstances which determine whether the motion of water shall be direct or sinuous, and of the law of resistance in parallel channels", *Philosophical Transactions of the Royal Society of London*, v. 174, n. Part III, pp. 935–982, 1883. doi: 10.1098/rstl.1883.0029.

[16] BAKKER, A. "Lecture 10 - Turbulence Models - Applied Computational Fluid Dynamics". Available: `http://www.bakker.org/dartmouth06/engs150/10-rans.pdf`, 2006. Accessed: 2020-07-22.

[17] CARLIER, J., STANISLAS, M. "Experimental study of eddy structures in a turbulent boundary layer using particle image velocimetry", *Journal of Fluid Mechanics*, v. 535, pp. 143–188, 2005. doi: 10.1017/S0022112005004751.

[18] BAKKER, A. "Lecture 5 - Solution Methods - Applied Computational Fluid Dynamics". Available: `http://www.bakker.org/dartmouth06/engs150/05-solv.pdf`, 2006. Accessed: 2020-07-27.

[19] BAKKER, A. "1Lecture 16 - Free Surface Flows - Applied Computational Fluid Dynamics". Available: http://www.bakker.org/dartmouth06/engs150/16-fsurf.pdf, 2006. Accessed: 2020-07-30.

[20] YANG, C. X., THAM, L. G., FENG, X. T., et al. "Two-Stepped Evolutionary Algorithm and Its Application to Stability Analysis of Slopes", *Journal of Computing in Civil Engineering*, v. 18, n. 2, pp. 145–153, 2004. doi: 10.1061/(ASCE)0887-3801(2004)18:2(145).

[21] JAOUËN, F., KOOP, A., VATINEL, L. "URANS Predictions of Low-Frequency Damping of a LNGC". In: *Proceedings of ASME 38th International Conference on Ocean, Offshore and Arctic Engineering*, OMAE2019-95171, Glasgow, Scotland, June 2019. doi: 10.1115/OMAE2019-95171.

[22] PIERSON, W. J., NEUMANN, G., JAMES, R. W. *Practical Methods for Observing and Forecasting Ocean Waves by Means of Wave Spectra and Statistics: H. O. Pub. No. 603*. 2nd ed. Mississippi, Hydrographic Office, 1958.

[23] IADC. "Dual activity drilling turns in 20-40% time savings", *Drilling Contractor Magazine*, September/October 2001. Disponível em: <https://www.drillingcontractor.org/dcpi/2001/dc-septoct01/s1-dualact.pdf>. pp. 26-28.

[24] AALBERS, A. B. "The Water Motions in a Moonpool", *Ocean Engineering*, v. 11, n. 6, pp. 557–579, 1984. doi: 10.1016/0029-8018(84)90001-5.

[25] NEWMAN, J. N. *Marine Hydrodynamics*. 1st ed. Cambridge, Massachussetts, USA, MIT Press, 1977. ISBN: 0262140268.

[26] MADHANI, J. T. *Sloshing motion of water in a moonpool*. M.sc. thesis, University of Strathclyde, Glasgow, Scotland, November 1985.

[27] HENRIQUES, J., PORTILLO, J., GATO, L., et al. "Design of oscillating-water-column wave energy converters with an application to self-powered sensor buoys", *Energy*, v. 112, pp. 852 – 867, 2016. ISSN: 0360-5442. doi: 10.1016/j.energy.2016.06.054. Disponível em: <http://www.sciencedirect.com/science/article/pii/S0360544216308283>.

[28] ARIS, R. "The symmetry of the stress tensor". In: *Vectors, Tensors and the Basic Equations of Fluid Mechanics*, 1st ed., cap. 5, pp. 102–104, New York, USA, Dover Publications, 1990. ISBN: 0486661105.

[29] VERSTEEG, H. K., MALALASEKERA, W. *An Introduction to Computational Fluid Dynamics: The Finite Volume Method*. 2nd ed. Cambridge, Massachussetts, USA, Pearson Education Ltd., 2007. ISBN: 0131274988.

[30] HADAMARD, J. S. "Sur les Problèmes aux Dérivées Partielles et Leur Signification Physique", *Princeton University Bulletin*, v. 13, n. 4, pp. 49–52, April 1902.

[31] ANSYS, INC. *ANSYS Fluent Theory Guide*. ANSYS, Inc., Canonsburg, PA, USA, August 2019. Release 2019 R3.

[32] STOKES, G. G. "On the Effect of the Internal Friction of Fluids on the Motion of Pendulums", *Transactions of the Cambridge Philosophical Society*, v. 9, n. Part II, pp. 8–106, 1851. doi: 10.1017/CBO9780511702266.002.

[33] SOMMERFELD, A. "Ein Beitrag zur hydrodynamischen Erkläerung der turbulenten Flüssigkeitsbewegüngen (A Contribution to Hydrodynamic Explanation of Turbulent Fluid Motions)". In: *Proceedings of the 4th International Mathematical Congress*, p. 116–124, Rome, Italy, April 1908.

[34] REYNOLDS, O. "On the dynamical theory of incompressible viscous fluids and the determination of the criterion", *Philosophical Transactions of the Royal Society of London*, v. 186, n. 0, pp. 123–164, 1895. doi: 10.1098/rsta.1895.0004.

[35] FAVRE, A. "Equations des gaz turbulents compressibles", *Journal de Mecanique*, v. 4, n. 3, pp. 361–391, 1965.

[36] BRADSHAW, P., CEBECI, T., WHITELAW, J. H. *Engineering Calculation Methods for Turbulent Flow*. 1st ed. London, Academic Press, 1981. ISBN: 0121245500.

[37] BOUSSINESQ, J. V. *Théorie Analytique de la Chaleur Mise en Harmonie avec la Thermodynamique et la Théorie Mécanique de la Lumière*. 1st ed. Paris, Gauthier-Villars, Imprimeur-Libraire, 1903. Tome II - Volume II.

[38] SPALART, P. R., ALLMARAS, S. R. "A one-equation turbulence model for aerodynamic flows". In: *30th Aerospace Sciences Meeting and Exhibit*, Reno, Nevada, USA, January 1992. doi: 10.2514/6.1992-439. AlAA-92-0439.

[39] WILCOX, D. C. *Turbulence Modeling for CFD*. 1st ed. La Cañada, California, USA, DCW Industries, Inc., 1994. ISBN: 0963605100. Second Printing.

[40] PRANDTL, L. "Bericht über Untersuchungen zur ausgebildeten Turbulenz", *ZAMM - Journal of Applied Mathematics and Mechanics / Zeitschrift für Angewandte Mathematik und Mechanik*, v. 5, n. 2, pp. 136–139, April 1925. doi: 10.1002/zamm.19250050212.

[41] BRADSHAW, P. "Bericht über Untersuchungen zur ausgebildeten Turbulenz", *Nature*, v. 249, n. 5453, pp. 135–136, May 1974. doi: 10.1038/249135b0.

[42] LAUNDER, B., SPALDING, D. "The numerical computation of turbulent flows", *Computer Methods in Applied Mechanics and Engineering*, v. 3, n. 2, pp. 269–289, March 1974. doi: 10.1016/0045-7825(74)90029-2.

[43] HENKES, R., VAN DER FLUGT, F., HOOGENDOORN, C. "Natural-convection flow in a square cavity calculated with low-Reynolds-number turbulence models", *International Journal of Heat and Mass Transfer*, v. 34, n. 2, pp. 377–388, February 1991. doi: 10.1016/0017-9310(91)90258-G.

[44] WILCOX, D. C. "Reassessment of the scale-determining equation for advanced turbulence models", *AIAA Journal*, v. 26, n. 11, pp. 1299–1310, 1988. doi: 10.2514/3.10041.

[45] MENTER, F. R. *Improved two-equation κ-omega turbulence models for aerodynamic flows*. Technical Report NASA-TM-103975, A-92183, NAS 1.15:103975, NASA Ames Research Center, Moffett Field, CA, USA, October 1992.

[46] MENTER, F. R. "Two-equation eddy-viscosity turbulence models for engineering applications", *AIAA Journal*, v. 32, n. 8, pp. 1598–1605, 1994. doi: 10.2514/3.12149.

[47] SIMCENTER STAR-CCM+. *User Guide*. Siemens PLM Software, 2018. Version 13.06.

[48] SMAGORINSKY, J. "GENERAL CIRCULATION EXPERIMENTS WITH THE PRIMITIVE EQUATIONS: I. THE BASIC EXPERIMENT*", *Monthly Weather Review*, v. 91, n. 3, pp. 99–164, 03 1963. ISSN: 0027-0644. doi: 10.1175/1520-0493(1963)091⟨0099:GCEWTP⟩2.3.CO;2.

[49] DEARDORFF, J. W. "A numerical study of three-dimensional turbulent channel flow at large Reynolds numbers", *Journal of Fluid Mechanics*, v. 41, n. 2, pp. 453–480, 1970. doi: 10.1017/S0022112070000691.

[50] HUNT, J.C.R. WRAY, A., MOIN, P. "Eddies, streams, and convergence zones in turbulent flows". In: *Proceedings of the 1988 Summer Program*, pp. 193–208, Stanford University, California, USA, December 1988.

[51] SCHLICHTING (DECEASED), H., GERSTEN, K. "Two–Layer Structure of the Velocity Field and the Logarithmic Overlap Law". In: *Boundary-Layer Theory*, 9th ed., cap. 17, pp. 519–524, Heidelberg, German, Springer-Verlag, 2017. ISBN: 978-3-662-52917-1.

[52] PATANKAR, S., SPALDING, D. "A calculation procedure for heat, mass and momentum transfer in three-dimensional parabolic flows", *International Journal of Heat and Mass Transfer*, v. 15, n. 10, pp. 1787 – 1806, 1972. ISSN: 0017-9310. doi: 10.1016/0017-9310(72)90054-3.

[53] PATANKAR, S. *Numerical Heat Transfer and Fluid Flow*. Series in computational methods in mechanics and thermal sciences. University of California, Hemisphere Publishing Corporation, 1980. ISBN: 0070487405.

[54] DOORMAAL, J. P. V., RAITHBY, G. D. "ENHANCEMENTS OF THE SIMPLE METHOD FOR PREDICTING INCOMPRESSIBLE FLUID FLOWS", *Numerical Heat Transfer*, v. 7, n. 2, pp. 147–163, 1984. doi: 10.1080/01495728408961817.

[55] ISSA, R. "Solution of the implicitly discretised fluid flow equations by operator-splitting", *Journal of Computational Physics*, v. 62, n. 1, pp. 40–65, 1986. ISSN: 0021-9991. doi: 10.1016/0021-9991(86)90099-9.

[56] COURANT, R., ISAACSON, E., REES, M. "On the solution of nonlinear hyperbolic differential equations by finite differences", *Communications on Pure and Applied Mathematics*, v. 5, n. 3, pp. 243–255, 1952. doi: 10.1002/cpa.3160050303.

[57] WARMING, R. F., BEAM, R. M. "Upwind Second-Order Difference Schemes and Applications in Aerodynamic Flows", *AIAA Journal*, v. 14, n. 9, pp. 1241–1249, 1976. doi: 10.2514/3.61457.

[58] LEONARD, B. "A stable and accurate convective modelling procedure based on quadratic upstream interpolation", *Computer Methods in Applied Mechanics and Engineering*, v. 19, n. 1, pp. 59–98, 1979. ISSN: 0045-7825. doi: 10.1016/0045-7825(79)90034-3.

[59] VAN LEER, B. "Towards the ultimate conservative difference scheme. V. A second-order sequel to Godunov's method", *Journal of Computational*

Physics, v. 32, n. 1, pp. 101–136, 1979. ISSN: 0021-9991. doi: 10.1016/0021-9991(79)90145-1.

[60] HARTEN, A. "High resolution schemes for hyperbolic conservation laws", *Journal of Computational Physics*, v. 49, n. 3, pp. 357–393, 1983. ISSN: 0021-9991. doi: 10.1016/0021-9991(83)90136-5.

[61] PEYRET, R. *Handbook of Computational Fluid Mechanics*. Nice, France, Elsevier Science & Technology Book, 1996. ISBN: 0125530102.

[62] HARLOW, F. H., WELCH, J. E. "Numerical Calculation of Time-Dependent Viscous Incompressible Flow of Fluid with Free Surface", *The Physics of Fluids*, v. 8, n. 12, pp. 2182–2189, 1965. doi: 10.1063/1.1761178.

[63] RHIE, C. M., CHOW, W. L. "Numerical study of the turbulent flow past an airfoil with trailing edge separation", *AIAA Journal*, v. 21, n. 11, pp. 1525–1532, 1983. doi: 10.2514/3.8284.

[64] HIRT, C., NICHOLS, B. "Volume of fluid (VOF) method for the dynamics of free boundaries", *Journal of Computational Physics*, v. 39, n. 1, pp. 201–225, 1981. ISSN: 0021-9991. doi: 10.1016/0021-9991(81)90145-5.

[65] YOUNGS, D. "Time-Dependent Multi-material Flow with Large Fluid Distortion". In: *Numerical Methods for Fluid Dynamics*, v. 24, pp. 273–285, Cambridge, Massachusetts, EUA, Academic Press, 01 1982.

[66] AMERICAN INSTITUTE OF AERONAUTICS AND ASTRONAUTICS (AIAA). *Guide for the Verification and Validation of Computational Fluid Dynamics Simulations*. AIAA G-077-1998(2002), American Institute of Aeronautics and Astronautics (AIAA), Reston, Virginia, USA, June 2002.

[67] ROACHE, P. J. *Verification and Validation in Computational Science and Engineering*. 1st ed. Albuquerque, New Mexico, USA, Hermosa Publishers, 1998. ISBN: 0913478083.

[68] JOURNAL OF FLUIDS ENGINEERING. "Procedure for Estimation and Reporting of Uncertainty Due to Discretization in CFD Applications", *Journal of Fluids Engineering*, v. 130, n. 7, pp. 1–4, July 2008. doi: 10.1115/1.2960953.

[69] 25TH ITTC 2008. *Uncertainty Analysis in CFD Verification and Validation Methodology and Procedures*. ITTC – Recommended Procedures and Guidelines 7.5-03-01-01 (Revision 02), International Towing Tank Conference (ITTC), Fukuoka, Japan, September 2008.

[70] HOLLAND, J. H. *Adaptation in Natural and Artificial Systems*. Ann Arbor, MI, University of Michigan Press, 1975.

[71] GOLDBERG, D. E. *Genetic Algorithms in Search, Optimization and Machine Learning*. 1st ed. USA, Addison-Wesley Longman Publishing Co., Inc., 1989. ISBN: 0201157675.

[72] DNV GL. *Modelling and analysis of marine operations*. Recommended Practice DNVGL-RP-N103, DNV GL, Høvik, Norway, July 2017. Edition July 2017.

[73] KNOTT, G., FLOWER, J. "Measurement of Energy Losses in Oscillatory Flow Through a Pipe Exit", *Applied Ocean Research*, v. 2, n. 4, pp. 155–164, October 1980. doi: 10.1016/0141-1187(80)90013-9.

[74] RAO, S. S. *Mechanical Vibrations*. 5th ed. University of Miami, USA, Pearson Education Ltd., 2011. ISBN: 0132128195.

[75] FROUDE, W. "On the influence of resistance upon the rolling of ships", *Naval Science*, v. 1, pp. 411–429, April to October 1872.

[76] HIMENO, Y. *Prediction of Ship Roll Damping - A State of the Art*. Publication Nr. 239, Department of Naval Architecture and Marine Engineering, Ann Arbor, Michigan, USA, September 1981.

[77] SIR THOMSON (LORD KELVIN), W. "On Ship Waves", *Proceedings of the Institution of Mechanical Engineers*, v. 38, n. 1, pp. 409–434, 1887. doi: 10.1243/PIME_PROC_1887_038_028_02.

[78] GAROFALLIDIS, D. A. *Experimental and Numerical Investigation of the Flow around a Ship model at Various Froude Numbers*. Ph.d. thesis, National Technical University of Athens, Athens, Greece, June 1996.

[79] NOBLESSE, F., ZHANG, C., HE, J., et al. "Observations and computations of narrow Kelvin ship wakes", *Journal of Ocean Engineering and Science*, v. 1, n. 1, pp. 52–65, 2016. ISSN: 2468-0133. doi: 10.1016/j.joes.2015.12.005.

[80] BENEDETTI, L., CHEN, W., CLELLAND, D., et al. "Dictionary of Hydromechanics - 2017 Edition". In: *28th International Towing Tank Conference (ITTC)*, pp. 111,133, September 2017. Prepared by the Quality Systems Group of the 28th ITTC.

[81] WAMIT, INC. *WAMIT User Manual*. WAMIT, Inc., Chestnut Hill, MA, USA, October 2012. Version 7.0.

[82] OORTMERSSEN, G. V. "Hydrodynamic Interaction Between Two Structures, Floating in Waves". In: *Proceedings of the 2nd International Conference on Behaviour of Offshore Structures, BOSS'79*, v. 1, pp. 339–356, London, England, 1979. Paper 26, Publication 634 of the NSMB, Paper: P1979-4 Proceedings.

Appendix A

Equation of Motion for the Moonpool in a Floating Vessel

This section provides the original deduction of the equation of motion for the *squared moonpool* that appears throughout this work. First of all, we need to describe the conservation law of momentum, so-called *second law of mechanics*. It states that the rate of change of linear momentum of the medium inside a control volume must be equal to the external force exerted on it. For an arbitrary volume Ω, with surface $d\Omega$, at time t, mathematical statement of second law is:

$$\frac{D}{Dt}\iiint_{\Omega} \rho v_j \, dV = \iiint_{\Omega} \rho f_i \, dV + \iint_{d\Omega} P_{jk} n_k \, dA \, , \tag{A.1}$$

where ρ is specific density $[kg/m^3]$, f_i is body force density $[m/s^2]$, P_{jk} is stress tensor in index notation $[N/m^2]$, n_k is the outward-pointing unit normal surface vector and

$$\frac{D}{Dt} \equiv \frac{\partial}{\partial t} + \vec{v} \cdot \vec{\boldsymbol{\nabla}} = \frac{\partial}{\partial t} + \sum_{i=1}^{3} \frac{\partial x_i}{\partial t} \frac{\partial}{\partial x_i} \tag{A.2}$$

is the material (or substantive) derivative, in which $\vec{v}$ is velocity vector $[m/s]$ and $\vec{\boldsymbol{\nabla}}$ is *nabla operator*.

Reynolds transport theorem states that:

$$\frac{D}{Dt}\iiint_{\Omega} \Psi \, dV = \iiint_{\Omega} \frac{\partial \Psi}{\partial t} \, dV + \iint_{d\Omega} \Psi \left(\vec{v} \cdot \vec{n}\right) \, dA \, , \tag{A.3}$$

where the function Ψ may be tensor, vector or scalar-valued

Using Equation (A.3) on left-hand side (LHS) of the conservation law (Equation (A.1)) yields:

$$\frac{\partial}{\partial t}\iiint_{\Omega} \rho v_j \, dV + \iint_{d\Omega} \rho v_j \left(\vec{v} \cdot \vec{n}\right) \, dA = \iiint_{\Omega} \rho f_i \, dV + \iint_{d\Omega} P_{jk} n_k \, dA \, . \tag{A.4}$$

Now, consider the control volume Ω that represents a rectangle shaped moonpool in Figure A.1.

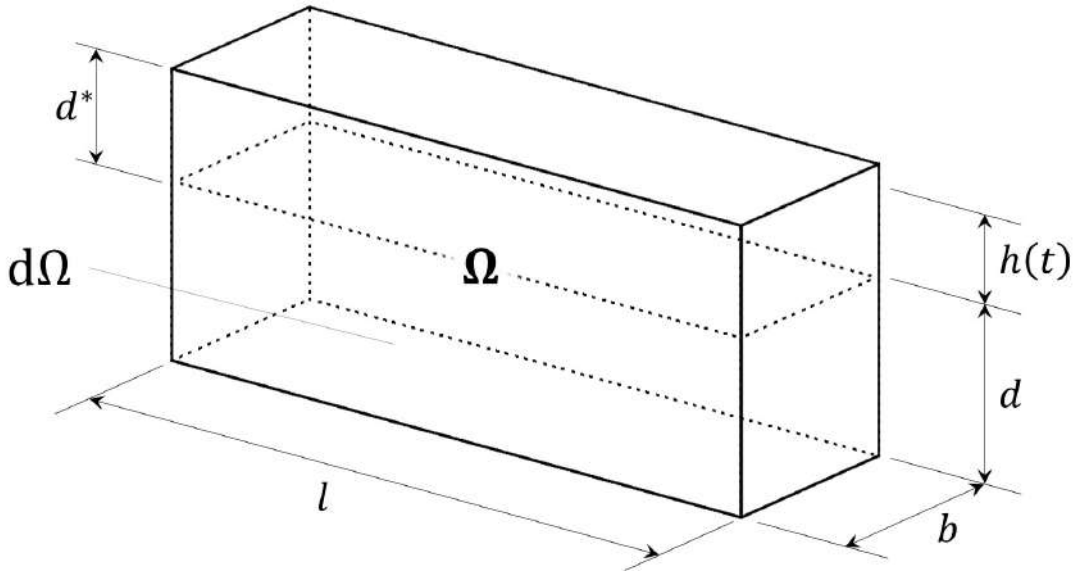

Figure A.1: The control volume Ω with surface $d\Omega$ of rectangular shaped moonpool.

Inside this chosen control volume, two media exist, water and air. It can be shown that the contribution in Equation (A.4) due to the air can be neglected, for:

$$\rho_{air} \ll \rho_w. \tag{A.5}$$

Therefore, as the only body force (f_i) acting in the system is due the gravity (g) field, the conservation law (Equation (A.4)) for moonpool control volume (Figure A.1) may be written as:

$$\frac{\partial}{\partial t}\left[\rho_w bl\,(d+h)\,\frac{\mathrm{d}h}{\mathrm{d}t}\right] - \rho_w bl\left(\frac{\mathrm{d}h}{\mathrm{d}t}\right)^2 = -\rho_w gbl\,(d+h) + \iint_{d\Omega} P_{jk} n_k\, dA\ . \tag{A.6}$$

Last term in the right-hand side (RHS) describes the forces due to external pressure. Pressure on vertical side of moonpool yield a net force which is zero due to symmetry. Upper and lower surface, however, should be considered separately.

At upper surface the moonpool is opened, so atmospheric pressure (p_{atm}) is the condition and the surface integral can be written as:

$$\iint_{Upper} P_{jk} n_k\, dA = blp_{atm}\ . \tag{A.7}$$

At lower surface the fluid pressure exists, which is given by *unsteady Bernoulli's law*:

$$p_{lower} + \frac{1}{2}\rho\left(\vec{\boldsymbol{\nabla}}\phi\right)^2 + \rho gz + \rho\frac{\partial\phi}{\partial t} + p_{atm} = 0\ , \tag{A.8}$$

where z is the elevation of the calculation point in relation to a reference plane (at draft $z = 0$), with the positive *z-direction* pointing upward, so in the direction opposite to the gravitational acceleration and the flow velocity ($\vec{\nabla}\phi$) can be described as the gradient of a velocity potential ϕ.

So:

$$p_{lower} = -\frac{1}{2}\rho\left(\frac{\mathrm{d}h}{\mathrm{d}t}\right)^2 + \rho g d - \rho\frac{\partial\phi}{\partial t} - p_{atm} \; . \tag{A.9}$$

Applying p_{lower} at the lower integral:

$$\iint_{Lower} p_{lower}\, dA = -\frac{1}{2}\rho b l\left(\frac{\mathrm{d}h}{\mathrm{d}t}\right)^2 + \rho b l g d - p_{atm} b l - \iint_{Lower}\rho\frac{\partial\phi}{\partial t}\, dA \; . \tag{A.10}$$

Substituting (A.10) and (A.7) in Equation (A.6) yields the equation of motion of the rectangle shaped moonpool water column for the case that the ship hull is fixed:

$$\rho_w b l\,(d+h)\,\frac{\mathrm{d}^2h}{\mathrm{d}t^2} + \frac{1}{2}\rho_w b l\left(\frac{\mathrm{d}h}{\mathrm{d}t}\right)^2 + \rho_w g b l h = \iint_{Lower}\rho\frac{\partial\phi}{\partial t}\, dA \; . \tag{A.11}$$

Assuming the fluid to be ideal (*isotropic* stress tensor P_{jk}) and irrotational ($\vec{\nabla}\times\vec{v}$) it is possible to obtain RHS of Equation (A.11). In linear potential theory, this result can be expressed by means of an added mass (M_a) and damping coefficient (B_l), neglecting higher order terms, by:

$$\iint_{Lower}\frac{\partial\phi}{\partial t}\, dA = M_a\frac{\mathrm{d}^2h}{\mathrm{d}t^2} + B_l\frac{\mathrm{d}h}{\mathrm{d}t} \; . \tag{A.12}$$

When no external wave force is present, the equation of motion for water in moonpool in a captive body is:

$$\left[\rho_w b l\,(d+h) + M_a\right]\ddot{h} + B_l\dot{h} + \rho_w g b l h + \frac{1}{2}\rho_w b l\dot{h}^2 = 0 \; , \tag{A.13}$$

The presence of viscous effects until now is neglected. A study of KNOTT and FLOWER [73], in which it is analyzed the presence of vortices at the in and outflow of water of a pipe, they included this damping with an additional contribution proportional to the velocity squared. The Equation (A.13) can be written as:

$$\left[\rho_w b l\,(d+h) + M_a\right]\ddot{h} + B_l\dot{h} + B_q\dot{h}\dot{h} + \rho_w g b l h = 0 \; . \tag{A.14}$$

It is possible to analyze the water oscillation inside the moonpool in a free floating vessel describing it as a system of two floating structures in waves. OORTMERSSEN [82] has outlined a detailed theory about it. It is assumed that the water inside the moonpool is described by a frictionless moving piston inside the vessel and all

moonpool motions except heave are determined by the vessel. Knowing that it is possible to write the moonpool oscillatory motion results inside of a free floating vessel as follows:

$$\begin{aligned}&\left[\rho_w bl\left(d+h\right)+M_a\right]\ddot{h}+B_l\dot{h}+B_q\dot{h}|\dot{h}|+\rho_w gblh+\\&\left[d_{hz}+\rho_w bl\left(d+h\right)+M_a\right]\ddot{z_h}+\left[e_{hz}+B_l\right]\dot{z_h}+\rho_w gblz_h\\&=F_{wh}\ .\end{aligned}\tag{A.15}$$